

Precise Measurement of the Neutron Skin Thickness of ^{208}Pb and ^{48}Ca

A Dissertation Presented

by

Weibin Zhang

to

The Graduate School

in Partial Fulfillment of the Requirements

for the Degree of

Doctor of Philosophy

in

Physics

Stony Brook University

June 2022

Stony Brook University

The Graduate School

Weibin Zhang

We, the dissertation committee for the above candidate for the Doctor of Philosophy degree, hereby recommend acceptance of this dissertation.

Abhay Deshpande – Dissertation Advisor
Professor, Department of Physics and Astronomy

James M. Lattimer – Chairperson of Defense
Professor, Department of Physics and Astronomy

Jiangyong Jia
Professor, Department of Physics and Astronomy

Ciprian Gal
Assistant Research Professor
Mississippi State University

This dissertation is accepted by the Graduate School.

Eric Wertheimer
Dean of the Graduate School

Abstract of the Dissertation

**Precise Measurement of the Neutron Skin Thickness
of ^{208}Pb and ^{48}Ca**

by

Weibin Zhang

Doctor of Philosophy

in

Physics

Stony Brook University

2022

Despite great leaps of development in nuclear physics over the past century, we still don't have a comprehensive understanding of nuclear structure. This is mainly due to the lack of precise knowledge of neutron distribution inside nucleus. Electromagnetic probes are ineffective in probing neutrons, unlike their charged partners, the protons. Therefore, it is of great importance to constrain the neutron distributions experimentally. Heavy nuclei have more neutrons than protons in order to balance the repulsion between protons. In such neutron-rich nuclei, the extra neutrons are pushed out to the surface by the nuclear symmetry energy, forming the so-called "neutron skin". The neutron skin can be probed with a well-established experimental technique – parity-violating electron scattering (PVES). Using the scattering of longitudinally polarized electrons by an unpolarized target, PREX-II and CREX measure the small parity-violating asymmetry in cross sections. Employing electrons with opposite helicities the weak form factor, the neutron distribution and the neutron skin thickness of the target nucleus are extracted. With excellent beam qualities and dedicated instrumentation at Jefferson Lab, the asymmetry measurements are statistics-limited. We report the results of these two high-precision measurements and their implications on broad topics, from the nuclear structures to the neutron stars.

Contents

List of Figures	vii
Acknowledgements	xi
1 Introduction	1
1.1 Point-Neutron Radius and Neutron Skin	1
1.1.1 Theoretical Models	5
1.2 Symmetry Energy	9
1.3 Nuclear Structure and Neutron Stars	13
1.3.1 Ab-initio Method	14
1.3.2 Nuclear Density Functional Theory (DFT)	16
1.3.3 Neutron Stars	18
1.4 Physics Beyond the Standard Model (SM)	19
1.5 Symmetry and Asymmetry	20
1.5.1 Parity Symmetry	20
1.5.2 Parity Violation	22
1.6 Dynamics	29
1.7 Why Pb208 and Ca48	30
2 Experimental Setup	32
2.1 Beam Parameters	35
2.1.1 Uncertainty Budget	35
2.1.2 Figure Of Merits (FOM)	35
2.1.3 Helicity Flip Frequency	39
2.2 Continuous Electron Beam Accelerator Facility (CEBAF)	39
2.3 Polarized Electron Beam	42
2.3.1 Polarized Electron Source	42
2.3.2 Polarization Control	44
2.3.3 Polarimeters	49
2.4 Monitors	53
2.4.1 BPMs	54
2.4.2 BCMs	55
2.4.3 SAMs	57
2.4.4 Beam Modulation	57

2.5	Target	58
2.5.1	Target Cooling	60
2.5.2	Raster	60
2.5.3	Beamline Collimator and Sieve Slit Collimators	61
2.5.4	Septum	64
2.5.5	High Resolution Spectrometer (HRS)	65
2.5.6	Detector Package	66
2.5.7	Data Acquisition (DAQ)	70
3	Data Analysis	75
3.1	Raw Data	75
3.1.1	Cut	78
3.1.2	Beam Conditions	80
3.1.3	Raw Asymmetry	83
3.2	Beam False Asymmetry Correction	84
3.2.1	Regression	85
3.2.2	Beam Modulation (Dithering)	90
3.2.3	Lagrange Multiplier	93
3.3	Result	95
4	Transverse Asymmetry	97
4.1	Motivation for the Transverse Asymmetry	97
4.2	Measurement of the Transverse Asymmetry: the Method	104
4.3	Data	105
4.3.1	Data Analysis	106
4.3.2	Systematic Uncertainties	109
4.3.3	Dynamics	113
4.3.4	Final Result	113
5	Systematic Uncertainties	116
5.1	Q^2 and θ	117
5.2	Carbon Contamination in PREX-II	117
5.3	The CREX Acceptance Function	124
5.3.1	Transportation Matrix	124
5.3.2	Scattering Angle θ_{lab}	126
5.3.3	Data	128
5.3.4	Simulation	130
5.4	Other Systematic Uncertainties	136
6	Results and Discussion	137
6.1	Final Numbers	137
6.1.1	Neutron Skin Thickness	137
6.1.2	Density Dependence of the Symmetry Energy	140
6.2	Physical Implication	141
6.2.1	Nuclear Structure	141

6.2.2	Neutron Stars	144
6.3	Future Outlook	145
Bibliography		149
A	Symmetry Energy	158
A.1	^{208}Pb Foils Measurement	158

List of Figures

1.1	Characteristic of FFs w.r.t. different density distribution functions	4
1.2	eA scattering	6
1.3	xsection of ^{48}Ca	7
1.4	fermi distribution	7
1.5	Neutron distribution from FSUGold	8
1.6	Coulomb distortion	8
1.7	PV asymmetry for ^{208}Pb and ^{48}Ca	9
1.8	Correlation between ^{208}Pb neutron skin thickness against slope of the symmetry energy (L). The linear fit is $\Delta r_{np} = 0.101 + 0.00147L$. [19]	12
1.9	Neutron EOS with different slope values	13
1.10	Separation of nuclear forces.	15
1.11	Feynman diagrams for nuclear interactions	15
1.12	An ab-initio calculation of the neutron skin thickness of ^{48}Ca	16
1.13	Feynman diagrams of elastic eA scattering.	19
1.14	Schematic plot of space reflection.	21
1.15	Parity transformation of the eA scattering	22
1.16	Equivalent plot of Fig. 1.15: flip spin instead of momentum.	22
1.17	Fermi's interpretation of beta decay, current $j_{n \rightarrow p}$ convert n into p and current $j_{\nu_e \rightarrow e}$ creates $(e, \bar{\nu}_e)$ pair.	22
1.18	W-boson exchange picture of β decay	25
1.19	Feynman diagrams of elastic e-N scattering in PREX-II/CREX.	28
1.20	Nuclear Landscape	30
2.1	Evolution of PVES experiments.	33
2.2	Scattering rate	37
2.3	Asymmetry and sensitivity for ^{208}Pb	38
2.4	Asymmetry and sensitivity for ^{48}Ca	38
2.5	FOM	38
2.6	JLab aerial view	40
2.7	CEBAF	41
2.8	Hall A	42
2.9	Excitation of electrons in the semiconductor. Excited electrons with $J_z = +1/2$ (-1/2) are right (left)-handed.	43
2.10	Energy band diagram of GaAs	43
2.11	Layout of a strained GaAs electron source and corresponding excitation plot.	44

2.12	The laser system at the CEBAF injector	45
2.13	Schematic plot of the laser table.	46
2.14	Phase shift by going through the PC.	46
2.15	Schematic plot of the double wien filters. Electron beam travels from left to right. [56]	49
2.16	Mott polarimeter	49
2.17	Sherman function	50
2.18	Compton Chicane	51
2.19	Compton analyzing power	52
2.20	Schematic plot of the Moller Polarimeter.	54
2.21	Schematic plot of the Hall A beam monitor system and beam modulation system	54
2.22	Schematic plot of a stripline BPM	55
2.23	Hall A BCM system [60].	56
2.24	Up: Schematic plot of the current converter; Down: TM_{010} and TM_{110} modes, the red arrows indicate the electric field.	57
2.25	Layout of SAMs [61].	58
2.26	Scattering chamber	59
2.27	Actual pictures of the production (left) and calibration (right) ladders.	60
2.28	Raster pattern	61
2.29	Picture of Pb targets after running. One can clearly see the shape of the raster pattern. Target 1 and 4 are melted.	62
2.30	Target temperature	62
2.31	beamline collimator	63
2.32	Target degradation	64
2.33	sieve slit collimators	64
2.34	pivot region	65
2.35	HRS	65
2.36	Q1 Collimator pairs	66
2.37	Picture of the detector package.	67
2.38	VDC	67
2.39	quartz	68
2.40	photo-electron spectrum of quartz	69
2.41	Electron position distribution, projected on the quartz plane.	69
2.42	Scatter plot of electrons on the left arm AT monitor plane.	70
2.43	Helicity timing diagram	72
2.44	Integrating timing	73
3.1	charge accumulation	76
3.2	Runtime and charge statistics of CREX runs (<code>ErrorFlag == 0</code>).	76
3.3	Helicity pattern	77
3.4	A run plot: detector yield and asymmetry distribution in run 6600	78
3.5	A minirun plot	79
3.6	A slug plot	79

3.7	BPM4aX distributionn in run 8019	81
3.8	Asymmetry slug-wise plot	82
3.9	Slug-wise plot of beam position and angle	83
3.10	Slug-wise mean value of the beam energy dispersion. Overall, an energy difference of ~ 10 ppb is achieved.	83
3.11	Slug-wise raw asymmetry average (left) and difference (right) for CREX. The right plot has three less slugs because there are three single-arm slugs.	84
3.12	Mulplots	84
3.13	Correlation plot in run 7679	85
3.14	Minirun-wise energy slope ($\partial(\text{asymmetry average})/\partial (\text{BPM12X})$) distribution in slug 202. The X-axis is the run number attached by a minirun number.	88
3.15	False asymmetry corection caused by the energy difference (BPM12X) in slug 202.	89
3.16	Regression correction asymmetry	90
3.17	Slug-wise scatter plot (left) and experiment-wise histogram (right) of the regression corrected null asymmetry.	91
3.18	An example of the beam modulation.	91
3.19	Dithering corrected asymmetry	93
3.20	Comparison of the corrected asymmetries with regression (black), dithering (blue) and the Lagrange multiplier (red).	95
3.21	Part-wise and pitt-wise scattering plot of the asymmetry corrected with the Lagrange multiplier.	96
4.1	Transverse asymmetry measured in PREX-I [68].	98
4.2	Feynman diagrams of AT	102
4.3	Rotation by π around the normal direction of the scattering plane.	103
4.4	Feynman diagrams of the OPE (left) and TPE (right).	104
4.5	Schematic plot of the scattering of a transversely polarized electron.	104
4.6	AT ^{48}Ca Mulplots	107
4.7	AT ^{48}Ca asymmetry plot	108
4.8	Sign corrected transverse asymmetry in chronological order. Each data-point means one slug.	110
4.9	PCREX AT result	115
5.1	Momentum distribution of an watercell run	117
5.2	Post target electron momentum distribution. The lower end tail comes from multi-scattering and radiation.	119
5.3	Theoretical asymmetries of the $e-^{12}\text{C}$ and $e-^{208}\text{Pb}$ scattering	123
5.4	HRS transportation plot.	126
5.5	HCS and TCS	127
5.6	Schematic plot of the vertex and apparent quantities.	128
5.7	Sieve pattern plots for the -10% septum current	129
5.8	Sieve pattern plots for the nominal (scaled from PREX-II)	129
5.9	Inner edge search (left arm)	130

5.10	Sieve plot of the CREX tune. Centered at (-0.3, -1.5), the new beam position for the new target.	132
5.11	Sieve pattern plots from simulation with different septum currents. The red circles label extra or missing holes.	132
5.12	Position of the pinch point and the Q1 collimator.	133
5.13	Ratio plot of simulation to data	133
5.14	Theta ratio plot	134
5.15	θ_{lab} and Q^2 comparison between the best models and data (apparent values). The red line is the simulation result while the blue line comes from data.	135
5.16	Acceptance function extracted with the best models.	135
6.1	Correlation between the weak radius/neutron skin thickness and Apv . .	139
6.2	Correlation plot between L and Rskin	140
6.3	FF and Rskin difference	141
6.4	2-neutron separation energy	142
6.5	Density distributions for the EM charge (red), weak charge (blue) and baryon (black) in the ^{208}Pb nucleus [71].	143
6.6	Light flux curve	145
6.7	Tidal deformability versus Rskin	146
6.8	Direct Urca threshold	147
6.9	Various (proposed) measurements of the running weak mixing angle along the energy scale.	147
A.1	charge asymmetry outlier in run 4117, minirun 0	159

Acknowledgements

text of acknowledgement

Chapter 1

Introduction

The Lead Radius Experiment-II (PREX-II) and the Calcium Radius Experiment (CREX) are high-precision experiments that measure the tiny parity-violating (PV) asymmetry, at parts-per-million (ppm) level, of longitudinally polarized electrons scattered off neutron-rich targets (^{208}Pb and ^{48}Ca), from which the weak form factor, weak charge and neutron distribution, and finally the neutron skin thickness of the target nucleus, will be extracted.

The PV asymmetry (\mathcal{A}_{PV}) comes from the interference between the electromagnetic (EM) and neutral weak one-boson exchange amplitudes, because weak interaction doesn't conserve parity. Since the EM interaction has been well understood, the PV asymmetry measurement allows us to derive the weak charge and therefore the neutron (which has almost all the weak charge) distribution inside a nucleus.

Parity-violating electron scattering (PVES) experiments require an electron beam with a high longitudinal polarization, which, for PREX-II and CREX, was provided by the Continuous Electron Beam Accelerator Facility (CEBAF) at Thomas Jefferson National Accelerator Facility (TJNAF, also known as JLab). The excellent beam qualities and dedicated instrumentation at JLab allowed the asymmetry measurements to be statistics-limited.

1.1 Point-Neutron Radius and Neutron Skin

Despite the development of modern physics, we don't have a clear way to compute the size of a nucleus, and maybe we don't even know what we mean when we say that. In a simple picture, one may estimate the nuclear radius as $R = R_0 A^{1/3}$, where A is the nuclear mass number and R_0 is an approximately constant coefficient that can be experimentally identified ($R_0 \approx 1.20 \text{ fm}$ [1]). However, this simple picture only works for spherical nuclei, it fails for deformed nuclei. It is better to calculate the radius of a nucleus from its nucleon density distribution. Physicists have calculated and precisely measured the point-proton (charge) radius of many nuclei, but neutron, due to its neutrality, remains a stubborn obstacle in our measurements of the inner structure of nuclei. Especially for heavy nuclei, where more neutrons than protons are needed to bound the nuclei, it is neutron radius

rather than proton radius that defines the size of a heavy nucleus.

When we talk about the proton or neutron radius, it is a concept under the framework of Quantum Mechanics (QM), rather than the classical radius of an object. In QM, a particle is represented by a wave function, whose magnitude is related to the probability of finding this particle in a specific state, so the neutron (proton) Root-Mean-Square (RMS) radius is defined as:

$$R_{p,n} \equiv \langle R_{p,n}^2 \rangle^{1/2} = \sqrt{\frac{\int d^3\mathbf{r} r^2 \rho_{p,n}(\mathbf{r})}{\int d^3\mathbf{r} \rho_{p,n}(\mathbf{r})}} \quad (1.1)$$

where $\rho(\mathbf{r})$ is the normalized proton (neutron) density at position \mathbf{r} .

$$\int d^3\mathbf{r} \rho_{p,n}(\mathbf{r}) = 1 \quad (1.2)$$

There are numerous papers in literature reporting high-precision (with an uncertainty at 0.01 fm level) measurement of the proton (charge) radius (R_p) of various nuclei through atomic and nuclear experiments [2, 3]. In contrast, there are few precise determinations of the neutron radius (R_n). The difficulty is that the neutron carries no electric charge, so one can measure its size through only strong or weak interaction. Both methods suffer from their own limitations.

The weak interaction is so weak ($\alpha_W = 10^{-6}$) that it is hard to control systematic uncertainties if measured directly. Hence people turn to measurement of the PV asymmetry. By taking the asymmetry between two electron beams with opposite helicities, many systematic uncertainties are cancelled, therefore high precision can be achieved.

In terms of the strong interaction, the effective coupling has large theoretical uncertainties rooted in the non-perturbative nature of the underlying Quantum Chromodynamics (QCD) at low energy scale, and the interpretation of hadronic measurement is usually model dependent.

Despite all these challenges, there has been a lot of effort and progress from the community to explore different aspects of neutron radius (and neutron skin thickness): the hadronic probes include pion [4], proton [5, 6], antiproton [7] and alpha particle [8]; atomic experiments like electric dipole polarizabilities [9] and pygmy dipole resonances [10] also provide inputs to our understanding. Experimentally, with model dependence, the current measures of R_n have a resolution of better than 1%. On the theory side, the most precise estimate of R_n appears to come from nuclear models that have been constrained primarily by data other than measurements of neutron radii. Therefore, a precise measurement of R_n will provide a powerful independent check of the basic nuclear theory.

Experimentally, the nucleon radius is measured from its corresponding form factors (FFs). According to QM, under the Born approximation, the matrix element (ME) for the scattering of a plane wave (a free particle) from a Coulomb-like potential (a target

nucleus) is:

$$\begin{aligned}
\mathcal{M}_{fi} &= \langle \Psi_f | V(\mathbf{r}) | \Psi_i \rangle = \int e^{-i\mathbf{p}_f \cdot \mathbf{r}} V(\mathbf{r}) e^{i\mathbf{p}_i \cdot \mathbf{r}} d^3 \mathbf{r} \\
&= \int e^{i(\mathbf{p}_i - \mathbf{p}_f) \cdot \mathbf{r}} d^3 \mathbf{r} \int \frac{Q_t \rho(\mathbf{r}')}{4\pi |\mathbf{r} - \mathbf{r}'|} d^3 \mathbf{r}' \\
&= \int \int e^{i\mathbf{q} \cdot \mathbf{r}} \frac{Q_t \rho(\mathbf{r}')}{4\pi |\mathbf{r} - \mathbf{r}'|} d^3 \mathbf{r} d^3 \mathbf{r}' \\
&= \int \int e^{i\mathbf{q} \cdot (\mathbf{r} - \mathbf{r}')} \frac{Q_t \rho(\mathbf{r}')}{4\pi |\mathbf{r} - \mathbf{r}'|} e^{i\mathbf{q} \cdot \mathbf{r}'} d^3 \mathbf{r} d^3 \mathbf{r}' \\
&= \int e^{i\mathbf{q} \cdot \mathbf{R}} \frac{Q_t}{4\pi |\mathbf{R}|} d^3 \mathbf{R} \int \rho(\mathbf{r}') e^{i\mathbf{q} \cdot \mathbf{r}'} d^3 \mathbf{r}' \\
&= (\mathcal{M}_{fi})_{\text{Mott}} F(\mathbf{q})
\end{aligned} \tag{1.3}$$

where \mathbf{p}_i (\mathbf{p}_f) denotes momentum of the incoming (outgoing) particle, $\mathbf{q} = \mathbf{p}_i - \mathbf{p}_f$ refers to the momentum transfer during the scattering and Q_t is the total charge of the target nucleus. The ME can be factorized into two parts. The amplitude of a Mott scattering, which is the scattering of a particle from a point-like nucleus with charge Q_t and a modification due to the inner structure of the target nucleus, which is called the FF:

$$F(\mathbf{q}) = \int \rho(\mathbf{r}) e^{i\mathbf{q} \cdot \mathbf{r}} d^3 \mathbf{r} \tag{1.4}$$

The FF is just the Fourier transform of the spatial density distribution. Conversely, once the FFs at different \mathbf{q} are known (measured), one can derive the charge distribution:

$$\rho(\mathbf{r}) = \int F(\mathbf{q}) e^{-i\mathbf{q} \cdot \mathbf{r}} d^3 \mathbf{q} \tag{1.5}$$

What's more, $F(\mathbf{q})$ is experimentally measurable, as shown in Eq. 1.3:

$$F(\mathbf{q}) = \frac{\mathcal{M}_{fi}}{(\mathcal{M}_{fi})_{\text{Mott}}} = \sqrt{\frac{\sigma_{\text{measured}}}{\sigma_{\text{Mott}}}} \tag{1.6}$$

The problem is, experimentally, there is no way to cover the whole phase space of \mathbf{q} ; we can measure only limited data points at selected \mathbf{q} values. Therefore, some phenomenological models are needed to extract the charge density distribution.

For a spherically symmetric density distribution, $\rho(\mathbf{r}) = \rho(|\mathbf{r}|) = \rho(r)$, one can calculate the corresponding FF as:

$$F(\mathbf{q}) = \int \rho(r) e^{iqr \cos \theta} 2\pi r^2 \sin \theta dr d\theta = 4\pi \int r \rho(r) \frac{\sin(qr)}{q} dr \tag{1.7}$$

One can see that for a Coulomb-like potential, $F(\mathbf{q})$ doesn't depend on the direction of \mathbf{q} , but only on its magnitude: q . For the convenience of Lorentz Invariance, F is usually written in terms of $Q^2 = -q^2$, rather than q , so we will use $F(q^2)$ or $F(Q^2)$ hereafter.

Some typical spherically symmetric density distributions and their corresponding FFs are shown in Fig. 1.1.

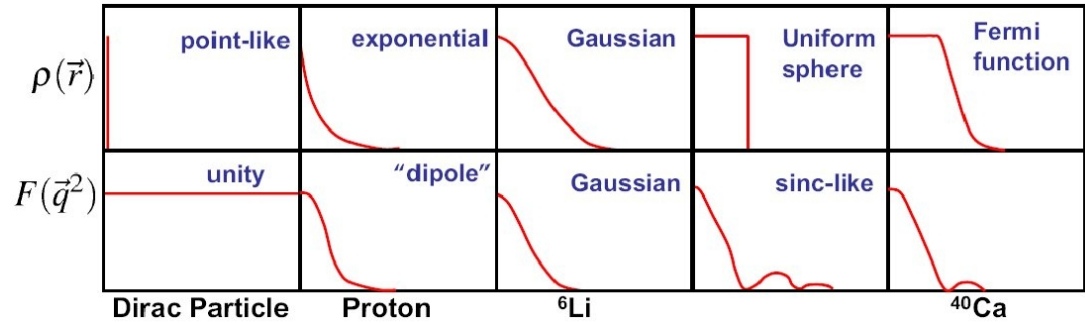


Figure 1.1: Characteristic of FFs w.r.t. different density distribution functions

In the small q^2 limit ($q^2 \ll 1$), one can do the Fourier expansion on both sides of Eq. 1.7:

$$F(q^2) = F(0) + \frac{dF}{dq^2} \Big|_{q^2=0} \times q^2 + \dots \quad (1.8)$$

$$\begin{aligned} F(q^2) &= 4\pi \int r \rho(r) \frac{\sin(qr)}{q} dr \\ &= 4\pi \int \rho(r) r \left(r - \frac{1}{6} q^2 r^3 + \dots \right) dr \\ &= \int \rho(r) \left(1 - \frac{1}{6} q^2 r^2 + \dots \right) 4\pi r^2 dr \\ &= 1 - \frac{1}{6} q^2 \langle R^2 \rangle + \dots \end{aligned} \quad (1.9)$$

Matching Eq. 1.8 to 1.9 yields

$$\langle R^2 \rangle = \int r^2 \rho(r) d^3 r = -6 \frac{dF(q^2)}{dq^2} \Big|_{q^2=0} \quad (1.10)$$

This equation prompts how to measure a RMS radius: one can measure the FFs at some small q^2 points, extrapolate them to $q^2 = 0$, then the slope at $q^2 = 0$ will be the RMS radius.¹

For charged proton, the FF will be the precisely measured EM FF:

$$\langle R_p^2 \rangle \approx \langle R_{ch}^2 \rangle = -6 \frac{dF_{EM}(q^2)}{dq^2} \Big|_{q^2=0} \quad (1.11)$$

¹This is why we use the RMS radius rather than the more physical definition of: $\langle R \rangle = \int r \rho(\vec{r}) d^3 r$.

Since neutron is neutral, its RMS radius will be measured from its weak charge FF:

$$\langle R_n^2 \rangle \approx \langle R_W^2 \rangle = -6 \frac{dF_W(q^2)}{dq^2} \Big|_{q^2=0} \quad (1.12)$$

The difference between these RMS radii is called the neutron skin thickness:

$$R_{\text{skin}} = R_n - R_p = \sqrt{\langle R_n^2 \rangle} - \sqrt{\langle R_p^2 \rangle} \quad (1.13)$$

a concept that was first suggested by Johnson and Teller [11] and first observed in the K^- meson capture processes [12].

The neutron skin is founded in neutron-rich atomic nuclei that have more neutrons than protons. Analog to the atomic electron shell model, the nuclear shell model proposes that protons and neutrons also arrange themselves in shells from low to high energy, without disturbing each other. The higher the energy level, the larger the orbit radius. For symmetric nuclei, we expect similar neutron radii to proton radii. For neutron-rich nuclei, the extra neutrons have to stay on higher energy orbits after filling all low energy ones, forming a larger radius than proton and therefore the neutron skin.

The deep reason for these extra neutrons form a neutron skin instead of a neutron core is the symmetry energy and its dependence on density. Symmetry energy represents the penalty for breaking the proton-neutron symmetry, whose value is positively related to density [13]. The core area has a higher nucleon density than the surface, the higher the density, the larger the symmetry energy, therefore the lower the binding energy ², the less stable the nuclei. So it is the symmetry energy that pushes these extra neutrons to the surface. On the other hand, the more nucleons on the surface, the stronger the surface tension, so the surface tension favors squeezing extra neutrons into the core. The balance between the symmetry energy and the surface tension determine the thickness of the neutron skin.

1.1.1 Theoretical Models

Though we don't know the actual neutron distribution, one would not expect too much difference between the proton and neutron distributions, even in nuclei with asymmetric numbers of protons and neutrons. So the proton distribution is a good starting point for the study of neutron distribution, given that we have quite good knowledge about proton distribution, learned from various eA and AA scatterings. The elastic scattering cross section is:

$$\frac{d\sigma}{d\Omega} = \left(\frac{d\sigma}{d\Omega} \right)_{\text{Mott}} |F(q^2)|^2 \quad (1.14)$$

The FF encodes information about the charge structure of a nucleus. It is an interference effect, finite size of the scattering center introduces a phase difference between

²the energy needed to break down a bounded nuclear system: $BE(N, Z) = M(N, Z)c^2 - Zm_p c^2 - Nm_n c^2$

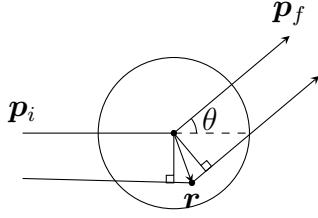


Figure 1.2: Schematic plot of eA scattering. As one can see, the wave scattered at position \mathbf{r} will travel extra distance compared to the one scattered at the object center, which leads to a phase difference of: $\delta = e^{i[\mathbf{p}_i \cdot \mathbf{r} + (-\mathbf{p}_f) \cdot \mathbf{r}]} = e^{i\mathbf{q} \cdot \mathbf{r}}$.

different plane waves scattered from different points in space.

Consider a simple hard ball model:

$$\rho(r) = \begin{cases} \frac{3}{4\pi R^3} & r \leq R \\ 0 & r > R \end{cases} \quad (1.15)$$

Then the FF will be:

$$F(q^2) = \frac{3}{(qR)^3} (\sin(qR) - qR \cos(qR)) \quad (1.16)$$

where $q = 2p \sin(\theta/2)$.

Given the Mott cross section:

$$\left(\frac{d\sigma}{d\Omega} \right)_{\text{Mott}} = \frac{Z^2 \alpha^2}{4E^2 \sin^4(\theta/2)} \cos^2(\theta/2) \quad (1.17)$$

the resulting cross section, as a function of the scattering angle, is shown in Fig. 1.3.

While the hard ball model doesn't reproduce the experimental distribution, it does characterize the real distribution and show how the FF modifies the cross section: the oscillating dips. A more realistic model of the density distribution is the Saxon-Woods distribution (also called the Fermi two-parameter model or the Fermi distribution):

$$\rho(r) = \frac{\rho(0)}{1 + \exp((r - R)/t)} \quad (1.18)$$

where $R = (1.2A^{1/3} - 0.48)$ fm denotes the nuclear force radius at which $\rho(r) = \frac{\rho(0)}{2}$, and $t \sim 0.4 - 0.5$ fm for $A > 40$ indicates the surface thickness, over which $\rho(r)$ falls from 90% to 10%.

Fig. 1.3 (right) uses a fine tuned three-parameter Fermi function:

$$\rho(r) = \frac{\rho_0(1 + \omega r^2/R^2)}{1 + \exp((r - R)/t)} \quad (1.19)$$

the central depression parameter ω allows the central density to be depressed or raised,

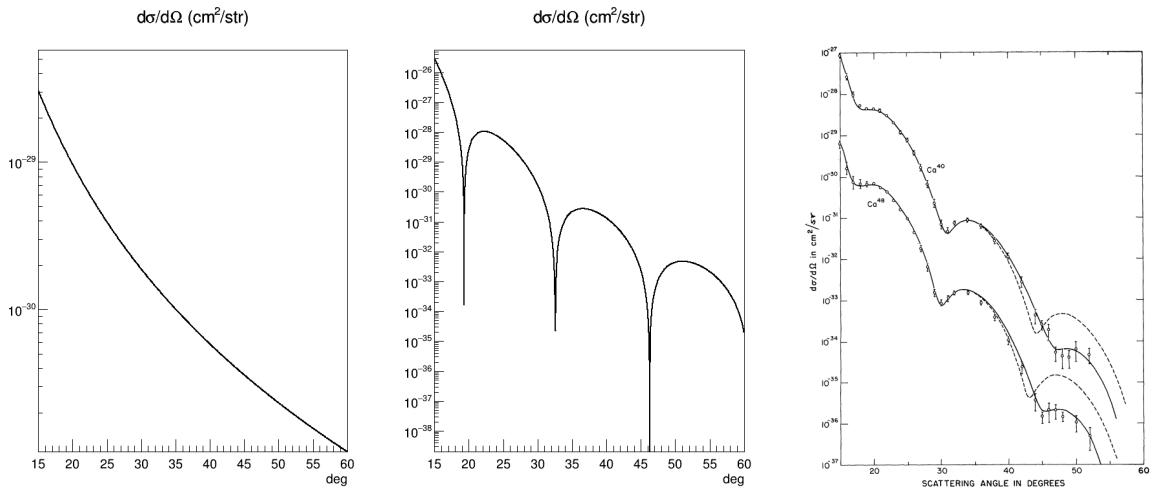


Figure 1.3: Left: Mott cross section of electron elastically scattered off a ⁴⁸Ca target. Parameters: $p = E = 757.5$ MeV. Middle: cross section of electron elastically scattered off Ca48 with the hard ball model (1.15). Parameters: $E = 757.5$ MeV, $R = A^{1/3}$ fm. Right: experimental values (dots) and theoretical prediction (solid line). The theoretical calculation assumes the charge distribution as a three-parameter Fermi function (1.19). The ⁴⁸Ca (⁴⁰Ca) cross sections are multiplied by 10^{-1} (10) to separate them [14]. A similar cross section plot of ²⁰⁸Pb can be found in [15].

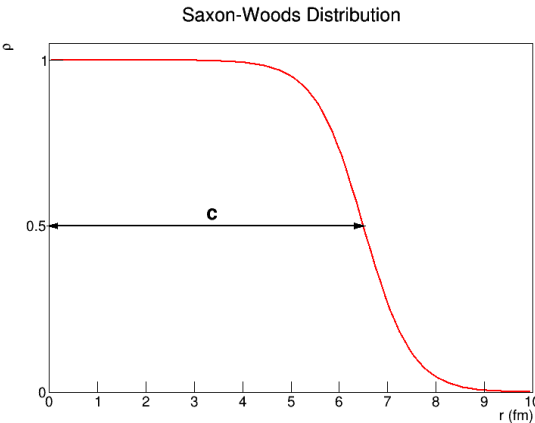


Figure 1.4: In the nuclear Shell Model, it is assumed that nucleons occupy different eigenstates of the same spherically symmetric average potential. This potential, unlike that in atomic shell model, needed to be guessed. It turns out that the Saxon-Woods model is a good candidate: $V(r) = -\frac{V(0)}{1+\exp((r-c)/a)}$ (c is the half-height radius and a represents diffuseness of the distribution). This potential is formed by all other nucleons, so it is approximately proportional to the nucleon density, therefore the same distribution for nucleon density.

depending on the sign of ω . More detailed discussion about the Fermi distribution can be found in [16].

One example model based on the Fermi distribution is the FSUGold [17], the neutron distribution of ^{208}Pb predicted by FSUGold is shown in Fig. 1.5.

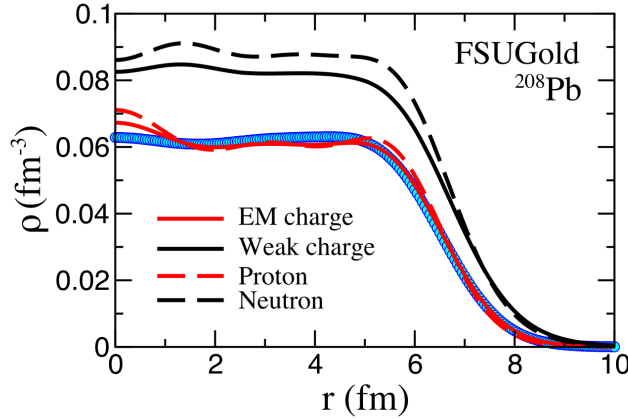


Figure 1.5: Neutron and weak charge distribution in ^{208}Pb predicted by the FSUGold model. The blue dots are experimental measurements of the charge distribution.

For medium and heavy nuclei, the Born approximation, where the incoming and outgoing waves are treated as plane waves, doesn't hold. In reality, the waves are distorted by the intense nuclear EM field, making them no longer plane waves. We have to take into account the Coulomb distortion effect, which will modify the PV asymmetry significantly. Coulomb distortion can be understood as multiple EM interactions with the same nucleus, so the distortion correction is proportional to $Z\alpha$. Obviously, this correction is more important for ^{208}Pb than for light and medium nuclei, because of its large Z value. Coulomb-distortion could reduce the PV asymmetry by as much as 30% as shown in Fig. 1.6.

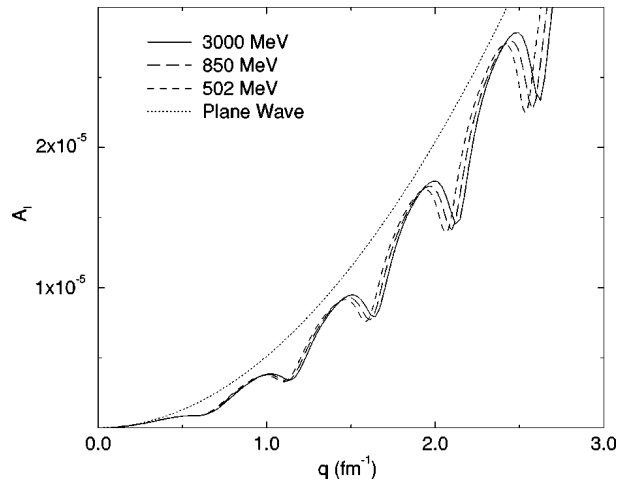


Figure 1.6: Comparison of PV asymmetries with and without the effect of Coulomb distortion for ^{208}Pb . The calculation assumes the same weak and charge densities, which are taken to be the three-parameter Fermi function [18].

With these information, one is able to solve the Dirac equation directly to know the PV asymmetry, as shown in Fig. 1.7.

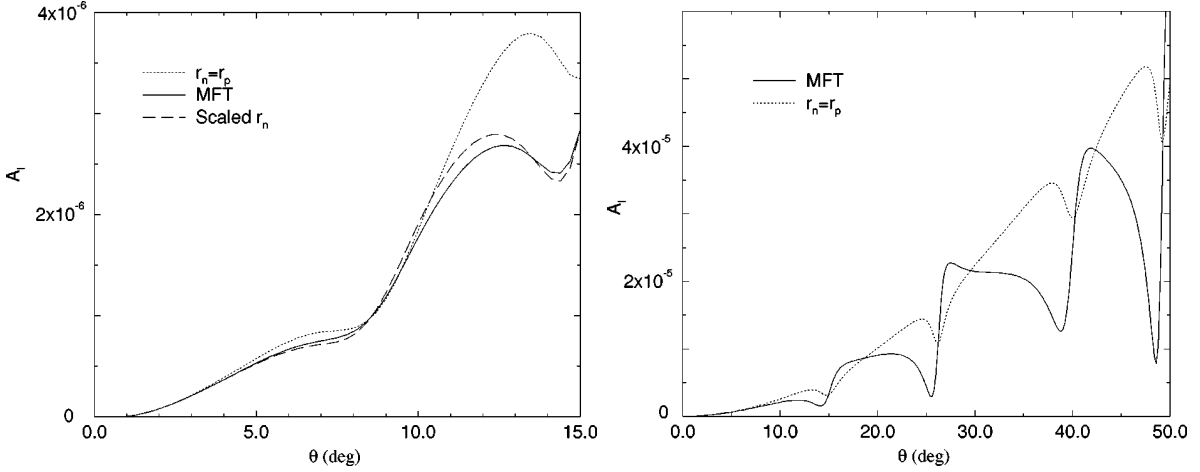


Figure 1.7: PV asymmetry for ^{208}Pb (left) and ^{48}Ca (right) versus scattering angle at 850 MeV (Coulomb distortion correction included). The dotted curve assumes the same weak and charge distributions (three-parameter Fermi function), while the solid curve is based on relativistic mean field densities (MFT). The dashed curve uses a stretched density distribution based on the three-parameter Fermi function [18].

1.2 Symmetry Energy

The binding energy of a nuclear system depends on both the total number of nucleons (A), and the difference between numbers of protons and neutrons. Using the liquid drop model (LDM), we get the Bethe-Weizsäcker Semi-empirical Mass Formula:

$$E \text{ (MeV)} = a_V A - a_S A^{2/3} - a_C \frac{Z(Z-1)}{A^{1/3}} - a_A \frac{(N-Z)^2}{A} + \delta a_p A^{-3/4}$$

$$\delta a_p A^{-3/4} = \begin{cases} +a_p A^{-3/4} & Z, N \text{ even} \\ 0 & A \text{ odd} \\ -a_p A^{-3/4} & Z, N \text{ odd (A even)} \end{cases} \quad (1.20)$$

- Volume term (a_V): strong force between nearby nucleons ($a_V \sim 16$ MeV)
- Surface term (a_S): correction to the volume term ($a_S \sim 18$ MeV)
- Coulomb term (a_C): repulsion due to EM charge ($a_C \sim 0.7$ MeV)
- Asymmetry term (a_A): correction from the Pauli exclusion principle ($a_A \sim 24$ MeV)

- Pairing term (δ): correction caused by the spin coupling effect ($a_p \sim 34$ MeV)

The first three terms are natural: the volume term reflects the short-range nature of the strong interaction; the surface term comes from the fact that nucleons on the surface aren't completely surrounded by other nucleons; and the Coulomb term reveals the EM interactions between protons.

The asymmetry term may not be so obvious. It is based solely on the Pauli exclusion principle. In heavy nuclei, more neutrons than protons are needed to balance the repulsion between protons. Due to the Pauli exclusion principle, the energy of these extra neutrons will be higher than the rest nucleons, therefore introducing this correction term.

The pairing term is a small correction due to nuclei's preference for 'paired spin'. Nuclei with even numbers of proton (Z) and neutron (N) are more stable than those with odd number of Z and N.

Regarding the nuclear system as a free Fermi gas of protons and neutrons, the kinetic energy (E_k) of this system will be:

$$E_k = E_N + E_Z = \frac{3}{5}ZE_F^p + \frac{3}{5}NE_F^n \quad (1.21)$$

Since the Fermi energy is proportional to $n^{2/3}$, E_k can be written as:

$$E_k = C(Z^{5/3} + N^{5/3}) \quad (1.22)$$

where C is a constant coefficient. Expand it in terms of $N - Z$ (see appendix A), we will get:

$$\begin{aligned} E_k &= 2^{-2/3}C \left(A^{5/3} + \frac{5}{9} \frac{(N - Z)^2}{A^{1/3}} \right) + O((N - Z)^4) \\ &= \frac{3}{5}E_F A + \frac{1}{3}E_F \frac{(N - Z)^2}{A} + O((N - Z)^4) \end{aligned} \quad (1.23)$$

The first term in Eq. 1.23 contributes to the volume term of the binding energy and the second term is minus the asymmetry term because E_k contributes to the binding energy negatively.

For a general discussion, we can ignore the Coulomb term in Eq. 1.20 to focus on the homogeneous nuclear (residual strong) interaction between nucleons, and the pairing term which is too small. So, instead of true nuclei, the object of discussion is extended to any nuclear system composed of Z charge-less protons and N neutrons. Now the equation of state (EOS) for nuclear matter is simplified.

$$\begin{aligned} E &= a_V A - a_S A^{2/3} - a_A \frac{(N - Z)^2}{A} \\ e &= \frac{E}{A} = a_V - a_S A^{-1/3} - a_A \frac{(N - Z)^2}{A^2} \end{aligned} \quad (1.24)$$

We can also discard the surface term in Eq. 1.24. Obviously, we can't guarantee any specific shape of the nuclear system; what's more, for the most common limit – the

infinite nuclear system, we don't need to consider the surface term at all, because an infinite system has no surface. By neglecting the surface term, we write:

$$\begin{aligned} E &= a_V A - a_A \frac{(N - Z)^2}{A} \\ e &= \frac{E}{A} = a_V - a_A \frac{(N - Z)^2}{A^2} = e_0(A) - a_A \beta^2 \end{aligned} \quad (1.25)$$

Here $\beta = \frac{N-Z}{N+Z}$ is defined as asymmetry between the number of neutrons and protons, which is called the isospin asymmetry.

For an infinite system, density, instead of A , will be a better choice to parameterize the EOS. So we replace N , Z and A with their corresponding density: ρ_n , ρ_p and ρ ($\beta = \frac{\rho_n - \rho_p}{\rho}$). Similarly, E is replaced by its density counterpart e . Therefore we are considering an infinite uniform nuclear system at 0 temperature that interacts only via the nuclear force. For any identified ρ , Eq. 1.25 will be:

$$e(\rho, \beta) = e(\rho, 0) + S(\rho) \beta^2 + O(\beta^4) \quad (1.26)$$

where $S(\rho)$ is a density dependent coefficient.

This is an expansion of the binding energy per nucleon around $\beta = 0$. Due to the isospin symmetry between proton and neutron, any isoscalar quantities F will remain unchanged under $n \leftrightarrow p$ interchange, while isovector quantities G will change sign. β is an isovector, so for a smooth $F(\beta)$, its expansion around $\beta = 0$ has even terms only:

$$F(\beta) = F_0 + F_2 \beta^2 + F_4 \beta^4 + \dots$$

On the other hand, for a smooth $G(\beta)$, its expansion around $\beta = 0$ has odd terms only:

$$G(\beta) = G_1 \beta + G_3 \beta^3 + \dots$$

e is an isoscalar, it doesn't change under $n \leftrightarrow p$ interchange as one can see from Eq. 1.25. The coefficient $S(\rho) = \frac{\partial^2 e(\rho, \beta)}{\partial \beta^2}$ is what we call the symmetry energy, a key parameter in describing a wide range of nuclear properties and phenomena. It describes how much energy would be released when exchanging all protons into neutrons for a symmetric nuclear system.

Not only is S itself important, but also its dependence on ρ . By convention, $S(\rho)$ is expanded around the nuclear saturation density ρ_0 (following the free Fermi gas assumption):

$$S(\rho) = S(\rho_0) + \frac{dS}{d\rho} \bigg|_{\rho_0} (\rho - \rho_0) + \frac{1}{2} \frac{d^2 S}{d\rho^2} \bigg|_{\rho_0} (\rho - \rho_0)^2 + \frac{1}{6} \frac{d^3 S}{d\rho^3} \bigg|_{\rho_0} (\rho - \rho_0)^3 + \dots \quad (1.27)$$

From which, we have some auxiliary parameters defined:

$$\begin{aligned}
S_0 &= S(\rho_0) \\
L &= 3\rho_0 \left. \frac{dS}{d\rho} \right|_{\rho_0} \\
K_{\text{sym}} &= 9\rho_0^2 \left. \frac{d^2S}{d\rho^2} \right|_{\rho_0} \\
Q_{\text{sym}} &= 27\rho_0^3 \left. \frac{d^3S}{d\rho^3} \right|_{\rho_0}
\end{aligned} \tag{1.28}$$

Among them, L represents S 's dependence on ρ .

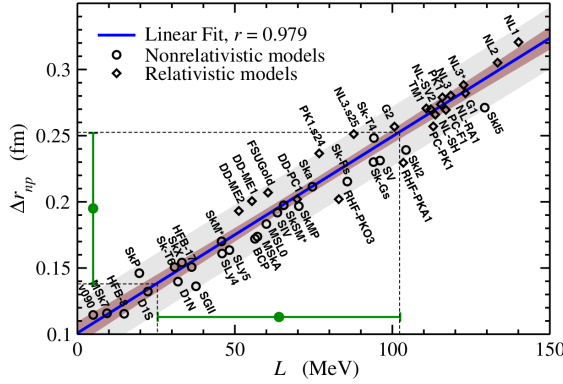


Figure 1.8: Correlation between ^{208}Pb neutron skin thickness against slope of the symmetry energy (L). The linear fit is $\Delta r_{np} = 0.101 + 0.00147L$. [19]

Being such an important parameter, great efforts have been devoted to extract S and L . Comparing Eq. 1.25 and 1.26, we can directly get:

$$S(\rho) \approx -a_A \tag{1.29}$$

The problem is this tells only the symmetry energy at the nuclear density ($\sim 1 \times 10^{44} \text{ m}^{-3}$). It says nothing about the symmetry energy at other density values, especially at the nuclear saturation density ($\sim 1.5 \times 10^{44} \text{ m}^{-3}$), let along the density dependence of the symmetry energy.

A more practical strategy to calculate $S(\rho)$ is the energy density functionals (EDF), which fits the binding energy throughout the nuclear mass table to find out the best EDF, then use it to calculate $S(\rho)$. Fitting parameterizations are constrained by nuclear density, point-proton RMS radii and nuclear binding energies. The issue is many EDFs can fit equally well with these constraints, but have quite different L values, as shown in Fig. 1.9. An experiment that could identify S (L) value without model dependence, would be helpful in understanding the symmetry energy and the EOS.

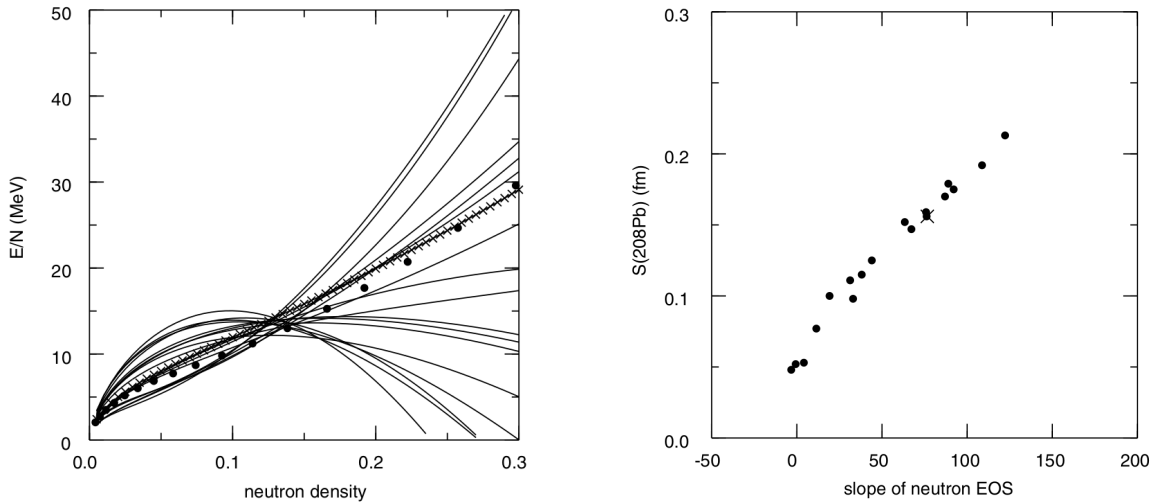


Figure 1.9: Left: Neutron EOS for 18 Skyrme [20] parameter sets. The filled circles are the Friedman-Panharipande (FG) variational calculations and the crosses are SkX predictions [21]. One can see that different models have very different symmetry energies. Right: Symmetry energy for nuclear EOS (in units of MeV fm³/neutron) at $\rho_n = 0.1$ neutron/fm³ vs the S value in ²⁰⁸Pb for 18 Skyrme parameter sets. The cross is SkX. Determination of S in ²⁰⁸Pb will greatly constrain the possible candidates. [22].

1.3 Nuclear Structure and Neutron Stars

Unlike particle physics, there is no nuclear standard model that can describe static properties and dynamics of atomic nuclei, such as the ground state binding energy, nuclear size and excitation spectrum.

The fundamental building blocks of nuclei are quarks and gluons. Theoretically, all properties of a nucleus can be derived directly from interactions of these elementary particles using QCD. Many groups do work in this direction, trying to derive nuclear structure from the underlying QCD directly. Unfortunately, at the low energy scale where nuclei lie in, the non-perturbative nature of QCD makes the problem so complicated that even the state-of-the-art lattice QCD technique can resolve only a small nuclear system with a few nucleons. This suggests that quarks and gluons are not the best degrees of freedom to describe nuclei, up to now.

Instead of quarks and gluons, nucleons and their intermediary particles pions, being the direct components of nuclei, are a more natural choice of degrees of freedom for the description of nuclei. This was how physicists studied a nuclear system in the beginning (1930s [23]). Many nuclear models were developed based on the meson-exchange phenomenology, called phenomenological interactions. With the uncovering of QCD, this approach was re-discovered from the aspect of QCD: quarks and gluons are confined in colorless nucleons and pions, the nuclear force is just the residual interaction between quarks and gluons. Being rooted in the underlying QCD, it is appropriate to describe nuclear systems in terms of nucleons and pions.

1.3.1 Ab-initio Method

Though we don't know how nuclear force emerges from the underlying QCD interaction, both the force and the interaction should share the same properties, especially the same symmetries and symmetry-breaking patterns. Based on this idea, in 1990s, S. Weinberg proposed a new framework: chiral effective field theory (χ EFT), which is an effective realization of the underlying QCD Lagrangian based on chiral symmetry [24].

Ab-initio methods try to calculate the wave function of nuclei by solving the many-body Schrödinger equation:

$$H |\psi\rangle = E |\psi\rangle \quad (1.30)$$

where the Hamiltonian is

$$H = T + V = \frac{1}{A} \sum_{i < j}^A \frac{(\mathbf{p}_i - \mathbf{p}_j)^2}{2m} + \sum_{i < j}^A V_{ij}^{NN} + \sum_{i < j < k}^A V_{ijk}^{NNN} + \dots \quad (1.31)$$

χ EFT requires that the potential should follow the same symmetries of QCD, like spacetime translation, rotation, parity transformation, etc. Most importantly, V should preserve the spontaneously broken chiral symmetry. Constrained by these symmetries, the operator for the potential takes the form of

$$\mathcal{O}_V = \{\mathbb{1}, \boldsymbol{\sigma}_i \cdot \boldsymbol{\sigma}_j, \mathbf{L} \cdot \mathbf{S}, S_{ij}\} \times \{\mathbb{1}, \boldsymbol{\tau}_i \cdot \boldsymbol{\tau}_j\} \quad (1.32)$$

where $\boldsymbol{\sigma}_i \cdot \boldsymbol{\sigma}_j$ ($\boldsymbol{\tau}_i \cdot \boldsymbol{\tau}_j$) denotes the spin (isospin) interaction, $\mathbf{L} \cdot \mathbf{S}$ indicates the spin-orbit interaction and tensor interaction is represented by

$$S_{ij}(\mathbf{x}) = 3(\boldsymbol{\sigma}_i \cdot \hat{\mathbf{x}})(\boldsymbol{\sigma}_j \cdot \hat{\mathbf{x}}) - \boldsymbol{\sigma}_i \cdot \boldsymbol{\sigma}_j \quad (1.33)$$

where $\hat{\mathbf{x}}$ is the unit vector along vector \mathbf{x} .

The typical momentum (soft scale) in nuclei is $p \sim m_\pi \sim \mathcal{O}(100 \text{ MeV})$, while the short-range structure involving heavier meson (hard scale) is about $\Lambda_\chi \sim m_\rho \sim \mathcal{O}(700 \text{ MeV})$. The clear gap between the soft and hard scales allows the separation of the long-range force from the short-range one, as shown in Fig. 1.10. The ‘effective’ in the name of χ EFT refers to the fact that only the long-range pion exchange in the low-energy scale will be considered, while heavier mesons will be integrated out as low-energy constants (LECs), which are phenomenologically fitted.

With the effective theory, one can expand the potential in terms of $\left(\frac{Q}{\Lambda_\chi}\right)^\nu$, where Q is the momentum transfer between two nucleons and Λ_χ is the cut off scale where short-range interactions becomes important, and finally ν is the power, defining the order of interactions. As shown in Fig. 1.11.

$$V = \sum_i V^{(i)} = V_{LO}^{(0)} + V_{NLO}^{(2)} + V_{NNLO}^{(3)} + V_{NNNLO}^{(4)} + \dots \quad (1.34)$$

In this way, one can calculate nuclear force to any precision, by including more higher

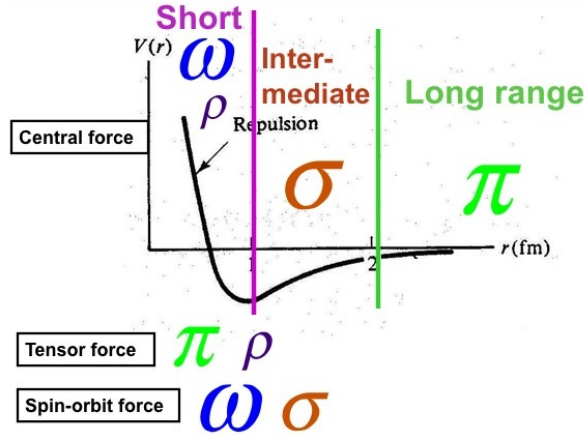


Figure 1.10: Separation of nuclear forces.

order terms, if not limited by computing power.

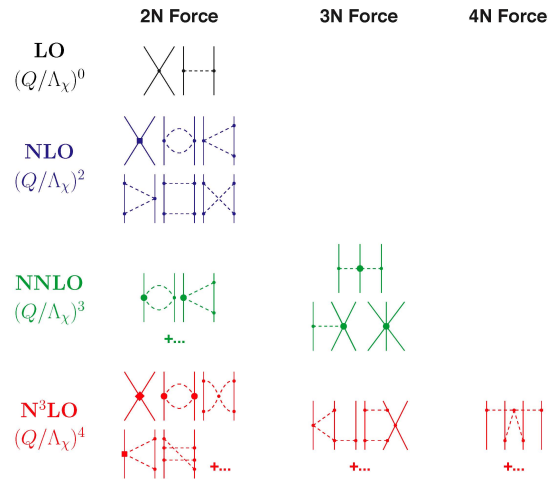


Figure 1.11: Feynman diagrams for nuclear interactions. Solid lines refer to nucleons while dashed lines represent exchanged pions. The first column shows nucleon-nucleon force, and the following two columns correspond to three-nucleon and four-nucleon forces. Rows show diagrams of leading order (LO), next-to-leading order (NLO) and so forth.

For example, the 1π -exchange potential between two nucleons is:

$$V_{2N}^{1\pi} = -\frac{g_A^2}{4F_\pi^2} \frac{(\boldsymbol{\sigma}_1 \cdot \mathbf{q})(\boldsymbol{\sigma}_2 \cdot \mathbf{q})}{\mathbf{q}^2 + M_\pi^2} \boldsymbol{\tau}_1 \cdot \boldsymbol{\tau}_2 \quad (1.35)$$

where g_A and F_π are the axial-vector coupling constant and the pion decay constant.

Once the nuclear force potential is selected, one can solve the Schrödinger equation to get eigenstate wave-functions, from which various properties can be extracted. With the help of the many-body methods, like self-consistent Green's function, coupled cluster

and renormalization group, etc. ab-initio method can be extended to nuclei of multiple nucleons.

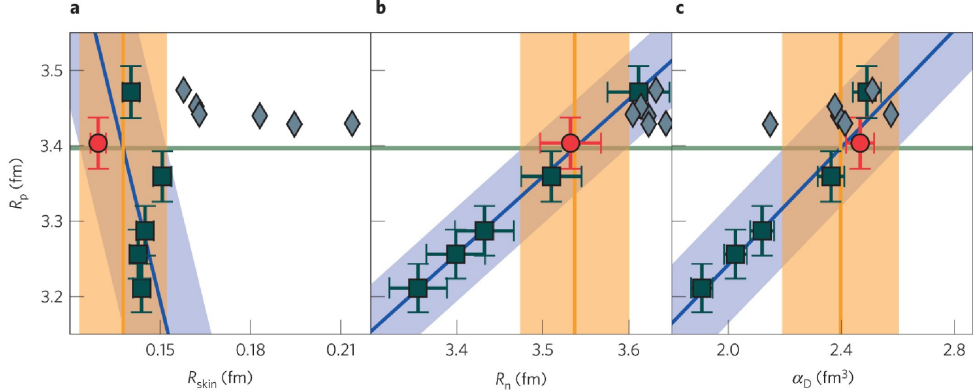


Figure 1.12: An ab-initio calculation of the neutron skin thickness of ^{48}Ca . From left to right, neutron skin thickness (a), neutron radius (b) and electric dipole polarizability (c) of ^{48}Ca are plotted versus its proton radius. The ab-initio predictions are shown as red circles and dark squares, while DFT results are represented by gray diamonds. The blue line represents a linear fit to ab-initio predictions and the blue band is the corresponding uncertainty of the blue line. The horizontal green line marks the experimental value of R_p , whose intersection with the blue line and the blue band yields the vertical orange line and orange band, respectively. [25].

1.3.2 Nuclear Density Functional Theory (DFT)

Despite the success of ab-initio methods with light and some medium nuclei, they are still unable to deal with heavy nuclei, because the required computing resources grow exponentially with the number of nucleons. Instead of building the nuclear theory from the bottom up, one may do it the opposite way, start from nuclear phenomenology, and try to go back to the underlying QCD. The method developed in this way is nuclear DFT.

The DFT method originates from solid-state physics, where it was originally used to deal with many-electron problem. It is based on the Hohenberg and Kohn (HK) theorem [18], which says one can write the total energy of a system based on the fermion (electron) density (density functional), then minimization of this density functional leads to the ground state density distribution. In this way, one can greatly reduce the number of degrees of freedom, from $3N$ to 3. The only problem is that the HK theorem doesn't tell us how to construct such a density functional.

Nuclear interactions are more complicate than the Coulomb interaction, because three-nucleon interaction is not negligible. Fortunately, the nuclear interaction is short-range. Given the experimental observation that the nucleon mean free path in nuclei is about or larger than the nuclear radius, nucleons don't experience nuclear interaction frequently. This validates the use of the mean-field method, namely nucleons move in a one-body

potential which averages over interactions with all other nucleons. The most widely used one is the Woods-Saxon potential.

Given the Hamiltonian of a nuclear system:

$$H = \sum_i^N -\frac{\hbar^2}{2m} \nabla_i^2 + \frac{1}{2} \sum_{i \neq j=1}^N V(i, j) \quad (1.36)$$

The Hartree-Fock (HF) energy of the system is:

$$E_{HF}(\rho) = \langle \Phi | H | \Phi \rangle \quad (1.37)$$

where $|\Phi\rangle$ is the Slater determinant made up with the single-particle wave function $|\phi\rangle$.

The HK theorem states that:

$$\frac{\delta}{\delta \rho(\mathbf{r})} \left(E_{HF} - \epsilon \int d^3r' \phi_j^*(\mathbf{r}') \phi_j(\mathbf{r}') \right) = 0 \quad (1.38)$$

With

$$\rho(\mathbf{r}) = \sum_i^N \phi_i^*(\mathbf{r}) \phi_i(\mathbf{r}) \quad (1.39)$$

It leads to the well-known HF equations:

$$\begin{aligned} -\frac{\hbar^2}{2m} \nabla^2 \phi_j(\mathbf{r}) + \sum_{l=1}^N \int d^3r' \phi_l^*(\mathbf{r}') V(\mathbf{r}, \mathbf{r}') (\phi_l(\mathbf{r}') \phi_j(\mathbf{r}) - \phi_l(\mathbf{r}') \phi_l(\mathbf{r}')) &= \epsilon_j \phi_j(\mathbf{r}) \\ \langle j | \frac{-\hbar^2}{2m} \nabla^2 | j \rangle + \sum_{l=1}^N \langle jl | V(1 - P_{12}) | jl \rangle &= \epsilon_j \end{aligned} \quad (1.40)$$

where P_{12} exchanges particles 1 and 2. So the total energy is:

$$E_{HF} = T + \frac{1}{2} \sum_{jl} \int d^3r d^3r' \phi_j^*(\mathbf{r}') \phi_l^*(\mathbf{r}') V(\mathbf{r}, \mathbf{r}') (\phi_j(\mathbf{r}') \phi_l(\mathbf{r}') - \phi_l(\mathbf{r}') \phi_j(\mathbf{r}')) \quad (1.41)$$

where T is the kinetic energy.

By knowing the interaction (potential term $V(\mathbf{r}, \mathbf{r}')$), one can calculate the density distribution and therefore the total energy of the system, and other properties. One successful model is the Skyrme force

$$\begin{aligned} V_{\text{Skyrme}}(\mathbf{r}_1, \mathbf{r}_2) &= t_0(1 + x_0 P_\sigma) \delta(\mathbf{r}_1 - \mathbf{r}_2) + \frac{1}{2} t_1(1 + x_1 P_\sigma) (\mathbf{k}^{\dagger 2} \delta(\mathbf{r}_1 - \mathbf{r}_2) + \delta(\mathbf{r}_1 - \mathbf{r}_2) \mathbf{k}^2) \\ &+ t_2(1 + x_2 P_\sigma) \mathbf{k}^\dagger \cdot \delta(\mathbf{r}_1 - \mathbf{r}_2) \mathbf{k} + \frac{1}{6} t_3(1 + x_3 P_\sigma) \delta(\mathbf{r}_1 - \mathbf{r}_2) \rho^\alpha \left(\frac{\mathbf{r}_1 + \mathbf{r}_2}{2} \right) \\ &+ iW_0(\boldsymbol{\sigma}_1 + \boldsymbol{\sigma}_2) \cdot \mathbf{k}^\dagger \times \delta(\mathbf{r}_1 - \mathbf{r}_2) \mathbf{k} \end{aligned} \quad (1.42)$$

which has up to 10 parameters that are constrained by the experimental data, like nuclear mass, radius and binding energy.

By measuring the neutron skin thicknesses of ^{208}Pb and ^{48}Ca , we can verify the credibilities of these ab-initio and DFT methods, and greatly constraint the parameter space in each model, helping to develop a more general nuclear theory.

1.3.3 Neutron Stars

Neutron star is the densest celestial body known, the pressure due to gravity is so strong that even atoms inside the star collapse, crushing together electrons and protons into neutrons, hence the name of neutron star. Primarily neutron stars are observed either as pulsars or in binary systems. By exploring basic properties of neutron stars, we will touch some fundamental questions that are shared between nuclear physics and astrophysics. For example:

- What is the high density phase of QCD?
- What is the structure of many compact and energetic celestial bodies? and what determines their EM, neutrino and gravitational radiations?

In spite of a 18 orders of magnitude difference in their sizes (fm vs km), the neutron star and the nuclear neutron skin share the same EOS. It is the pressure of neutron-rich matter that supports the neutron skin against its surface tension and a neutron star against its gravity. So the neutron skin thickness and the size of a neutron star are connected, through the pressure of neutron-rich matter, more specifically, the density dependence of the symmetry energy L . The larger the neutron skin thickness, the larger the symmetry energy slope L , the larger the pressure, and therefore the larger the radius of a neutron star, at the same mass.

Quantitatively, a neutron star has mostly neutrons and only a few protons, so its isospin asymmetry $\beta \approx 1$. Eq. 1.26 is simplified to:

$$e(\rho) = e(\rho, 0) + S(\rho) \quad (1.43)$$

Pressure is derived to be:

$$P = \rho^2 \frac{de}{d\rho} \simeq \rho^2 \frac{dS}{d\rho} \approx \frac{L\rho^2}{3\rho_0} \quad (1.44)$$

We see that the pressure of neutron-rich matter depends on L .

For a cold neutron star, the correlation between its radius and its pressure is [26]:

$$R \simeq C(\rho, M) P^{0.23-0.26} \quad (1.45)$$

where C is a coefficient that depends on the density ρ and the stellar mass M .

Once the L value is fixed by an experimental measurement of the neutron skin thickness in ^{208}Pb , one can calculate the radius of a cold neutron star.

1.4 Physics Beyond the Standard Model (SM)

PVES experiments are always a promising avenue for the search of physics beyond the SM in precision frontier, because of the high precision they can achieve. The Feynman diagrams from flavor-conserving PVES are shown in Fig. 1.13

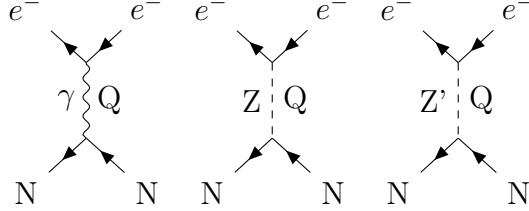


Figure 1.13: Feynman diagrams of elastic eA scattering.

Knowing that the EM interaction is much larger than the neutral weak current and the possible new interaction, we can approximate:

$$|\mathcal{A}_\gamma + \mathcal{A}_Z + \mathcal{A}_{\text{new}}|^2 \approx A_\gamma^2 \left[1 + 2 \frac{\mathcal{A}_Z}{\mathcal{A}_\gamma} + 2 \frac{\mathcal{A}_{\text{new}}}{\mathcal{A}_\gamma} \right] \quad (1.46)$$

If the new interaction amplitude \mathcal{A}_{new} is comparable to \mathcal{A}_Z or our measurement of \mathcal{A}_Z is precise enough, we will be able to distinguish any possible deviation, prompting on the existence of new physics.

Any PV interaction can be described in the SM as:

$$\mathcal{L}_{PV} = -\frac{G_F}{\sqrt{2}} [\bar{e}\gamma_\mu\gamma_5 e(C_{1u}\bar{u}\gamma^\mu u + C_{1d}\bar{d}\gamma^\mu d) + \bar{e}\gamma_\mu e(C_{2u}\bar{u}\gamma^\mu\gamma^5 u + C_{2d}\bar{d}\gamma^\mu\gamma^5 d)] \quad (1.47)$$

where C_{iq} is the constant coefficient predicted by the SM:

$$\begin{aligned} C_{1q} &\equiv 2g_A^e g_V^q & C_{2q} &\equiv 2g_V^e g_A^q \\ g_A &= I_3 & g_V &= I_3 - 2Q \sin^2 \theta_W \end{aligned} \quad (1.48)$$

These coefficients or their combinations give favorable experimental observables:

$$\begin{aligned} C_{1u} &= -\frac{1}{2} + \frac{4}{3} \sin^2 \theta_W & \tilde{\alpha} &= -C_{1u} + C_{1d} = -(1 - 2 \sin^2 \theta_W) \\ C_{1d} &= \frac{1}{2} - \frac{2}{3} \sin^2 \theta_W & \tilde{\beta} &= -C_{2u} + C_{2d} = -(1 - 4 \sin^2 \theta_W) \\ C_{2u} &= -\frac{1}{2} + 2 \sin^2 \theta_W & \tilde{\gamma} &= -C_{1u} - C_{1d} = \frac{2}{3} \sin^2 \theta_W \\ C_{2d} &= \frac{1}{2} - 2 \sin^2 \theta_W & \tilde{\delta} &= -C_{2u} - C_{2d} = 0 \end{aligned} \quad (1.49)$$

where θ_W is the weak mixing angle.

Most PVES experiments measure the weak charge (the weak mixing angle) directly, like E158 at SLAC and the upcoming MOLLER at JLab. Compared to these experiments, PREX/CREX are less sensitive to new physics, because PREX/CREX measurements involve many weak charge sources inside a nucleus and their distribution. Though new physics is not the main goal of the PREX/CREX collaboration, the possibility for new physics is not completely cut off.

1.5 Symmetry and Asymmetry

Symmetry is a powerful framework in modern physics. For any physical system, by applying the proper symmetry requirements, one can derive (guess) the Lagrangian of the system, and therefore properties and Equation Of Motion (EOM) of the system.

Common space-time symmetries can be separated into continuous symmetries and discrete ones. Continuous symmetries include translation, rotation and boost, while discrete symmetries have space reflection (P) and time reversal (T). Another important discrete symmetry is charge conjugation (C).

Playing such a key role, the violation of any symmetry is also important. Currently, it is widely accepted that continuous symmetries are conserved by all interactions while weak interaction violates some discrete symmetries, namely C, P, and their combination CP. There are some speculations that the strong interaction can violate the CP symmetry, but no experimental observation reported yet.

1.5.1 Parity Symmetry

Parity symmetry is a discrete symmetry which states that the physical laws in the mirror (reflection) world should be the same as that in the real world.

The parity operation will flip the sign of any spatial coordinate:

$$P : \mathbf{r} \rightarrow -\mathbf{r} \quad (1.50)$$

The same for any spatial vector, like momentum (\mathbf{p}), angular momentum (\mathbf{L}) and the EM vector potential (\mathbf{A}).

In the language of QM, the parity operator ($\hat{\pi}'$) will transform a wave function, as shown in Eq. 1.51.

$$\hat{\pi}'\psi(x, y, z) = \eta\psi(-x, -y, -z) \quad (1.51)$$

where η is a coefficient picked up by the transformation. One would expect the state goes back to itself after 2 times of parity transformations:

$$|\hat{\pi}'^2\psi(x, y, z)|^2 = |\psi(x, y, z)|^2 \quad \hat{\pi}'\psi(x, y, z) = e^{i\phi/2}\psi(-x, -y, -z) \quad (1.52)$$

which means $\hat{\pi}'$ is an unitary operator. The pick up phase can be absorbed into the

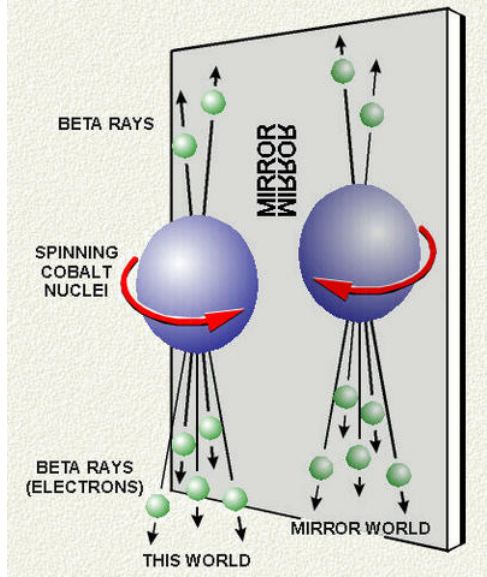


Figure 1.14: Schematic plot of space reflection.

operator to get the new parity operator (what we use hereafter):

$$\hat{\pi} = \hat{\pi}' e^{-i\phi/2} \quad (1.53)$$

Then we have

$$\hat{\pi}^2 = 1 \quad (1.54)$$

So $\hat{\pi}$ has eigenvalues of $p = \pm 1$. States with eigenvalue of $+1$ are called parity-even states and the others with eigenvalue of -1 the parity-odd states.

For any scalar potential, $V(\mathbf{r}) = V(r)$ ($[\hat{\pi}, V] = 0$), the parity operator $\hat{\pi}$ commutes with the Hamiltonian ($[\hat{\pi}, \mathcal{H}] = 0$). So the energy eigenstates are also the eigenstate of $\hat{\pi}$. Among these, the orbital angular momentum eigenstates are of special interest. Given an orbital angular momentum \mathbf{L} with z-axis projection L_z , one will have:

$$\hat{\pi} |\mathbf{L}, L_z\rangle = (-1)^L |\mathbf{L}, L_z\rangle \quad (1.55)$$

Another quantity which is similar to the orbital angular momentum in most aspects but different in parity is spin. Spin is also an angular momentum, but it is an intrinsic property, rather than a space-time motion. While $\hat{\pi}$ is an operation of the space, spin is not affected by $\hat{\pi}$. So the parity of a spin state is randomly assigned as long as particles and their anti-particles have opposite parities: electron, proton and neutron are assigned even parity and their anti-particles have odd parity.

Now we can discuss helicity, which is the projection of the spin on the momentum direction:

$$H \equiv \frac{\mathbf{s} \cdot \mathbf{p}}{|\mathbf{s} \cdot \mathbf{p}|} \quad (1.56)$$

If a particle's spin is parallel (anti-parallel) to its momentum, we call it a right (left)-

handed particle. Obviously, when we apply the parity operator to a helicity eigenstate, we will flip its helicity because spin does not change and momentum will flip its sign, as shown in Fig. 1.15.

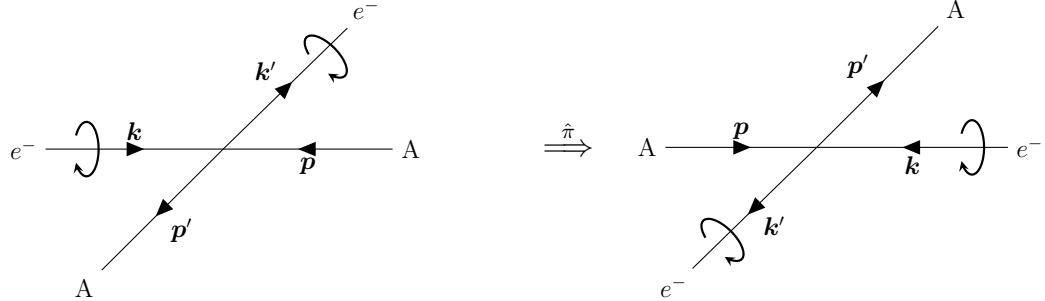


Figure 1.15: Parity transformation of the eA scattering

If parity is not conserved, there will be a difference between the two scattering processes in Fig. 1.15, which is exactly what we measured in PREX-II/CREX. Experimentally, it is easier to flip the spin direction rather than the momentum direction, as shown in Fig. 1.16, which is an equivalent plot of Fig. 1.15.

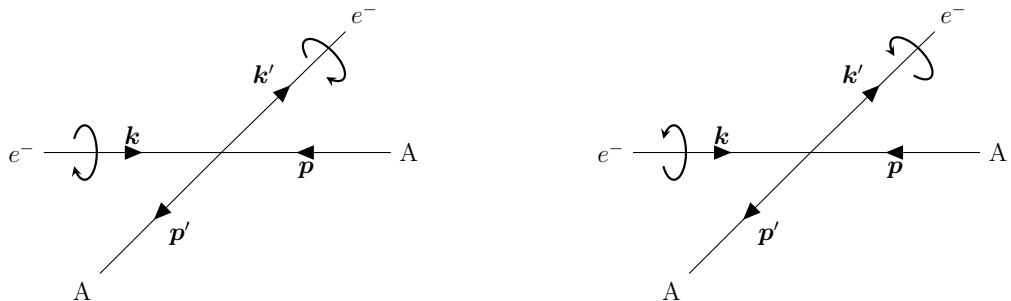


Figure 1.16: Equivalent plot of Fig. 1.15: flip spin instead of momentum.

1.5.2 Parity Violation

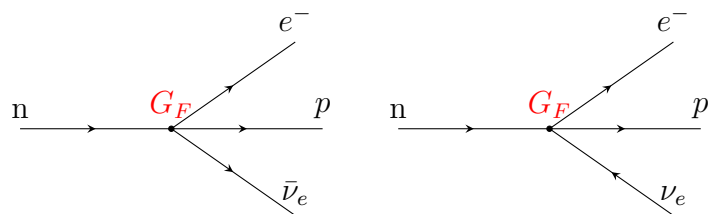


Figure 1.17: Fermi's interpretation of beta decay, current $j_{n \rightarrow p}$ convert n into p and current $j_{\nu_e \rightarrow e}$ creates $(e, \bar{\nu}_e)$ pair.

The story of parity violation traces back to the early age of particle physics. To explain the beta decay, Fermi proposed the four-fermion interaction (Fermi's interaction) in 1933 [27], which is a low-energy limit of the weak interaction. In his theory, in analogy to the EM interaction (emission of a photon by an electron: $\mathcal{M} = ej_\mu^{em} A^\mu$) Fermi interpreted the β decay as emission of the $(e, \bar{\nu}_e)$ pair, during the process a neutron converts itself into a proton, therefore it is coupling of two currents:

$$\mathcal{M} = G_F(\bar{p}\mathbb{O}^\mu n)(\bar{e}\mathbb{O}_\mu \nu_e) = G_F j_{(n \rightarrow p)}^\mu j_\mu^{(\nu_e \rightarrow e)} \quad (1.57)$$

Where $G_F = 1.166 \times 10^{-5} \text{GeV}^{-2}$ is the coupling constant that can be experimentally determined and \mathbb{O} represents the possible operators. Out of the five possible Lorentz invariant bi-linear forms (Scalar (S: $\mathbb{O} = \mathbb{1}$), pseudo-scalar (P: $\mathbb{O} = \gamma^5$), Vector (V: $\mathbb{O} = \gamma^\mu$), Axial vector (A: $\mathbb{O} = \gamma^\mu \gamma^5$) and Tensor (T: $\mathbb{O} = \sigma^{\mu\nu} = \frac{i}{2}(\gamma^\mu \gamma^\nu - \gamma^\nu \gamma^\mu)$), Fermi selected the vector current to keep in line with the EM interaction: $j^\mu = \bar{u}\gamma^\mu u$.

V-A Theory

In 1956, T. D. Lee and C. N. Yang, both being Fermi's students, postulated the revolutionary idea of parity violation for solving the $\tau - \theta$ puzzle [28], and they succeeded. Only one year later, their hypothesis was experimentally tested by Wu et al in the decay of polarized ^{60}Co nuclei [29], establishing the fact that parity is not conserved in weak interactions and therefore the weak current is not a pure vector-like quantity. Based on the experimental result that parity is maximally violated (left-handed electrons interact weakly but right-handed don't) [30], Sudarshan and Marshak [31], also Feynman and Gell-Mann [32], updated Fermi's theory by replacing the vector current with a new current to accommodate parity violation:

$$\mathcal{M} = \frac{G_F}{\sqrt{2}}(\bar{p}\gamma^\mu(\mathbb{1} - \gamma^5)n)(\bar{e}\gamma_\mu(\mathbb{1} - \gamma^5)\nu_e) \quad (1.58)$$

The factor of $\frac{1}{\sqrt{2}}$ was introduced to keep G_F unchanged (Fermi's original theory was not aware the fact that neutrino was left-handed only, resulting in a decay phase space twice the real value in nature, to fix the problem, we can either modify the value of G_F or introduce a correction factor $\frac{1}{\sqrt{2}}$). The V and A parts of the V-A theory refer to the vector and axial vector current, responsible for Fermi transitions and Gamow-Teller transitions respectively.

$$j_V^\mu = \bar{u}\gamma^\mu u \quad j_A^\mu = \bar{u}\gamma^\mu \gamma^5 u \quad (1.59)$$

The form of V-A as $\mathbb{1} - \gamma^5$ happens to be the projection operator:

$$P_R = \frac{\mathbb{1} + \gamma^5}{2} \quad P_L = \frac{\mathbb{1} - \gamma^5}{2} \quad (1.60)$$

By definition of γ matrix, one can easily verify that:

$$\begin{aligned} \left(\frac{\mathbb{1} - \gamma^5}{2}\right)^2 &= \frac{\mathbb{1} - \gamma^5}{2} & \gamma^\mu \frac{\mathbb{1} - \gamma^5}{2} &= \frac{\mathbb{1} + \gamma^5}{2} \gamma^\mu \\ \gamma^\mu \frac{\mathbb{1} - \gamma^5}{2} &= \frac{\mathbb{1} + \gamma^5}{2} \gamma^\mu \frac{\mathbb{1} - \gamma^5}{2} \end{aligned} \quad (1.61)$$

Then one can see the handedness of the new current:

$$\mathcal{M} = \frac{4G_F}{\sqrt{2}} (\bar{p} \gamma^\mu \frac{\mathbb{1} - \gamma^5}{2} n) (\bar{e} \gamma_\mu \frac{\mathbb{1} - \gamma^5}{2} \nu_e) = \frac{4G_F}{\sqrt{2}} (\bar{p}_L \gamma^\mu n_L) (\bar{e}_L \gamma_\mu \nu_{e,L}) \quad (1.62)$$

Only left (right)-handed particles (antiparticles) can interact in the weak interaction. In analogy to EM interaction, the coupling constant is proportional to a weak charge (weak isospin T_3): right-handed fermions (left-handed antifermions) will have $T_3 = 0$ and left-handed fermions have the same weak charge.

Given the fact that the charge current (which changes particle's electric charge) connects two types of fermions and lepton number is conserved in the weak interaction, it is natural to group them in a lepton doublet:

$$f_L = \begin{pmatrix} \nu_l \\ l \end{pmatrix}_L \quad (1.63)$$

This implies that for left-handed fermions: $T = \frac{1}{2}$, $T_3 = \pm \frac{1}{2}$

Applying the V-A theory to more decay and scattering processes ($\mu^+ \rightarrow e^+ + \nu_e + \bar{\nu}_\mu$, $\pi^- \rightarrow l + \bar{\nu}_l$ etc.), we will have two charge currents:

$$j_\mu^- = \bar{\nu}_{e,L} \gamma_\mu e_L \quad j_\mu^+ = \bar{e}_L \gamma_\mu \nu_{e,L} \quad (1.64)$$

which can be written in a more compact way w.r.t. the lepton doublet:

$$j_\mu^\pm = \bar{f}_L \gamma_\mu t^\pm f_L \quad (1.65)$$

where,

$$t^+ = \begin{pmatrix} 0 & 1 \\ 0 & 0 \end{pmatrix} = \frac{1}{2}(\sigma^1 + i\sigma^2) \quad t^- = \begin{pmatrix} 0 & 0 \\ 1 & 0 \end{pmatrix} = \frac{1}{2}(\sigma^1 - i\sigma^2) \quad (1.66)$$

One can see clearly the SU(2) symmetry by the t^\pm expression, the raising (t^+) and lowering matrices (t^-) are the combination of the first two Pauli matrices. Then one should consider the third component:

$$j_\mu^3 = \bar{f}_L \gamma_\mu \frac{1}{2} t^3 f_L = \frac{1}{2} (\bar{\nu}_{e,L} \gamma_\mu \nu_{e,L} - \bar{e}_L \gamma_\mu e_L) \quad (1.67)$$

This is a neutral current. The question is how to interpret it. The only known neutral current at that time is the EM current, but this hypothetical term can't be the EM current because neutrino is neutral. The neutral current remained a mystery until Glashow, Salam

and Weinberg postulated the GSW model, which interprets j^3 as part of a more complete neutral current that includes j^{em} – the so-called $SU(2)_L \times U(1)$.

W Bosons

One problem with Fermi's theory is that the cross section ($\sigma \sim G_F^2 E^2$) will diverge at high energy, to which the solution was the introduction of mediating mesons: W^\pm . Unlike photon that mediates EM interaction, W boson is charged, and has a heavy mass implied from the short-range nature of the weak interaction. The introduction of W fields just makes the weak interaction more similar to the EM interaction:

$$\mathcal{L} = g_W (J^+ W^+ + J^- W^-) \quad (1.68)$$

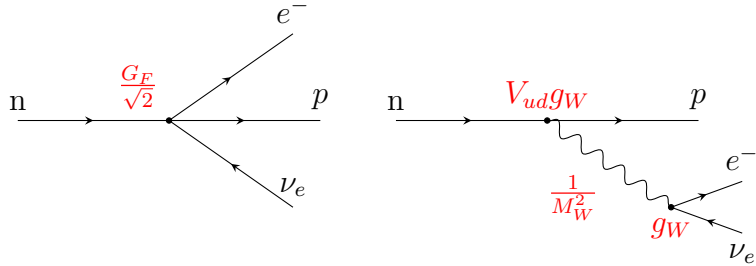


Figure 1.18: W-boson exchange picture of β decay

Given the similarity between weak interaction and EM interaction, it is natural to unify them into a multiplet of gauge fields. Based on Yang and Mills' non-abelian gauge theory, Salam and Weinberg successfully came up with a unified framework for both interactions – the $SU(2)_L \times U(1)$ structure first suggested by Glashow. The $SU(2)$ part is generated by ‘weak isospin’, the subscript L referring to the fact that only left-handed fermions couple to gauge boson of $SU(2)$, and the $U(1)$ part comes from the ‘weak hypercharge’. There are 4 vector bosons:

$$W^1, W^2, W^3, B$$

These bosons will couple to both left-handed and right-handed fermions. For simplicity, consider only the first generation leptons here:

$$\psi_1 = \begin{pmatrix} \nu_e \\ e^- \end{pmatrix} \quad \psi_2 = \nu_{e,R} \quad \psi_3 = e_R^- \quad (1.69)$$

The left-handed doublet ψ_1 interacts with all bosons, so the covariant derivative is:

$$D_\mu = \partial_\mu - ig \frac{\sigma^a}{2} W_\mu^a - ig' y_1 B_\mu \quad (1.70)$$

where y_1 is the hypercharge of ψ_1 . The corresponding coupling Lagrangian is:

$$\mathcal{L}_{int,L} = -i\bar{\psi}_1\gamma^\mu(g\frac{\sigma^a}{2}W_\mu^a + g'y_1B_\mu)\psi_1 = -i(g\mathbf{j}^\mu\mathbf{W}_\mu + g'y_1\bar{\psi}_1\gamma^\mu\psi_1B_\mu) \quad (1.71)$$

Right-handed singlets don't couple to weak vector bosons, therefore the covariant derivative for right-handed fermions is:

$$D_\mu = \partial_\mu - ig'y_{2(3)}B_\mu \quad (1.72)$$

$y_{2(3)}$ is the hypercharge of $\psi_{2(3)}$ and the Lagrangian:

$$\mathcal{L}_{int,R} = -ig'(y_2\bar{\psi}_2\gamma^\mu\psi_2 + y_3\bar{\psi}_3\gamma^\mu\psi_3)B_\mu \quad (1.73)$$

So the complete interacting Lagrangian is:

$$\mathcal{L}_{int} = \mathcal{L}_{int,L} + \mathcal{L}_{int,R} = -i(g\mathbf{j}^\mu\mathbf{W}_\mu + g'\mathbf{j}_Y^\mu B_\mu) \quad (1.74)$$

where \mathbf{j}^μ is the weak isospin current. It couples to a weak isos triplet of vector bosons: $\mathbf{W} = (W^1, W^2, W^3)$ with coupling strength g ; and the weak hypercharge current $\mathbf{j}_Y^\mu = \sum_{i=1}^3 y_i\bar{\psi}_i\gamma^\mu\psi_i$ couples to an isosinglet vector boson B^μ with strength g' .

Weak Neutral Current

Because the GSW model preserves the SU(2) structure, it is obvious to reproduce the charged current:

$$W^\pm = \frac{1}{\sqrt{2}}(W^1 \mp iW^2) \quad j^\pm = j^1 \pm ij^2 \quad (1.75)$$

$$j^1W^1 + j^2W^2 = \frac{1}{\sqrt{2}}(j^+W^+ + j^-W^-) \quad (1.76)$$

As for the other 2 bosons, there is no way to satisfy $y_1 = y_2 = y_3$ and $g'y_i = eQ_i$ at the same time, so B is not pure A (photon). Since both fields are neutral, one needs to mix them to get something matching experimental results:

$$\begin{pmatrix} A \\ Z \end{pmatrix} = \begin{pmatrix} \cos\theta_W & \sin\theta_W \\ -\sin\theta_W & \cos\theta_W \end{pmatrix} \begin{pmatrix} B \\ W^3 \end{pmatrix} \Leftrightarrow \begin{pmatrix} B \\ W^3 \end{pmatrix} = \begin{pmatrix} \cos\theta_W & -\sin\theta_W \\ \sin\theta_W & \cos\theta_W \end{pmatrix} \begin{pmatrix} A \\ Z \end{pmatrix} \quad (1.77)$$

The mixing angle is known as the Weinberg angle.

Rewrite Eq. 1.74 in terms of W^\pm , Z and A :

$$\begin{aligned} i\mathcal{L} = & \frac{g}{\sqrt{2}}(j^+W^+ + j^-W^-) \\ & + \sum_{i=1}^3 \bar{\psi}_i\gamma^\mu \left\{ \left[g\frac{\sigma^3}{2}\sin\theta_W + g'y_i\cos\theta_W \right] A_\mu + \left[g\frac{\sigma^3}{2}\cos\theta_W - g'y_i\sin\theta_W \right] Z_\mu \right\} \psi_i \end{aligned} \quad (1.78)$$

where $g_W = g/\sqrt{2}$ is the coupling constant of weak charged current.

The neutral part can be expressed with corresponding charge:

$$\begin{aligned} i\mathcal{L}_{NC} &= \sum_{i=1}^3 \bar{\psi}_i \gamma^\mu \psi_i [(g \sin \theta_W I_3 + g' \cos \theta_W Y) A_\mu + (g \cos \theta_W I_3 - g' \sin \theta_W Y) Z_\mu] \\ &= ej_{EM}^\mu Q A_\mu + g_Z j_Z^\mu Q_Z Z_\mu \end{aligned} \quad (1.79)$$

where I_3 is the weak isospin and Y is the weak hypercharge. Similarly, Q is the EM charge in units of electron charge and Q_Z is the weak neutral charge. e and g_Z are coupling constant for EM and neutral weak interaction respectively. With I_3 and Y varying for different fermions, we have the following relationship:

$$e = g \sin \theta_W = g' \cos \theta_W = \frac{gg'}{g^2 + g'^2} \quad (1.80)$$

So the Weinberg angle is identified as:

$$\tan \theta_W = \frac{g'}{g} \quad (1.81)$$

and:

$$Q = I_3 + Y \implies Y = Q - I_3 \quad (1.82)$$

The value of weak hypercharge depends on the definition, if one keeps the $\frac{1}{2}$ factor in the B current, then one will get:

$$\frac{Y}{2} = Q - I_3 \Rightarrow Y = 2(Q - I_3) \quad (1.83)$$

This is the traditional formula. In this thesis we will use the definition of Eq. 1.82.

As for the neutral weak current, the value of g_Z , Q_Z and J_Z depend on our choice, as long as:

$$g_Z Q_Z J_Z = (g \cos \theta_W I_3 - g' \sin \theta_W Y) \bar{\psi} \gamma^\mu \psi \quad (1.84)$$

The traditional choice is:

$$\begin{aligned} g_Z &= \frac{g}{\cos \theta_W} = \frac{e}{\sin \theta_W \cos \theta_W} \\ Q_Z &= I_e \cos^2 \theta_W - Y \sin^2 \theta_W = I_3 - Q \sin^2 \theta_W \end{aligned} \quad (1.85)$$

One can also absorb Q_Z into J_Z to get:

$$J_Z = \sum \bar{\psi}_i \gamma^\mu (I_3 - Q \sin^2 \theta_W) \psi_i = \sum_f \bar{f} \gamma^\mu \frac{c_v - c_a \gamma^5}{2} f \quad (1.86)$$

with

$$c_v = I_3 - 2Q \sin^2 \theta_W \quad c_a = I_3 \quad (1.87)$$

So we come to a striking prediction of the GSW model: the existence of the neutral weak interaction. That was experimentally verified in 1973 in the Gargamelle neutrino experiment [33].

PREX-II and CREX Observations

What will be measured in PREX-II and CREX originates from the interference of this neutral weak current and the EM current.

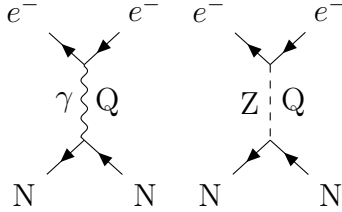


Figure 1.19: Feynman diagrams of elastic e-N scattering in PREX-II/CREX.

$$\mathcal{A}_{PV} = \frac{\left(\frac{d\sigma}{d\Omega}\right)^R - \left(\frac{d\sigma}{d\Omega}\right)^L}{\left(\frac{d\sigma}{d\Omega}\right)^R + \left(\frac{d\sigma}{d\Omega}\right)^L} = \frac{|\mathcal{M}^R|^2 - |\mathcal{M}^L|^2}{|\mathcal{M}^R|^2 + |\mathcal{M}^L|^2} \quad (1.88)$$

where: $\mathcal{M}^{R,L} = \mathcal{M}_\gamma + \mathcal{M}_Z^{R,L}$. Because EM amplitude is much larger than the weak amplitude: $\mathcal{M}_\gamma \gg \mathcal{M}_Z^{R,L}$

$$\begin{aligned} \mathcal{A}_{PV} &\approx \frac{2\mathcal{M}_\gamma(\mathcal{M}_Z^R - \mathcal{M}_Z^L)}{2\mathcal{M}_\gamma^2} \\ &= \frac{\mathcal{M}_Z^R - \mathcal{M}_Z^L}{\mathcal{M}_\gamma} \propto \frac{\left(\frac{d\sigma}{d\Omega}\right)_W}{\left(\frac{d\sigma}{d\Omega}\right)_{EM}} \\ &= \left(\frac{\mathcal{M}_Z^R - \mathcal{M}_Z^L}{\mathcal{M}_\gamma}\right)_{point} \times \frac{Q_W}{Z} \frac{F_W(Q^2)}{F_{EM}(Q^2)} \\ &\approx \frac{g_Z^2/M_Z^2}{e^2/Q^2} \frac{(j_Z^{e,R} - j_Z^{e,L})j_Z^n}{j_\gamma^e j_\gamma^p} \times \frac{Q_W}{Z} \frac{F_W(Q^2)}{F_{EM}(Q^2)} \quad (Q^2 \ll M_Z^2) \\ &= -\frac{8G_F/\sqrt{2}}{4\pi\alpha/Q^2} \frac{(\bar{e}_L\gamma^\mu I_3 e_L)_{\frac{1}{2}}^1 (\bar{n}_L\gamma_\mu I_3 n_L)}{(\bar{e}_L\gamma^\mu e_L)(\bar{p}\gamma_\mu p)} \times \frac{Q_W}{Z} \frac{F_W(Q^2)}{F_{EM}(Q^2)} \\ &= -\frac{G_F Q^2}{4\pi\alpha\sqrt{2}} \frac{Q_W}{Z} \frac{F_W(Q^2)}{F_{EM}(Q^2)} \end{aligned} \quad (1.89)$$

The weak isospin for electron and neutron is: $I_3(e^-) = I_3(n) = -\frac{1}{2}$. The factor of $\frac{1}{2}$ in line 5 of Eq. 1.89 arises from the fact that the target is unpolarized. In the low Q^2 region of $Q^2 \sim 0.01 - 1 \text{ GeV}^2$, one can estimate the PV asymmetry as

$$-\mathcal{A}_{PV} \sim \frac{G_F Q^2}{4\pi\alpha\sqrt{2}} \lesssim 10^{-7} - 10^{-4} \quad (1.90)$$

The FFs can be further decomposed into point-nucleon FFs:

$$\begin{aligned} F_{EM}(q) &= Q_p^\gamma F_p(q) + Q_n^\gamma F_n(q) = F_p(q) \\ F_W(q) &= Q_p^Z F_p(q) + Q_n^Z F_n(q) \end{aligned} \quad (1.91)$$

Where Q^γ and Q^Z are the EM charge and weak charge respectively. $F_p(q)$ and $F_n(q)$ are the FFs of point-proton and neutron density distributions.

$$F_{p,n}(q) = \int d^3r j_0(qr) \rho_{p,n}(r) \quad (1.92)$$

For weak charges including radiative corrections

$$\begin{aligned} Q_p^\gamma &= 1 & Q_n^\gamma &= 0 \\ Q_p^Z &= 0.0719 & Q_n^Z &= -0.9877 \end{aligned} \quad (1.93)$$

Ignoring the proton's weak charge, one will get:

$$\mathcal{A}_{PV} = -\frac{G_F Q^2}{4\pi\alpha\sqrt{2}} \frac{Q_{wk}}{Z} \frac{F_n(q)}{F_p(q)} \quad (1.94)$$

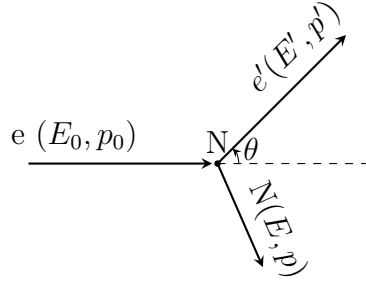
A more precise result by including the proton's weak charge is:

$$\mathcal{A}_{PV} = -\frac{G_F Q^2}{4\pi\alpha\sqrt{2}} \frac{Q_{wk}}{Z} \left[\frac{F_n(q)}{F_p(q)} - \frac{Z}{N} (1 - 4 \sin^2 \theta_W) \right] \quad (1.95)$$

When ignoring the nuclear inner structure (at tree level), Eq. 1.95 reduces to:

$$\mathcal{A}_{PV} = -\frac{G_F Q^2}{\pi\alpha\sqrt{2}} \left(\sin^2 \theta_W + \frac{1}{4} \left[\frac{N}{Z} - 1 \right] \right) \quad (1.96)$$

1.6 Dynamics



Energy and momentum are conserved in elastic scattering:

$$E_0 + M = E' + E \quad \mathbf{p}_0 = \mathbf{p}' + \mathbf{p}$$

where M is the mass of the target nucleus.

Ignore the electron's mass, we have $E_0 \approx p_0$ and $E' \approx p'$:

$$\begin{aligned}
 E^2 &= M^2 + \mathbf{p}^2 = M^2 + (\mathbf{p}_0 - \mathbf{p}')^2 \\
 &= M^2 + (E_0 - E' \cos \theta)^2 + (E' \sin \theta)^2 \\
 &= M^2 + E_0^2 + E'^2 - 2E_0 E' \cos \theta \\
 &= (E_0 + M - E')^2
 \end{aligned} \tag{1.97}$$

So we get:

$$M(E_0 - E') = E_0 E' (1 - \cos \theta) \implies E' = \frac{M E_0}{M + E_0 (1 - \cos \theta)} \tag{1.98}$$

Q^2 dependence on the scattering angle θ is calculated as:

$$Q^2 = -q^2 = -[(E_0 - E')^2 - (\mathbf{p}_0 - \mathbf{p}')^2] = 2E_0 E' (1 - \cos \theta) \tag{1.99}$$

1.7 Why Pb208 and Ca48

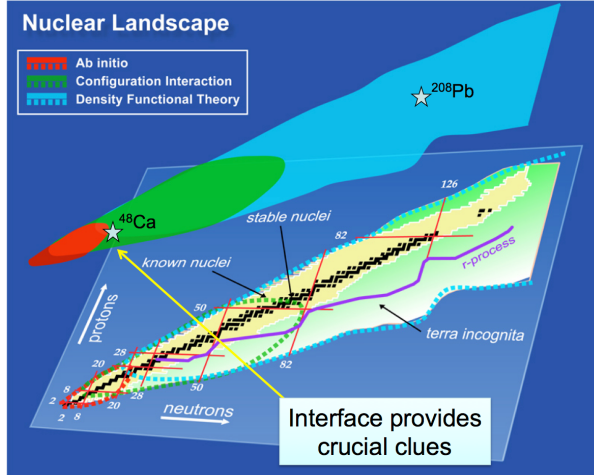


Figure 1.20: Nuclear Landscape

As tiny as the neutron skin thickness, to measure it relatively accurately, it is better to have a thicker neutron skin. So the target element is desired to have a large neutron excess. Unfortunately, most medium and heavy nuclei that have extra neutrons are unstable because of those extra neutrons. Only some nuclei with specific number of protons and neutrons are stable, those specific numbers are called the magic number. The magic number arises from the nucleon shell structure – when a shell is fully filled and the next higher energy shell is empty, and hence it is hard to separate out a nucleon from that closed shell.

Nuclei whose numbers of protons and neutrons are both magic are called doubly magic nuclei, which are more stable than single magic nuclei. Of all the known neutron-rich doubly magic nuclei, ^{10}He , ^{28}O , ^{48}Ca , ^{78}Ni , ^{132}Sn and ^{208}Pb , ^{48}Ca and ^{208}Pb are the only two that are stable, hence they are chosen for PREX-II and CREX.

For double magic nuclei, the energy of the first excited state is much larger than that of ground state. The energies needed to excite ^{48}Ca and ^{208}Pb are 3.84 and 2.6 MeV respectively. Together with the high momentum resolution of our spectrometers, we can easily separate inelastic scatterings from elastic ones, giving grounds for our choice of flux integration detection.

Other advantages of ^{48}Ca and ^{208}Pb include

- Both nuclei are spin-0, so that we don't need to worry about the target polarization.
- ^{208}Pb is heavy while ^{48}Ca is moderately heavy. As is discussed in the previous section, the elastic scattering is quasi, not exact. The small energy change is caused by the target recoil. The heavier the target nucleus, the smaller the recoil effect, therefore the better our measurement of Q^2 and the scattering angle.

Finally, one more reason for the choice of ^{48}Ca : ^{48}Ca lies in the medium region of the nuclear landscape, as shown in Fig. 1.20. Compared to ^{208}Pb , it is a smaller system that is accessible from ab-initio methods [25]. So it allows direct comparison to Chiral Effective Field Theory (EFT) calculations, which is very sensitive to three-nucleon forces. In other words, it can be used to probe three-nucleon forces. On the other hand, it is large enough to apply the DFT methods. By measuring the neutron skin thickness of ^{48}Ca , we hope to provide some inputs for bridging these two approaches.

Chapter 2

Experimental Setup

Over the past 30 years, PVES has been a well-established and powerful experimental technique in atomic, nuclear and particle physics. Its success traces back to Lee and Yang's prediction of parity violation in beta decay in 1956 and the following experimental proof by Wu in 1957. Shortly later, Zel'dovich first predicted the existence of parity-violating weak neutral current and proposed to measure it in electron-proton scattering in 1959 [34]. But it was only about 20 years later that people was able to experimentally observe the PV asymmetry in electron scattering experiments. In 1978, C.Y. Prescott etc. (E122 experiment at SLAC) measured the PV asymmetry in the inelastic scattering of longitudinally polarized electrons from an unpolarized deuterium target [35]. With this successful demonstration, more efforts were made to improve this experimental technique, which matured and boomed at the turn of last century. Many experiments were conducted to probe the contribution of strange sea quarks to nucleons' EM FFs (SAMPLE, G0, HAPPEX and A4) and test the Electroweak sector of the SM at low energy scale (E158, PVDIS, Qweak). It was PREX-I that first proposed the application of PVES to probe the structure of nuclei, then followed by PREX-II and CREX. Future programs (Moller, SoLID and MESA experiments) will continue the development of PVES and push it to a higher precision.

The idea of PVES experiments is very simple: scatter longitudinally polarized electrons off unpolarized target (H, D, He, C, Ca, Pb etc.), then measure number of scattered electrons (N); reverse the beam helicity and do the same measurement. The PV asymmetry between different helicities will be:

$$\mathcal{A}_{PV} = \frac{N^+/I^+ - N^-/I^-}{N^+/I^+ + N^-/I^-} \quad (2.1)$$

where I is the beam current, and the superscript denote the beam helicity. Repeat the above procedure millions of times to get a statistically precise result because the asymmetry is usually teeny tiny.

The devil is in the details. Generally, PVES experiments require two experimental conditions: a high-energy polarized electron beam and fast flipping of the beam polarization. Both requirements actually come to the same dependence: an intense source of

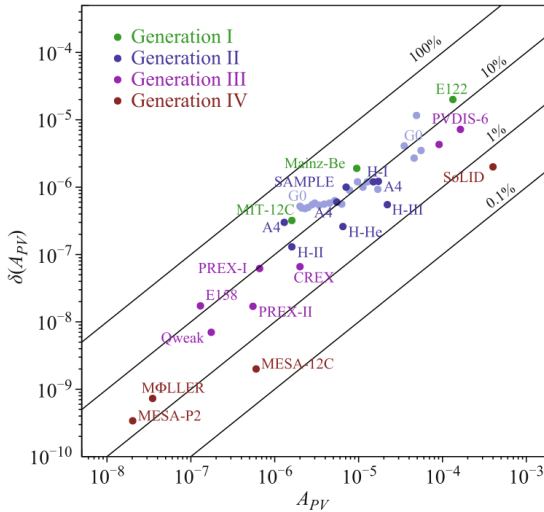


Figure 2.1: Evolution of PVES experiments, solid lines represent the relative precision. Generation I experiments (E122 (1978) [35], MIT-12C (1989) [36] and Mainz-Be (1990) [37]) did pioneering work to pave the way for PVES. Generation II experiments (the SAMPLE collaboration [38] at the MIT-Bates accelerator, the G0 [39] and HAPPEX [40] collaboration at JLab and the A4 collaboration [41] at the Maizer Mikrotron (MAMI) accelerator) were devoted to the exploration of strange FFs in nucleons. Generation III experiments (E158 at SLAC [42], Qweak [43] and PVDIS [44]) tested the SM at low energy and measured the neutron skin thickness of nuclei (PREX-I/II and CREX). The planned Generation IV experiments (SoLID program [45] and MOLLER experiment [46] at JLab, P2 experiment on the future Mainz Energy-recovery Superconducting Accelerator (MESA) [47]) will continue to test the SM and explore the structure of nucleons with higher precision. (MESA-12C is the same experiment as MESA-P2 with a different ^{12}C target)

polarized electrons with quick response. It took a few decades to develop such an electron source. Right now, the electron source at JLab can reach a polarization of about 90%, continued efforts are being made to improve the polarization further.

The fast flipping requirement originates from the consideration to cancel various noises. To measure such a tiny quantity, it is essential to control the experimental conditions as the same as possible between different helicity states. One easy and effective method to meet such a requirement is fast flipping (10^2 – 10^3 Hz) of the beam helicity: the faster the helicity reversal, the smaller the random noise in beam conditions, target density and other apparatus, the smaller the introduced false asymmetry. This requirement makes PVES out of the capacity of storage ring accelerators.

Though the fast reversal of the electron helicity, many efforts are still needed to control the beam fluctuation, making it as small as possible. This is called parity-quality beam (PQB). Possible systematic uncertainties in the source (injector) and accelerator will be controlled through the slow reversal of the beam helicity. In terms of the target deformity under electron bombardment, a raster with very high scanning rate (\sim kHz) will minimize

this uncertainty. As for detection of scattered electrons, electron flux rather than single electron will be counted due to high scattering rate ($\gtrsim \text{MHz}/\mu\text{A}$) in such experiments.

The two sister experiments are conducted in Hall A at JLab. The CEBAF accelerator at JLab is one of the few facilities in the world that can do PVES experiments (other facilities include MIMA and its successor MESA, the Facility for Antiproton and Ion Research (FAIR) and the Facility for Rare Isotope Beams (FRIB)). CEBAF provided excellent polarized electron beams (helicity correlated difference at sub-nanometer level) to Hall A, with dedicated apparatus (polarimeter, target chamber, high resolution spectrometer (HRS) and others) in Hall A, we were able to measure this tiny PV asymmetry precisely.

	PREX-II	CREX
Target	^{208}Pb	^{48}Ca
Target Thickness (mm)	$0.2554 + 0.5520 + 0.2566^{\textcolor{red}{1}}$	6
Target Density (g/cm ³)	11.38	1.855
Number of Target	10	$1 + 1^{\textcolor{red}{2}}$
Number of Used Target	6	2
Beam Energy (GeV)	0.953	2.18
Beam Current (μA)	50-85	100-150
Average Beam Polarization (%)	89.7	87.1
Beam Bunch Rate (MHz)	499	499
Electrons/Bunch ($\times 10^6$)	1.75	3.76
Helicity Flip Rate (Hz)	120/240	120
Power on the Target	$\sim 100 \text{ W}$ 70 μA	$\sim 350 \text{ W}$ 150 μA
Scattering Angle (deg)	4.7	4.51
Q^2 (GeV ²)	0.00616	0.0297
Scattering Rate (MHz/ $\mu\text{A}/\text{arm}$)	$\sim 30^{\textcolor{red}{3}}$	~ 0.2
Scattering Rate (1/bunch/arm)	~ 4.5	~ 0.05
xsection (mbarn)	3930.6	5.3
Acceptance (msr)	0.0037	0.0037
Collected Charge (C)	114	412
Predicted \mathcal{A}_{pv} (ppm)	0.6	2
Proposed Precision	3%	2.4%
Error on R_n (fm)	0.05	0.02

Table 2.1: Summary of experimental design and setup for PREX-II and CREX.

¹ ^{208}Pb target composes of 3 foils: upstream Diamond + ^{208}Pb + downstream Diamond

²Only 1 was prepared for the experiment. After the target accident, a new one was prepared.

³This rate doesn't include the contribution from the diamond foils

2.1 Beam Parameters

PREX-II and CREX are follow-up experiments to PREX-I, which also ran at JLab in 2010. With quite good control over systematic uncertainties, but unfortunately, many technical challenges are encountered during the experiment, PREX-I's result is statistics-limited, achieving a precision of 10% [48]:

$$\mathcal{A}_{Pb} = 656 \pm 60 \text{ (stat)} \pm 14 \text{ (syst) parts-per-billion (ppb)}$$

Based on the experience and lessons learned from PREX-I, PREX-II and CREX have more well-established designs, which help to meet the goal of high-precision.

One important feature of these two experiments is the redundancy design for critical components: there are two slow helicity reversal systems for systematic uncertainty control, two polarimeters for polarization measurement, multiple beam position monitors (BPMs) and beam current monitors (BCMs) for beam parameter monitoring, multiple ^{208}Pb targets and finally two HRS for reception of the scattered electrons.

2.1.1 Uncertainty Budget

The goal of PREX-II is to achieve the 1% precision in the ^{208}Pb neutron radius proposed by PREX-I, which requires the precision of PV asymmetry measurement better than 3% [19]. CREX proposed a similar goal, that a precision of 0.02 fm ($\sim 0.6\%$) in the ^{48}Ca neutron radius will be an essential benchmark to test various microscopic models [49], which correspond to a 2.4% total uncertainty in PV asymmetry.

As said above, PREX-I already has impressive control over systematic uncertainties (2.1%), so will the PREX-II and CREX. The main concern is to collect as much scattered electrons as possible to reduce statistical uncertainty, which is inversely proportional to \sqrt{N} , with N being the total number of scattered electrons.

$$\frac{\delta \mathcal{A}}{\mathcal{A}} = \sqrt{\sigma_{\text{stat}}^2 + \sigma_{\text{sys}}^2} \quad \sigma_{\text{stat}} = \frac{\sigma_{\text{det}}}{\mathcal{P}\sqrt{N}} \quad (2.2)$$

where σ_{det} is the detector uncertainty and \mathcal{P} refers to the beam polarization.

2.1.2 Figure Of Merits (FOM)

The choice of beam energy and scattering angle is a compromise of competing factors. PV asymmetry prefers larger beam energy and larger scattering angle, while scattering rate falls dramatically with beam energy and scattering angle. Q^2 also likes smaller beam energy and scattering angle, and calculation shows that the sensitivity of PV asymmetry w.r.t. neutron radius is oscillating along beam energy. All these considerations are incorporated into the FOM, which is defined as:

$$\text{FOM} = R \times \mathcal{A}^2 \times \epsilon^2 \quad (2.3)$$

Experiment	PREX-I (%)	PREX-II (%)	CREX (%)
Charge Normalization	0.2	0.1	0.1
Beam Asymmetry	1.1	1.1	0.3
Detector Non-Linearity	1.2	1.0	0.3
Transverse Asymmetry	0.2	0.2	0.1
Polarization	1.3	1.1	0.8
Target Contamination	0.4	0.4	0.2
Inelastic Scattering	< 0.1%	< 0.1	0.2
Effective Q^2	0.5	0.4	0.8
Total Systematic	2.1	2	1.2
Statistical	9.1	2.2	2.1
Total	9.2	3	2.4

Table 2.2: Budget of systematic and statistical uncertainties in both experiments [49, 50]

where R is the scattering rate, \mathcal{A} the PV asymmetry and ϵ the sensitivity of \mathcal{A} w.r.t. R_n . One difference here is that FOMs for most PVES experiments have only R and \mathcal{A}^2 , the inclusion of ϵ in our FOM helps to achieve a higher precision in R_n measurement.

Rate

For a data set of N independent events sampled from one normal distribution $X \sim N(x_0, \sigma_0)$, the statistical uncertainty on the measured mean value will be:

$$\text{var}(\bar{x} = \frac{1}{n} \sum x_i) = \frac{1}{n^2} \text{var}(x_i) = \frac{\sigma_0^2}{n} \implies \sigma(\bar{x}) = \frac{\sigma_0}{\sqrt{n}}$$

Assume one want to measure a 1 ppm asymmetry to 1% statistical uncertainty,

$$\frac{\sigma_{\mathcal{A}}}{\mathcal{A}} = \frac{1}{\mathcal{A}} \frac{\sigma_{\text{det}}}{\sqrt{2N}} \approx \frac{1}{\mathcal{A} \sqrt{2N}} = 1\% \implies N = 5 \times 10^{15} \quad (2.4)$$

a factor of 2 is included because there are two HRS arms. One need to count $\sim 10^{15}$ scattered electrons. Given a counting rate of 1 MHz, it will take $\frac{5 \times 10^{15}}{1 \text{ MHz}} = 5 \times 10^9 \text{ s} \approx 160 \text{ years}$, a completely unacceptable time scale. As a solution, the integrated flux technique is adopted for a higher scattering rate, which is:

$$\frac{dR(\theta)}{d\Omega} = \frac{d\sigma}{d\Omega} I t \frac{\rho}{A} \times N_A \quad (2.5)$$

- $\frac{d\sigma}{d\Omega}$ is the fractional cross section in the unit of cm^2/str .
- I is the beam current in the unit of electrons/s.
- t is the target thickness in the unit of cm.
- ρ is the target density in the unit of g/cm^3 .

- A is the atomic number.
- $N_A = 6.022 \times 10^{23}$ is the Avogadro's constant.

The differential cross section is calculated by our theorist friends with values of 3930.6 mbarn and 5.3 mbarn for ^{208}Pb and ^{48}Ca at their corresponding kinematics. Other parameters can be checked out in Table 2.1.

The total rate will be the integration over the acceptance:

$$R = \int \frac{dR(\theta)}{d\Omega} d\Omega = \frac{dR}{d\Omega} d\Omega \quad (2.6)$$

PREX-II and CREX have an acceptance defined by the septum magnet and the Q1 collimator, which is $d\Omega = 0.0037$ str.

As shown in Fig. 2.2, for both ^{208}Pb and ^{48}Ca , the scattering rate falls quickly along both the beam energy and the scattering angle, so one would like a low beam energy and a small scattering angle (equivalently a small \mathbf{q}) for a high scattering rate.

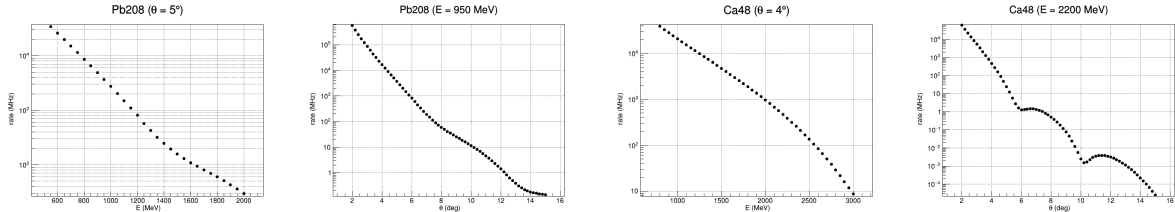


Figure 2.2: Scattering rate versus the beam energy and the scattering angle for ^{208}Pb and ^{48}Ca , the other parameters (energy in the scattering angle plot and vice versa) are fixed to their design values.

Asymmetry and Sensitivity

As shown in Eq. 2.4, the asymmetry itself matters, a 2 times larger asymmetry means the run time can be reduced to one quarter, a huge save of the beam time. So we should choose a kinematic region where the asymmetry is large. Besides, asymmetry's sensitivity (ϵ) to the neutron radius is also important. Keep in mind that our final goal is to extract the neutron radius from the PV asymmetry, the more sensitive the asymmetry to the neutron radius, the more precise the extracted neutron radius. The sensitivity is calculated as the relative change of \mathcal{A} with 1% change in the neutron radius.

$$\epsilon = \frac{\delta \mathcal{A}/\mathcal{A}}{\delta R/R} = \frac{|\mathcal{A}_{\text{stretched}} - \mathcal{A}|/\mathcal{A}}{1\%} \quad (2.7)$$

Though asymmetry is what will be measured, one can estimate its value based on some theoretical models, as is calculated by our theorist friends in [18].

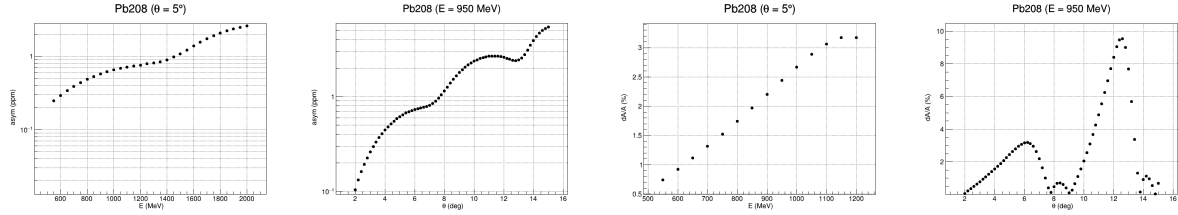


Figure 2.3: Asymmetry and sensitivity plot for ^{208}Pb . The asymmetry increases along the beam energy and goes upward with oscillation along the scattering angle. The sensitivity also increases against the beam energy and oscillates against the scattering angle. The sensitivity plot is calculated with 1% change in the neutron radius and it shows the absolute value. With $E = 950$ MeV, there is a local maximum around $\theta \sim 6^\circ$.

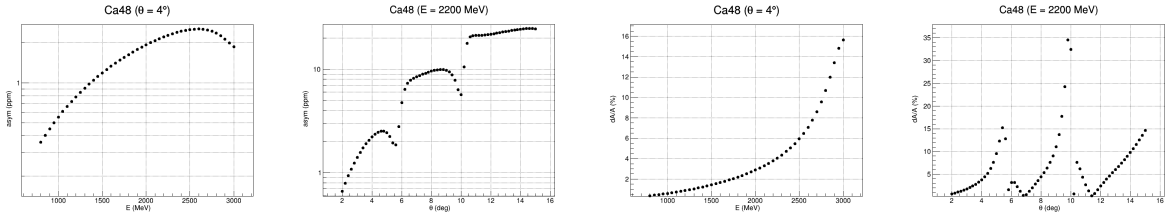


Figure 2.4: Similar asymmetry and sensitivity plot for ^{48}Ca , the asymmetry maximizes around 2500 MeV with $\theta = 4^\circ$ and there is a local maximum about 4.5° when $E = 2200$ MeV. As for the sensitivity, it increases monotonously along the beam energy and comes to a regional maximum around 5° with $E = 2200$ MeV.

Based on the theoretical result, we can optimize the kinematics for both nuclei (consider only the statistical uncertainty here):

$$\frac{\delta R}{R} = \frac{\delta \mathcal{A}}{\mathcal{A}} \frac{1}{\epsilon} = \frac{\sigma_{det}}{\mathcal{P}} \frac{1}{\sqrt{N} \mathcal{A} \epsilon} \quad (2.8)$$

To minimize $\delta R/R$, it is equivalent to maximize

$$\text{FOM} = N \times \mathcal{A}^2 \times \epsilon^2 \quad (2.9)$$

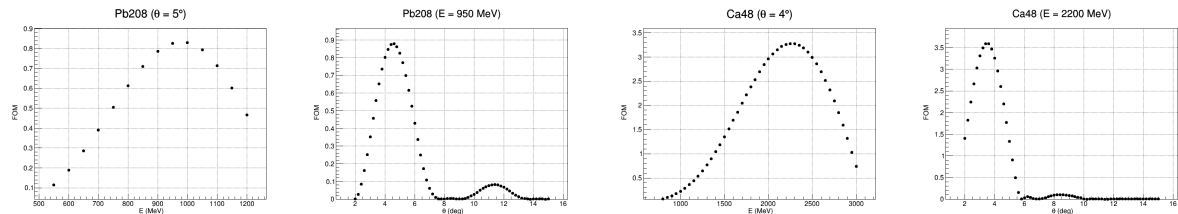


Figure 2.5: For both nuclei, FOM supports a small scattering angle. As for the beam energy, FOM maximizes around 950 (2200) MeV for ^{208}Pb (^{48}Ca).

Given practical constraints on how low an angle (4°) we can reach with septum magnets, the beam energy and the scattering angle were chosen to be 950 (2200) MeV and 5 (4) degree for ^{208}Pb (^{48}Ca). The beam energy of CREX is exactly a natural 1-pass beam energy in CEBAF in the 12 GeV era.

2.1.3 Helicity Flip Frequency

The main consideration for the choice of the 120 Hz (240 Hz) flip frequency was to cancel the 60 Hz power line noise, which is the major source of noise in PVES experiments.

There are a few methods to cancel this low frequency noise in a PVES experiment.

1. Set the flip frequency to a very high value, say 1 kHz, then the change of fluctuations caused by this low frequency noise will be negligible between two nearby helicity windows and cancelled in the asymmetry calculation. This method can eliminate many low frequency noises and was adopted in the Qweak experiment.
2. Integrate over this 60 Hz noise within a helicity window, which means $f = \frac{60}{n}$ Hz ($n = 1, 2, \dots$). This way no 60 Hz line noise will be recorded at all.
3. Select a flip frequency of $f = n \times 60$ Hz, then use helicity pattern to cancel the 60 Hz noise. For example, if $f = 120$ Hz, then every $f/30 = 4$ continuous helicity windows form a helicity pattern, asymmetry will be calculated based on helicity patterns. This was used in PREX-II/CREX.

In terms of cancelling the 60 Hz line noise, the second method works best, it removes the line noise completely, while other two methods also cancel the noise in their asymmetry calculation, it broadens the asymmetry width. But in a comprehensive consideration, the frequency in the second method is not high enough to cancel other low frequency noises. As for the first method, it is best in terms of removing low frequency noises, the only drawback is that with a fixed settle time T_{settle} – the time needed to settle a helicity state, the higher the frequency, the lower the T_{stable} – the stable time window during which we integrate scattered electrons, and therefore the longer the run time. As a compromise, the third method was chosen for PREX-II/CREX.

2.2 Continuous Electron Beam Accelerator Facility (CEBAF)

CEBAF is able to deliver multi-GeV continuous wave (cw) electron beams of different energies and different intensities to four experimental halls simultaneously. With the 12 GeV upgrade, the injector energy is increased from 67.5 MeV to 123 MeV. The north and south 1497 MHz linear accelerators (LINACs) each has 25 superconducting radial frequency (SRF) cryomodules, capable of accelerating electrons at the peak rate of $1.1 \times 2 = 2.2$ GeV/turn. With 11 arcs of magnets connecting the LINACs, Hall A, B and C

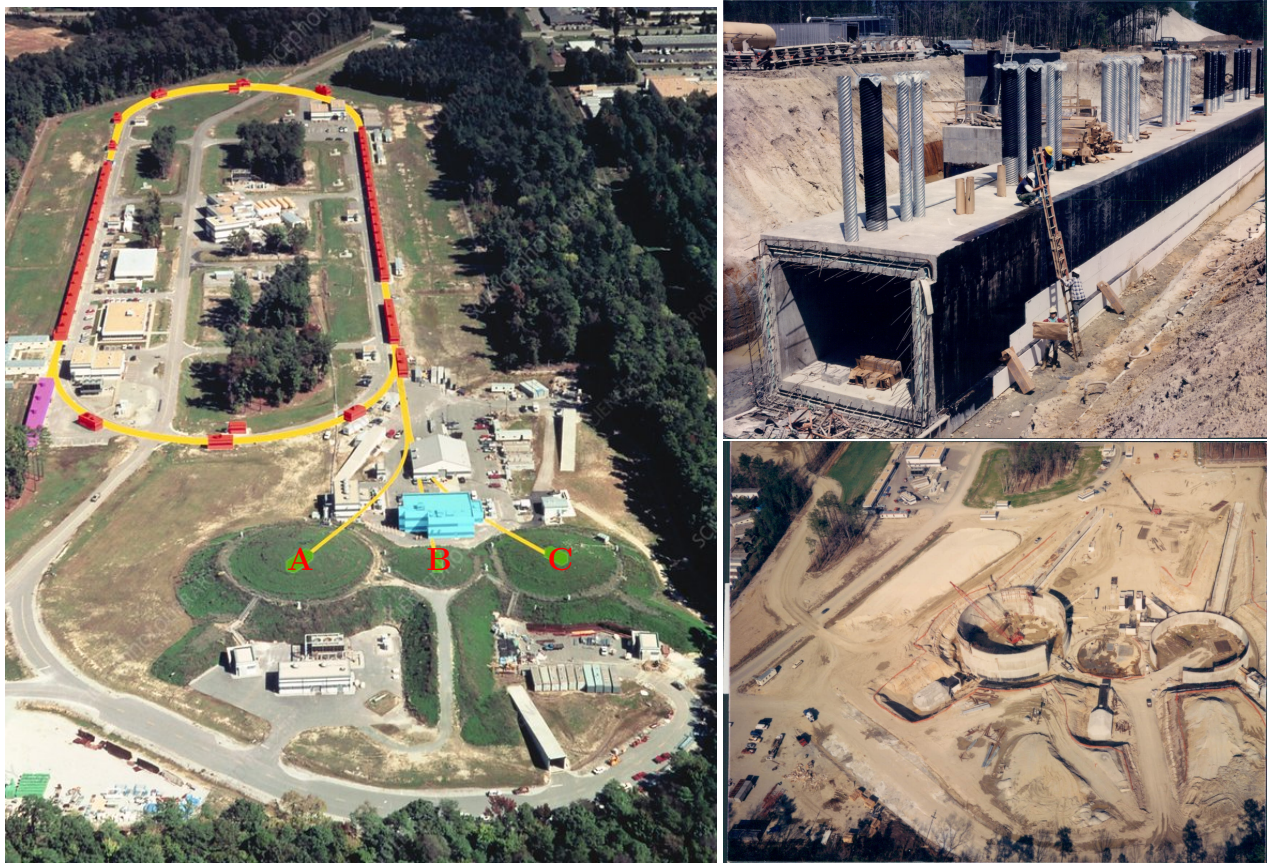


Figure 2.6: Aerial view of JLab accelerator site, yellow line tells the position of the CEBAF accelerator and the three experimental halls are marked out as A/B/C (Hall D locates on the top left corner, after the exit of the north LINAC). The accelerator tunnel is 30 feet (~ 9 m) underground and 10 feet (~ 3 m) high, with a circumference of about 7/8 mile (1.4 km). There are two superconducting LINACs (red lines), each of 1/4 mile (400 m). The pink part on the mid left is the location of injector. The right two plots show the tunnel and experimental halls under construction.

can receive up to $2.2 \times 5 = 11$ GeV cw beams. Hall D, with an extra half circle, can receive up to 12 GeV cw beams. With this design, different nuclear experiments can be carried out in different halls without interfering each other, theoretically.

As one can see in Fig. 2.7, laser pulse ($\lambda = 780$ nm) from four lasers (Hall D laser is not shown in the plot) shoot in the electron gun (two electron guns in total) that operates at -130 kV to excite electrons, which interweaving with each other, forming a chain of electron bunches, with a phase difference of 120° from nearby bunches (Hall D doesn't have its own slit in the chopper, therefore it follows either Hall A or Hall C). This electron chain is sent into the north LINAC by the injector and accelerated by both LINACs. After reaching the desired energy, they will be kicked out at the exit of the south LINAC and delivered to experimental halls (A, B and C) for various experiments.

The maximum beam current of $200 \mu\text{A}$ at (old) highest energy of 5 GeV available at

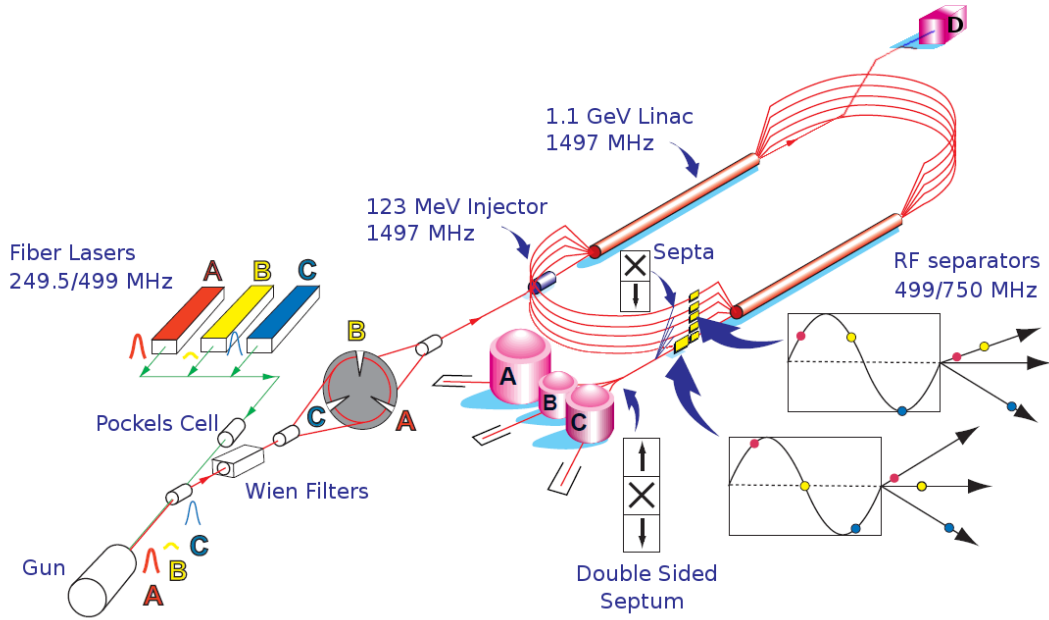


Figure 2.7: Schematic plot of CEBAF. The circular plate with three slits is the beam chopper, which has no slit for Hall D, that's why Hall D beams have to follow electron beams of other halls. During acceleration, low energy beams will be kicked into higher arcs, while high energy beams will go through lower arcs. The magnetic field increases from higher arcs to lower arcs to keep electron trajectories have the same radii.

CEBAF is limited by the rf power ($1 \text{ MW} = 5 \text{ GeV} \times 200 \mu\text{A}$) and by the beam power on the beam dump. While Hall B and D require only tiny amount of cw beams (at nA level), it is actually Hall A and C that consume almost all the electron beams, both can receive a few tenths to over one hundred μA cw beams.

While all four halls at JLab are dedicated to the study of nuclear structure, they focus on different aspects. Hall A concentrates on form factors of various nuclei, Hall B digs into generalized parton distributions, Hall C devotes itself to precise determination of valance quark properties in nuclei, and finally, the newly established Hall D explores origin of confinement through exotic mesons.

Because all four halls shared the same electron source and the same accelerator, cooperation is needed to make them work at the same time. In terms of the electron source, PVES experiments usually have priority over other experiments to maintain quality of the polarized electron beam. As for the LINACs, if one hall wants a smaller energy, say 1 GeV, then the LINAC power will be reduced to 1 GeV/turn, which will be applied to other electron beams, therefore limiting the highest energy available in other halls. Careful schedule is needed to make sure every hall gets what they want.

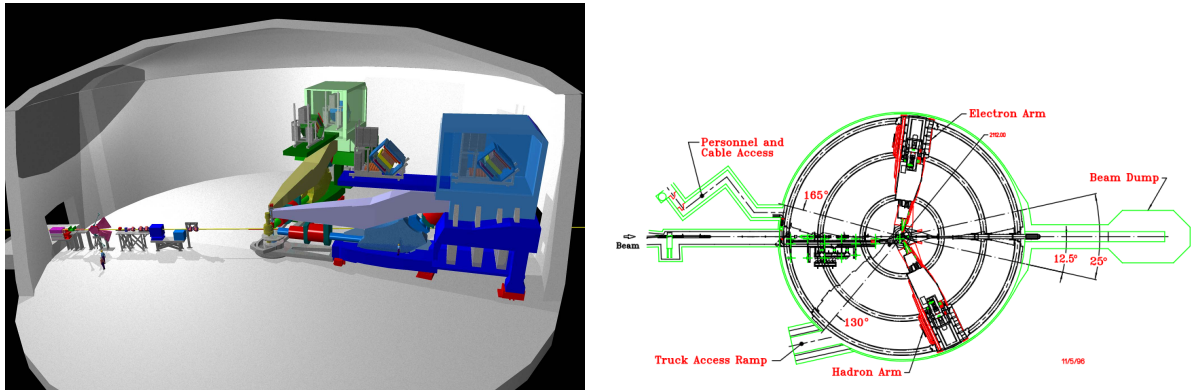


Figure 2.8: 3D and bird view of Hall A [51]. Originally, the 2 spectrometers were called High Resolution Hadron Spectrometer (HRHS) and High Resolution Electron Spectrometer (HRES), but they are essentially identical to each other and can be used interchangeably. so now they are called left arm (LHRS) and right arm HRS (RHRS).

2.3 Polarized Electron Beam

2.3.1 Polarized Electron Source

PVES experiments motivate the development of the polarized electron source, which is required to produce stable high-polarization electron beams at a wide range of intensity, from nA to A depending on the experiment. The source should be capable of rapid helicity reversal ($\sim 100 - 1000$ Hz) with negligible impact on other properties of the electron beam.

Currently, GaAs-based semiconductor photoemission source is the only choice on the market that can be used as the polarized electron source. Historically, this kind of electron source was the only one that could satisfy high peak currents required by the low duty factors of the old accelerators and rapid helicity reversal required by PVES experiments. That is why it is the only player on the market now. Over the past few decades, pulsed beam has been replaced by continuous beam while this electron source is inherited and further developed. The polarized electron source used by CEBAF can produce electron beams with polarization greater than 85%, much larger than the 37% polarization from its inauguration at SLAC. [35]

The design was first proposed independently by Garwin, Pierce and Siegmann [52] and by Lampel and Weisbuch [53]. The idea is straightforward: when circularly polarized laser light with carefully selected energy $E_{\text{gap}} < h\nu < E_{\text{gap}} + \Delta$ shoot on the semiconductor, only electrons on the valance band $P_{3/2}$ will be pumped into the conduction band $S_{1/2}$. The selection rule makes sure only those transitions that satisfy $\Delta m_j = +1$ (-1) can occur for circularly right (left) incoming photons, as shown in Fig. 2.9. The ratio of the transition rate is also marked out in circle in the plot, which can be calculated from the Clebsch-Gordan coefficient easily. The excited electrons are polarized and different states have different pumping rate, in this way, polarized electron beam is produced, with a

polarization of: $\mathcal{P} = (3-1)/(3+1) = 50\%$, for both helicities.

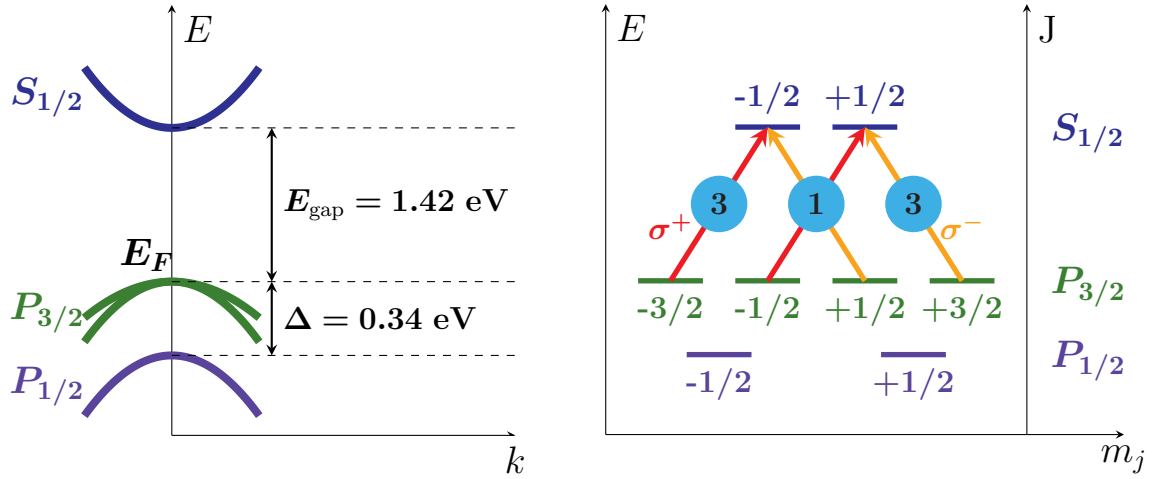


Figure 2.9: Excitation of electrons in the semiconductor. Excited electrons with $J_z = +1/2$ ($-1/2$) are right (left)-handed.

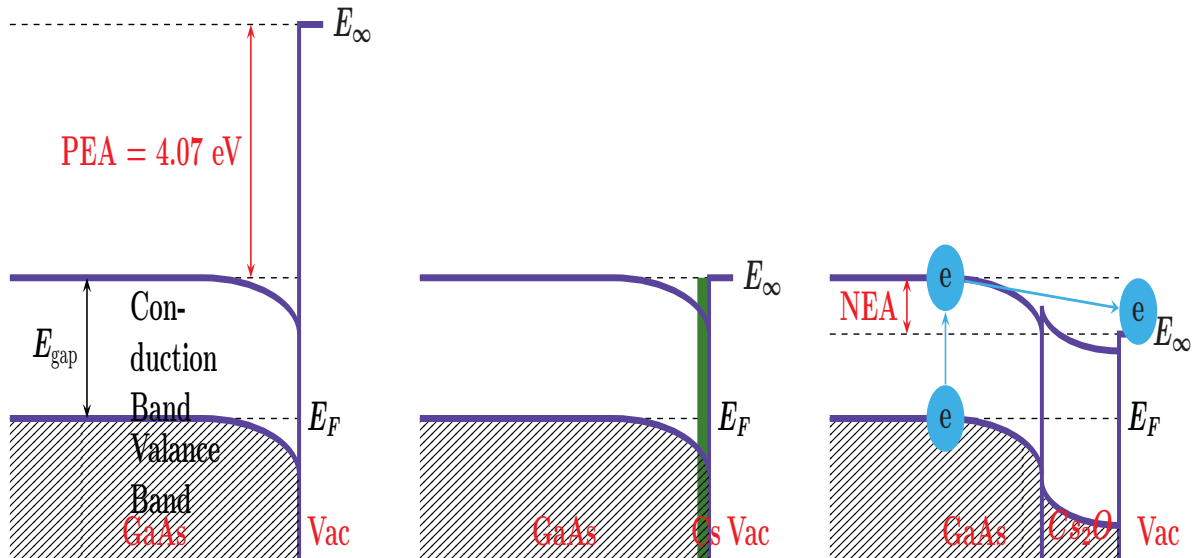


Figure 2.10: The energy band diagram of GaAs near its surface. Left: bare p-type GaAs, the large positive electron affinity (PEA) prevents electrons from escaping the surface; Middle: p-type GaAs with a cesiated surface, the electron affinity (EA) is 0, but electrons still can't escape the surface easily; Right: GaAs with layer of cesium oxide; the electron vacuum energy E_∞ is lowered to make a negative EA so that electrons can break free from the surface easily. [54]

The next challenge is to liberate the polarized electrons from the material, without degenerating the polarization significantly. As shown in Fig. 2.10, for bare GaAs, a

4.07 eV electron affinity (EA) prevents any electrons from leaving the surface. To solve this problem, a condition known as negative electron affinity (NEA) is used, that is to make the energy of the electron in the vacuum just outside the surface lower than the conduction band energy by adding a layer a cesium oxide on the surface of a pure GaAs semiconductor.

By the NEA technique, one is able to get polarized electron beams, but never reach the ideal 50% polarization: achieved polarization ranges between 25 to 43%. The polarization loss is due to spin dilution as electrons diffuse to the semiconductor surface. From this aspect, one can increase the polarization by reducing the thickness of the GaAs crystal. However, even the thinnest GaAs crystal can't give a polarization greater than 50%. New strategies are needed. The answer is the strained GaAs [54].

With a strained layer, the degeneracy of the $P_{3/2}$ state is split, only states with $m_j = \pm 3/2$ will be pumped, therefore reaching a 100% polarization, in ideal case. The real polarization achieved by the CEBAF electron source is about 88%.

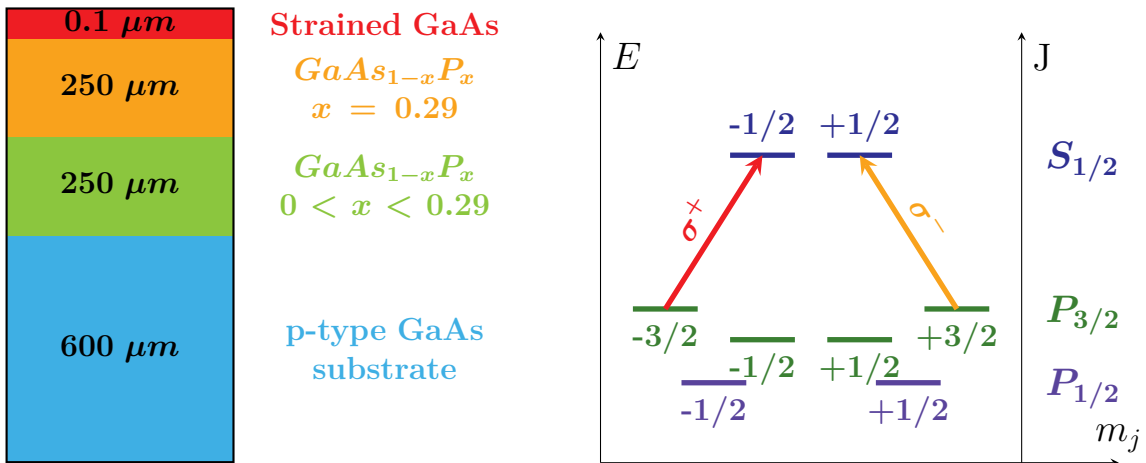


Figure 2.11: Layout of a strained GaAs electron source and corresponding excitation plot.

2.3.2 Polarization Control

Pockels Cell

With a proper electron source to produce polarized electron beams, we need more control over the beam polarization. We should be able to flip the beam polarization quickly while keeping the polarization as stable as possible. It is not easy and time consuming to manipulate electrons directly, while manipulating photons is much easier. One just need to reverse the circular polarization of the incident laser pulse, the electron beam polarization will be flipped. An easy way to do the job is a half-wave plate, by inserting it into or retracting it from the optical path, the phase of the laser pulse will be changed by π , therefore flip the laser circular polarization.

The drawback of the half-wave plate is that the mechanical movement is not fast enough. For PVES experiments, the fast flipping of the beam polarization is done by

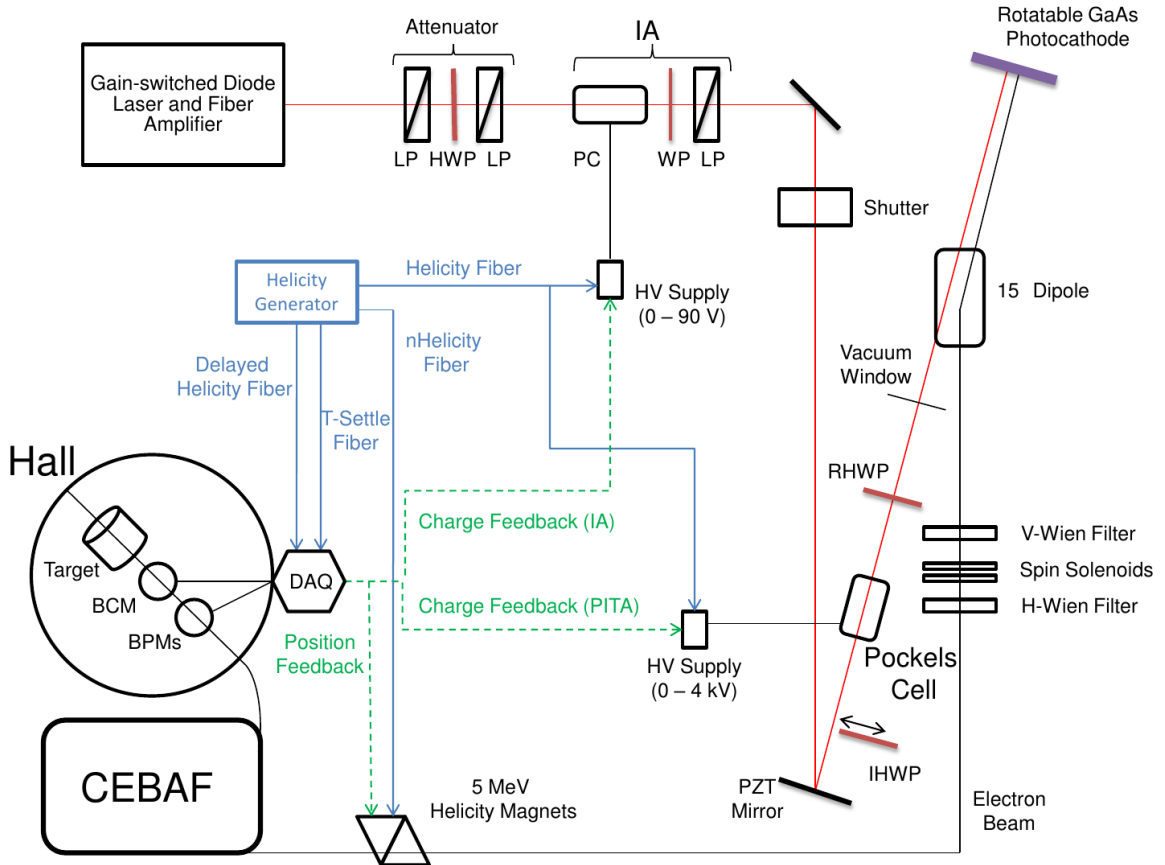


Figure 2.12: The laser system at the CEBAF injector

a component called Pockels Cell (PC), which is a Rubidium Titanylo Phosphate (RTP) crystal. PC operates based on the Pockels effect, which is the production of birefringence in the crystal under an electric field, the resulted birefringence is proportional to the strength of the applied electric field. By applying appropriate high voltage (~ 1.5 kV), PC will act as a quarter wave plate (photon amplitude along fast and low axes E_x , E_y will have a phase difference of $\pm\frac{\pi}{2}$ depending on the polarity of the applied electric field), converting a linearly polarized laser beam into a circularly polarized one. And reserve the electric field polarity will reverse the polarization of the laser beam. This transition can be very fast, up to 1 kHz, with a dead time of about 60 μ s.

Polarization Induced Transport Asymmetry (PITA, or Phase Induced Transmission Asymmetry) [55]

The above discussion is an ideal case that PC will be an exact quarter wave plate and other optical components also work flawlessly. In reality, there is always some deviations from the perfect circular polarization, resulting in systematic effects on beam position, spot size and intensity. If the deviation is polarization correlated, it will introduce a false

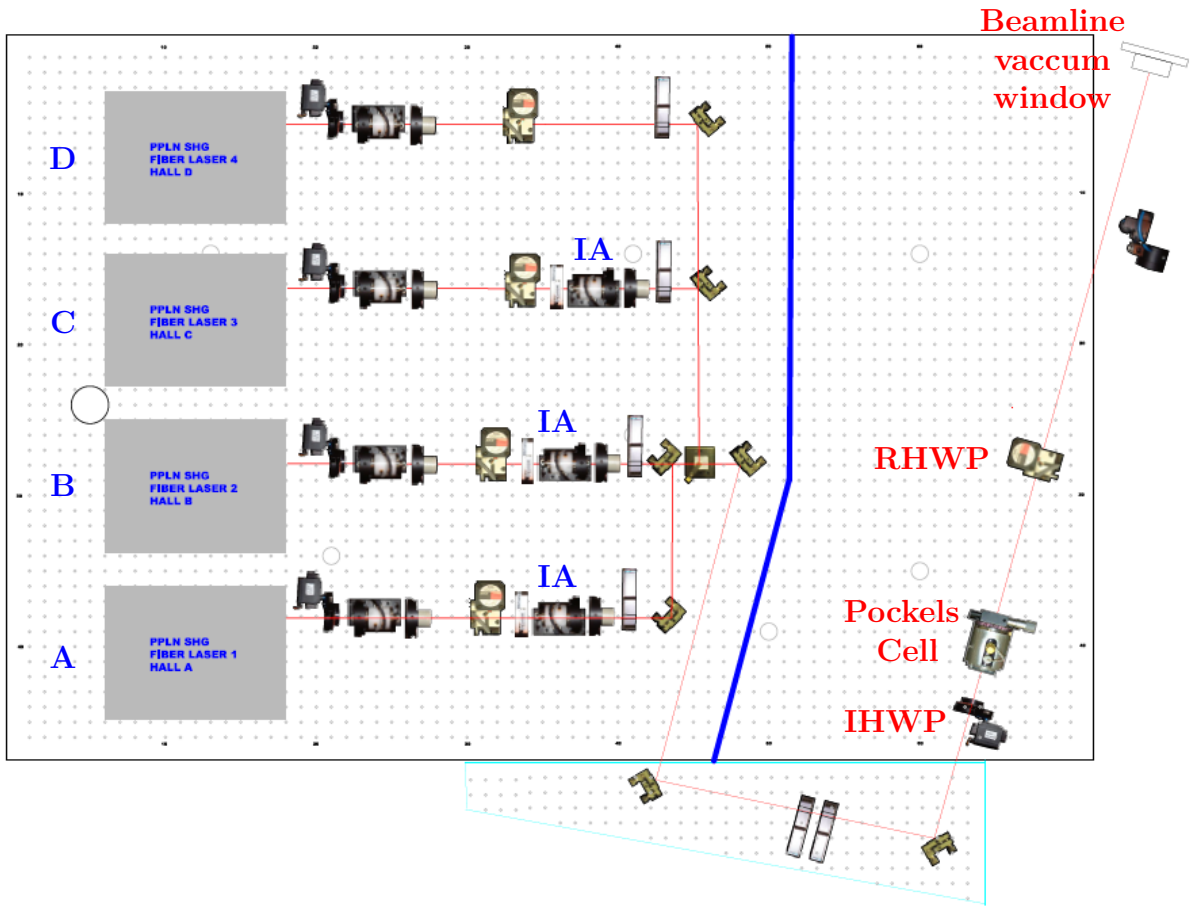


Figure 2.13: Schematic plot of the laser table.

asymmetry to our PV asymmetry measurement, which is called the PITA effect. The PITA effect is the dominant piece of the helicity correlated beam asymmetry (HCBA), which is the largest false asymmetry in our measurement.

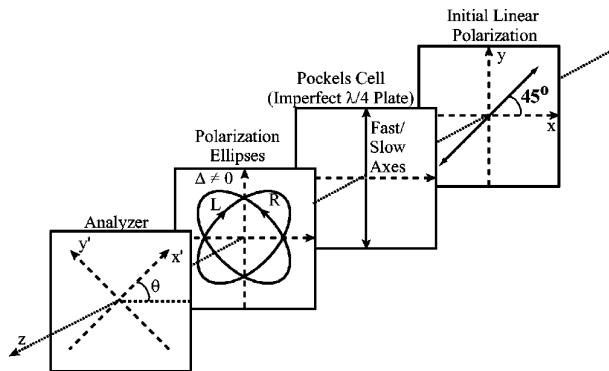


Figure 2.14: Phase shift by going through the PC.

The PITA effect is characterized by the PC induced phase shift δ :

$$\delta^{R(L)} = \mp \left(\frac{\pi}{2} + \alpha \right) - \Delta \quad (2.10)$$

where α and Δ represent the symmetric and asymmetric offset phase shift respectively. The resultant slightly elliptical beam has a residual linear component, leading to an intensity asymmetry (to first order):

$$\mathcal{A}_I = \frac{I^R - I^L}{I^R + I^L} = -\frac{\epsilon}{T} [\Delta \cos(2\theta)] \quad (2.11)$$

where ϵ/T ($\ll 1$) defines the “analyzing power” with $\epsilon = T_{x'} - T_{y'}$ and $T = (T_{x'} + T_{y'})/2$. $T_{x'(y')}$ is the transmission coefficient along the axis x' (y') of the downstream analyzer. θ is the angle between the PC’s fast axis and the x' axis of the analyzer.

Considering other optical components along the laser path, like the rotatable half-wave plate (RWP) and the vacuum window, the unknown tiny birefringence in these components will also contribute to Δ , resulting in a modified intensity asymmetry:

$$\mathcal{A}_I = \frac{I^R - I^L}{I^R + I^L} = -\frac{\epsilon}{T} [\cos(2\theta) \cdot (\Delta - \Delta^0)] \quad (2.12)$$

where Δ^0 represents the asymmetric offset phase shift due to all other components.

To minimize the intensity asymmetry, one would like to keep $\Delta - \Delta^0$ as small as possible. Fortunately, *Delta* is tunable, by changing the applied electric field. As shown in Fig. 2.12, our charge feedback system will monitor the charge intensity asymmetry and automatically adjust the HV supplied to the PC to maintain a small \mathcal{A}_I . Over PREX-II and CREX, the average charge intensity asymmetry is about 100 ppb.

As shown in Fig. 2.12, the charge feedback system also controls the HV supply of the Intensity Attenuator (IA). IA, together with the slit in the beam chopper, control the intensity of the outgoing electron beams (Δ does a fine tune to the beam intensity). So, IA also plays a key role in achieving a small charge intensity asymmetry by equalizing beam intensities across helicity states.

Another important element is the RWP, which lies downstream the PC. It helps to equalize any residual linear polarization left in the PC to establish a quantum efficiency (QE) independent of helicity.

Slow Helicity Reversal

Fast reversal of the PC can minimize a lot of random noise from beam and target density fluctuations. Nevertheless, some helicity correlated (HC) false asymmetries remain, such as the electronic pickup between accelerator electronic systems and the experimental DAQ system or the residual birefringence effect. It is the job of the slow helicity reversal to cancel these systematic false asymmetries.

There are two methods to make slow helicity reversal – the insertable half-wave plate

(IHWP) and the double Wien Filters. Prior to 2009, IHWP was the only available approach at CEBAF to do slow helicity reversal. A new mechanism was introduced during PREX-I and Qweak experiments for better systematic precision – the wien filter.

The IHWP lies upstream of the PC, as said above, it is easy to change the beam helicity by inserting or retracting the IHWP. Slow helicity reversal enables us to identify the possible systematic uncertainties. The idea is simple, assume the true and a systematic false asymmetry to be \mathcal{A}_0 and $\Delta\mathcal{A}$, then the measured asymmetry by inserting (retracting) the IHWP will be:

$$\mathcal{A}^{+(-)} = \pm\mathcal{A}_0 + \Delta\mathcal{A} \quad (2.13)$$

Because IHWP doesn't affect the systematic uncertainty, the true asymmetry will be:

$$\mathcal{A}_0 = \frac{\mathcal{A}^+ - \mathcal{A}^-}{2} \quad (2.14)$$

As good as the IHWP, it resolves only some of the HC beam variations, namely the residual birefringence from the laser optical system and is powerless in dealing with other HC effects, like HC beam size variations that are introduced via PC focusing [56], which is addressed by the wien filter.

The double wien filters manipulate the electron spin directly by EM fields without affecting the electron movement and is able to achieve any spin orientation. It consists of two wien filters and two intervening solenoids between them, as shown in Fig 2.15. A wien filter is such a cavity with proper electric and magnetic fields ($qE = qvB$) that are perpendicular to each other and to the electron moving direction, so that it rotates only the electron spin.

Electrons coming from the photocathode are longitudinally polarized, the vertical wien filter will make the electron spin vertical oriented, then the spin will be rotated to left/right by the following spin solenoid, depending on the polarity of the solenoid. A wien flip means to change the polarity of the spin solenoid. Finally, the horizontal wien filter will fine tune the spin direction to optimize the longitudinal polarization in the experimental hall.

Note that electrons at the exit of the double wien filters are not longitudinally polarized, because electron spin will precess when travel through the accelerator, causing a rotation in the horizontal plane. Therefore, a carefully selected initial spin direction is needed to make sure the spin is (anti) parallel to the electron momentum at the target. This tells another function of the double wien filters: to set a non-longitudinal initial spin to cancel out the shift caused by the spin precession during acceleration, so that the electron beam is exactly longitudinally polarized at the target.

With both the IHWP and the double wien filters, we are able to cancel most systematic false asymmetries, achieving very small systematic errors.

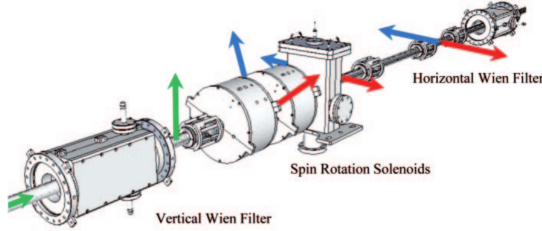


Figure 2.15: Schematic plot of the double wien filters. Electron beam travels from left to right. [56]

2.3.3 Polarimeters

With polarized electron beams, we need to measure their polarizations. There are three polarimeters to measure the beam polarization: the Mott polarimeter at the injector and the Compton and Moller polarimeters in Hall A. As their names imply, they use the cross section asymmetry of the Mott, Compton and Moller scatterings to measure the polarization of the electron beam. Since these are all pure quantum electrodynamics (QED) processes, their cross sections are well understood and analyzing powers are easily calculable to high orders.

While the Mott and Moller measurements are invasive, they can't be done frequently (Moller measurement happens about every 10 days). The non-invasive Compton polarimeter is the only choice for beam polarization monitoring. The Mott polarimeter measures the beam polarization before it enters the accelerator, so it is not used for the determination of the beam polarization during PREX-II/CREX.

Mott Polarimeter

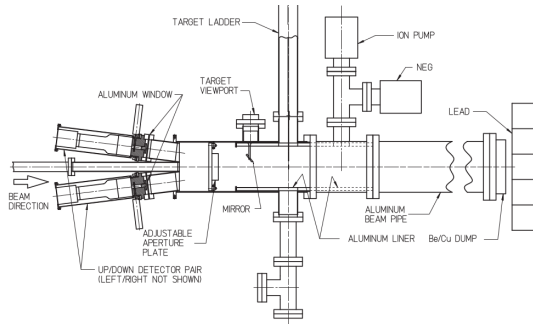


Figure 2.16: Schematic plot of the Mott polarimeter. It has 4 symmetric detector ports (up and down, left and right – left/right detectors are not shown in the plot). The back scattering angle is 172.6° , where the highest analyzing power is achieved from theoretical calculations of the Sherman function. [57]

The 5-MeV Mott polarimeter lies at the CEBAF injector, between the double wien filters and the Injection Chicane, it measures the single spin cross section asymmetry of

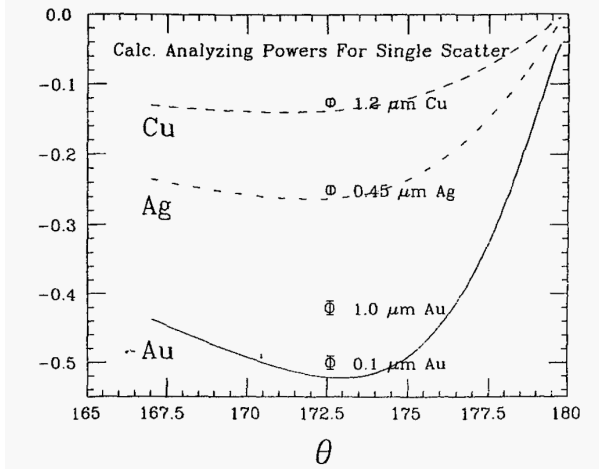


Figure 2.17: The Sherman function for different high-Z targets at 5 MeV, dots represent experimental measurements.

5 MeV electron beams scattered off a high-Z target. Comparing the measurement to the Sherman function S [58] – the analyzing power, one will derive the transverse polarization of the beam:

$$\mathcal{A}_{LR} = \frac{N_L - N_R}{N_L + N_R} = S(\theta) \mathbf{P} \cdot \hat{\mathbf{n}} \quad (2.15)$$

where θ is the scattering angle and $\hat{\mathbf{n}}$ is the unit normal vector of the scattering plane. The same formula applies to the up-down asymmetry. Because the asymmetry comes from the coupling of the electron spin and the induced magnetic field by the nucleus in the electron's rest frame (spin-orbit coupling), the scattering potential is:

$$V(r, \mathbf{L}, \mathbf{S}) = V_{\text{Coulomb}} + V_{\text{so}}(r, \mathbf{L}, \mathbf{S}) = \frac{Ze}{r} + \frac{Ze^2}{2m^2r^3} \mathbf{L} \cdot \mathbf{S} \quad (2.16)$$

So only the transverse polarization, rather than the longitudinal one, can be measured using a Mott polarimeter. Nevertheless, it provides an independent check of the initial beam polarization from the injector and its high precision (its total uncertainty can be as small as 0.61% [57]) helps to normalize the polarization measurement in the experimental halls.

Compton Polarimeter

The Compton polarimeter locates at the entrance to Hall A (about 20 m upstream the target chamber), using the elastic scattering between polarized photons and electrons to measured the polarization of the electron beam. As shown in Fig. 2.18, when the Compton polarimeter is on, the electron beam will be bent into the Compton Chicane to interact with the polarized photons nearly head-on (with a tiny crossing angle of 23.5 mrad). The Fabry-Perot Cavity is locked to and filled with circularly polarized ($> 99\%$) green laser beam ($\lambda = 532$ nm, $E = 2.334$ eV). The back-scattered photons will be detected by a

Gadolinium Orthosilicate (GSO) crystal calorimeter right of the interaction region, while the unscattered electron beam will be sent back to the beam pipe to bombard the target. Due to interaction with photons, the scattered electrons will be less energetic than the incoming ones. Under the same dipole field, the scattered electrons will be bent more than the unscattered ones, as shown by the red dash line in Fig. 2.18. This separation allows to count the scattered electrons, together with the measurement of scattered photons, one can identify the scattering asymmetry and then the polarization of the electron beam.

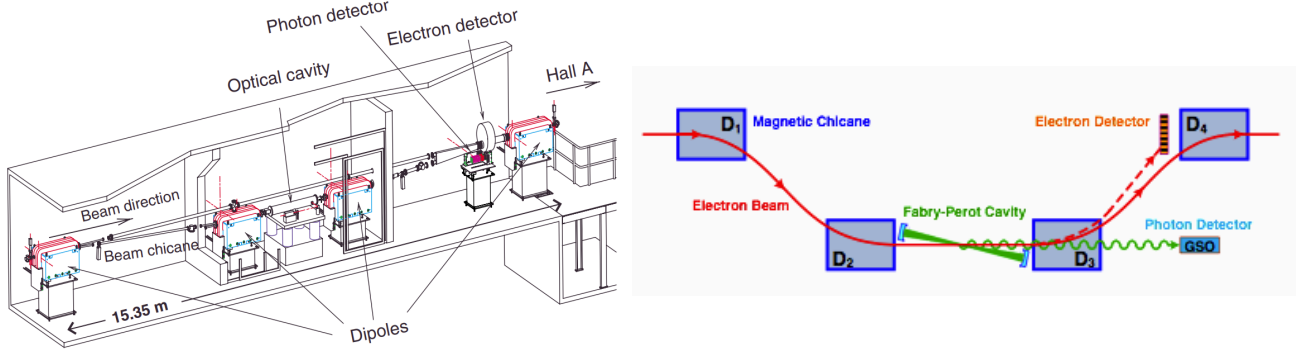


Figure 2.18: Left: schematic plot of the Compton Chicane [59]; Right: schematic plot of the electron-photon scattering.

The energy of the scattered photon is:

$$E_\gamma \approx E_{\text{laser}} \frac{4a\gamma^2}{1 + a\theta_\gamma^2\gamma^2} \quad (2.17)$$

where $\gamma = E_{\text{beam}}/m_e$ is the Lorentz factor of the incoming electron, $a = \frac{1}{1+4\gamma E_{\text{laser}}/m_e}$ and θ_γ is the scattering angle w.r.t. the electron momentum. The maximum energy of the scattered photon appears at $\theta_\gamma = 0$, which is the back scattering. For PREX-II (CREX) beam energy of 0.95 (2.2) GeV, $E_\gamma^{\text{max}} \sim 32.55$ (167.02) MeV.

Define $\rho = \frac{E_\gamma}{E_\gamma^{\text{max}}}$, the cross section for the unpolarized Compton scattering will be:

$$\frac{d\sigma}{d\rho} = 2\pi r_0^2 a \left[\frac{\rho^2(1-a)^2}{1-\rho(1-a)} + 1 + \left(\frac{1-\rho(1+a)}{1-\rho(1-a)} \right)^2 \right] \quad (2.18)$$

$r_0 = \frac{\alpha\hbar c}{mc^2}$ is the classical electron radius; then the analyzing power is:

$$\mathcal{A}_l = \frac{\sigma_{\Rightarrow}^{\rightarrow} - \sigma_{\Rightarrow}^{\leftarrow}}{\sigma_{\Rightarrow}^{\rightarrow} + \sigma_{\Rightarrow}^{\leftarrow}} = \frac{2\pi r_0^2 a}{d\sigma/d\rho} (1 - \rho(1+a)) \left[1 - \frac{1}{(1 - \rho(1-a))^2} \right] \quad (2.19)$$

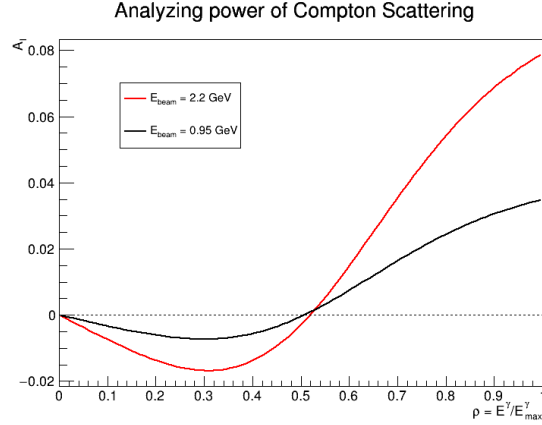


Figure 2.19: The Compton analyzing power increases with the incoming electron energy. Note that the analyzing power will change sign at $\rho \sim 0.5$ for both PREX-II and CREX beam energies.

The measured asymmetry will be:

$$\mathcal{A}_{\text{exp}} = \mathcal{P}_e \mathcal{P}_\gamma \mathcal{A}_l = \frac{N_\gamma^R - N_\gamma^L}{N_\gamma^R + N_\gamma^L} \Rightarrow \mathcal{P}_e = \frac{\mathcal{A}_{\text{exp}}}{\mathcal{P}_\gamma \mathcal{A}_l} \quad (2.20)$$

The advantage of the Compton polarimeter is that it can tolerate quite high current (up to $\sim 200 \mu\text{A}$ at JLab), plus its non-invasive operation, making it a beam polarization monitor. The disadvantage is, compared to the Mott or Moller polarimeter, its analyzing power is quite low at GeV energy level, while increase the beam energy will lead to a high background in the photon detection due to synchrotron radiation. Overall, the Compton polarimeter is able to achieve a 1% absolute systematic uncertainty.

Moller Polarimeter

The Moller polarimeter lies downstream of the Compton polarimeter and upstream of the target chamber. It uses elastic electron-electron scattering to measure the cross section asymmetry between beams with different polarizations.

$$\begin{aligned} \frac{d\sigma}{d\Omega} &= \frac{d\sigma_0}{d\Omega} \left(1 + \sum_{i,j=x,y,z} \mathcal{P}_b^i \cdot \mathcal{P}_t^j \cdot \mathcal{A}_{ij}(\theta_{CM}) \right) \\ \frac{d\sigma_0}{d\Omega} &= \frac{\alpha^2}{s} \left(\frac{4 - \sin^2 \theta_{CM}}{\sin^2 \theta_{CM}} \right)^2 \end{aligned} \quad (2.21)$$

With $\frac{d\sigma_0}{d\Omega}$ being the unpolarized Moller scattering cross section, s the Mandelstam variable: $s = 2m_e(E + m_e) \approx 2m_e^2\gamma$, \mathcal{P}_b (\mathcal{P}_t) the polarization of the beam (target), θ_{CM} and \mathcal{A}_{ij} the scattering angle and analyzing power in the COM frame.

Assuming incoming electrons move in the z direction and the scattering happens in

the xz plane, then in the ultra-relativistic limit:

$$\begin{aligned}\mathcal{A}_{zz} &= \frac{\sin^2 \theta_{CM} (7 + \cos^2 \theta_{CM})}{(3 + \cos^2 \theta_{CM})^2}, & \mathcal{A}_{xx} = -\mathcal{A}_{yy} &= \frac{\sin^4 \theta_{CM}}{(3 + \cos^2 \theta_{CM})^2} \\ \mathcal{A}_{xz} = \mathcal{A}_{zx} &= \frac{2 \sin^4 \theta_{CM} \cos \theta_{CM}}{\gamma (3 + \cos^2 \theta_{CM})^2}, & \mathcal{A}_{xy} = \mathcal{A}_{yz} = \mathcal{A}_{yz} = \mathcal{A}_{zy} &= 0\end{aligned}\quad (2.22)$$

\mathcal{A}_{zz} is maximized to be $\frac{7}{9}$ at $\theta_{CM} = 90^\circ$. This θ_{CM} value was used in the Moller measurement.

The polarized target electrons come from a magnetized Fe-alloy foil, which is saturated by a very strong (4 T) longitudinal magnetic field created by superconducting Helmholtz coils, as shown in Fig. 2.20. So Eq. 2.21 is simplified to:

$$\frac{d\sigma}{d\Omega} = \frac{d\sigma_0}{d\Omega} (1 + \mathcal{P}_b^z \cdot \mathcal{P}_t^z \cdot \mathcal{A}_{zz}(\theta_{CM})) \quad (2.23)$$

The Moller pair (the scattered incident electron and recoil target electron) centered around $\theta_{CM} = 90^\circ$ ($\theta_{lab} < 3^\circ$), are separated from the undeflected beam by set of magnets, then goes through collimators (at the exit of the dipole, not shown in Fig. 2.20) that define the acceptance, and finally is detected by electron detectors in coincidence. The measured asymmetry between spin-parallel and anti-parallel cross section is:

$$\mathcal{A}_{exp} = \frac{N^+ - N^-}{N^+ + N^-} = \mathcal{P}_b \mathcal{P}_t \langle \mathcal{A}_{zz} \rangle \Rightarrow \mathcal{P}_b = \frac{\mathcal{A}_{exp}}{\mathcal{P}_t \langle \mathcal{A}_{zz} \rangle} \quad (2.24)$$

with $\langle \mathcal{A}_{zz} \rangle$ being the average analyzing power over the acceptance, which is about 0.75 for PREX-II and CREX.

The target foil is cooled by conduction through the target, whose temperature will climb quickly with increase beam current, causing damage to the target polarization. Therefore the Moller polarimeter can only operate at very low current ($\lesssim 1\mu\text{A}$). The extrapolation from the polarization measurement at a low current to a high current where PREX-II and CREX run at, is a large source of systematic uncertainty. During PREX-II and CREX, the target polarization was measured to be $\mathcal{P}_t \sim 8\%$, leading to an effective analyzing power of $\mathcal{A}_{eff} = \mathcal{P}_t \langle \mathcal{A}_{zz} \rangle \approx 6\%$. This relative large analyzing power makes the Moller measurement quite precise. Overall, the Moller polarimeter in Hall A can achieve a systematic uncertainty less than 1%.

2.4 Monitors

Besides beam polarization, another significant source of systematic uncertainty is the beam false asymmetry – the difference in beam position, angle, energy and current between different helicity states. Because there is no way to ensure exactly the same beam parameters between different helicity states, even with the fast helicity flipping. We monitor these quantities with redundant specialised devices – beam position monitors and

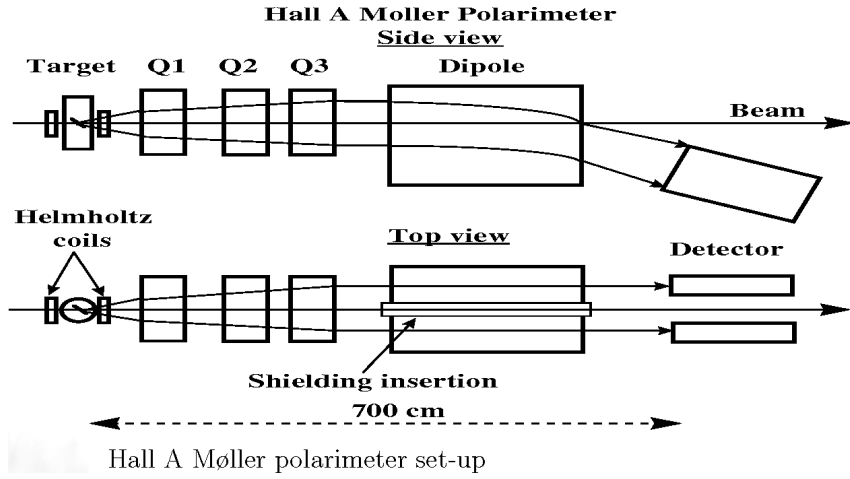


Figure 2.20: Schematic plot of the Møller Polarimeter.

beam current monitors. For PREX-II and CREX, there is another independent monitor system – small angle monitors (SAMs). These monitors are able to measure the beam difference as precise as:

$$\Delta x \sim 10 \text{ nm} \quad \Delta x' \sim 1 \text{ nrad} \quad \Delta p/p \sim 0.0001 \quad \Delta I/I \sim 100 \text{ ppb}$$

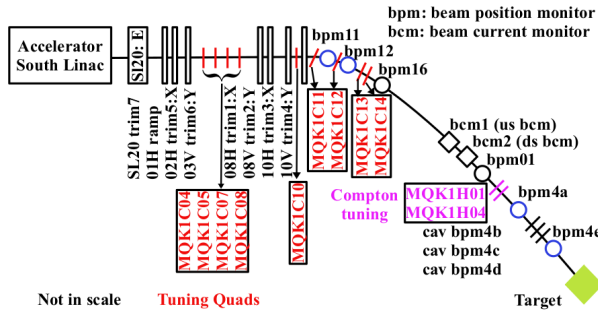


Figure 2.21: Schematic plot of the Hall A beam monitor system and beam modulation system

2.4.1 BPMs

Hall A has a series of BPMs along the beam pipe leading to the target chamber to monitor the beam conditions, among them, six switched electrode electronics (SEE) stripline BPMs are important to PREX-II and CREX, their readouts are used to extract beam parameters. They are shown in Fig. 2.21. BPM4a and BPM4e locate 5.725 m and 1.642 m upstream of the target chamber, they are used to determine the beam position and angle at the target. BPM11 and BPM12 are positioned on the arc area to measure

the beam energy using the bending radius of the electron trajectory. BPM1 and BPM16 are backup monitors.

A stripline BPM consists of a 4-wire antenna array of open ended thin wire striplines, the voltage induced by the electron bunch in each electrode is sensitive to the beam position. Therefore one can extract (x', y') positions from opposite 2 pickup signals.

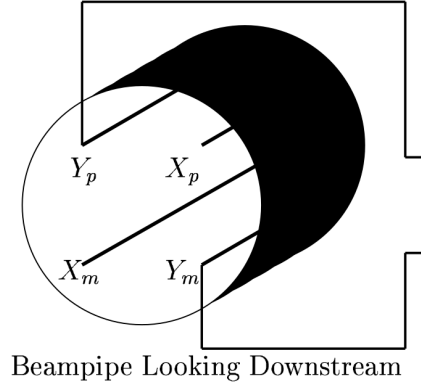


Figure 2.22: Schematic plot of a stripline BPM.

$$x' = \frac{1}{S_x} \frac{X_p - X_m}{X_p + X_m} \quad y' = \frac{1}{S_y} \frac{Y_p - Y_m}{Y_p + Y_m} \quad (2.25)$$

where the proportional constant S_x (S_y) is the position sensitivity. The pickup voltage responds linearly to the beam displacement when it is small. In the case of Hall A BPMs, the four striplines are rotated 45° w.r.t. to the hall coordinate system, so a -45° rotation is needed to recover the hall (x, y) from the extracted BPM (x', y') .

Besides these stripline BPMs, PREX-II and CREX also utilized 3 cavity BPMs (see discussion below), shown as bpm4b/c/d between BPM4a and BPM4e in Fig. 2.21, to measure beam conditions for low current calibration runs. Because stripline BPMs don't work when beam current is lower than $0.5 \mu\text{A}$. These cavity BPMs are not used in normal production runs.

2.4.2 BCMs

One technique to measure the beam current is current transformation. Various BCMs based on this idea may have different designs, features and performances, the key component is the same – the current transformer (CT). When beam bunch travel through the beam pipe, it will induce a magnetic field in the beam pipe (the core), which in turn will induce a current in the secondary winding (toroid), whose output is proportional to the beam current. To make a precise measurement, it is important to shield any outside magnetic field and separate the segment of beam pipe where the BCM lies in from the rest.

The BCM system in Hall A consists of two radio frequency (rf) cavities and an unser monitor in between, as shown in Fig. 2.23. The unser monitor is a parametric current transformer (PCT), which will output a direct current (DC) voltage equivalent to 4 mV per μA of beam [60].

In PREX-II and CREX, the unser monitor is not used for the beam current measurement, because its voltage output drifted quickly after only a few minutes of running. Instead, it is used to calibrate the rf-cavity monitors on either side of it, whose readout is used for the runtime beam current measurement.

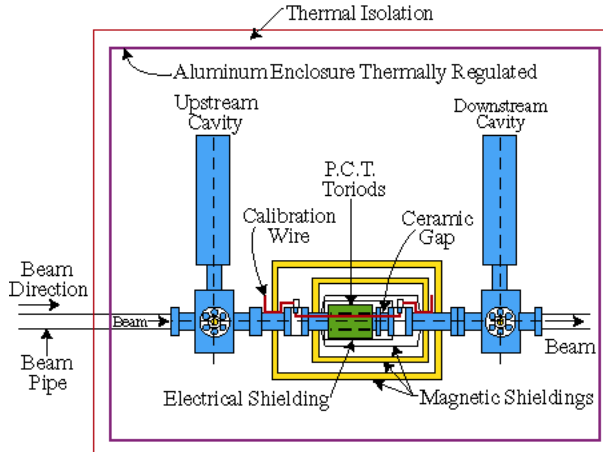


Figure 2.23: Hall A BCM system [60].

A rf cavity is a metallic chamber that sustains an EM field (infinite number of resonant EM modes), by special design of its shape, a particular EM mode can efficiently transfer energy to or from a charged particle. The frequently heard accelerating cavity need to provide an electric field along beam velocity; while a decelerating cavity, which will absorb energy from the coming charged particles, can be used as a beam diagnostic monitor. The induced voltage is proportional to the traversing charge q :

$$V = 2k_{loss}q \quad (2.26)$$

where k_{loss} is the loss factor, which depends only on the electric field distribution, therefore is sensitive to the beam position and particle velocity. To measure beam intensity, one would prefer the EM mode whose electric field doesn't depend on r position, these are TM_{010} like modes; while for measurement of beam position, exactly the opposite is wanted, the electric field should have an azimuth angle and r dependence, which are TM_{110} like modes.

The 2 rf-cavity current monitors are of Pill box type (the electric field is concentrated near axis, while the magnetic field is concentrated at outer cylindrical wall), which operates at TM_{010} mode. The voltage readout will be down-converted to lower frequencies signals, then filtered, amplified and further processed before writing into the data stream. Due to the non-linearity of the readout converter at low currents ($\lesssim 5 \mu\text{A}$), actually 3

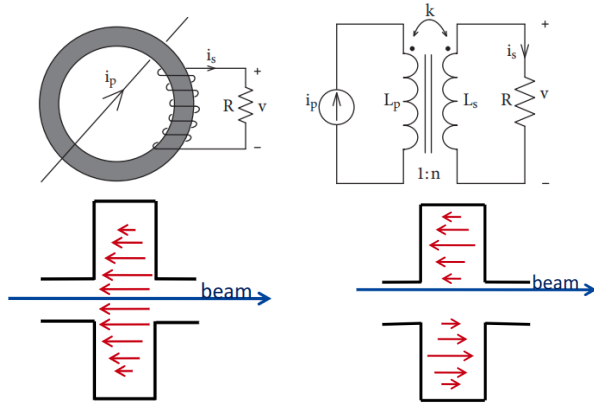


Figure 2.24: Up: Schematic plot of the current converter; Down: TM₀₁₀ and TM₁₁₀ modes, the red arrows indicate the electric field.

signals (the same signal with different gains: x1, x3 and x10) are recorded to extend the linear region to low currents, at the expense of saturation at high currents [51].

2.4.3 SAMs

For further understanding of beam dynamics, electronic noise and the possible target boiling effect, a luminosity monitoring system, called the small angle monitors, was installed in the dump pipe, about 7 m downstream of the target pivot. As shown in Fig. 2.25, the SAMs system consist of eight detector modules, symmetrically positioned around the dump pipe. Each detector module has a quartz tile (active detector), attached to a lightguide. the Cherenkov light radiated by electrons will be read out by a PMT at the end of the lightguide. As its name implies, SAMs are designed to monitor small angle ($\sim 1^\circ$) scattered and secondary flux from the target, thus it can also be used to inspect the target conditions. E.g., a bubble in the target that forms and disappears within one helicity window is unknown to both BPMs and BCMs, but SAMs will see it. Each detector's readout is sensitive to beam parameters. E.g., the sum of the readout of a symmetric pair monitors is sensitive to change in the beam current and energy, while their difference tells the fluctuation in the beam position and angle. The symmetric design helps to disentangle these beam parameters. So it provide an independent check of the measurement of BPMs and BCMs and can be used to eliminate the possible beam or electronic noise.

2.4.4 Beam Modulation

Another system shown in Fig. 2.21 is the beam modulation system, which lies in beamline arc right after the Beam Switch Yard where electron chains are separated into Hall A/B/C beams. It consists of six air-core coils and an energy vernier in the last cavity of the south LINAC. The total number of seven coils provides a redundancy w.r.t. the number of free degrees of the beam phase space, making sure to cover the whole beam

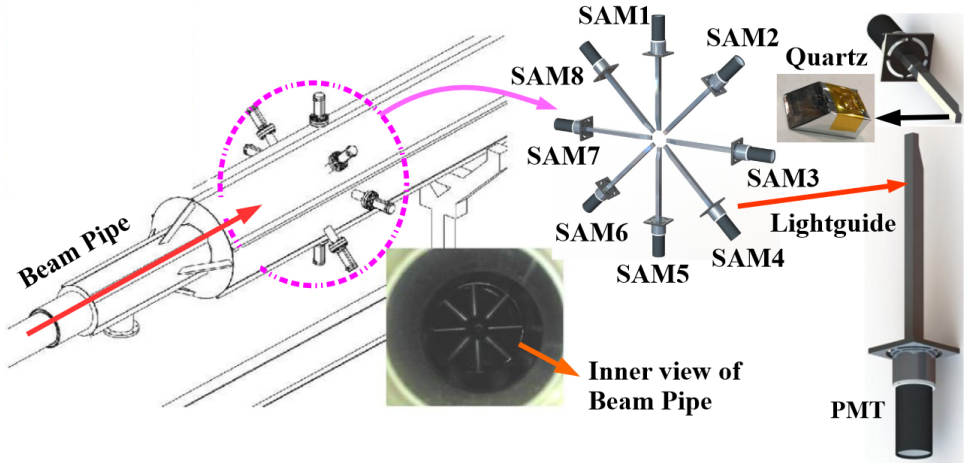


Figure 2.25: Layout of SAMs [61].

phase space at the target. Coil (trim) 1, 3, 5 are responsible for modulating beam x position and coil 2, 4, 5 will modulate beam y position. These coils (vernier) are driven by a VME-DAC (Digital-Analog Converter), which in turn is controlled by the parity data acquisition (DAQ). It takes 4.267 s for each coil (vernier) to modulate the beam, a whole modulation cycle takes 85.68 s (\sim 1 beam modulation every 10 mins during run time).

The beam modulation system is used for beam false asymmetry correction. When beam is modulated, BPMs and detectors will record corresponding changes in their read-out. With these values, the detector sensitivity w.r.t. jitters in beam parameters can be calculated, which then will be used to correct the measured asymmetry. Therefore, the modulation should be much larger than the natural jitters in the beam, a typical position modulation is a sinusoid of amplitude about 200 μ m and the energy vernier will result in a beam displacement of 0.75 mm in BPM11/12.

2.5 Target

For the sake of statistics, the designed current is quite large, as shown in Table 2.1. With such high currents, the electron beam will deposit quite a lot of heat on the target. It will be a disaster if the heat is not taken away as soon as possible, to keep a stable target temperature. For PREX-II, because Pb itself is not a good thermal conductor ($\kappa = 35$ W/(m·K)), auxiliary diamond foils ($\kappa > 1000$ W/(m·K)) are used to form a D-Pb-D sandwich target to help the heat dissipation. The thickness of the diamond foil matters, one lesson learned from PREX-I is that with a thin (0.15 mm) diamond foil, its thermal conductivity dropped greatly (from 1000 W/(m·K) to 100 W/(m·K)) after about 1 week of running with 70 μ A cw beams, resulting in some Pb targets were melted. While a thicker diamond foil (0.25 mm) will protect Pb foils from melting under the same conditions. In PREX-II, a factor of 2 safety margin was adopted. Conservatively

assuming 1 week running for each Pb target, 35 days of beam time requires 5 targets, and 10 isotopically pure Pb sandwich targets with thick diamond layers were deployed to ensure the success of PREX-II, each new target is able to sustain up to $85 \mu\text{A}$ cw beams.

While Ca itself is an excellent thermal conductor ($\kappa = 200 \text{ W}/(\text{m}\cdot\text{K})$), no need of auxiliary materials and higher current can be applied. The isotopically pure ^{48}Ca is much more expansive than the pure ^{208}Pb foil, so only one ^{48}Ca target (with a purity of 95.99%) was prepared for CREX. After the target accident, the new ^{48}Ca target was a stack of three separated foils with a similar total thickness to the old one.

Targets are firmly mounted in bays of target ladders, whose axes are perpendicular to the beam line. The ladder is movable along its axis by an alternating current (AC) servo motor, which can receive remote instructions through the internet. The motion along the ladder axis can be precise to 0.1 mm.

There are 2 target ladders in total, one for production targets and the other one for calibration targets. The production ladder has 16 target slots in total: 10 ^{208}Pb targets, two Calcium isotope targets – ^{40}Ca and ^{48}Ca , and four other calibration and diagnostic targets. The calibration ladder has only 5 targets: a carbon hole, a watercell, a thin C foil, a thin natural Pb and a thin ^{40}Ca target. The production ladder is horizontal while the calibration ladder is rotated 45° anti-clockwise w.r.t. the production ladder, as shown in Fig. 2.26 and 2.27.

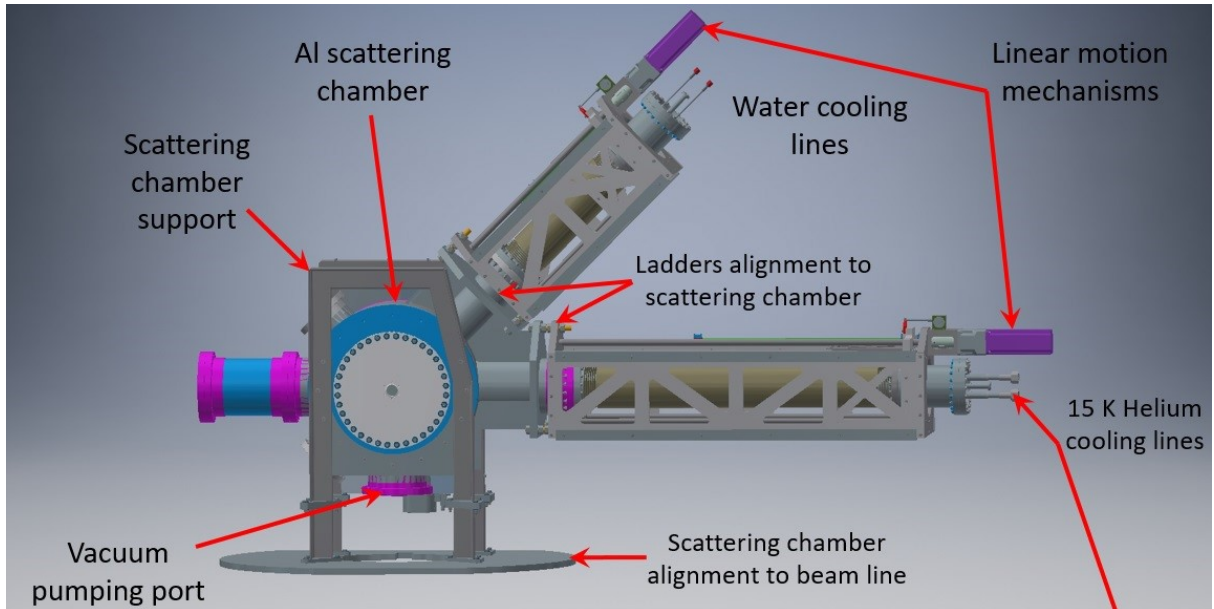


Figure 2.26: Design plot of the scattering chamber and the two target ladders. The horizontal one is the production ladder and the other one being the calibration ladder.

The ^{40}Ca and ^{48}Ca targets are installed on the cold heat sink in dedicated cylindrical sockets at the end of the production ladder. The fact that the ^{48}Ca and the ^{208}Pb targets share the same ladder means they actually have the same z location, therefore the same scattering angle, though they proposed different scattering angles ($5^\circ/4^\circ$ for

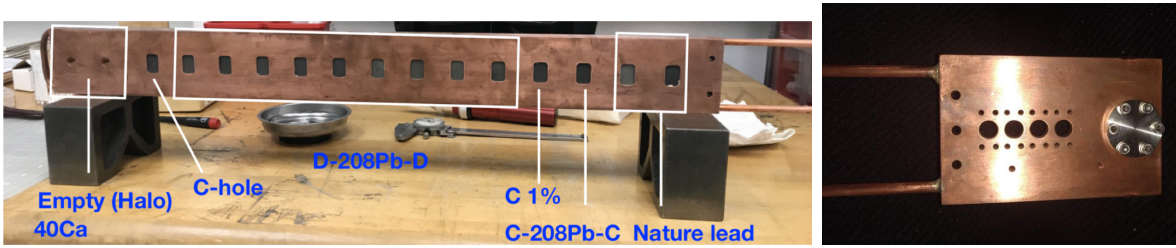


Figure 2.27: Actual pictures of the production (left) and calibration (right) ladders.

PREX-II/CREX). It being so to simplify the design, construction and installation of the target chamber.

Special care is needed for the ^{48}Ca target, the pressure should be less than 10^{-6} torr to avoid the Ca oxidation. The vacuum of the target chamber is maintained by a turbo-molecular pumping system, which creates a 10^{-7} (10^{-8}) torr vacuum for the calibration (production) ladder in the target chamber. When the beam is not on, gate valves are closed to isolate the target chamber from upstream and downstream beam pipes. By way of precaution, a nitrogen purge system is installed to purge air in case of long term vacuum loss or the chamber needs to be brought up to atmospheric pressure. Every time we warmed up the ^{48}Ca target, gas boiling was needed before restarting the data taking.

2.5.1 Target Cooling

The production ladder is cryogenically cooled due to high power from electron beams, while the calibration ladder is water cooled, the calibration runs need only $\lesssim 1 \mu\text{A}$ level beam current. Both ladders are made of cooper. The cooper frame of the production ladder is cooled by 15 K, 12 atm gaseous helium, which runs through the cooling tube surrounding the frame. Contact between the target and the frame and within each layer of the ^{208}Pb sandwich target are also important. Belleville washers are used to clamp the lead and diamond foils to ensure contact, besides, a thin layer of Apiezon L vacuum grease is applied to their interface to improve thermal conductivity. One hypothesis for the sudden failure of the Pb target after one week of running is that the vacuum grease doesn't last long. In the diamond/copper interface, a silver-based paste compound is used for the same purpose. For a D-Pb-D sandwich target with a thick diamond foil, the heat loading will be $\sim 100 \text{ W}$ at $70 \mu\text{A}$ with a $4 \times 6 \text{ mm}$ raster, the cooling system would keep the Pb target stay at $\sim 60 \text{ K}$ (melting point at 600 K) assuming good contact and smooth heat conduction. For the ^{48}Ca target, the $150 \mu\text{A}$ beam current will produce about 370 Watts heat on the target, which raised the target temperature up to $\sim 300 \text{ K}$ (melting point at 1115 K).

2.5.2 Raster

Despite the helium cooling, the target foil still deforms (even melts) under the electron bombardment. Small non-uniformities in the target thickness vary the scattering rate,

over the course of the experiment they eventually generate large enough noise to swamp the tiny weak-scattering signal. Actually, this is how we inspect the status of a target, it prompts us to replace a target if the measured asymmetry width increases significantly.

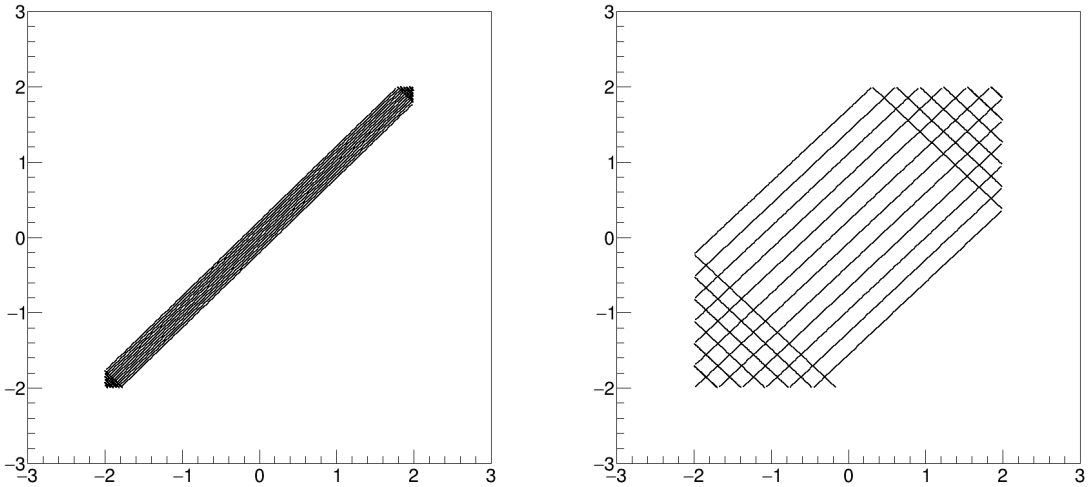


Figure 2.28: Raster pattern with different frequency difference between X and Y. Left: $|f_y - f_x| = 120$ Hz; Right: $|f_y - f_x| = 8 * 120$ Hz. The raster shape is a 4×4 mm square.

The solution to this problem is the raster, which is a set of dipole magnets between the Compton and the Moller polarimeters that deflect the beam at about 25 kHz to spread the beam on the target. One thing we learned from PREX-I is that we could significantly reduce the sensitivity to target-thickness variations by synchronizing the helicity flip frequency with the raster frequency so that it samples exactly the same areas on the target. Any noise from target thickness variations cancels by taking the difference of a helicity pair or quadruplet.

As shown in Fig. 2.28, the Lissajous pattern depends on the frequency difference between X and Y axes, the larger the frequency difference, the larger the scanning area. The ratio of f_y/f_x should be an irrational number to prevent a closed Lissajous pattern. The actual frequencies used are $f_x = 25.44$ and $f_y = 24.48$ kHz. for PREX-II, the raster size is 4×6 mm, and CREX has a raster size of 2×2 mm.

Another reason for having the raster is heat dissipation, the larger the raster size, the quicker the heat dissipation will be, the lower the target temperature, as shown in Fig. 2.30.

2.5.3 Beamline Collimator and Sieve Slit Collimators

One problem that failed PREX-I is the excessive radiation, which damages electronics in the hall and the o-ring on the target exit flange, leading to leaks and ultimately halting the experiment. With this experience, the new design of the pivot area (the center of the

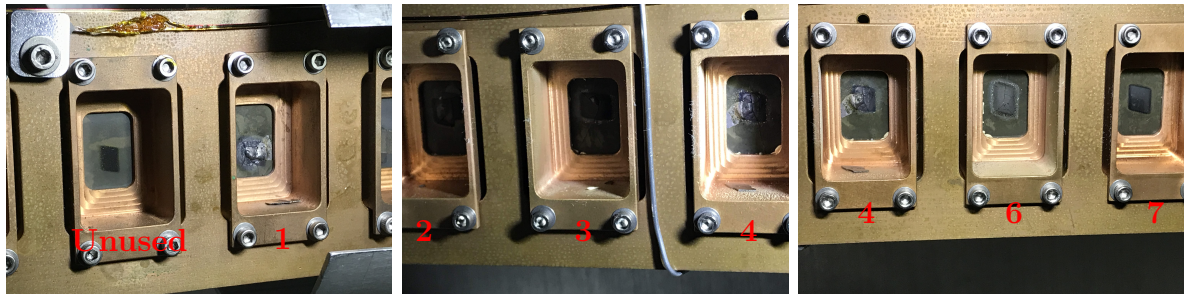


Figure 2.29: Picture of Pb targets after running. One can clearly see the shape of the raster pattern. Target 1 and 4 are melted.

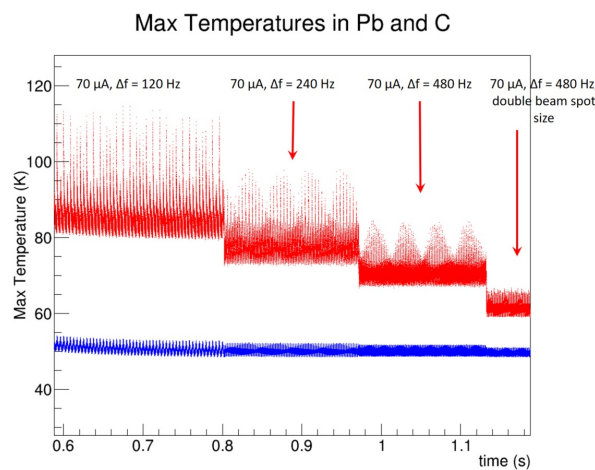


Figure 2.30: Simulation of target temperature evolution with different raster frequency differences. The larger the raster frequency difference (Δf), the larger the size of the raster area, the lower the highest target temperature.

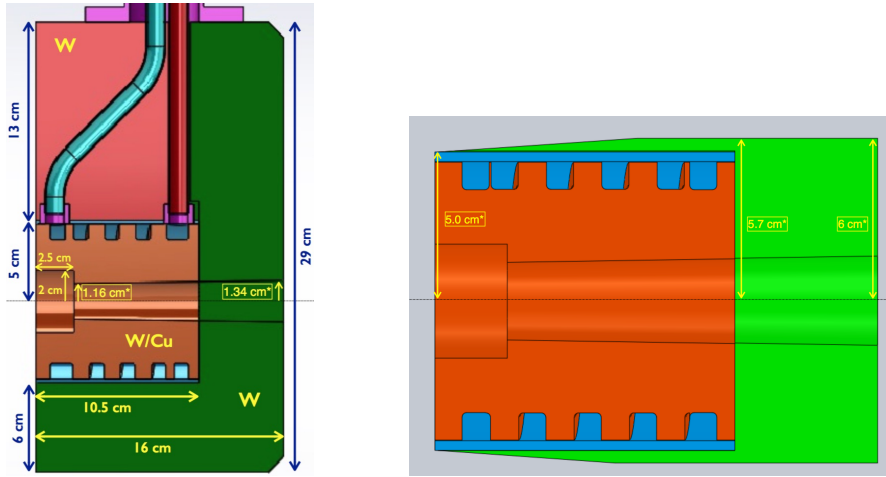


Figure 2.31: Side and top view of the beamline collimator. Beam travels from left to right.

two HRS where the target chamber lies in) for PREX-II and CREX pays more attention to radiation near the target region. The idea is to lead as much radiation to the beam dump as possible, and absorb the rest in one key component – the beamline collimator.

The beamline collimator is placed 83 cm downstream of the production target. It consists of an inner collimator and a housing jacket made of sintered tungsten; the inner collimator, in turn, has the same structure of a 70% W/30% Cu alloy collimator and a copper jacket. As shown in Fig. 2.31, there is a cylinder notch in the front of the inner collimator, to make sure the electrons/radiation are completely absorbed inside the collimator.

The beamline collimator is water cooled, with a maximum heat loading of about 3.65 kW from the ^{208}Pb target. The power on the beamline collimator is another signal for the degradation of target. When the temperature of the outgoing water increases dramatically, it is time to replace the ^{208}Pb target, as shown in Fig. 2.32

Besides the beamline collimator, a few other devices are installed to further eliminate the radiation level in the hall. These devices include the high-density polyethylene (HDPE) neutron shield around the beamline collimator region and a skyshine shield consisting of a 6 cm thick tungsten block and massive concrete blocks. These extra shields are used to block high energy neutrons from the collimator.

On both sides of the beamline collimator are the 5 mm thick stainless steel sieve slit collimators (about 1.1 m from the target), which are used for optics studies, helping electron trajectory reconstruction. When we take production data, the sieve slit collimators are moved out of the spectrometer acceptance; when we take optics data to measure the scattering angle and Q^2 , they are put in to cover the whole spectrometer acceptance, without interfering the inner bore of the the beamline collimator. With known (x, y) position of each hole on the sieve plane, and the track information from the vertical drift chamber (VDC), we can reconstruct the beam transport matrices.

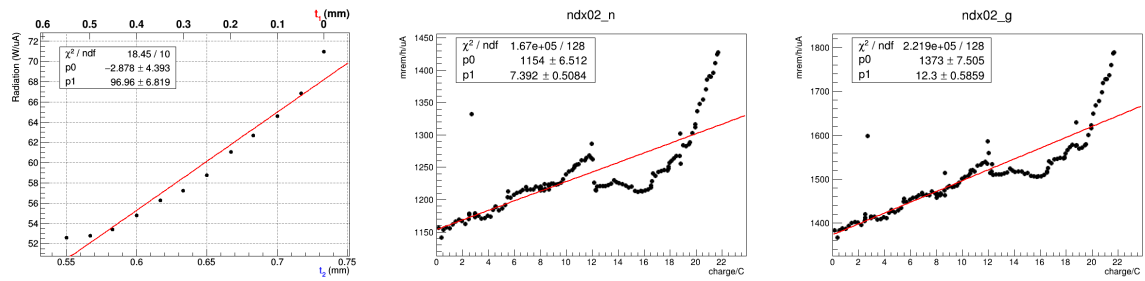


Figure 2.32: Left: a simple model of target degradation – assuming the raster area (t_1) is becoming thinner and the rest is becoming thicker (t_2), both uniformly and the total mass keeps intact. The plot shows how the power deposition on the beamline collimator changes in this model. Middle and Right: actual neutron and photon radiation level monitored along charge accumulation.

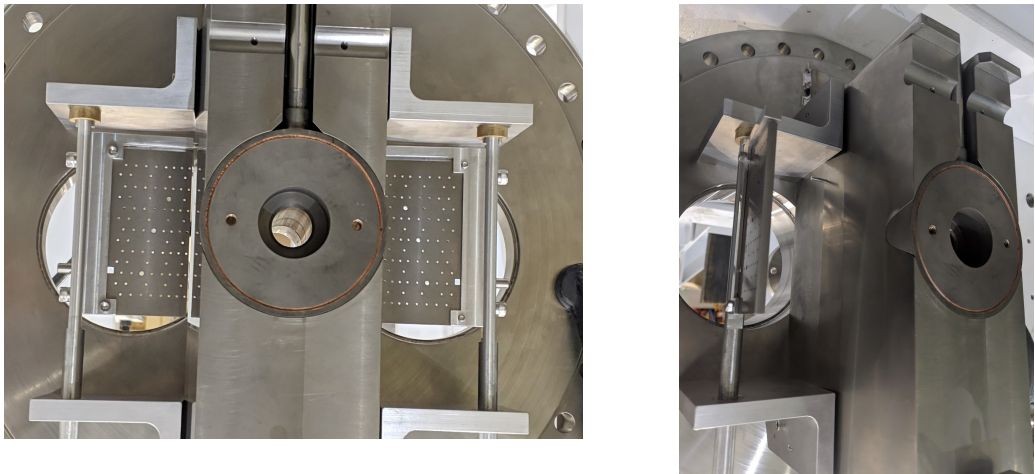


Figure 2.33: Front pictures of the beamline collimator and sieve slit collimators, looking downstream. In the left picture, one can clearly see a cylinder is removed from the central collimator. The sieve planes lie after the beamline collimator and are movable like windors, they can be opened or closed from outside.

2.5.4 Septum

The septum magnet is required to bridge the scattered electrons at small angle into the HRS. As said before, the designed scattering angle is about 5° while the smallest angle that HRS can reach is 12.5° , so a septum magnet is needed to bend the scattered electrons into the HRS.

The septum magnets are normal conducting magnets that consist of three coils, by applying large current, they will produce a strong magnetic field (up to ~ 1 T in the central region). A non-magnetic stainless vacuum box will connect the upstream collimator box and the downstream HRS vacuum pipe on both ends of the septum. The septum beampipe (the one that leads to the beam dump) is made of magnetic stainless steel to shield the magnetic field from the septum. On both ends of the septum beampipe, there

are magnetic steel box to shield the fringe magnetic field from septum.

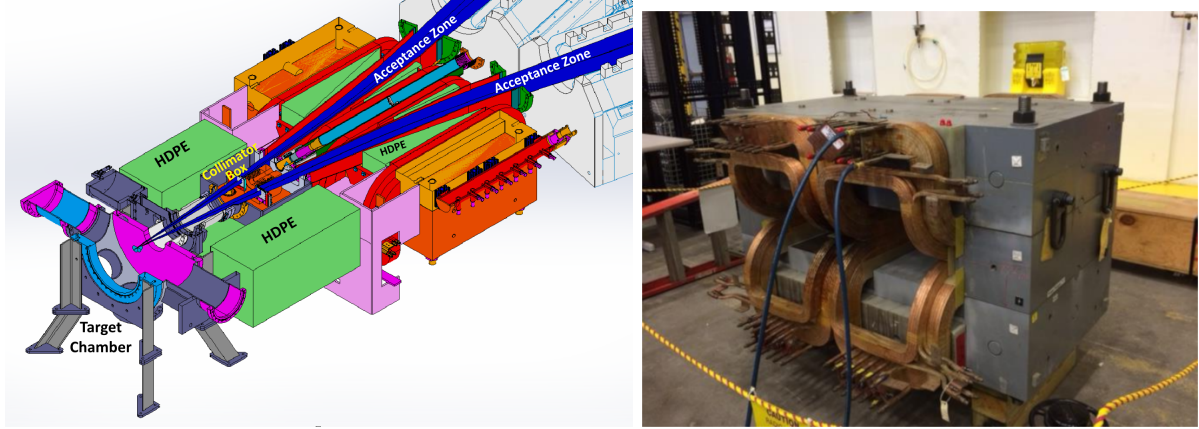


Figure 2.34: Left: design plot of the pivot region; septums are represented by red coils. Right: actual picture of septums.

2.5.5 High Resolution Spectrometer (HRS)

Spectrometer is a key component for every Hall A experiment. PREX-II and CREX use the HRS pair. Each HRS consists three superconducting quadrupoles and one dipole. The maximum magnetic field of the three quadrupoles are 1.2, 1.0 and 1.0 T respectively while the dipole can provide up to 1.7 T field [51]. The incoming electrons will be bent 45° up in the vertical plane and then received by electron detectors. HRS has a small angular acceptance (± 28 mrad horizontally, ± 60 mrad vertically, the solid angle being 7.8 msr), but can move over a wide range of angle around the hall ($12.5^\circ - 165^\circ$). As its name implies, it achieves a very high momentum resolution at the $dp/p \sim 10^{-4}$ level over a wide range of momentum (0.8 - 4 GeV). This capacity helps to reject most inelastically scattered electrons. Because a small difference in momentum (2-3 MeV) will lead to a large separation in the detector plane, thus leaving us a relatively clean data with a very small background from inelastic scattering, as shown in Fig. 2.35 .

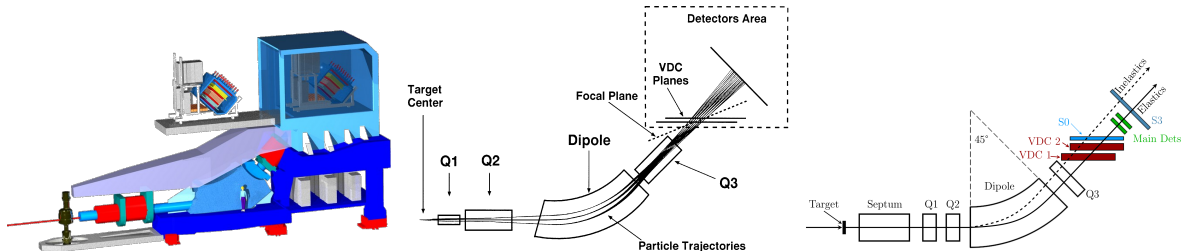


Figure 2.35: Schematic plot of the HRS and particle rays inside. [62] The ‘focal plane’ in the middle plot, by design, should be at an angle of 45° w.r.t the central ray, but is actually rotated to 70° due to lackness of sextupole winding in Q3. When we talk about the HRS focal plane, we usually refer to the VDC lower plane.

Before the entrance of the Q1 quadrupoles is a Q1 collimator, which defines the spectrometer acceptance. It is strictly required that the symmetry between left/right, and up/down of Q1 collimators should be preserved to reduce any possible systematic uncertainties.



Figure 2.36: Picture of Q1 collimator pairs, looking downstream. Q1 collimator is the blue piece surrounded by a circular steel. The pipe between the two Q1 collimators, covered by tin foils, is the beampipe leading to the beam dump.

2.5.6 Detector Package

The standard HRS detector package in each arm consists of trigger scintillators for triggering, a pair of VDCs for particle tracking, Cherenkov type detectors and shower counters (calorimeters) for particle identification (PID). In PREX-II and CREX, only parts of these detectors are needed, namely VDCs and S0/S3 triggers, others are removed for safety. We built our own Cherenkov counters that can suffer high electron flux to integrate scattered electrons. The detector package is shown in Fig. 2.37.

Vertical Drift Chamber (VDC)

Each VDC detector package consists of two drift chambers, one lower and one upper chamber with a vertical separation of 0.23 m (0.335 m between the same U or V planes of the lower and upper chamber), to enable precise position and angle measurement. The drift chamber is actually a multiwire proportional chamber (MWPC) with two layers of sense wires – U and V planes in the horizontal plane, which are orthogonal to each other and have a vertical separation of 26 mm. Each wire plane consists of 368 tungsten wires with the width of adjacent wires being 4.24 mm, corresponding to 6 mm in the spectrometer cross section due to the 45° cross angle between the axis of the spectrometer and the VDC plane.

VDC uses the drift time of ionized particles in the chamber to reconstruct the electron trajectory. A single plane can achieve a position resolution of ~ 235 mm full width at half

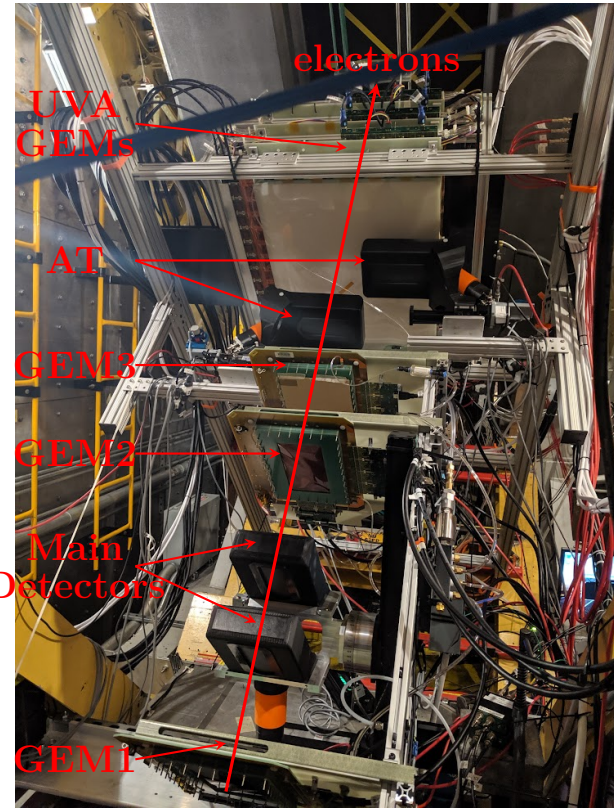


Figure 2.37: Picture of the detector package.

maximum (FWHM), the angular resolution is 6 mrad FWHM for θ (out-of-plane angle) and 2.3 mrad FWHM for ϕ (in-plane angle) [63].

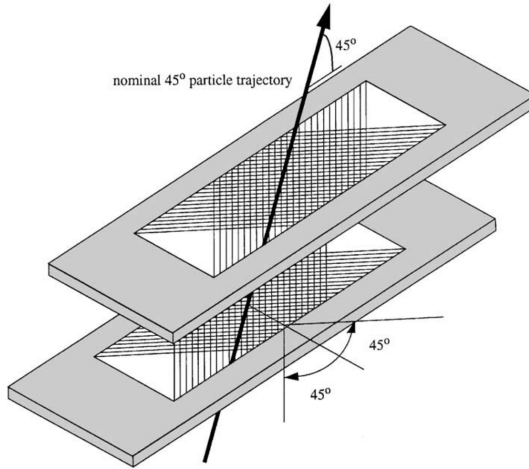


Figure 2.38: Schematic plot of a VDC detector with two drift chambers. U and V wires are shown in each chamber. The black arrow indicates the incoming electron [63].

VDCs are on for only optics runs in PREX-II and CREX, when we collect electrons

one by one to measure their scattering angle and energy, otherwise they are off during normal production runs.

Trigger

Same as VDCs, triggers are only used in counting mode for optics study. The standard detector package consists of multiple trigger planes, only two of them are used : the S0 and S3 plastic scintillators. The S0 scintillator locates between VDCs and the main detectors while S3 lies behind the main detectors, they have a sensitive area of 170 cm long by 25 cm wide. Their signals are logically combined to provide different trigger rate. The trigger rate is controlled to be less than 50 kHz most of the time (the up limit of a VDC is about 250 kHz).

Main Detector

The main detector of PREX-II and CREX is the 5 mm thick fused silica (quartz) tiles, with a size of 16 cm long by 3.5 cm wide (3 cm \times 3 cm active area). Two identical quartz detectors are installed with the upstream one used as the main detector and the downstream one as the backup (also used for a cross check in PREX-II). They are tilted to be perpendicular to the electron rays. The high refractive index of quartz ($n \approx 1.45$) means the opening angle ($\theta \approx \arccos \frac{1}{n}$) in Fig. 2.39 is about 46° , larger than the critical angle ($\theta_c = \arcsin \frac{1}{n} = 43.6^\circ$). Therefore, the Cherenkov light produced by high energy electrons will be totally reflected inside the quartz and finally collected by the PMT. The high photon yield makes it easier to resolve the electron peak, which is beneficial given the fact that non-linearity of the PMTs is one of the major contributors to systematic uncertainties.

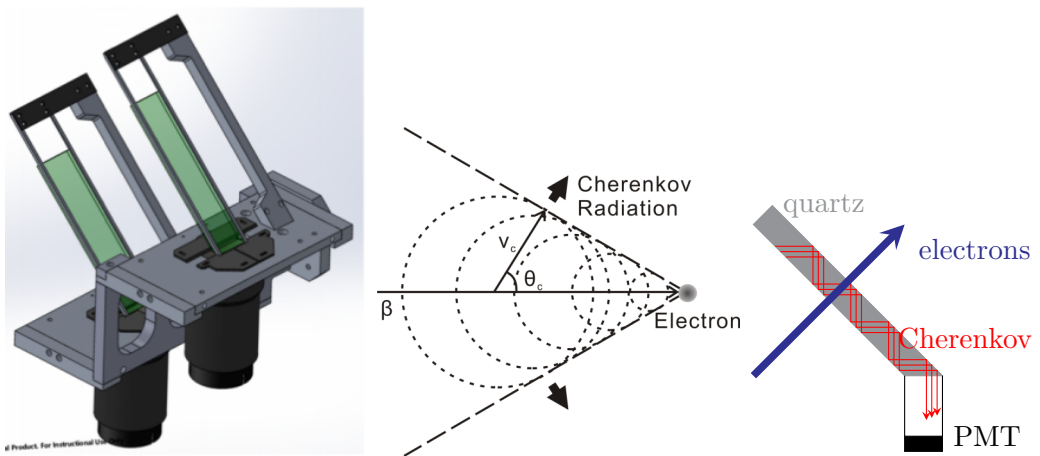


Figure 2.39: Left: CAD drawing of the quartz detector; Middle: schematic plot of the Cherenkov radiation, the angle between the electron and the Cherenkov radiation is $\cos \theta = \frac{v_c}{v_e} = \frac{c}{nv_e} = \frac{1}{n\beta} \approx \frac{1}{n}$; Right: electron flux goes through a quartz detector.

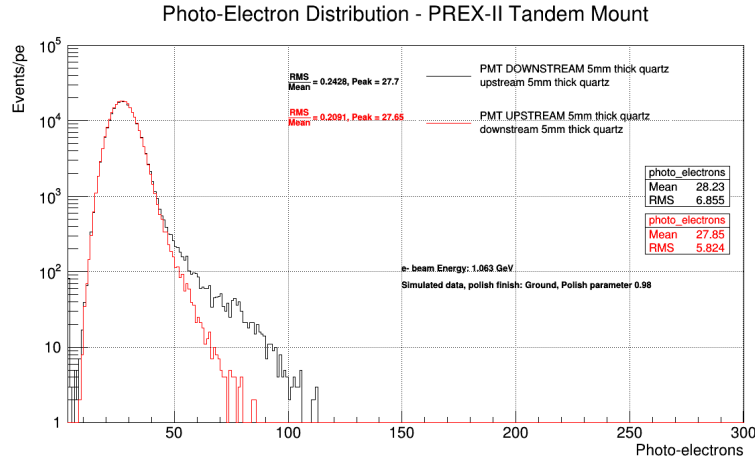


Figure 2.40: Simulation result of the photo-electron (PE) spectrum for single electron passing through the main detectors. The wider tail in the downstream detector is due to particle showering in the upstream quartz [61].

The width of the photon-electron distribution will increase the statistical uncertainty:

$$\sigma_{\mathcal{A}} = \sigma_{\text{stat}} \times \sqrt{1 + \left(\frac{\sigma_{\text{PE}}}{\langle \text{PE} \rangle} \right)^2} \quad (2.27)$$

where σ_{PE} is the RMS of the distribution. The RMS can be parameterized into 2 parts: the Gaussian principle part which is inversely proportional to the quartz thickness and a Landau tail which comes from the showering process and is proportional the thickness. A thicker thickness will increase the photon-electron yield while a thinner one can reduce the showering. The final decision of a 5 mm thickness is a compromise between these two parts to minimize detector resolution $\sigma_{\text{PE}}/\langle \text{PE} \rangle$.

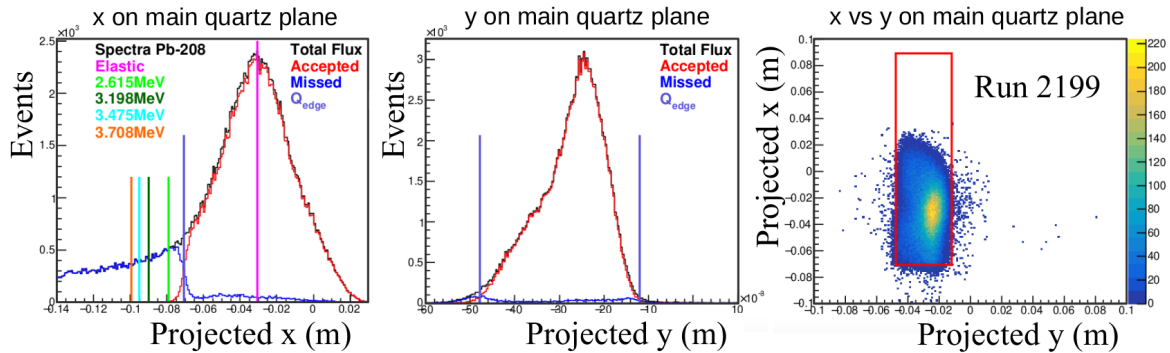


Figure 2.41: Electron position distribution, projected on the quartz plane. The positions of the first four excited states are shown in the left plot. The red rectangle on the right plot shows the relative position of the quartz. Plots from Devi Adhikari [61].

There is a homemade motion control system in each arm to move the main detectors. The control system can be operated remotely, therefore we can conveniently tune the position of the main detectors whenever there is a change in the beam conditions or any other apparatus.

AT Monitors

About 1 m downstream the main detector is a pair of AT monitors, as shown in Fig. 2.37, which use exactly the same quartz piece as the main detectors. They are used to monitor transverse polarization in the beam.

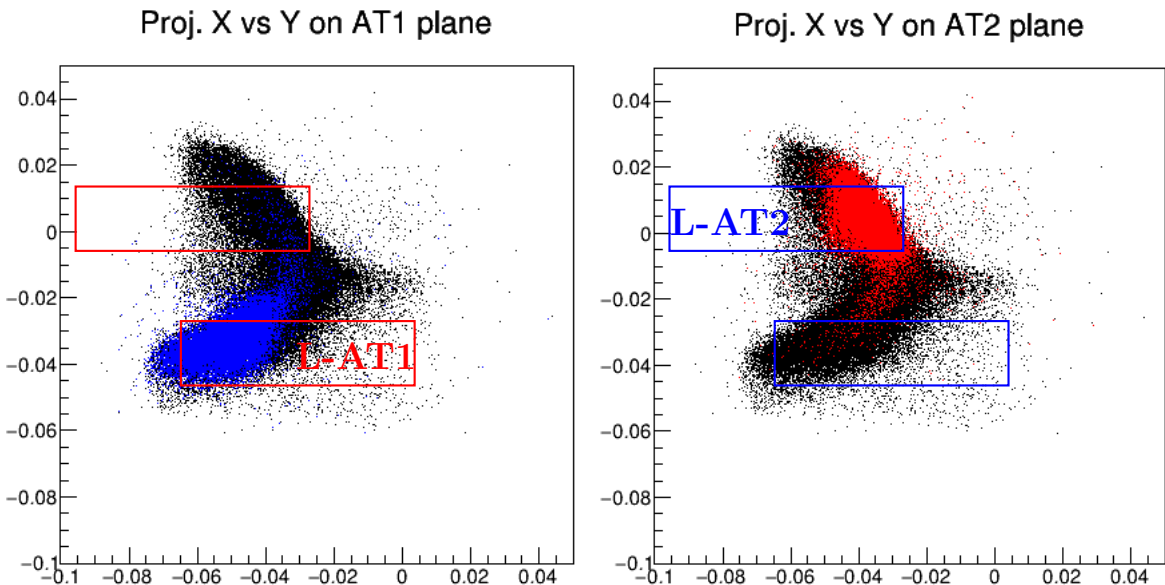


Figure 2.42: Scatter plot of electrons on the left arm AT monitor plane. Red and blue dots represent electrons scattered either above or below the horizontal scattering plane, respectively. The red and blue rectangles show the relative positions of the two AT detectors.

2.5.7 Data AcQuisition (DAQ)

JLab has its own framework of hardwares and softwares to aquire data, which is called CODA (CEBAF Online Data Acquisition) [64]. It is a distributed system that can be scaled from a few detector channels to tens of thousands of channels needed in an experiment. CODA version 2.6.2 is used for PREX-II and CREX.

Data acquisition works in 2 modes: the integrating mode and the counting mode, both have their own DAQs, because they have different triggers and read from different detectors.

Integrating DAQ

The integrating DAQ consists of four primary DAQ systems spread in the injector, the Counting House (CH) and the hall (LHRS/RHRS). They are controlled by the CODA Run Control system in the CH, and triggered by the helicity signal.

The helicity signal is produced by a helicity control board [65], which is an advanced programmable logic generator, located in the Injector Service Building. It has four timing modes: three fixed-frequencies of 30, 120 and 240 Hz and a fourth free-running mode. In fixed-frequency mode, as used for PREX-II/CREX, the phase is locked to the ‘beam sync’: the accelerator’s 60 Hz AC line synchronized global timing reference, which means the last helicity window in a helicity pattern may be shorter or longer than other helicity windows because the 60 Hz line signal wanders from time to time, shown as the beam sync jitter in the second timing diagram in Fig. 2.43. To ensure that all helicity windows have the same integrating time, an artificial deadtime is introduced, which is $T_{\text{dead}} = 51.33 \mu\text{s}$, as shown in Fig. 2.44. This slightly reduces the integration time: $T_{\text{int}} = T_{\text{stable}} - T_{\text{dead}}$.

The helicity signal sent to injector components (PCs, IAs and the double wien filters) can be regarded as real time due to their geographical vicinity. The T_{settle} signal sent to Hall A will stop (the falling edge) data taking in the previous helicity window, then hold for T_{settle} time to allow settlement of the high voltage in PCs and readout of the previous helicity data. Its rising edge tells the start time of data taking in current helicity window. The delay caused by signal transportation in fiber optics cables to Hall A is about 100 ns, 1 μs is reserved between the T_{settle} and the helicity signals to inform the hall of the change of helicity, as shown in Fig. 2.43. Actually, this is not necessary, because $T_{\text{settle}} = 90 \mu\text{s}$ is long enough to allow such a delay in signal transportation, as well as the delay caused by beam transportation in the accelerator, which is $1.4 \text{ km/c} = 4.7 \mu\text{s}$.

The actual helicity signal (DLY RPT) sent to Hall A will be delayed (by 8 helicity windows in PREX-II/CREX), so that no monitors along the beamline or detectors in the hall know the helicity of the current window, making sure that the monitors/detectors are not helicity sensitive. In the DAQ side, we need to verify that the helicity pattern is expected based on the helicity pattern signal and the measured helicity agrees with the delayed helicity signal, to ensure that the helicity information is correct. When doing data analysis, the data needs to be shifted by the number of delayed helicity windows to match the actual helicity pattern. The helicity pattern is pseudo-randomly chosen by the helicity board using a 30-bit shift register.

The analog signals from the main detectors and various beam monitors are converted to voltage by a customised I-to-V pre-amplifier developed for the Qweak experiment, the voltage output is fed to a 18-bit ADC (Analog-Digital-Converter), sampled and integrated there. The 18-bit ADC was also a product of previous parity experiments. The detector signal is sampled every 2 μs and integrated into four sub-blocks for each helicity window (1024 samples per sub-block, 4096 samples per helicity window at 120 Hz). The ADC will be triggered 80 μs after the start of T_{settle} , as shown in Fig. 2.44, this allows 10 μs wait time for ADC to void any possible effects from the external triggering Nuclear Instrument Module (NIM) pulse on the internal signal processing. To synchronize the data collection

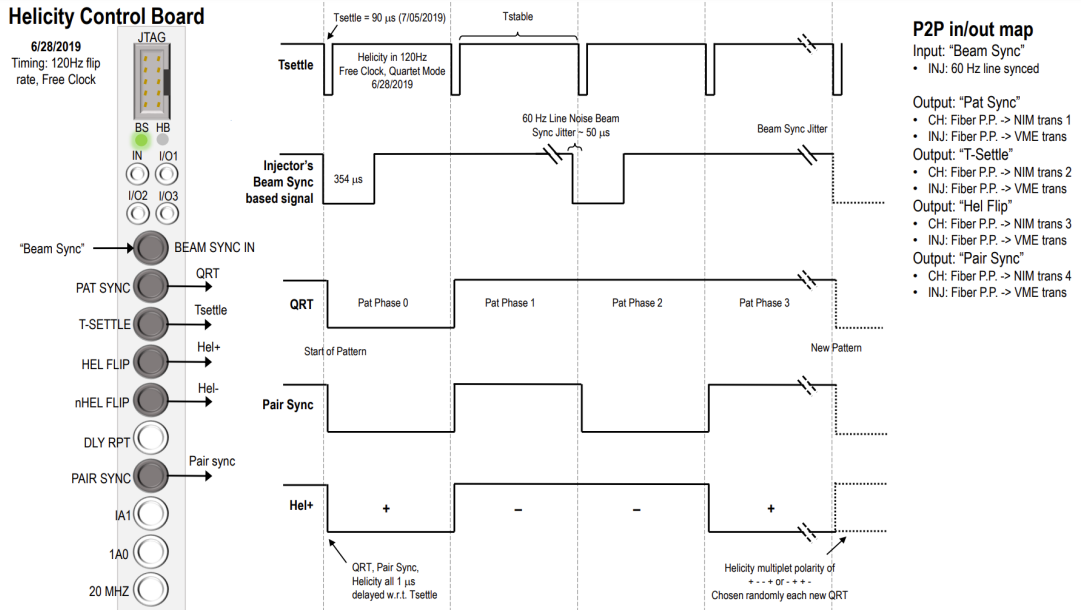


Figure 2.43: Helicity timing diagram. The Tsettle signal (falling edge) indicates the start of a new helicity window, which is chosen as the $t=0$ reference point for all timing diagram, it goes to the CH/hall. The QRT (Pattern Sync) signal indicates the start of each helicity pattern, it goes to the CH. The Pair Sync signal toggles between 0 and 1, indicating the start and end of a helicity pair, it goes to the CH. This signal is not important, all it tells can be inferred from the QRT signal. The Hel+ signal decides the helicity of the current window, it goes to the laser table in the injector. The Hel- signal is a complementary signal to Hel+, so that the board always keeps the same current regardless of the helicity state, preventing helicity correlated electrical pickup from the board. This signal is not shown in the plot, it goes to the helicity magnets (the double wien filters). The delayed helicity (DLY RPT) signal is delayed by n (specified by the user) windows w.r.t. the Hel+ signal. It tells what the helicity was n windows before. It goes to the CH. This signal is not shown in the plot.

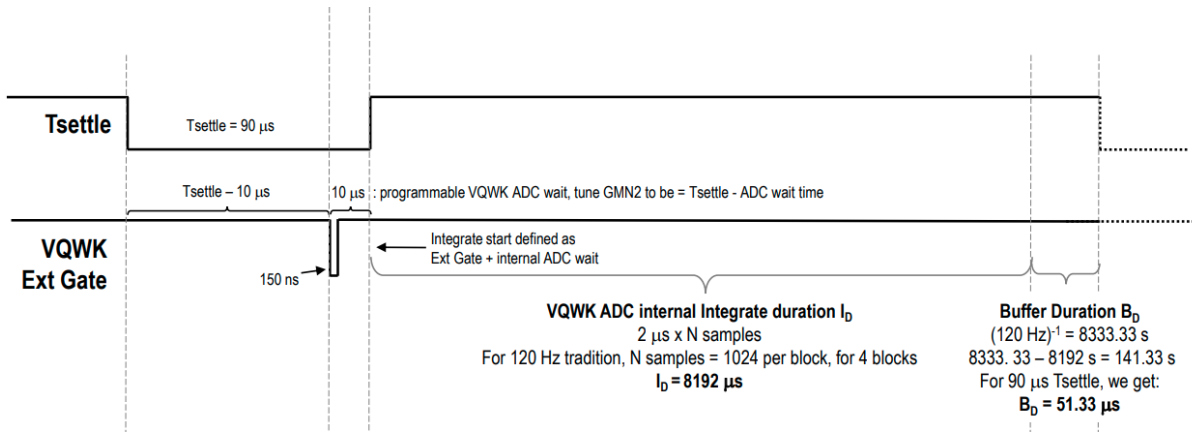


Figure 2.44: Integrating timing

(integration), a HAPPEX Timing Board (HAPTB) is used, which receives the Tsettle signal and produces the integration gate signals, distributing them to each ADC/scalar to trigger the signal integration/collection.

Each DAQ has its own VME crate holding all necessary hardware modules, a read out controller (ROC) controls the VME crate. All these crates (ROCs) are managed by a trigger supervisor (TS), which has its own VME crate. The TS is triggered by the Tsettle signal, which in turn triggers the ROCs. By receiving the trigger signal, ROC will read data stored in their memory buffer and send it to the CODA system, which will build, transport and store events. We have an analyzer JAPAN (Just Another Parity ANalyzer) to monitor data quality online and analyze data off-line.

Counting DAQ

The two counting DAQs, one for each HRS, are different from the integrating DAQs, in both hardwares and softwares. In contrast to integrating electrons, the counting DAQ record and reconunstruct track for scattered electrons, one by one. The counting DAQ reads data from the scintillators, VDCs and GEMs, the main detectors are not used in the counting DAQ. The counting DAQ is triggered by the scintillators, different logical combinations of the scintillator signals could trigger different counting rates. Most of the time, we use the S0 trigger signal, as discussed in the scintillator sector.

The analyser used for decoding counting mode data is the general Hall A analyser, which will read out the hit information in each detector and reconstruct the electron track based on these hits. By reversing the optics matrix, it will calculate the electron info (position, angle and energy) at the target, allowing to measure the scattering angle and Q^2 , to tune the optics matrix, to do detector alignment and check backgrounds.

EPICS

Besides the two DAQ systems, there is a site-wise slow (relative to the helicity frequency) control system, called Experimental Physics and Industrial Control System

(EPICS) [66], to monitor and control every important apparatus and quantity, such as various magnets, beam current/position/energy, vacuum level, temperature, gas flow, high voltage supply etc. EPICS polls a series of input/output controllers (IOCs) and record their average values about every second. It provides real-time monitoring of the whole system: both the accelerator and detectors, and allows us to trace back the status whenever there are some problems.

Chapter 3

Data Analysis

As mentioned before, though of the fast helicity flipping and tremendous effort to keep the electron beam in exactly the same conditions through opposite helicity states, there is no way to achieve such a goal. There are always various noises produced in various parts of the accelerator, though being very small in a general sense, they are large enough to flood what we are measuring, if not dealt with properly.

We use the same methods to process both PREX-II and CREX data sets, therefore we will discuss only CREX data here, anything that is different in PREX-II will be listed out.

3.1 Raw Data

CREX started commissioning around December 2019, we took the first good run on Dec 12. Six slugs (slug 100 - 105) were collected before the Christmas break. After the Christmas break, data taking was resumed until Jan 18 2020 when the first ^{48}Ca target was damaged. It took 5 days to prepare a new target. Then things moved on quite smoothly, we had 2 days of transverse asymmetry (AT) measurement from Feb 10 to Feb 12. We were a little over halfway on collected charge when Covid-19 hit and the lab was

Number of Good Slugs	121
Number of Good Runs	1384
Number of Good Miniruns	8525
Number of Good Quadruplets	86832046
Charge Asymmetry	~ 100 ppb
Position Difference	~ 10 nm
Angle Difference	~ 1 nrad
Energy Difference	~ 10 ppb
Raw Asymmetry	2087 ppm
Regressed Asymmetry	2090 ppm

Table 3.1: CREX data statistics.

shut down at the end of March 2020. Fortunately, the lab reopened four months later, we had the chance to continue the electron bombardment for another one month. The experiment stopped data taking on Sep 18 2020. A total charge of 480 C was collected, among which 390 C was judged as good.

The data set is clearly separated into three periods: before the AT, after the AT and before the Covid, and after the Covid, in chronological order. A more reasonable split is to separate them by their wien-flip states, whose result almost overlaps with the chronological separation.

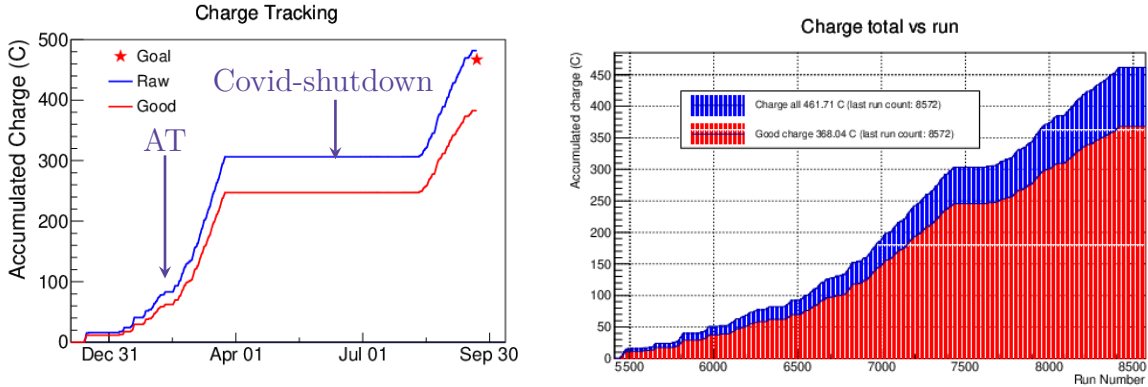


Figure 3.1: Charge accumulation versus time (left) and the run number (right). The long plateau on the left plot is due to the Covid shutdown, which is shown around run 7500 on the right plot. One sees that data taking is most efficient after the AT and before the Covid, the last month (after the Covid) is not bad while the first two months are not so efficient due to various hardware problems.

CREX collects 1451 production runs, among them, 1386 are identified as ‘Good’ and used for final analysis. The good runs consists of 1362 both arms runs, 6 left arm runs and 18 right arm runs. Each good production run takes about 1 hour and collects about 0.3 C with a charge efficiency of 80%.

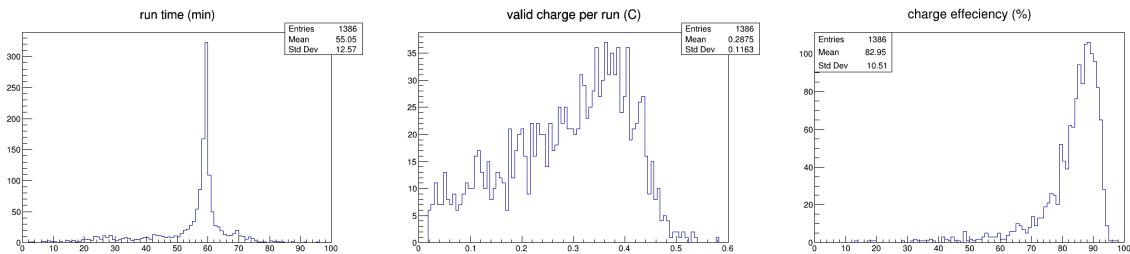


Figure 3.2: Runtime and charge statistics of CREX runs (`ErrorFlag == 0`).

Though electrons come bunch by bunch, the bunch frequency of 499 MHz is much larger than our helicity flip frequency of 120 Hz, so electron beams can be regarded as continuous. All scattered electrons in one helicity window will be integrated as 1 readout (event). Every four continuous helicity events are grouped into one quadruplet (in case of

the 240 Hz flipping frequency in PREX-II, every eight helicity events form one octuplet). In order to cancel the 60 Hz line power noise, the PV asymmetry is calculated based on helicity quadruplets (octuplets in the case of 240 Hz flipping frequency), whose frequency will be $120/4$ ($230/8$) = 30 Hz, as shown in Fig. 3.3. CREX collected about 87 million such good helicity quadruplets.

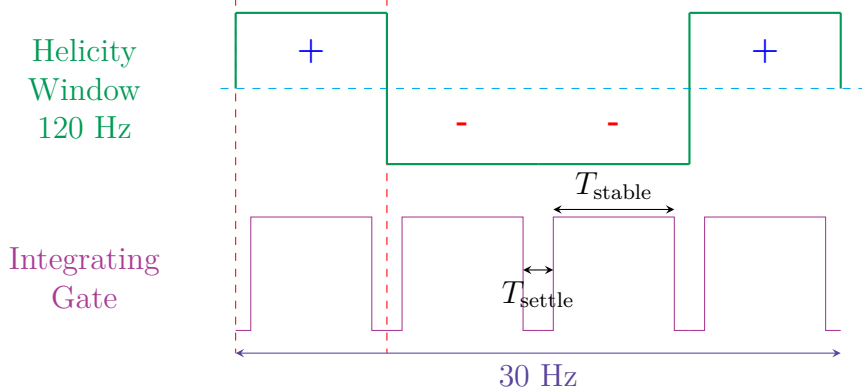


Figure 3.3: Schematic plot of the helicity pattern. In CREX, $T_{\text{settle}} = 90 \mu\text{s}$, which allows the PC to stabilize after a voltage polarity flipping, avoiding any cross effect from the previous helicity state. The corresponding deputy factor is 98.92%.

Every run is separated into multiple miniruns to account for the fact that beam conditions are changing quickly. It is inappropriate to calculate the detector slope – detector's response to the beam fluctuations, over a 60 mins time scale. Minirun will be more proper, the beam conditions, and therefore the slope value should be more stable during such a shorter time period. Every minirun contains 9000 good quadruplets, which counts about 5 mins in data collection. The last minirun in each run contains whatever number of good quadruplets left that can't be divided into 2 miniruns. Miniruns whose number of samples is less half of the standard (4500) will be discarded. CREX has 8543 miniruns from 1386 good runs, among them, 2 miniruns are discarded because of their small sample size and 16 miniruns are discarded due to noisy beam conditions or large beam shifts that are not caught in the previous two respins, as shown in Table 3.2 and 3.3. To avoid another respin, these miniruns are simply removed.

run	minirun	number of samples
7720	0	4352
8082	0	4391

Table 3.2: Two miniruns that have too small good samples (with cut `ErrorFlag == 0`).

Runs will be grouped into slugs. One slug is defined as all runs between two changes of the IHWP. With a stable beam, we could collect three slugs per day, so each slug takes about 8 hours or longer in case of any accidents. CREX collects 124 slugs, after the data cleaning and combination to remove slugs with only 1 run, 121 slugs are kept.

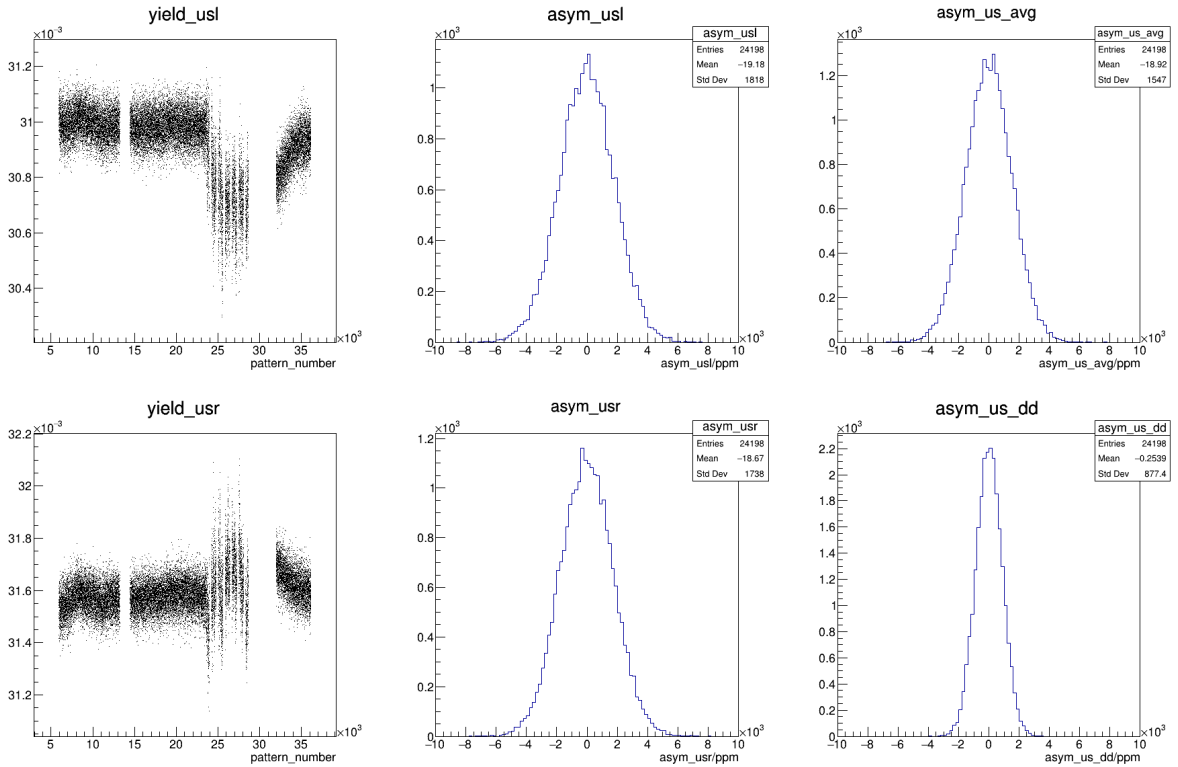


Figure 3.4: A run plot: detector yield and asymmetry distribution in run 6600, selected with `ErrorFlag == 0`. The shift in the second half of the yield plot is caused by the beam position/angle fluctuation. The right 2 plots are average and difference of the asymmetry of LHRs and RHRs. Ideally, the difference should be 0 and the average is what we want to measure.

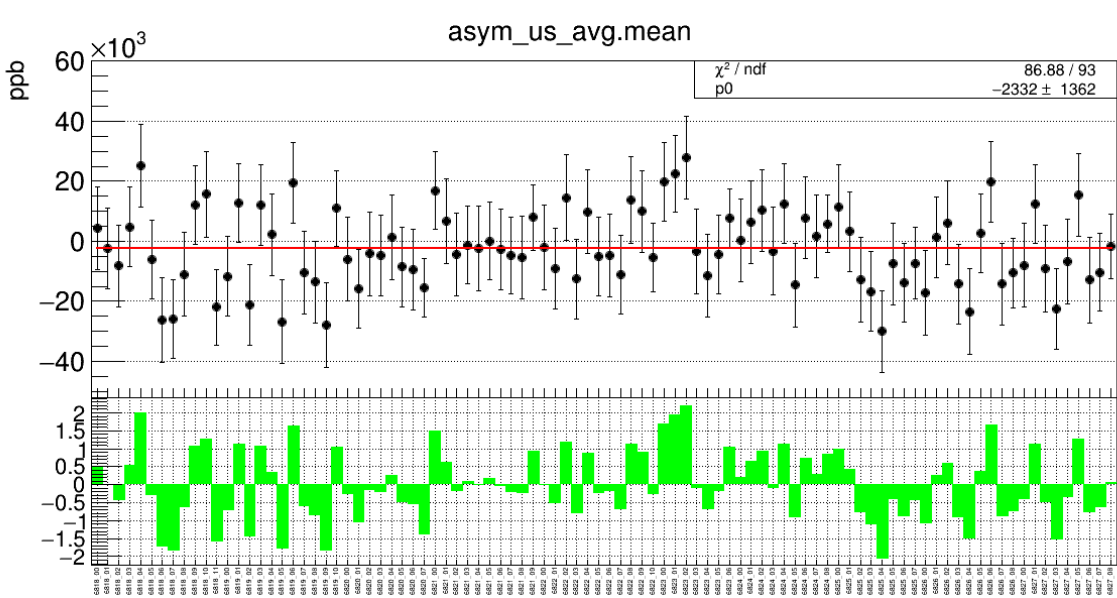
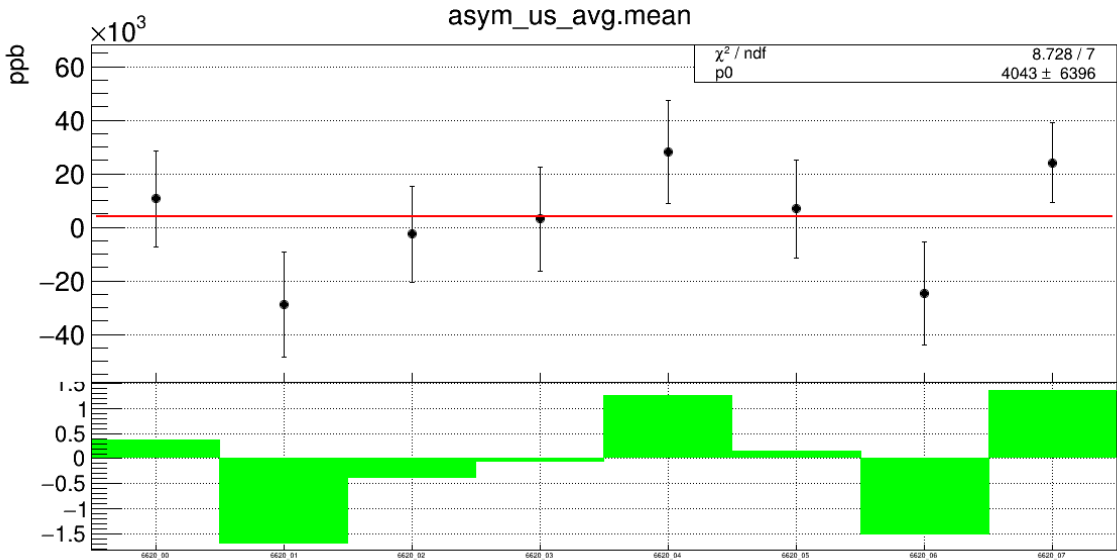
run	minirun	run	minirun
6564	4	7211	4
6567	2, 4	7889	0
6571	3, 4	7942	5
6593	2	8036	2
6983	8	8240	1
7149	6	8549	0, 1, 4

Table 3.3: List of Miniruns that had larger asymmetry outliers and therefore are removed.

Finally, slugs are split into periods, with different wien flip states. We have three periods as said before.

3.1.1 Cut

A loose cut is applied in the event level to select as much as possible good events. During data taking, the JAPAN analyzer will check various hardware failures, the beam



stability level, helicity information and others. Based on the total 23 checks, an error code (`ErrorFlag`), which is the bit-wise OR of the result against every check, is assigned to each event. Events that pass every check will have a null error code (`ErrorFlag == 0`).

The various hardware failure checks detects the ADC readout in the detectors and monitors, making sure we are not recording saturation or null values; the sample size is

wien-flip	slugs
Right	100-137
Left	138-185
Right	186-223

Table 3.4: Wien-flip separation in terms of slugs.

also verified. These checks help to identify the problematic hardware channels in case of any hardware failures.

The beam stability level checks keep track of the beam conditions based on their mean and RMS values. These checks compare the detector/monitor readout to a user-set upper and lower limit to filter out outliers; besides, for some ADC channels, there are cuts on the RMS of a moving time window of 200 (configurable) consecutive events, if the RMS value is too large, all events in that time window fail the RMS check. Finally, the burplevel check compares the current event readout with the average value of the previous 10 (configurable) events, events with difference larger than the burplevel cut fail this check. With these checks, we can make sure the good quality of the data we collect.

One example of such stability cut is the beam current cut. In case of beam trip due to various accidents, the beam drops and then recovers quickly. The beam in the process of falling and rising is usually unstable, so we require the event beam current should be larger than the stable beam current minus 30 μA (15 μA in PREX-II).

Apart from these checks, we have an analysis shift worker to check monitor/detector yields and their differences/asymmetries for each run after prompting. Additional cuts can be applied if large beam excursion, drift or any other anomalies are observed. These cuts are run specific, added one by one when needed.

During the online and the two offline analysis, we use cut `ErrorFlag == 0` to select good quadruplets, which excluded all beam modulation events. Actually, some beam modulation events are usable for our asymmetry analysis and are included in our final published result, which counts for about 5% of the CREX data set. To be consistent with the published result, all following plots are produced with the cut `ErrorFlag&0xda7e6bff == 0` if not mentioned otherwise.

3.1.2 Beam Conditions

As explained before, the key to measure a teeny tiny asymmetry value is to keep all experimental conditions as the same as possible between different helicity windows. Among all the conditions that need precise control, the hardest one is the beam condition. Any fluctuation in any component along the long accelerator line will cause changes to the beam condition, therefore introducing false asymmetry to our measurement. Despite various difficulties, the CEBAF staff worked hard to provide us excellent beams with tiny difference between different helicity windows, as displayed below.

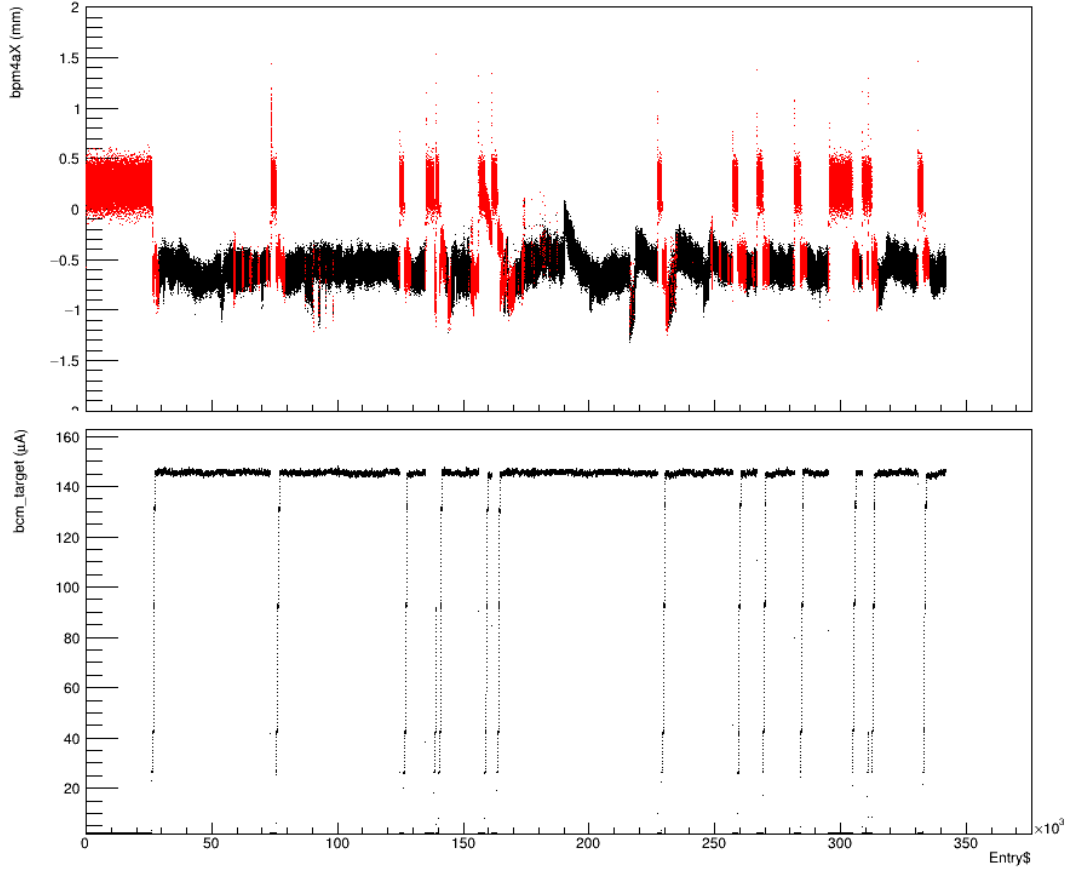


Figure 3.7: BPM4aX distribution (top) in run 8019, the bottom plot is the corresponding beam current distribution. Black points are good events (`ErrorFlag == 0`) and red points are bad ones (`ErrorFlag != 0`). One can clearly see that all beam trips and most beam jitters are recognized by our stability checks.

Beam Current

The raw asymmetry we measure is normalized to the beam current, because beam current varied from run to run; and even within a single run, beam currents are slightly different between helicity windows. The normalized raw asymmetry is:

$$\mathcal{A}_{\text{raw}} = \frac{(D/I)^+ - (D/I)^-}{(D/I)^+ + (D/I)^-} \approx \frac{D^+ - D^-}{D^+ + D^-} - \frac{I^+ - I^-}{I^+ + I^-} = \mathcal{A}_D - \mathcal{A}_I \quad (3.1)$$

where D represents a detector readout.

This equation shows that the charge asymmetry contributes to the raw asymmetry directly, so we need to keep the charge asymmetry as small as possible, which is done through the charge feedback system. Overall, charge asymmetry is about hundreds of ppb. One can also tell from Fig. 3.8 that period 2 has relatively good beam conditions

than the other two periods.

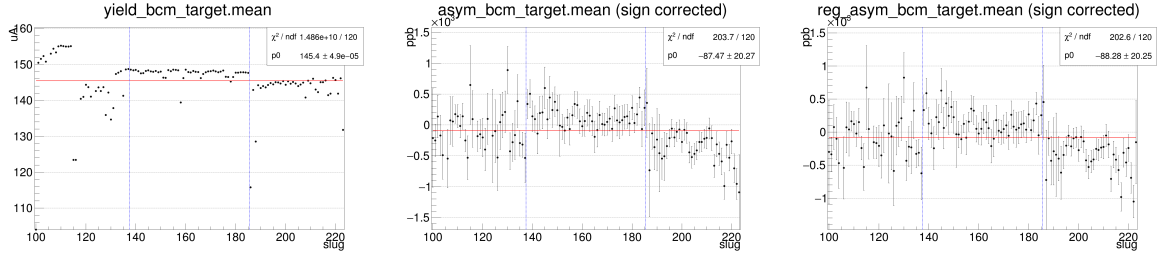


Figure 3.8: Slug-wise mean value of the beam current, asymmetry and regressed asymmetry in CREX. The blue dashed lines separate the data set into three periods with different wien-flip states. Most of the time, CREX run at $\sim 150 \mu\text{A}$, an overall $\sim 100 \text{ ppb}$ charge asymmetry is achieved.

Beam Position, Angle and Energy

We don't have a direct measurement of the beam position and angle at the target, these information can be inferred from various BPMs. Given the distance between the target and BPM4a as $D1 = 5.725 \text{ m}$ and the distance between BPM4a and BPM4e as $D2 = 4.083 \text{ m}$, the beam position and angle at the target will be:

$$T_{X,Y} = \text{BPM4a}_{X,Y} + \frac{\text{BPM4e}_{X,Y} - \text{BPM4a}_{X,Y}}{D2} D1 \quad (3.2)$$

$$\theta_{X,Y} = \frac{\text{BPM4e}_{X,Y} - \text{BPM4a}_{X,Y}}{D2}$$

Using Eq. 3.2, the overall difference of the beam position/angle at the target is calculated to be:

$$\text{diff}_{X,Y} \sim 10 \text{ nm} \quad \text{diff}_{\theta_{X,Y}} \sim \text{nrad}$$

Again, the second period has a more stable beam than the other two periods.

The beam momentum/energy is measured by BPM12X, whose dispersion tells the deviation (dp) from the standard value (p0). The design value of the dispersion for CREX is $D = 4.0 \text{ m}$, and an actual measurement gives $\sim 3.8 \text{ m}$. I use 4.0 m here. As can be seen in Fig. 3.10, CEBAF provides a beam with energy dispersion as small as $\sim 10 \text{ ppb}$.

$$\frac{dp}{p} = \frac{\text{diff_BPM12X}}{D} \quad (3.3)$$

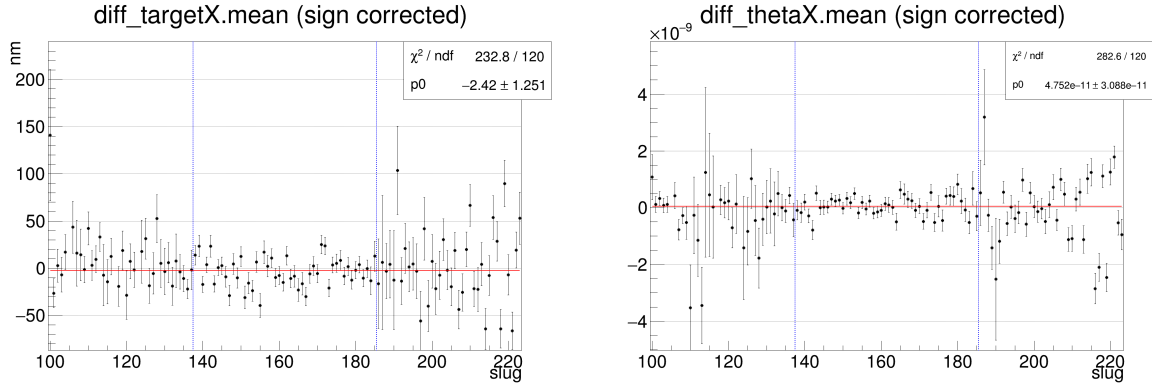


Figure 3.9: Slug-wise mean value of the beam position (left) and angle (right) difference at the target. Very precise control of the beam conditions is achieved. The Y dimension plots are similar and are not shown here.

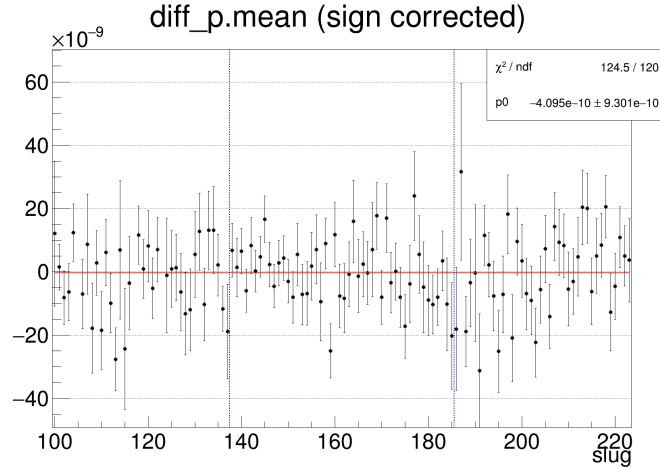


Figure 3.10: Slug-wise mean value of the beam energy dispersion. Overall, an energy difference of ~ 10 ppb is achieved.

3.1.3 Raw Asymmetry

The raw asymmetry is calculated as:

$$\mathcal{A}_{\text{raw}} \equiv \begin{cases} \frac{d^+ - d^- - d^- + d^+}{d^+ + d^- + d^- + d^+} & (+ - - + \text{ pattern}) \\ \frac{-d^- + d^+ + d^+ - d^-}{d^+ + d^- + d^- + d^+} & (- + + - \text{ pattern}) \end{cases} \quad (3.4)$$

where $d = \frac{D}{I}$ is the normalized detector integrating yield in one helicity window, the upper-script indicate the helicity of the beam. The detector yield is calibrated with their corresponding pedestals.

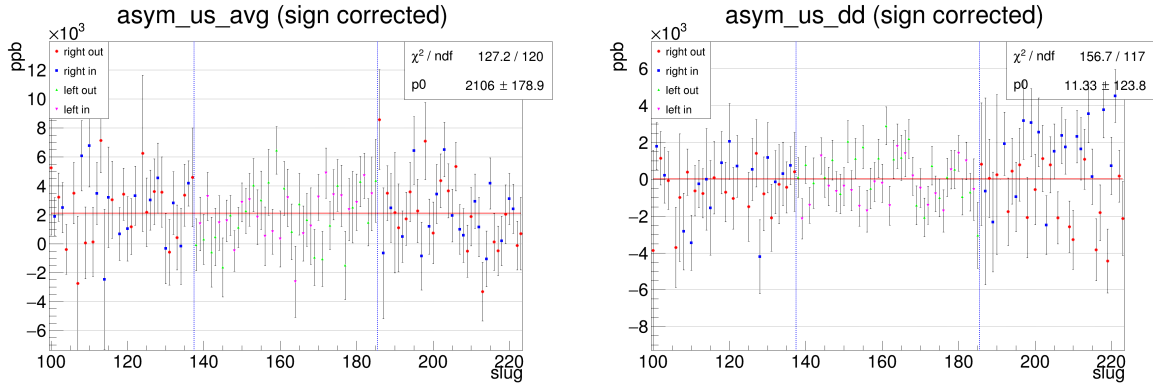


Figure 3.11: Slug-wise raw asymmetry average (left) and difference (right) for CREX. The right plot has three less slugs because there are three single-arm slugs.

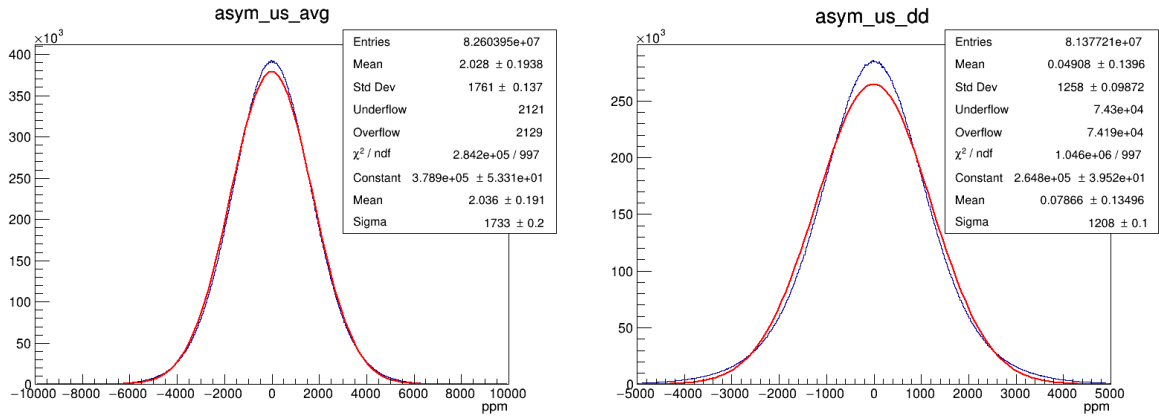


Figure 3.12: Mulplot of the CREX raw asymmetry average (left) and difference (right). The blue line is the data and the red line is a Gaussian fit. The difference plot has less entries because single arm runs have no difference.

3.2 Beam False Asymmetry Correction

As shown in the previous few plots about beam conditions, there are false asymmetries caused by the beam. The helicity correlated beam asymmetry (HCBA), is the largest contributor to the false asymmetry.

As one may notice in Fig. 3.13, a beam jitter will cause fluctuation in the detector yield, with approximately a linear correlation. So to remove the false asymmetries caused by beam jitters, we just need to know the correlation between the detector yield and each beam parameter – the detector slope.

There are 2 methods to calculate the slope value, regression and beam modulation, we will discuss them in details in the following sections.

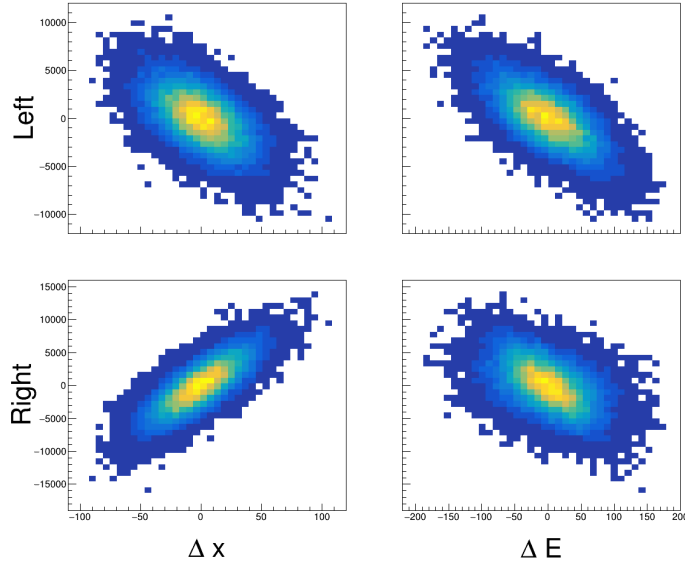


Figure 3.13: Correlation between the detector yield and the beam position/energy in run 7679. The left/right detector yields change oppositely when the beam position shifts, and they move in the same direction w.r.t. fluctuations in the beam energy.

3.2.1 Regression

The first method to calculate the slope is the regression – a perfect scheme for the application of this statistical tool.

Bear in mind that regression itself doesn't tell us any relationships or rules, it only works under the assumption that the relationship between variables is predictable (given by the user) and the dependent variables follow a known distribution function $P(\epsilon)$, which, again, will be told by the user:

$$Y = f(X) + \epsilon$$

With these prior knowledge, regression is able to extract the most likely coefficients in the predicted model.

The Model

Considering one monitor and one detector. Assuming the reading noise of the detector follows the Gaussian distribution and the monitor is precise (one can absorb the monitor noise into the beam fluctuation):

$$\begin{aligned} M &= m \\ D &= d + \epsilon(0, \sigma_0^D) \end{aligned} \tag{3.5}$$

here, the capital letters (D and M) represent the measured values while the small letter (m and d) mean the true values. σ_0^D is the variance of the noise in the detector.

Then the difference between beams of opposite polarization will follow also the Gaussian distribution with a larger variance:

$$\begin{aligned}\Delta M &= M^+ - M^- = m^+ - m^- = \Delta m \\ \Delta D &= D^+ - D^- = (d^+ + \epsilon(0, \sigma_0^D)) - (d^- + \epsilon(0, \sigma_0^D)) = \Delta d_0 + \epsilon(0, \sqrt{2}\sigma_0^D) = \Delta d + \epsilon(0, \sigma_1^D)\end{aligned}\quad (3.6)$$

Again, Δm and Δd are the real differences while ΔM and ΔD are the measured values.

The probability for measuring ΔD will be:

$$P(\Delta D) = \frac{1}{\sigma_1^D \sqrt{2\pi}} e^{-\frac{1}{2} \left(\frac{\Delta D - \Delta d}{\sigma_1^D} \right)^2} \quad (3.7)$$

We will have a bunch of independent data points: $(\Delta M, \Delta D)_i$ and we want to extract the relationship between Δd and Δm : $\beta \equiv \frac{\partial d}{\partial m}$. Given the tininess of Δm (compared to its normal yield), a first order correlation is precise enough. This is exactly a linear regression problem.

$$\begin{aligned}\Delta d &= 0 + \beta \Delta m \\ \mathcal{A}_{\text{cor}} &= \mathcal{A}_{\text{raw}} - \beta \Delta M\end{aligned}\quad (3.8)$$

where \mathcal{A}_{cor} is the corrected asymmetry.

For any real data point $(\Delta m, \Delta d)_i$, the possibility to measure $(\Delta M, \Delta D)_i$ is:

$$P_i(\Delta D | \Delta M) = \frac{1}{\sigma_1^D \sqrt{2\pi}} e^{-\frac{1}{2} \left(\frac{\Delta D - \beta \Delta M}{\sigma_1^D} \right)^2} \quad (3.9)$$

For the accumulated data of one minirun, the total probability will be:

$$P = \prod_i^n P_i(\Delta D | \Delta M) = \prod_i^n \frac{1}{\sigma_1^D \sqrt{2\pi}} e^{-\frac{1}{2} \left(\frac{\Delta D_i - \beta \Delta M_i}{\sigma_1^D} \right)^2} \quad (3.10)$$

To maximize P , it is equivalently to minimize:

$$\chi^2 = \sum_i (\Delta D - \beta \Delta M)_i^2 \quad (3.11)$$

where i sums over all samples in one minirun.

Maximization of P w.r.t. β means a zero derivative:

$$\frac{\partial P}{\partial \beta} = P \times \sum_i \frac{\Delta M_i}{\sigma_1^D} \left(\frac{\Delta D_i - \beta \Delta M_i}{\sigma_1^D} \right) = 0 \quad (3.12)$$

which gives β as:

$$\sum_i \Delta M_i (\Delta D_i - \beta \Delta M_i) = 0 \quad (3.13)$$

↓

$$\beta = \frac{\sum \Delta D_i \Delta M_i}{\sum \Delta M_i^2} \quad (3.14)$$

Extending the independent variable to be multi-dimensional, we have:

$$\Delta D = (\beta_1 \ \ \beta_2 \ \ \cdots \ \ \beta_m) \begin{pmatrix} \Delta M^1 \\ \Delta M^2 \\ \vdots \\ \Delta M^m \end{pmatrix} + \epsilon(0, \sigma^D) \quad (3.15)$$

where m is the number of BPMs used for the asymmetry analysis.

$$\frac{\partial P}{\partial \beta_\nu} \propto \sum_i \Delta M_i^\nu (\Delta D_i - \sum_\mu \beta_\mu M_i^\mu) = 0 \quad (3.16)$$

Arrange Eq. 3.16 in a matrix:

$$\begin{pmatrix} \sum_i \Delta D_i \Delta M_i^1 \\ \sum_i \Delta D_i \Delta M_i^2 \\ \vdots \\ \sum_i \Delta D_i \Delta M_i^m \end{pmatrix} = \begin{pmatrix} \sum_i \Delta M_i^1 \Delta M_i^1 & \sum_i \Delta M_i^1 \Delta M_i^2 & \cdots & \sum_i \Delta M_i^1 \Delta M_i^m \\ \sum_i \Delta M_i^2 \Delta M_i^1 & \sum_i \Delta M_i^2 \Delta M_i^2 & \cdots & \sum_i \Delta M_i^2 \Delta M_i^m \\ \vdots & \vdots & \ddots & \vdots \\ \sum_i \Delta M_i^m \Delta M_i^1 & \sum_i \Delta M_i^m \Delta M_i^2 & \cdots & \sum_i \Delta M_i^m \Delta M_i^m \end{pmatrix} \begin{pmatrix} \beta_1 \\ \beta_2 \\ \vdots \\ \beta_m \end{pmatrix} \quad (3.17)$$

Define the covariance of any two variables as:

$$\text{cov}(x, y) = \sum_i x_i y_i \quad (3.18)$$

and

$$M_{m \times m} = \begin{pmatrix} \text{cov}(\Delta M^1, \Delta M^1) & \text{cov}(\Delta M^1, \Delta M^2) & \cdots & \text{cov}(\Delta M^1, \Delta M^m) \\ \text{cov}(\Delta M^2, \Delta M^1) & \text{cov}(\Delta M^2, \Delta M^2) & \cdots & \text{cov}(\Delta M^2, \Delta M^m) \\ \vdots & \vdots & \ddots & \vdots \\ \text{cov}(\Delta M^m, \Delta M^1) & \text{cov}(\Delta M^m, \Delta M^2) & \cdots & \text{cov}(\Delta M^m, \Delta M^m) \end{pmatrix} \quad (3.19)$$

The coefficient vector will be extracted as:

$$\begin{pmatrix} \beta_1 \\ \beta_2 \\ \vdots \\ \beta_m \end{pmatrix} = M^{-1} \begin{pmatrix} \text{cov}(\Delta D, \Delta M^1) \\ \text{cov}(\Delta D, \Delta M^2) \\ \vdots \\ \text{cov}(\Delta D, \Delta M^m) \end{pmatrix} \quad (3.20)$$

Theoretically and practically, we need only 5 BPMs to cover the whole phase space of the beam motion. The 5 BPMs we chose in CREX analysis are BPM1X, BPM4aY, BPM4eX, BPM4eY and BPM12X.

Slope Values

With Eq. 3.20, the slope values w.r.t. to the chosen BPMs are calculated. Fig. 3.14 shows the asymmetry's response to changes in the beam energy, it justifies the usage of miniruns. As one can see in the plot, miniruns within the same run may have different slope values up to a few percent. This is expected because the detector slope is not a constant, it depends on the detector yield. Remember Eq. 3.8 is based on the assumption that the beam fluctuations are tiny. When there are relatively large shifts in the beam, new slopes are needed. Therefore, a minirun-wise slope value is more stable than a run-wise one, and corrects the false asymmetry more precisely. This also means that the regression correction can deal with only small fluctuation around the mean value, it is imprecise to do the same correction for outliers, that's why we need to remove miniruns with beam condition outliers.

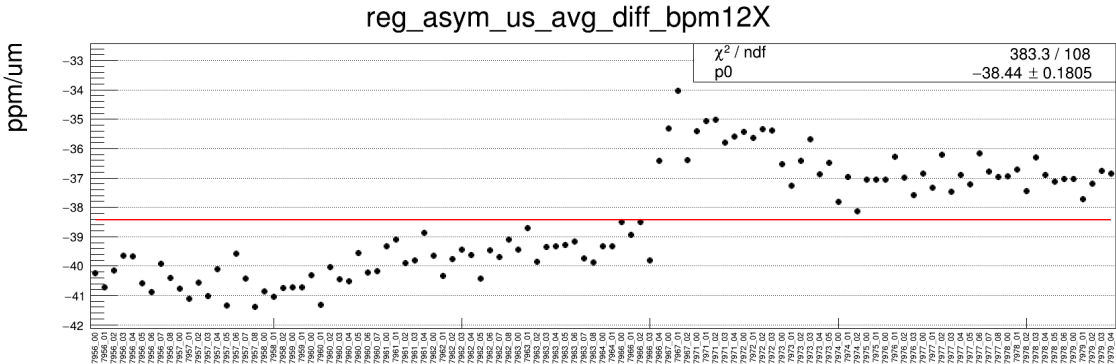


Figure 3.14: Minirun-wise energy slope ($\partial(\text{asymmetry average})/\partial (\text{BPM12X})$) distribution in slug 202. The X-axis is the run number attached by a minirun number.

Table 3.5 summarise the approximative slope values w.r.t. the 5 five BPMs we chose. Overall, our detector is sensitive to fluctuations in the X direction (the disperse direction) and the beam energy, and is dull to jitters in the Y direction.

BPM	slope (ppm/ μm)
1X	~ -40
4aY	~ 15
4eX	~ 40
4eY	~ 0
12X	~ -40

Table 3.5: Slope values of the asymmetry average w.r.t. different BPMs.

Corrections

With the slope values, we can calculate the corresponding false asymmetry correction:

$$\mathcal{A}_{\text{false}} = \beta \times (\text{diff in BPM}) \quad (3.21)$$

The main correction comes from differences in the X direction and the energy. A typical correction is about a few ppm, as shown in Fig. 3.14. Due to detector's insensitivity to fluctuations in the Y direction, its correction is relatively small, at the level of a few hundred ppb. Note that corrections from each beam parameter don't add up, they actually cancel with each other, leaving a relatively small total correction, usually a few ppm.

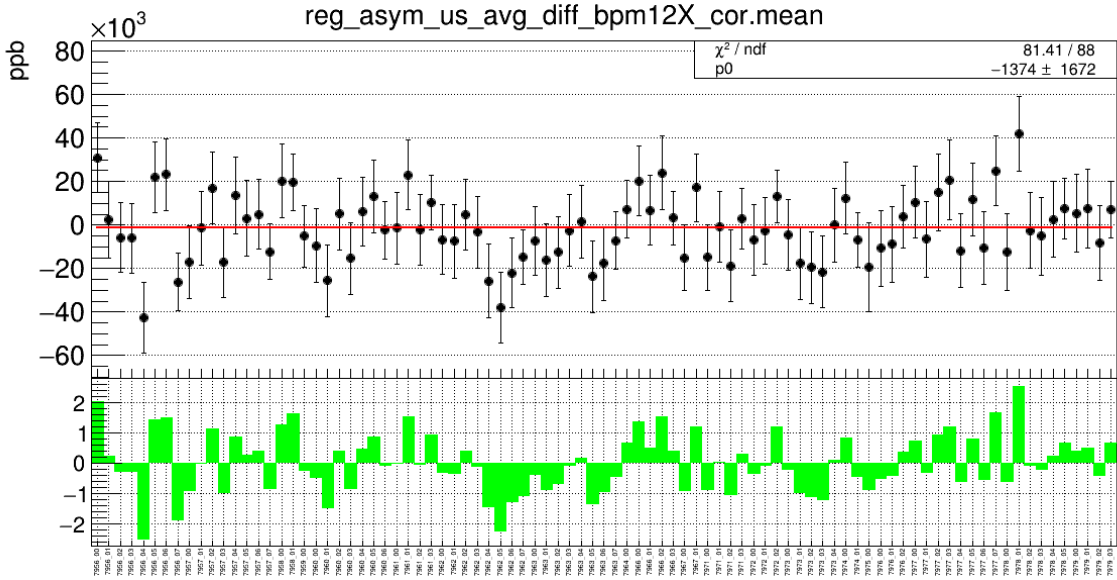


Figure 3.15: False asymmetry coreection caused by the energy difference (BPM12X) in slug 202.

BPM	correction
1X	a few tenths ppm
4aY	a few hundreds ppb
4eX	a few tenths ppm
4eY	a few hundreds ppb
12X	a few tenths ppm

Table 3.6: Typical false asymmetry corections from each BPM.

Regression Result

The asymmetry after the regression correction reads 2080 ± 84.01 ppb, as shown in the left plot of Fig. 3.16. Compared to the raw asymmetry of 2106 ± 178.9 ppb, the mean value doesn't change much, which is expected because we assumed that the false asymmetry follows the Gaussian distribution, therefore regression should just remove the noise without changing the mean value. The width of the asymmetry distribution after regression reduces by a factor of 2, as shown in the right plot of Fig. 3.16.

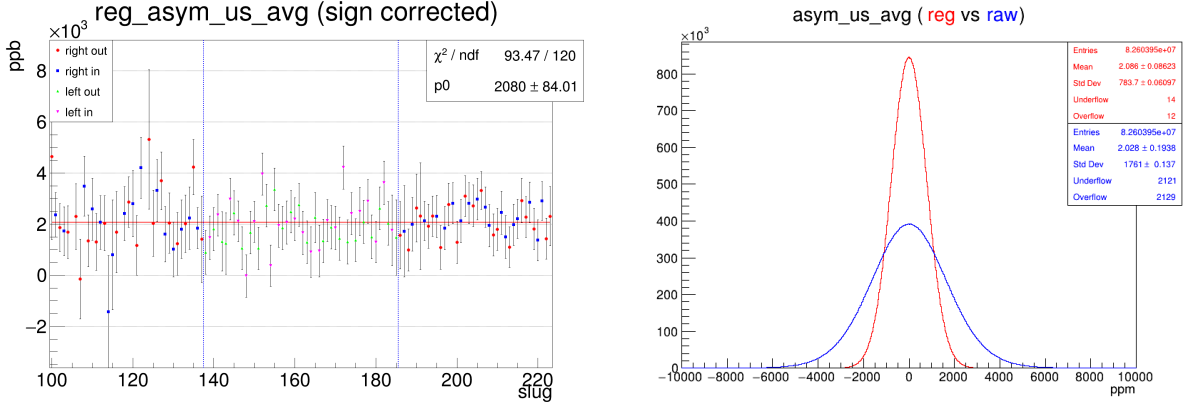


Figure 3.16: Left: slug-wise scatter plot of the regression corrected asymmetry. Right: Comparison of the experiment-wise distributions of the asymmetry before and after the regression correction.

Null Result

One way to check the correctness of our result is the null asymmetry, which is the difference between the LHRs and RHRs asymmetry (divided by 2). In the ideal case, the null asymmetry will be 0. Our measurement shows exactly the expectation, the corrected null asymmetry is about 85 ppb, very close to zero.

3.2.2 Beam Modulation (Dithering)

Another way to do the beam false asymmetry correction is the beam modulation. After all, if we want to know detector's response to the beam fluctuations, we can measure it directly – which is the beam modulation. By modulating the beam position/angle/energy intentionally, changes measured in monitors and detectors will tell us the slope values. The key point is to make sure that the modulating amplitude is larger than that of a natural beam fluctuation, so that we can extract the real response.

To express the idea mathematically, let D (M) be the Detector (Monitor) yield and C be the modulation coil input, we have:

$$\frac{\partial D}{\partial C_\alpha} = \sum_\mu \frac{\partial D}{\partial M_\mu} \frac{\partial M_\mu}{\partial C_\alpha} \quad (3.22)$$

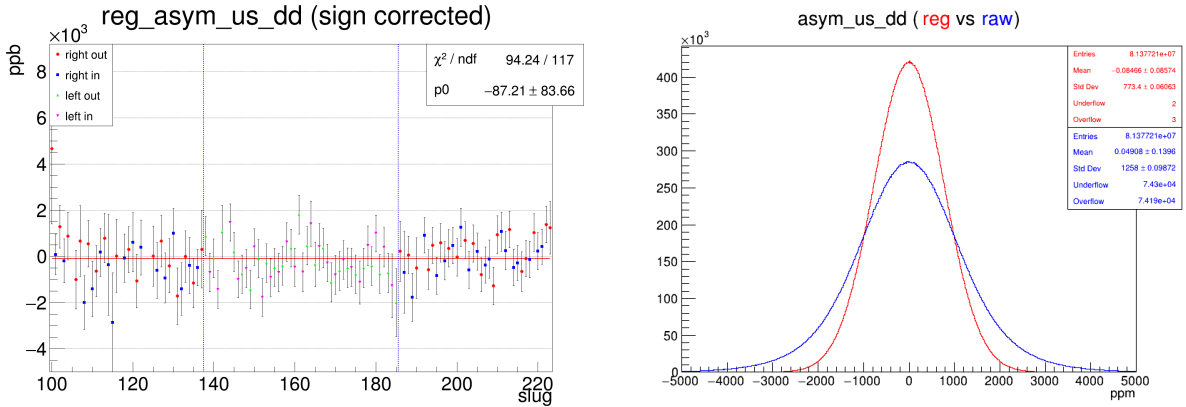


Figure 3.17: Slug-wise scatter plot (left) and experiment-wise histogram (right) of the regression corrected null asymmetry.

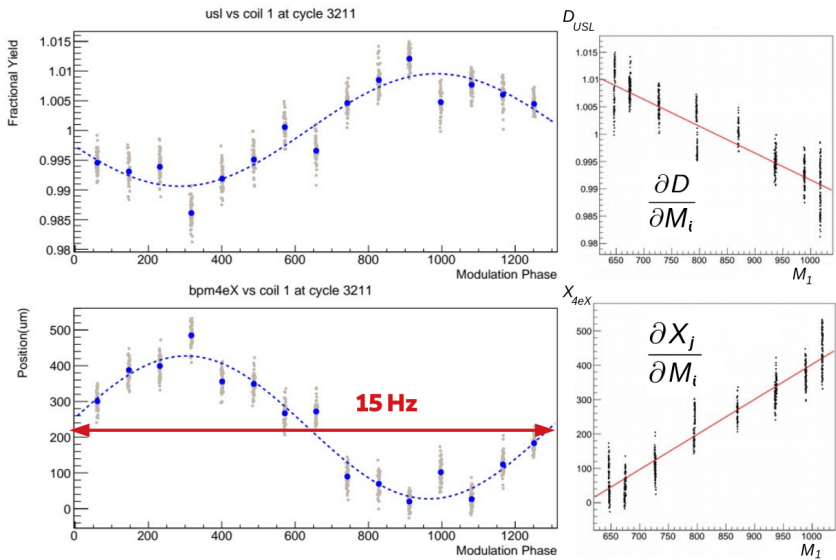


Figure 3.18: An example of the beam modulation.

where α indexes the number of the coils and μ sums over BPMs. In an alternative form:

$$\frac{\partial D}{\partial M_\mu} = \sum_{\alpha} \frac{\partial D}{\partial C_\alpha} \frac{\partial C_\alpha}{\partial M_\mu} = \sum_{\alpha} \frac{\partial D}{\partial C_\alpha} \left(\frac{\partial M_\mu}{\partial C_\alpha} \right)^{-1} \quad (3.23)$$

the slope value $\frac{\partial D}{\partial M}$ is what we want to know.

Define a matrix B as:

$$B_{n \times m} = \begin{pmatrix} \frac{\partial M_1}{\partial C_1} & \frac{\partial M_2}{\partial C_1} & \dots & \frac{\partial M_m}{\partial C_1} \\ \frac{\partial M_1}{\partial C_2} & \frac{\partial M_2}{\partial C_2} & \dots & \frac{\partial M_m}{\partial C_2} \\ \vdots & \vdots & \ddots & \vdots \\ \frac{\partial M_1}{\partial C_n} & \frac{\partial M_2}{\partial C_n} & \dots & \frac{\partial M_m}{\partial C_n} \end{pmatrix} \quad (3.24)$$

where n and m are the number of coils and monitors (BPMs), respectively.

The slope vector can be expressed as:

$$\begin{pmatrix} \frac{\partial D}{\partial M_1} \\ \frac{\partial D}{\partial M_2} \\ \vdots \\ \frac{\partial D}{\partial M_n} \end{pmatrix} = B^{-1} \begin{pmatrix} \frac{\partial D}{\partial C_1} \\ \frac{\partial D}{\partial C_2} \\ \vdots \\ \frac{\partial D}{\partial C_n} \end{pmatrix} \quad (3.25)$$

To make the matrix B invertable, we must have

$$n = m \quad (3.26)$$

which is the same number of monitors and coils.

The calculation of the sensitivity is the same as that of the regression slope:

$$\frac{\partial D}{\partial C} = \frac{\text{cov}(D, C)}{\bar{D} \cdot \text{cov}(C, C)} \quad \frac{\partial M}{\partial C} = \frac{\text{cov}(M, C)}{\bar{M} \cdot \text{cov}(C, C)} \quad (3.27)$$

where \bar{D} (\bar{M}) is the averse yield of the detector (monitor) and cov is the covariance. The mean yield in the denominator is for the normalization.

These sensitivities and their combinations are used for the beam quality monitoring during the charge collection. The possible large beam fluctuations will result in sharp changes in or abnormal values of these quantities.

Run Segments

As mentioned before, the modulation system consists of seven coils, a complete cycle of the modulation takes about 2 mins, during which, a stable beam is required. Unfortunately, such requirement is usually not met. Chances are beam trips off during a beam modulation, resulting in incomplete cycles. Though only five out of the total seven coils are needed to cover the whole beam parameter phase space, it still hurt if we discard those cycles that don't have the chosen five coils, considering that beam modulations don't happen frequently (about 1 modulation per 10 mins). So the strategy is to calculate the run-wise modulation sensitivities and slopes using all cycles in one run, rather than the cycle-wise values, to make use of as much modulation data as possible.

Though the run-wise strategy to save incomplete cycles, some runs are still lack of the dithering data. To enable the dithering correction for these runs, we separate runs into segments based on the beam conditions. An average dithering slope is calculated using run-wise values within a segment and then this average value is used as the dithering slope for each run in that segment. The separation of segments happen when there are changes in the beam setup or when we observe shift in the slope values. A detailed list of segments can be found in Cameron's thesis [67].

Dithering Result

The dithering corrected asymmetry of 2085 ± 84.22 ppb is 0.24% away from the regression corrected result of 2080 ± 84.01 ppb, cross checking the correctness of both methods. The difference between the asymmetries corrected with these 2 methods is shown in the right plot of Fig. 3.19. For most slugs, the difference is about zero, taking into account its uncertainty.

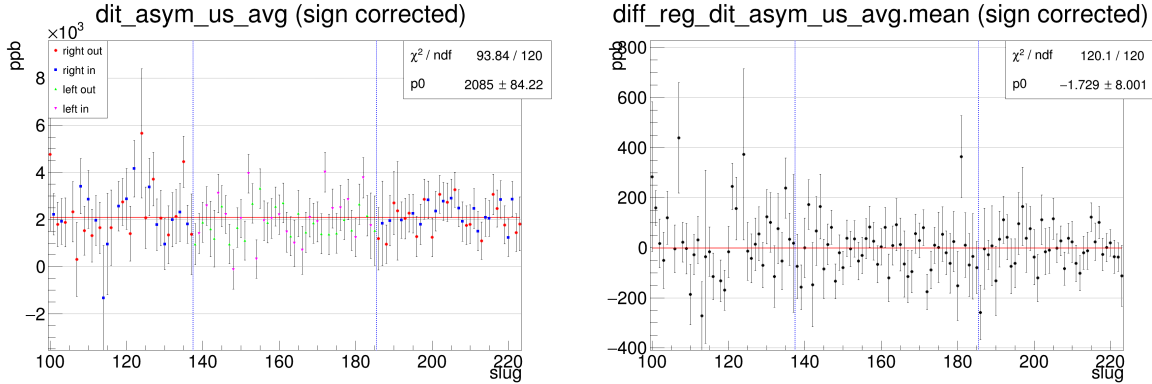


Figure 3.19: Left: slug-wise scatter plot of the asymmetry corrected with the beam modulation. Right: difference between the asymmetry values corrected by the regression and beam modulation.

3.2.3 Lagrange Multiplier

As said before, we should use miniruns for a more precise false asymmetry correction. However, segment-wise slopes are used, in the dithering correction, due to the short of the modulation data. Being more precise than the dithering correction, the regression method is less accurate, because of the natural noise in detectors/monitors. The modulation amplitude is larger than that of the noise (of course, the amplitude should be small w.r.t. the yield: $\lesssim 1\%$), therefore being more accurate by suppressing the effect of those noises.

Given the advantages and disadvantages of these two methods, it is natural to try to combine them, which leads to the Lagrangian analysis – regression with constraints from the beam modulation.

From Eq. 3.11, the χ^2 for the asymmetry regression is derived as:

$$\chi^2 = \sum_i \left(\mathcal{A}_{\text{raw}} - \sum_{\mu} \beta_{\mu} \Delta M_{\mu} \right)_i^2 \quad (3.28)$$

where i sums over samples and μ iterates over selected BPMs.

The Lagrangian multiplier for this constraint problem will be:

$$\mathcal{L} = \sum_i \left(\mathcal{A}_{\text{raw}} - \sum_{\mu} \beta_{\mu} \Delta M_{\mu} \right)_i^2 + \sum_{\alpha} \lambda_{\alpha} \left(\sum_{\mu} \beta_{\mu} \frac{\partial M_{\mu}}{\partial C_{\alpha}} - \frac{\partial D}{\partial C_{\alpha}} \right) \quad (3.29)$$

α indexes the selected coils.

Set the gradient of \mathcal{L} to zero:

$$\begin{aligned}\frac{\partial \mathcal{L}}{\partial \beta_\mu} &= -2\Delta M_\mu \sum_i \left(\mathcal{A}_{\text{raw}} - \sum_\nu \beta_\nu \Delta M_\nu \right)_i + \sum_\alpha \lambda_\alpha \frac{\partial M_\mu}{\partial C_\alpha} \\ &= 2 \left(\sum_\nu \beta_\nu \cdot \text{cov}(\Delta M_\mu, \Delta M_\nu) - \text{cov}(\mathcal{A}_{\text{raw}}, \Delta M_\mu) \right) + \sum_\alpha \lambda_\alpha \frac{\partial M_\mu}{\partial C_\alpha} = 0 \quad (3.30) \\ \frac{\partial \mathcal{L}}{\partial \lambda_\alpha} &= \left(\sum_\mu \beta_\mu \frac{\partial M_\mu}{\partial C_\alpha} - \frac{\partial D}{\partial C_\alpha} \right) = 0\end{aligned}$$

The difference between the second formula of Eq. 3.30 and the normal beam modulation method may be confusing, because they are actually the same if we consider only five BPMs. The constraint from the beam modulation is so strong that it identifies the slope values directly. Changes happen when we include more BPMs in the analysis, with more BPMs than coils, the solution to the constraint is not unique anymore, so that we can apply the Lagrange multiplier method.

Write Eq. 3.30 in a matrix form:

$$\begin{pmatrix} M_{m \times m} & (B^T)_{m \times n} \\ B_{n \times m} & \mathbf{0}_{n \times n} \end{pmatrix} \begin{pmatrix} \beta_1 \\ \vdots \\ \beta_m \\ \frac{\lambda_1}{2} \\ \vdots \\ \frac{\lambda_n}{2} \end{pmatrix} = \begin{pmatrix} \text{cov}(\mathcal{A}_{\text{raw}}, \Delta M_1) \\ \vdots \\ \text{cov}(\mathcal{A}_{\text{raw}}, \Delta M_m) \\ \frac{\partial D}{\partial C_1} \\ \vdots \\ \frac{\partial D}{\partial C_n} \end{pmatrix} \quad (3.31)$$

where the M and B matrices are defined in Eq. 3.19 and 3.24, and m (n) refers to the number of BPMs (coils) with $m > n$. In our analysis, we use all 12 BPMs, so $m = 12$ and $n = 5$.

Eq. 3.31 can be solved to be

$$\begin{pmatrix} \boldsymbol{\beta} \\ \boldsymbol{\lambda} \end{pmatrix} = \begin{pmatrix} M & B^T \\ B & \mathbf{0} \end{pmatrix}^{-1} \times \begin{pmatrix} \mathbf{Y}_1 \\ \mathbf{Y}_2 \end{pmatrix} \quad (3.32)$$

where $\boldsymbol{\beta}$ and $\boldsymbol{\lambda}$ are the slope vector and the Lagrange multiplier vector, \mathbf{Y}_1 is the covariance between the raw asymmetry and the monitor difference, and \mathbf{Y}_2 is the detector sensitivity. As what we did in the beam modulation, the sensitivity values are segment-wise average values.

Lagrange Multiplier Result

The asymmetry corrected with the Lagrange multiplier is shown in Fig. 3.20. Compared with the corrected asymmetries using the other two methods, only tiny difference

is observed.

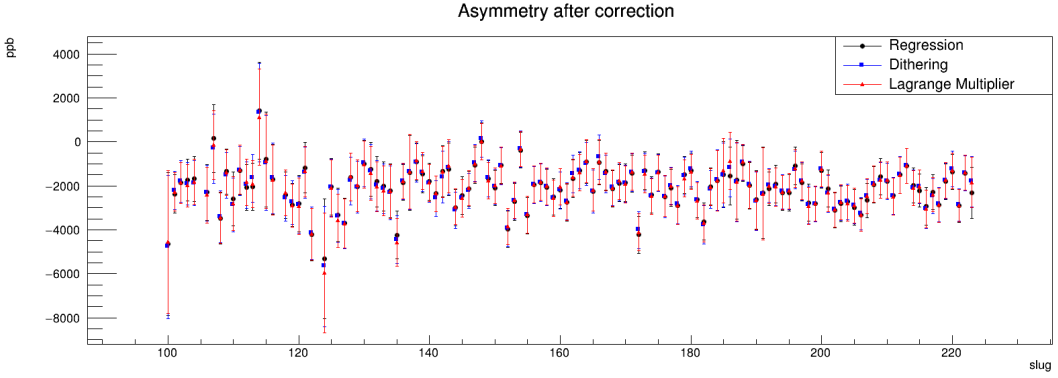


Figure 3.20: Comparison of the corrected asymmetries with regression (black), dithering (blue) and the Lagrange multiplier (red).

3.3 Result

As discussed before, the slow helicity reversal using the IHWP and the double wien filters allow us to check the possible systematic bias. Define a part as all runs with the same IHWP state in a period. By looking at the part asymmetry in Fig. 3.21, one see that asymmetries measured with opposite IHWP states or opposite wien-flip states overlap with each other within a 1σ uncertainty, verifying the unbiasedness of our measurement.

The pitt plot in Fig. 3.21 shows the asymmetry distribution for each pitt. The concept of pitt originated from Mark Pitt. The idea is to combine nearby slugs of alternating IHWP states to have the same (similar) number of events for opposite IHWP states. Every pitt includes about 4 slugs, the detailed range definition of each pitt can be found in Cameron's thesis.

The Final Number

From the pitt plot in Fig. 3.21, the final corrected asymmetry (blinded) is read as:

$$\mathcal{A}_{\text{cor}} = 2081 \pm 83.77 \text{ ppb} \quad (3.33)$$

The number used in the published paper is

$$\mathcal{A}_{\text{cor}} = 2080 \pm 83.77 \text{ ppb} \quad (3.34)$$

The difference lies in the 2 miniruns I discard in Table 3.2 because of too small samples.

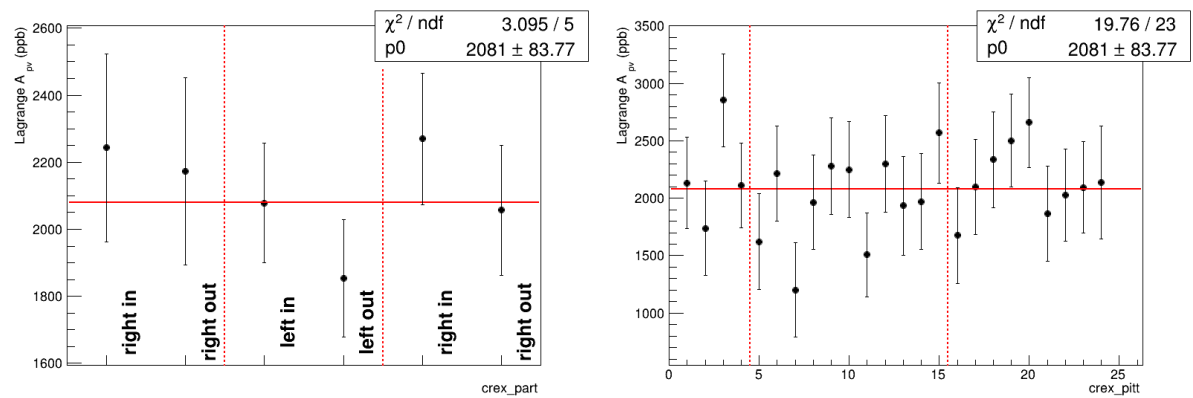


Figure 3.21: Part-wise and pitt-wise scattering plot of the asymmetry corrected with the Lagrange multiplier.

Chapter 4

Transverse Asymmetry

The beam normal single spin asymmetry (BNSSA, also known as the transverse single spin asymmetry or transverse asymmetry) is different from the PV asymmetry, it is purely EM and therefore parity-conserving. It arises from the interference between the one-photon and two-photon exchanges (OPE and TPE), therefore it is sensitive to the TPE amplitude. By measuring it, we can probe the strength of the TPE, an important part of the electron elastic scattering that may explain the myth of the proton radius: the radius difference between measurements with different methods.

The transverse asymmetry is also an important systematic uncertainty to the PV asymmetry measurement, because there is always some residual transverse polarizations in the electron beam. With $\mathcal{A}_n \sim \alpha_{EM} m_e / E_e$, its magnitude of 10^{-5} (10 ppm) for a GeV level electron beam is much larger than \mathcal{A}_{PV} , so a complete understanding and precise measurement of the transverse asymmetry is needed to ensure the accuracy of \mathcal{A}_{PV} .

Being a routine and bonus of a PV experiment, PREX-I also measured the transverse asymmetry of some nuclei, namely 1H , 4He , ^{12}C and ^{208}Pb . Surprisingly, PREX-I saw a zero transverse asymmetry in ^{208}Pb , while the transverse asymmetries of other light nuclei agree with theoretical predictions, as shown in Fig. 4.1. One of the reason for PREX-II is that we want to verify the zero measurement in ^{208}Pb , which is still a puzzle to physicists.

As its name implies, BNSSA depends on only one spin, either the target or the electron beam. A polarized electron beam is better than a polarized target in that it is hard to polarize nuclei, especially heavy nuclei.

4.1 Motivation for the Transverse Asymmetry

The Scattering Theory

Consider the scattering of a free ($t_0 \rightarrow -\infty$) particle from a time independent potential $V(\mathbf{r})$, which decays quickly as $r \rightarrow \infty$. The evolution from the free initial state $|i\rangle$ is

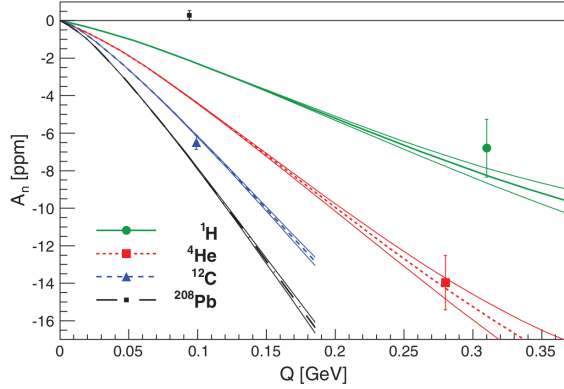


Figure 4.1: Transverse asymmetry measured in PREX-I [68].

denoted as $|\psi(t)\rangle_S$ (under the Schrödinger picture and $\hbar = 1$):

$$|\psi(t)\rangle_S = U(t) |\psi(t_0)\rangle = \lim_{t_0 \rightarrow -\infty} U(t, t_0) |i\rangle \quad (4.1)$$

where $U(t, t_0)$ is the evolution operator:

$$U(t, t_0) = \exp\left(\frac{1}{i}(H_0 + V)(t - t_0)\right) = \exp(-i(H_0 + V)(t - t_0)) \quad (4.2)$$

H_0 is the free Hamiltonian and $H = H_0 + V$ is the complete Hamiltonian with the interaction term.

The projection of $\psi(t)$ to a free final state $|f\rangle$ defines the so-called S-matrix (the order of the subscripts matters):

$$S_{if} \equiv \lim_{t \rightarrow +\infty} \langle f | \psi(t) \rangle = \lim_{t \rightarrow \infty} \lim_{t_0 \rightarrow -\infty} \langle f | U(t, t_0) | i \rangle \quad (4.3)$$

which defines the S operator:

$$S_{if} = \langle f | S | i \rangle \implies S = U(+\infty, -\infty) \quad (4.4)$$

The S-matrix describes the scattering amplitude from a free initial state $|i\rangle$ to a free final state $|f\rangle$. Conservation of the probability indicates unitarity of the S matrix:

$$S^\dagger S = \sum_f |\langle f | U(+\infty, -\infty) | i \rangle|^2 = 1 \quad (4.5)$$

It is easier to evaluate $U(t)$ in the interaction picture. Define

$$|\psi(t)\rangle_I \equiv \exp\left(-\frac{1}{i}H_0t\right) |\psi(t)\rangle_S = \exp(iH_0t) \exp(-i(H_0 + V)t) |i\rangle \quad (4.6)$$

The subscript I and S denote the interaction and Schrödinger picture respectively. The evolution of $|\psi(t)\rangle_I$ is:

$$\begin{aligned}
\frac{d}{dt} |\psi(t)\rangle_I &= [\exp(iH_0t)(iH_0) \exp(-i(H_0 + V)t) + \exp(iH_0t)(-i)(H_0 + V) \exp(-i(H_0 + V)t)] |\psi(t)\rangle_I \\
&= -i \exp(iH_0t) V \exp(-i(H_0 + V)t) |\psi(t)\rangle_I \\
&= -i \exp(iH_0t) V \exp(-iH_0t) \cdot \exp(iH_0t) \exp(-i(H_0 + V)t) |\psi(t)\rangle_I \\
&= -i V_I(t) |\psi(t)\rangle_I
\end{aligned} \tag{4.7}$$

where $V_I(t) = \exp(iH_0t)V \exp(-iH_0t)$ is the time dependent interaction term. Eq. 4.7 leads to the Dyson series:

$$U(t, t_0) = 1 - i \int_{t_0}^t dt_1 V_I(t_1) U(t_1, t_0) = \sum_{n=0}^{\infty} \frac{(-i)^n}{n!} \int_{t_0}^t dt_1 \cdots \int_{t_0}^t dt_n T[V_I(t_1) \cdots V_I(t_n)] \tag{4.8}$$

T means the time-ordering:

$$T(V_I(t_1)V_I(t_2)) \equiv \begin{cases} V_I(t_1)V_I(t_2) & t_1 \leq t_2 \\ V_I(t_2)V_I(t_1) & t_2 \leq t_1 \end{cases} \tag{4.9}$$

With Eq. 4.8, we have an iterative expression:

$$\begin{aligned}
\langle f | U(t, t_0) | i \rangle &= \langle f | i \rangle - i \langle f | \int_{t_0}^t dt_1 V_I(t_1) U(t_1, t_0) | i \rangle \\
&= \delta_{if} - i \sum_m \int_{t_0}^t dt_1 \langle f | \exp(iH_0t_1) V \exp(-iH_0t_1) | m \rangle \langle m | U(t_1, t_0) | i \rangle \\
&= \delta_{if} - i \sum_m \langle f | V | m \rangle \int_{t_0}^t dt_1 \exp(i(E_f - E_m)t_1) \langle m | U(t_1, t_0) | i \rangle
\end{aligned} \tag{4.10}$$

Truncate Eq. 4.10 into the first order ($\langle m | U(t_1, t_0) | i \rangle = \delta_{im}$) and define $T_{if} = \langle f | V | i \rangle$, we write:

$$\langle f | U(t, t_0) | i \rangle = \delta_{if} - iT_{if} \int_{t_0}^t dt_1 \exp(i(E_f - E_i)t_1) \tag{4.11}$$

and

$$\begin{aligned}
S_{if} &= \lim_{t \rightarrow +\infty} \lim_{t_0 \rightarrow -\infty} \langle f | U(t, t_0) | i \rangle \\
&= \delta_{if} - iT_{if} \int_{-\infty}^{\infty} dt_1 \exp(i(E_f - E_i)t_1) \\
&= \delta_{if} + i2\pi\delta(E_f - E_i)T_{if}
\end{aligned} \tag{4.12}$$

In the matrix form:

$$S = 1 + i2\pi T \tag{4.13}$$

S being unitary implies

$$S^\dagger S = (1 - i2\pi T^\dagger)(1 + i2\pi T) = 1 + i2\pi(T - T^\dagger) + (2\pi)^2 T^\dagger T = 1 \quad (4.14)$$

which reads

$$T - T^\dagger = i(2\pi)T^\dagger T = i(2\pi)TT^\dagger \quad (4.15)$$

In terms of the matrix element:

$$\begin{aligned} \delta(E_f - E_i)(T_{if} - T_{if}^\dagger) &= \sum_m i2\pi\delta(E_f - E_m)\delta(E_m - E_i)T_{fm}T_{mi}^\dagger \\ T_{if} - T_{if}^\dagger &= \sum_m i2\pi\delta(E_m - E_i)T_{fm}T_{mi}^\dagger = ia_{if} \end{aligned} \quad (4.16)$$

where

$$a_{if} = \sum_m (2\pi)\delta(E_m - E_i)T_{fm}T_{mi}^\dagger \quad (4.17)$$

is the absorptive part of the transition amplitude T_{if} . $|m\rangle$ extends to all on-shell intermediate states.

The two parts of S are easy to understand. The constant piece denotes the evolution of one free particle into another free particle without any interactions; obviously, it can evolve only into itself. The T matrix describes the interaction (transition amplitude) between the free initial particle $|i\rangle$ and the free final particle $|f\rangle$, which tells the interaction cross section.

A free particle state can be completely described by its momentum \mathbf{p} (ignoring the spin for now). For an incoming electron $|\mathbf{p}_i\rangle$, the probability to transform into the final state of $|\mathbf{p}_f\rangle$ is:

$$dP = (\text{phase space}) \times (\text{transition probability}) = \frac{d\mathbf{p}_f}{(2\pi)^3} \times |S_{\mathbf{p}_i\mathbf{p}_f}|^2 \quad (4.18)$$

For a non trivial case of $|f\rangle \neq |i\rangle$, we have:

$$S_{if} = i2\pi\delta(E_f - E_i)T_{if} \quad (4.19)$$

The differential cross section will be:

$$d\sigma = \frac{dP}{\mathcal{L}\Delta t} \quad (4.20)$$

where \mathcal{L} is the luminosity, indicating number of particles hitting the target per unit area per unit time, in our case of incoming plane wave, $\mathcal{L} = \rho v = v$, and Δt is the interaction time.

$$d\sigma = \frac{1}{v\Delta t} \frac{d\mathbf{p}_f}{(2\pi)^3} 2\pi\delta(E_f - E_i) 2\pi\delta(E_f - E_i)|_{E_f=E_i} |T_{if}|^2 \quad (4.21)$$

Transform one δ expression back to the integrating form:

$$2\pi\delta(E_f - E_i)|_{E_f=E_i} = \int_{-\infty}^{+\infty} dt \exp(-i(E_f - E_i)t)|_{E_f=E_i} = \int_{-\infty}^{+\infty} dt \quad (4.22)$$

Physically, we don't go back or into infinity in time, because the real particle is a finite wave packet rather than a plane wave. The integration above should be finite and close to the interaction time

$$\int_{-\infty}^{+\infty} dt \rightarrow \Delta t \quad (4.23)$$

Thus we have a defined cross section

$$d\sigma = \frac{1}{v} \frac{d\mathbf{p}_f}{(2\pi)^3} 2\pi\delta(E_f - E_i)|T_{if}|^2 \quad (4.24)$$

The cross section is proportional to $|T_{if}|^2$, as already known to us.

T-Symmetry

Time symmetry is an important discrete symmetry, which states that physical laws should keep unchanged under the time reversal operation. Time reversal is the operation that flips the time arrow, so that time runs backward after time reversal. Obviously, vectors that are first order derivatives of time will also reverse sign, such as the momentum, angular momentum and magnetic field.

Express the time reversal operation with QM:

$$|\tilde{\psi}\rangle = \hat{\mathcal{T}}|\psi\rangle \quad (4.25)$$

where $\hat{\mathcal{T}} : t \rightarrow -t$ is the time reversal operator.

In terms of the scattering discussed above, a particle will flip its momentum and spin (angular momentum) under the time reversal, and pick up a phase.

$$|\tilde{\psi}\rangle = \hat{\mathcal{T}}|\psi_{\uparrow}(\mathbf{k})\rangle = \eta|\psi_{\downarrow}(-\mathbf{k})\rangle \quad (4.26)$$

η is the phase difference and $|\eta|^2 = 1$ (two times of the time reversal operation should transform a state back to itself.). The the T matrix in terms of the time reversed states is:

$$T_{\tilde{i}\tilde{f}} = \langle \tilde{f} | V | \tilde{i} \rangle \quad (4.27)$$

It is well known that the EM interaction is invariant under time reversal.

$$|T_{if}|^2 = |T_{\tilde{f}\tilde{i}}|^2 \quad (4.28)$$

With these concepts, one can also define the T-odd quantities which are proportional

to the difference of the magnitude of a normal T element and its time reversed version:

$$\begin{aligned}
T\text{-odd} &\propto |T_{if}|^2 - |T_{\tilde{i}\tilde{f}}|^2 \\
&= |T_{if}|^2 - |T_{fi}|^2 \\
&= |T_{if}|^2 - |T_{if}^\dagger|^2 \\
&= |T_{if}|^2 - |T_{if} - ia_{if}|^2 \\
&= -i(T_{if}a_{if}^* - T_{if}^*a_{if}) - |a_{if}|^2 \\
&= 2\text{Im}(T_{if}a_{if}^*) - |a_{if}|^2
\end{aligned} \tag{4.29}$$

Transverse Asymmetry

Denote the incoming and outgoing transversely polarized electron as $|\mathbf{k}\rangle$ and $|\mathbf{k}'\rangle$, the scattering is shown in Fig. 4.2.

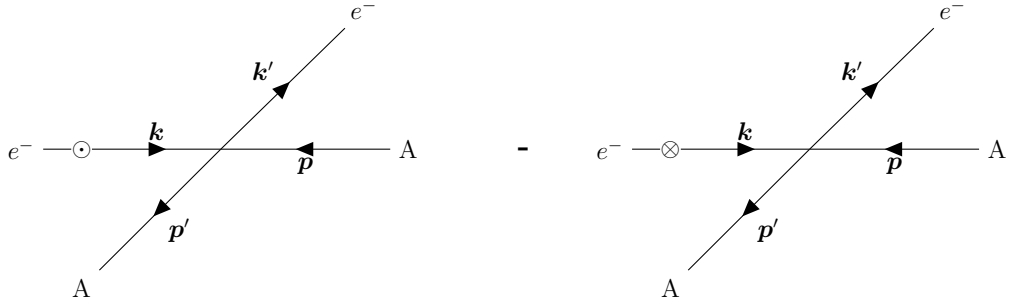


Figure 4.2: Feynman diagrams of a transversely polarized electron scatters off an unpolarized nuclear target in the COM frame. The vector in or out of the plane indicates the electron's spin direction.

The transverse asymmetry will be:

$$\mathcal{A}_n \equiv \frac{N_\uparrow - N_\downarrow}{N_\uparrow + N_\downarrow} = \frac{|T_\uparrow(\mathbf{k}, \mathbf{k}')|^2 - |T_\downarrow(\mathbf{k}, \mathbf{k}')|^2}{|T_\uparrow(\mathbf{k}, \mathbf{k}')|^2 + |T_\downarrow(\mathbf{k}, \mathbf{k}')|^2} \tag{4.30}$$

where $T(\mathbf{k}, \mathbf{k}') = \langle \mathbf{k}' | V | \mathbf{k} \rangle$ is the scattering amplitude and the arrow subscript indicates electron's spin direction. $T_\downarrow(\mathbf{k}, \mathbf{k}')$ is related to $T_\downarrow(-\mathbf{k}, -\mathbf{k}')$ by a rotation around the normal direction of the scattering plane, as shown in Fig. 4.3

$$T_\downarrow(\mathbf{k}, \mathbf{k}') = e^{i\pi} T_\downarrow(-\mathbf{k}, -\mathbf{k}') \tag{4.31}$$

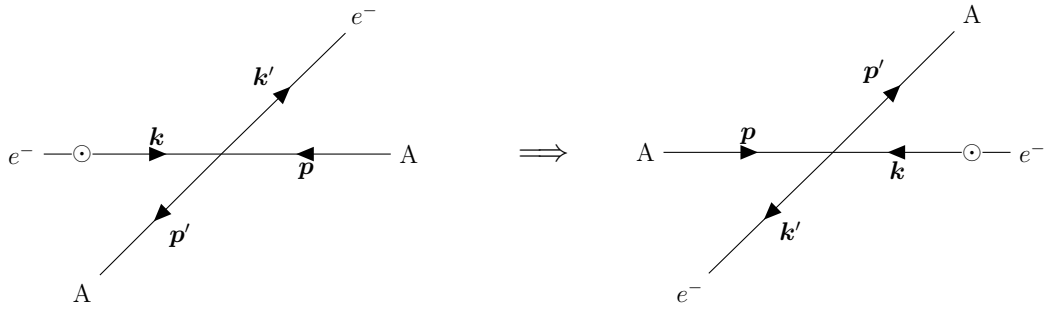


Figure 4.3: Rotation by π around the normal direction of the scattering plane.

Let $T_{if} = T_{\uparrow}(\mathbf{k}, \mathbf{k}')$, then $T_{\tilde{i}\tilde{f}} = T_{\downarrow}(-\mathbf{k}, -\mathbf{k}')$ and

$$\begin{aligned}
 \mathcal{A}_n &\approx \frac{|T_{\uparrow}(\mathbf{k}, \mathbf{k}')|^2 - |T_{\downarrow}(-\mathbf{k}, -\mathbf{k}')|^2}{2|T_{\uparrow}(\mathbf{k}, \mathbf{k}')|^2} \\
 &= \frac{|T_{if}|^2 - |T_{\tilde{i}\tilde{f}}|^2}{2|T_{if}|^2} \\
 &= \frac{2\text{Im}(T_{if}a_{if}^*) - |a_{if}|^2}{2|T_{if}|^2}
 \end{aligned} \tag{4.32}$$

We see that the transverse asymmetry is a T-odd quantity. For the EM interaction

$$T_{if} \propto \alpha \quad a_{if} \propto \alpha^2 \tag{4.33}$$

Because $\alpha \simeq \frac{1}{137}$ is small, we can expand Eq. 4.32 in order of α . To the lowest order

$$\mathcal{A}_n = 0 \tag{4.34}$$

and to the first order

$$\mathcal{A}_n = \frac{\text{Im}(T_{if}a_{if}^*)}{|T_{if}|^2} \tag{4.35}$$

T_{ij} represents the OPE interaction while a_{ij} represents the TPE interaction. So the physical interpretation of Eq. 4.34 and 4.35 is that the time symmetry requires the transverse asymmetry to be zero under the Born approximation (OPE only) and the (lowest order) non-zero transverse asymmetry comes from the interference between OPE and TPE.

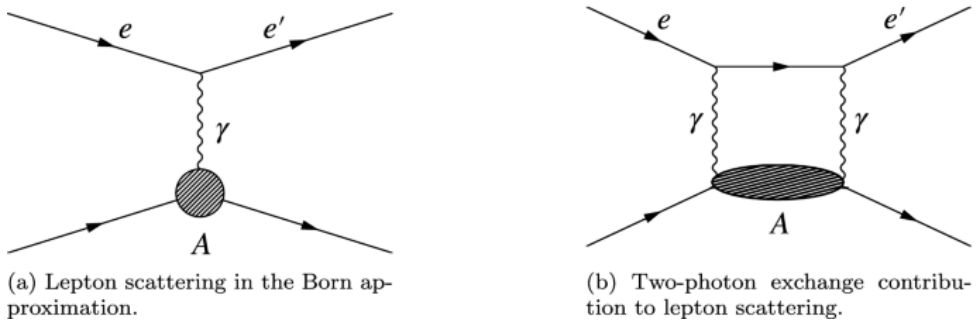


Figure 4.4: Feynman diagrams of the OPE (left) and TPE (right).

4.2 Measurement of the Transverse Asymmetry: the Method

The experimentally measured transverse asymmetry will be

$$\mathcal{A}_{\text{mea}} = \mathcal{A}_n \mathcal{P}_e \cdot \hat{n} = \mathcal{A}_n \mathcal{P}_n \sin(\phi_s - \phi_e) = \mathcal{A}_n \mathcal{P}_n \sin \phi \quad (4.36)$$

where \mathcal{P}_e is the electron spin vector, whose magnitude is the polarization, and \mathcal{P}_n being its transverse component, ϕ_s being its angle w.r.t. the lab horizontal plane; $\hat{n} = \frac{\mathbf{k} \times \mathbf{k}'}{|\mathbf{k} \times \mathbf{k}'|}$ is the unit normal vector of the scattering plane and ϕ_e the angle between the scattering plane and the horizontal plane. As shown in Fig. 4.5. So $\phi = \phi_s - \phi_e$ is the angle between the spin vector and the scattering plane.

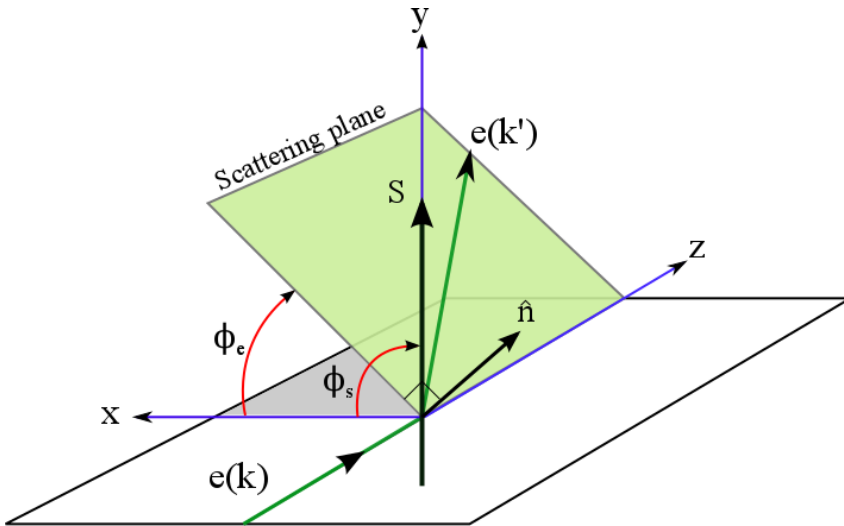


Figure 4.5: Schematic plot of the scattering of a transversely polarized electron.

Eq. 4.36 shows the angle dependence of the transverse asymmetry. Experimentally, it is convenient to select the angle ϕ being 90° . With the lab horizontal plane as the scattering plane, the electron spin will be vertical, being perpendicular to the scattering

Exp (Energy)	Target	$\langle \theta \rangle (\circ)$	$\langle Q^2 \rangle (\text{GeV}^2)$	$\langle \sin \phi \rangle$
PREX-II (0.95 GeV)	^{12}C	4.87	0.0067	0.967
	^{40}Ca	4.81	0.0067	0.964
	^{208}Pb	4.69	0.0064	0.966
CREX (2.18 GeV)	^{12}C	4.77	0.033	0.969
	^{40}Ca	4.55	0.031	0.970
	^{48}Ca	4.53	0.031	0.970
	^{208}Pb	4.60	0.032	0.969

Table 4.1: Dynamics of the AT measurement in PREX-II/CREX.

plane, as done in PREX-II and CREX. Detailed dynamics for the AT measurement are listed in Table 4.1.

To achieve the transverse polarization, a different configuration of the double wien filters is needed. Specifically, we just rotate the spin to the vertical direction using the vertical wien filter, the following rotations we do for the longitudinal polarization, as shown in Fig. 2.15, are omitted (the spin solenoid's rotating angle is set to 0°). Because the spin is parallel/anti-parallel to the magnetic field in the accelerator arc area, there is no spin precession as in the case of the longitudinal polarization.

In terms of the measurement of the transverse polarization, neither Moller, nor Compton polarimeter is used, because their analyzing powers go to 0 at the limit of transverse polarization. Without a direct measurement of the polarization in the hall, we turn to the Mott polarimeter in the injector. As said above, the beam transportation from injector to Hall A is symmetric and flat, which means the vertical component of the polarization is preserved (can be safely assumed $> 99.9\%$), so the measurement in the injector can be used as that in the hall.

Except the difference in the configuration of the double wien filters, everything else is the same as in the case of the longitudinal polarization (the Compton Chicane is off).

Polarization Measurement

The 5 MeV Mott polarimter is used to verify the transverse polarization, which gives about 87% transverse polarization for both PREX-II and CREX runs. The Mott data is summarized in Table 4.2.

The actual value we use for the transverse asymmetry calculation is the average longitudinal polarization measured shortly before and after the AT runs, with confidence in our pretty wien filter settings and that the accelerator won't change the beam transverse polarization. The polarization result is shown in Table 4.3

4.3 Data

We spent 1 (2) days in PREX-II (CREX) for the transverse asymmetry measurement, and collected 25 (56) good AT runs in PREX-II (CREX).

exp	run	IHWP	UD (%)	LR (%)	Vertical Pol (%)
PREX-II	8966	OUT	0.0704732 ± 0.435101	-34.193 ± 0.418556	-87.2048
	8967	IN	0.421465 ± 0.432328	33.9616 ± 0.419132	86.6146
CREX	9081	IN	-1.16128 ± 0.334165	-34.1276 ± 0.325363	-87.0380
	9082	OUT	-0.105704 ± 0.328932	34.0755 ± 0.324116	86.9051
	9083	IN	-0.613295 ± 0.333657	-34.3502 ± 0.32453	-87.6057
	9084	OUT	-0.0248337 ± 0.326988	34.4674 ± 0.318313	87.9046
	9085	IN	-1.15795 ± 0.33341	-34.0401 ± 0.32742	-86.8148

Table 4.2: Mott measurements during PREX-II and CREX AT runnings. The Up-Down asymmetry measures the horizontal transverse polarization while the Left-Right asymmetry measures the vertical transverse polarization; The Mott analyzing power is $\mathcal{A}_{\text{Mott}} = 0.3921 \pm 0.0016$, so the vertical polarization is $\frac{\mathcal{A}_{\text{LR}}}{\mathcal{A}_{\text{Mott}}}$.

Exp	Compton (%)	Moller (%)	P_n (%)
PREX-II	88.5533 ± 0.447	89.67 ± 0.8	89.7 ± 0.8
CREX	86.67 ± 0.63	86.897 ± 0.778	86.8 ± 0.6

Table 4.3: Average Compton and Moller polarization measured near the AT runs. The PREX-II AT uses only the Moller result while the CREX one uses the average value of the Compton and the Moller measurements.

exp	target	IHWP	# runs	run number
PREX-II	^{12}C	IN	3	4106-4107, 4133
		OUT	4	4108-4109, 4131-4132
	^{208}Pb	IN	7	4115-4119, 4129-4130
		OUT	6	4110-4114, 4128
CREX	^{40}Ca	IN	3	4123-4125
		OUT	2	4126-4127
	^{48}Ca	IN	9	6344-6345, 6354-6355, 6380-6382, 6407-6408
		OUT	10	6346-6348, 6356-6357, 6383-6385, 6405-6406
	^{40}Ca	IN	7	6351-6352, 6394-6396, 6401-6402
		OUT	7	6349-6350, 6398-6400, 6403-6404
	^{12}C	IN	6	6361-6363, 6389-6391
		OUT	5	6359-6360, 6386-6388
	^{208}Pb	IN	7	6367-6371, 6377-6378
		OUT	5	6372-6376

Table 4.4: AT runs in PREX-II/CREX

4.3.1 Data Analysis

Using the data set after 2 respins and following the standard analysis procedure, the transverse asymmetry is extracted. As shown in Eq. 4.36, \hat{n} of the scattering plane for LHRs and RHRs are opposite to each other, so the measured transverse asymmetries

have opposite sign in LHR5/RHR5. To combine measurement from both arms, we use the asymmetry (double) difference, instead of the asymmetry average as in the main analysis. The asymmetry difference is defined as (up to a ‘-’ sign):

$$\mathcal{A}_{dd} = \frac{\mathcal{A}_L - \mathcal{A}_R}{2} \quad (4.37)$$

A simple cut of `ErrorFlag == 0` is applied to select good quadruplets (in PREX-II, run 4112 is a long run with its data split into two rootfiles, the second one contains only a small size of samples, therefore is ignored in our AT analysis. Besides, the first minirun of run 4117 is removed due to the large charge asymmetry in that minirun). The good quadruplets are first grouped into miniruns, the average of these miniruns for each target will be what we wanted. One can also extract the transverse asymmetry from the histogram filled with all quadruplets – the mulplot, whose mean value will be our final result. Statistically, there is no difference between these two methods, they use the same data set and weight each sample equivalently, so they can be used to cross check each other. The mulplots and minirun average plots for CREX ^{48}Ca are shown below in Fig. 4.6 and Fig. 4.7, as an example.

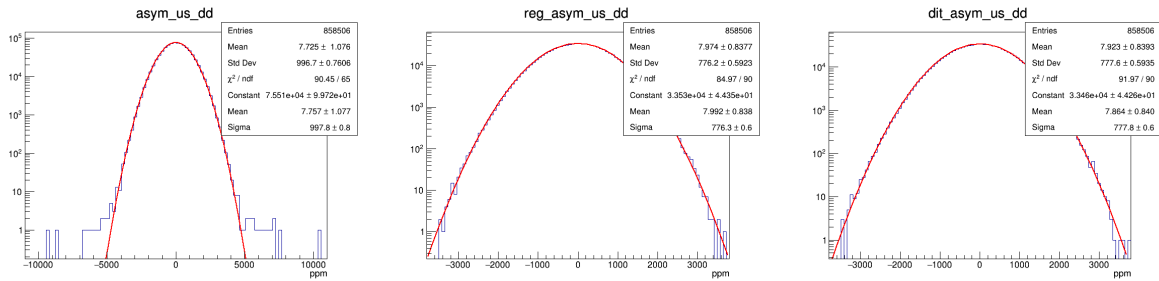


Figure 4.6: Mulplots for CREX ^{48}Ca . The red line is a Gaussian fit. One can clearly see how the false asymmetry correction reduces the width of the distribution (note that the first plot has a larger X-range than the other two).

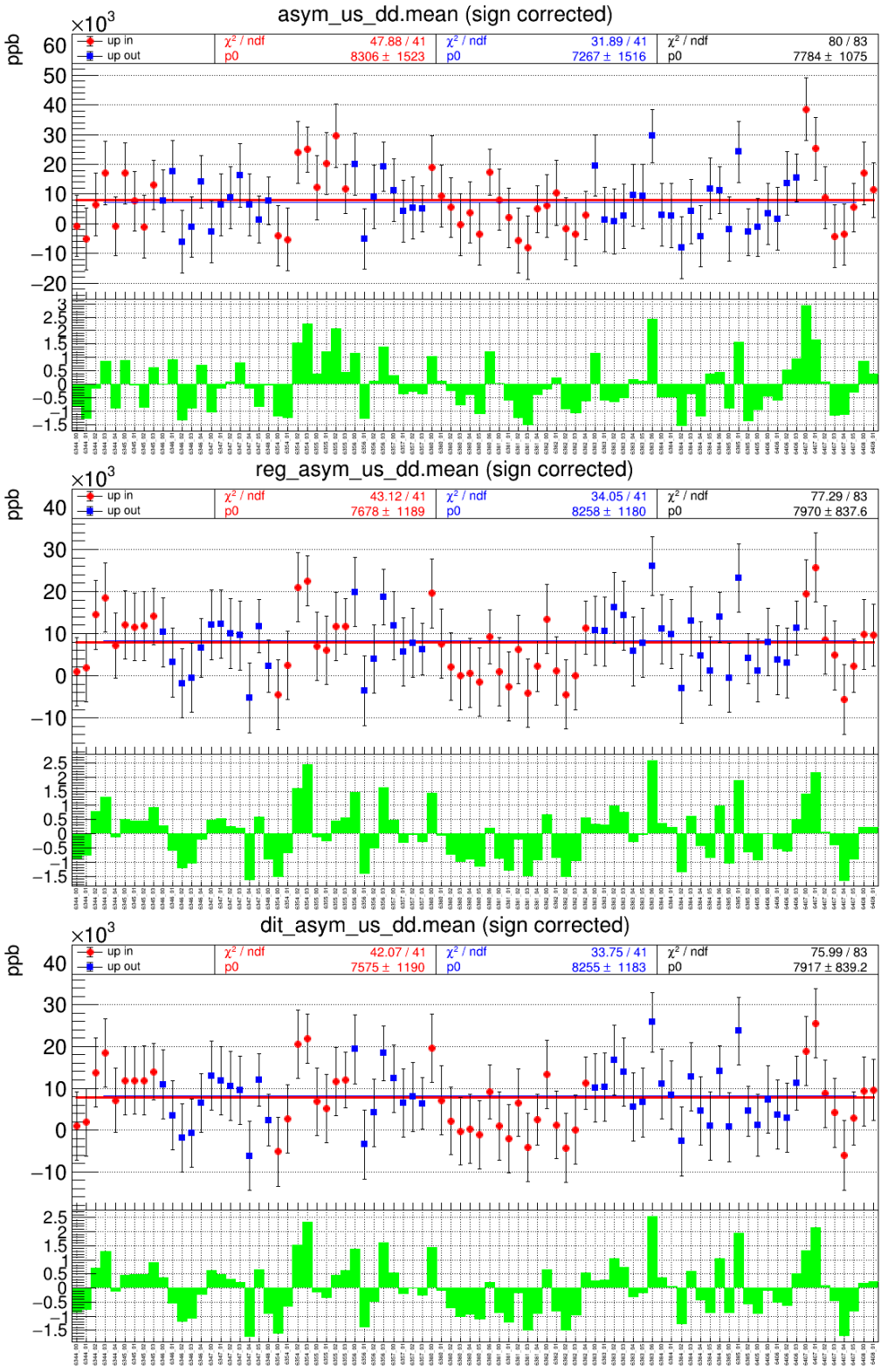


Figure 4.7: Sign corrected minirun-wise scatter plot of the raw, regression corrected and dithering corrected transverse asymmetry of ^{48}Ca in CREX. Different colors represent different IHWP states (in/out). In each plot, the top pad shows the mean and error of the title variable for each minirun, the three fit lines indicate the zero order polynomial fit to IHWP=in, IHWP=out and all datapoints respectively; the bottom pad is the pull histogram, which is the ratio of the deviation from the mean value of all datapoints over each datapoint's error.

The minirun mean and mulplot mean for each target are summarized in the following tables.

Target	Minirun Average (ppb)			Mulplot (ppb)		
	raw	reg	dit	raw	reg	dit
IHWP IN						
^{12}C	4205.3 ± 1113.7	5173.9 ± 501.5	5169.4 ± 502.2	4129.8 ± 1117.7	5105.0 ± 504.9	5103.5 ± 505.6
^{40}Ca	3055.8 ± 1762.8	5507.5 ± 419.3	5517.4 ± 420.7	2979.8 ± 1763.3	5501.8 ± 420.0	5511.7 ± 421.4
^{208}Pb	-266.2 ± 974.3	54.9 ± 183.5	27.6 ± 185.7	-381.0 ± 975.2	56.0 ± 183.5	22.4 ± 185.8
IHWP OUT						
^{12}C	6111.0 ± 992.8	5685.5 ± 437.4	5740.6 ± 437.9	6055.9 ± 995.8	5619.1 ± 440.1	5669.4 ± 440.6
^{40}Ca	5707.3 ± 1687.7	5069.0 ± 397.0	5093.7 ± 399.7	5775.6 ± 1687.8	5033.6 ± 396.7	5033.6 ± 399.2
^{208}Pb	-132.7 ± 927.4	-52.3 ± 176.1	-26.1 ± 178.7	data can't be reproduced due to lost of run 4112		
COMBINED						
^{12}C	5267.8 ± 740.8	5464.5 ± 329.6	5493.9 ± 330.0	5209.7 ± 743.5	5393.2 ± 331.8	5427.0 ± 332.2
^{40}Ca	4439.2 ± 1219.1	5276.3 ± 288.3	5294.7 ± 289.8	4444.9 ± 1219.7	5275.3 ± 288.5	5293.9 ± 290.0
^{208}Pb	-196.2 ± 671.8	-0.9 ± 127.0	-0.3 ± 128.8	data can't be reproduced due to lost of run 4112		

Table 4.5: PREX-II raw and corrected transverse asymmetry

Target	Minirun Average (ppb)			Mulplot (ppb)		
	raw	reg	dit	raw	reg	dit
IHWP IN						
^{12}C	6815.5 ± 1397.2	7767.7 ± 1182.2	7660.5 ± 1183.4	6885.1 ± 1397.9	7725.7 ± 1182.1	7618.8 ± 1183.3
^{40}Ca	8661.9 ± 1643.5	8777.5 ± 1265.2	8764.4 ± 1267.5	8581.7 ± 1645.3	8743.9 ± 1265.3	8733.3 ± 1267.6
^{48}Ca	8306.5 ± 1523.3	7677.5 ± 1188.9	7575.2 ± 1190.3	8275.7 ± 1524.9	7658.9 ± 1189.0	7553.5 ± 1190.3
^{208}Pb	2742.6 ± 2469.1	3052.4 ± 2285.9	3079.7 ± 2288.1	2771.1 ± 2469.6	3101.8 ± 2286.2	3129.9 ± 2288.3
IHWP OUT						
^{12}C	8607.9 ± 1558.2	8789.1 ± 1313.5	8791.5 ± 1314.6	8512.9 ± 1558.8	8778.2 ± 1313.6	8780.0 ± 1314.7
^{40}Ca	8023.6 ± 1751.5	7967.4 ± 1353.3	7994.2 ± 1355.0	8168.4 ± 1755.1	7960.2 ± 1353.4	7987.0 ± 1355.2
^{48}Ca	7267.1 ± 1516.3	8257.8 ± 1180.2	8254.7 ± 1183.3	7184.5 ± 1517.6	8267.8 ± 1180.3	8270.3 ± 1183.5
^{208}Pb	2089.1 ± 2456.4	2420.2 ± 2263.4	2456.9 ± 2266.2	2075.1 ± 2456.8	2401.2 ± 2263.8	2440.7 ± 2266.6
COMBINED						
^{12}C	7614.4 ± 1040.3	8224.8 ± 878.7	8166.8 ± 879.5	7600.8 ± 1040.8	8235.1 ± 878.8	8177.3 ± 879.6
^{48}Ca	8363.1 ± 1198.5	8399.7 ± 924.2	8405.0 ± 925.6	8377.3 ± 1200.4	8383.5 ± 924.3	8390.4 ± 925.7
^{48}Ca	7784.4 ± 1074.7	7969.8 ± 837.6	7916.9 ± 839.2	7725.4 ± 1075.7	7974.4 ± 837.7	7923.5 ± 839.3
^{208}Pb	2414.2 ± 1741.4	2733.1 ± 1608.4	2765.3 ± 1610.1	2422.6 ± 1741.7	2751.0 ± 1608.6	2784.8 ± 1610.4

Table 4.6: CREX raw and corrected transverse asymmetry

As shown in the above tables, the final result from the two false asymmetry correction methods – regression and dithering, agree with each other. We chose the dithering corrected values to extract the transverse asymmetry. The slug-wise plots of the transverse asymmetry are shown in Fig. 4.8

4.3.2 Systematic Uncertainties

Various corrections to the raw asymmetry will introduce corresponding uncertainties. Such as the beam false asymmetry correction, purity and detector/monitor non-linearity correction. These uncertainties affect the precision of the measurement, we should know them precisely.

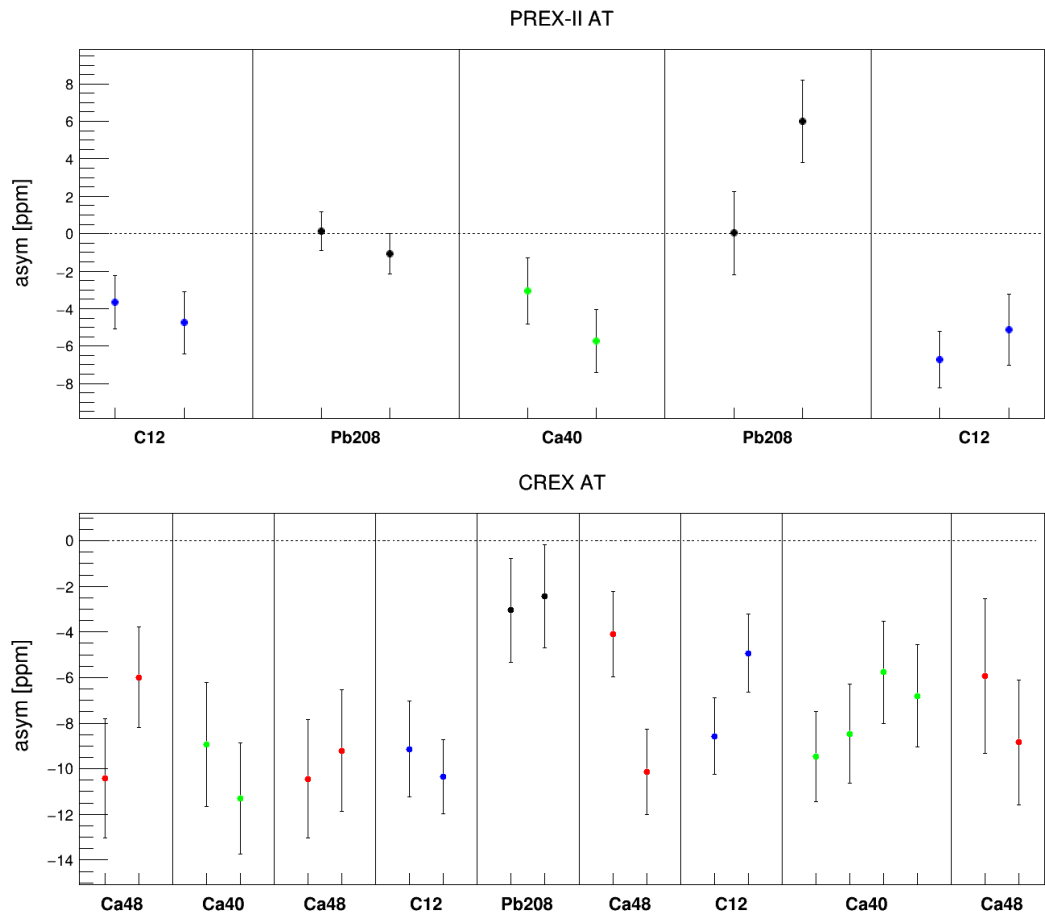


Figure 4.8: Sign corrected transverse asymmetry in chronological order. Each datapoint means one slug.

Beam Correction

To count the uncertainty caused by the beam correction, the difference between corrections with the regression and dithering methods is used. More specifically, we find that for most runs, the difference between the corrections from the most significant BPMs with these two methods is less than 5%. Therefore, a conservative estimate of 5% of the correction with dithering is used as the systematic uncertainty of the beam false asymmetry correction. The correction from each BPM (or their combinations) will be the product of the target-wise dithering slope and the average difference in each BPM (or their combinations), root-sum-square of 5% of these corrections give out the uncertainty. The result is shown in Table 4.7.

Purity Correction

For the target purity correction, we need to consider only the ^{208}Pb and ^{48}Ca target. As we will discuss in the following chapter, the contamination in the ^{208}Pb target come

Exp	Target	$\mathcal{A}_{\text{raw}} \pm d\mathcal{A}_{\text{raw}}$ (ppb)		$\mathcal{A}_{\text{dit}} \pm d\mathcal{A}_{\text{dit}}$ (ppb)		$\Delta\mathcal{A} \pm d(\Delta\mathcal{A})$ (ppb)		$d\Delta\mathcal{A}/d\mathcal{A}_{\text{dit}}$
PREX-II	^{12}C	-5268	741	-5494	330	226.1	29.4	9%
	^{40}Ca	-4439	1219	-5295	290	195.9	42.4	15%
	^{208}Pb	196.2	672	0.257	129	855.5	71.0	55%
CREX	^{12}C	-7614	1040	-8167	880	552.4	37.8	4%
	^{40}Ca	-8363	1198	-8405	926	351.1	48.9	5.3%
	^{48}Ca	-7784	1075	-7917	839	41.9	86.7	10%
	^{208}Pb	-2414	1741	-2765	1610	132.5	27.8	2%

Table 4.7: Beam correction to transverse asymmetry.

from the diamond foils sandwiching the ^{208}Pb foil to cool the target, while the impurity in ^{48}Ca target is mainly the ^{40}Ca isotope. The ^{40}Ca target has an abundance larger than 99.6%, so it is regarded as a pure target.

$$\begin{aligned} \mathcal{A}_{\text{mea}} &= \frac{R_t \mathcal{A}_t + \sum_i R_i \mathcal{A}_i}{R_t + \sum_i R_i} = \frac{\mathcal{A}_t + \sum_i f_i \mathcal{A}_i}{1 + \sum_i f_i} \\ \mathcal{A}_t &= (1 + \sum_i f_i) \mathcal{A}_{\text{mea}} - \sum_i f_i \mathcal{A}_i \end{aligned} \quad (4.38)$$

where R and \mathcal{A} are the scattering rate and asymmetry of each nucleus, the subscript t and i refer to the target and various impurity elements in the target, $f_i = \frac{R_i}{R_t}$ is the rate fraction. We use simulations to calculate the scattering rate for each different target, asymmetry value comes from the measurement. The diamond (C) rate fraction in the ^{208}Pb target is:

$$f_C = \frac{R_C}{R_{Pb}} = \begin{cases} 0.0671 \pm 0.0057 & E = 0.95 \text{ GeV} \\ 0.6089 \pm 0.0609 & E = 2.2 \text{ GeV} \end{cases} \quad (4.39)$$

The ^{48}Ca case is a little complicated, because the ^{48}Ca target is a stack of 3 different pieces with different purities. The upstream 2 pieces are the remnant of the damaged old target with a ^{48}Ca abundance of 95.99%, the downstream piece is a new foil with a ^{48}Ca abundance of 90.04%. Based on the fact that the contamination mainly come from various isotopes of ^{48}Ca : ^{40}Ca ($\sim 10\%$), ^{42}Ca ($\sim 0.1\%$) and ^{44}Ca ($\sim 0.2\%$), whose scattering rates and asymmetries are similar to that of ^{48}Ca , so we simplily count the non- ^{48}Ca fraction in the ^{48}Ca target, which leads to:

$$f\left(\frac{\text{non-}^{48}\text{Ca}}{^{48}\text{Ca}}\right) = 9.07 \pm 0.18\% \quad (4.40)$$

Using equation 4.38, the asymmetry after the purity correction is shown in Table 4.8

Exp	Target	$\mathcal{A}_{\text{cor}} \pm d\mathcal{A}_{\text{stat}}$ (ppb)
PREX-II	^{12}C	-5494 330
	^{48}Ca	-5295 290
	^{208}Pb	369 137
CREX	^{12}C	-8167 880
	^{40}Ca	-8405 926
	^{48}Ca	-7873 919
	^{208}Pb	523 2646

Table 4.8: Purity corrected transverse asymmetry. The statistical uncertainties are calculated following the uncertainty propagation equation.

Detector Non-linearity

For the uncertainty caused by the non-linearity in detector's response to the incoming electron flux, it is bounded to be $< 0.5\%$ in bench tests.

Exp	Target	\mathcal{A}_{raw} (ppb)	$d\mathcal{A}_{\text{sys}}$ (ppb)	$\frac{d\mathcal{A}_{\text{sys}}}{\mathcal{A}_{\text{raw}}}$
PREX-II	^{12}C	-5268	26	0.50%
	^{40}Ca	-4439	22	0.50%
	^{208}Pb	196.2	1	0.50%
CREX	^{12}C	-7614	38	0.50%
	^{40}Ca	-8363	42	0.50%
	^{48}Ca	-7784	39	0.50%
	^{208}Pb	-2414	12	0.50%

Table 4.9: Systematic uncertainty due to the detector non-linearity.

For uncertainty come from the BCM non-linearity, a conservative estimate of 1% is used, as shown in Table 4.10, the charge asymmetry is the minirun-wise average value.

Exp	Target	\mathcal{A}_q (ppb)	$d\mathcal{A}_q$ (ppb)	$\frac{d\mathcal{A}_q}{\mathcal{A}_q}$
PREX-II	^{12}C	-52.863	0.5	1.00%
	^{40}Ca	-104.763	1.0	1.00%
	^{208}Pb	140.602	1.4	1.00%
CREX	^{12}C	50.09	0.5	1.00%
	^{40}Ca	47.81	0.5	1.00%
	^{48}Ca	27.35	0.3	1.00%
	^{208}Pb	-1.61	0.0	1.00%

Table 4.10: Systematic uncertainty due to the BCM non-linearity

4.3.3 Dynamics

ϕ Angle

It is said above that we chose the angle ϕ to be 90° , but no way to achieve exactly that value. The actually value will be a little away from the designed value, as we measured from the data. By drawing the $\sin \phi$ distribution from data, the average from the distribution is taken as the measured value. The result is shown in the following table.

Exp	Target	LHRS $\sin \phi$	RHRS $\sin \phi$	average
PREX-II	^{12}C	0.96660	0.96700	0.9668
	^{40}Ca	0.96430	0.96440	0.9644
	^{208}Pb	0.96625	0.96665	0.9665
CREX	^{12}C	0.96950	0.96790	0.9687
	^{40}Ca	0.97090	0.96920	0.9701
	^{48}Ca	0.97110	0.96880	0.9700
	^{208}Pb	0.96980	0.96830	0.9691

Table 4.11: Average $\sin \phi$ values for different AT targets.

Q^2

Similar to the extraction of the ϕ angle, we draw the Q^2 distribution for each target, and then took the mean value. The results are shown in the following table.

Exp	Target	LHRS Q^2 (GeV 2)	RHRS Q^2 (GeV 2)	Average Q^2 (GeV 2)	Average Q (GeV)
PREX-II	^{12}C	$0.0068 \pm 4\text{E-}6$	$0.0066 \pm 5\text{E-}6$	$0.00671 \pm 3.21\text{E-}6$	$0.082 \pm 1.96\text{E-}5$
	^{40}Ca	$0.0068 \pm 5\text{E-}6$	$0.0067 \pm 6\text{E-}6$	$0.00673 \pm 4.17\text{E-}6$	$0.082 \pm 2.54\text{E-}5$
	^{208}Pb 8	$0.0065 \pm 5\text{E-}6$	$0.0063 \pm 6\text{E-}6$	$0.00640 \pm 4.06\text{E-}6$	$0.080 \pm 2.54\text{E-}5$
	^{208}Pb 9	$0.0065 \pm 4\text{E-}6$	$0.0063 \pm 5\text{E-}6$	$0.00640 \pm 3.50\text{E-}6$	$0.080 \pm 2.18\text{E-}5$
CREX	^{12}C	$0.0328 \pm 2\text{E-}5$	$0.0334 \pm 2\text{E-}5$	$0.0331 \pm 1.31\text{E-}5$	$0.182 \pm 3.61\text{E-}5$
	^{40}Ca	$0.0306 \pm 2\text{E-}5$	$0.0309 \pm 2\text{E-}5$	$0.0308 \pm 1.22\text{E-}5$	$0.175 \pm 3.48\text{E-}5$
	^{48}Ca	$0.0304 \pm 1\text{E-}5$	$0.0307 \pm 2\text{E-}5$	$0.0306 \pm 1.07\text{E-}5$	$0.175 \pm 3.05\text{E-}5$
	^{208}Pb	$0.0319 \pm 3\text{E-}5$	$0.0322 \pm 3\text{E-}5$	$0.0320 \pm 1.99\text{E-}5$	$0.179 \pm 5.56\text{E-}5$

Table 4.12: Average Q^2 values for different AT targets.

4.3.4 Final Result

With Eq. 4.36, the transverse asymmetry is calculated to be:

$$\mathcal{A}_n = \frac{\mathcal{A}_{\text{cor}}}{\mathcal{P}_n \cdot \sin \phi} \quad (4.41)$$

The statistical uncertainty is:

$$d\mathcal{A}_n(\text{stat}) = \frac{d\mathcal{A}_{\text{cor}}(\text{stat})}{\mathcal{P}_n \cdot \sin \phi} \quad (4.42)$$

and the systematic uncertainty is:

$$\left(\frac{d\mathcal{A}_n(\text{sys})}{\mathcal{A}_n} \right)^2 = \left(\frac{d\mathcal{A}_{\text{cor}}(\text{sys})}{d\mathcal{A}_{\text{cor}}} \right)^2 + \left(\frac{d\mathcal{P}_n}{\mathcal{P}_n} \right)^2 \quad (4.43)$$

where

$$d\mathcal{A}_{\text{cor}}^2(\text{sys}) = d\mathcal{A}^2(\text{det nonlin}) + d\mathcal{A}^2(\text{BCM nonlin}) + d\mathcal{A}^2(\text{beam correction}) \quad (4.44)$$

For the ^{208}Pb and ^{48}Ca target, we need to include uncertainties from contaminations. Various systematic uncertainties are summarized in Table 4.13.

Exp	PREX-II			CREX			
Target	^{12}C	^{40}Ca	^{208}Pb	^{12}C	^{40}Ca	^{48}Ca	^{208}Pb
Beam correction	0.03	0.05	0.08	0.04	0.06	0.10	0.03
Polarization	0.06	0.05	< 0.01	0.08	0.08	0.08	< 0.01
Non-linearity	0.03	0.03	< 0.01	0.05	0.05	0.05	0.01
Tgt. impurity	< 0.01	< 0.01	0.04	< 0.01	< 0.01	0.10	0.80
Inelastic	< 0.01	< 0.01	< 0.01	0.08	0.15	0.08	< 0.01
Tot. Syst	0.07	0.08	0.09	0.13	0.18	0.19	0.75
Statistical	0.38	0.34	0.16	1.05	1.10	1.09	3.15
Total	0.39	0.34	0.18	1.05	1.11	1.11	3.23

Table 4.13: AT uncertainty contributions in units of ppm

The final result is shown in Table 4.14:

Exp	Target	\mathcal{A}_n (ppm)	$d\mathcal{A}_{\text{stat}}$ (ppm)	$d\mathcal{A}_{\text{sys}}$ (ppm)	$d\mathcal{A}_{\text{stat+sys}}$ (ppm)
PREX-II	^{12}C	-6.34	0.38	0.07	0.39
	^{40}Ca	-6.12	0.34	0.08	0.34
	^{208}Pb	0.43	0.16	0.09	0.18
CREX	^{12}C	-9.71	1.05	0.10	1.05
	^{40}Ca	-9.98	1.10	0.11	1.11
	^{48}Ca	-9.35	1.09	0.17	1.11
	^{208}Pb	0.62	3.15	0.75	3.23

Table 4.14: Final result of the transverse asymmetry.

Comparing to the theoretical calculations [69], we confirm the anomaly appeared in PREX-I AT measurement, that is the ^{208}Pb transverse asymmetries are consistently 0 at

various Q values, as shown in Fig. 4.9. As for other light nuclei, they are not far away from their theoretical predictions.

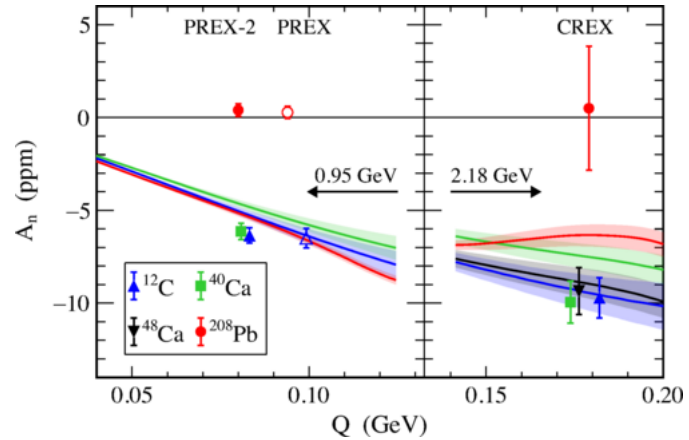


Figure 4.9: Transverse asymmetries measured in PREX-II/CREX. The PREX-I result is also included. Overlapping points are offset slightly in Q to distinguish them.

Chapter 5

Systematic Uncertainties

The systematic uncertainty control is a highlight of these two high-precision experiments. To achieve a smaller systematic uncertainty, a combination of the fast and slow helicity reversals are employed, which help to cancel many systematic uncertainties brought by the accelerator to the beam. Except the uncertainty from the machine, another important source of the systematic uncertainty is the detection process, namely the acceptance function.

After removing the false asymmetry from the beam, we proceed to correction of the background asymmetry, namely, the target contamination and the inelastic scattering, as shown in Eq. 5.1.

$$\mathcal{A}_{\text{PV}} = \frac{\mathcal{A}_{\text{cor}}/\mathcal{P} - \sum_i \mathcal{A}_i f_i}{1 - \sum_i f_i} \quad (5.1)$$

Here, i iterates through the background processes, \mathcal{A}_i and f_i refer to the asymmetry and rate fraction of a background process. The rate fraction is defined as:

$$f_i = \frac{R_i}{\sum_i R_i + R_{\text{Pb208}}} \quad (5.2)$$

with R being the scattering rate. In PREX-II, contamination from the diamond foils contributes the largest background correction.

Following the uncertainty propagation formula, the systematic uncertainty of \mathcal{A}_{PV} is:

$$(\delta \mathcal{A}_{\text{PV}})^2 = \left(\frac{\partial \mathcal{A}_{\text{PV}}}{\partial \mathcal{A}_{\text{cor}}} \delta \mathcal{A}_{\text{cor}} \right)^2 + \left(\frac{\partial \mathcal{A}_{\text{PV}}}{\partial \mathcal{P}} \delta \mathcal{P} \right)^2 + \sum_i \left[\left(\frac{\partial \mathcal{A}_{\text{PV}}}{\partial \mathcal{A}_i} \delta \mathcal{A}_i \right)^2 + \left(\frac{\partial \mathcal{A}_{\text{PV}}}{\partial f_i} \delta f_i \right)^2 \right] \quad (5.3)$$

with

$$\frac{\partial \mathcal{A}_{\text{PV}}}{\partial \mathcal{A}_j} = -\frac{f_j}{1 - \sum_i f_i} \quad \frac{\partial \mathcal{A}_{\text{PV}}}{\partial f_j} = \frac{\mathcal{A}_{\text{PV}} - \mathcal{A}_j}{1 - \sum_i f_i} \quad (5.4)$$

5.1 Q^2 and θ

Physical interpretation of \mathcal{A}_{PV} requires the precise knowledge of the scattering angle and corresponding Q^2 , which are determined using a watercell target. As shown in

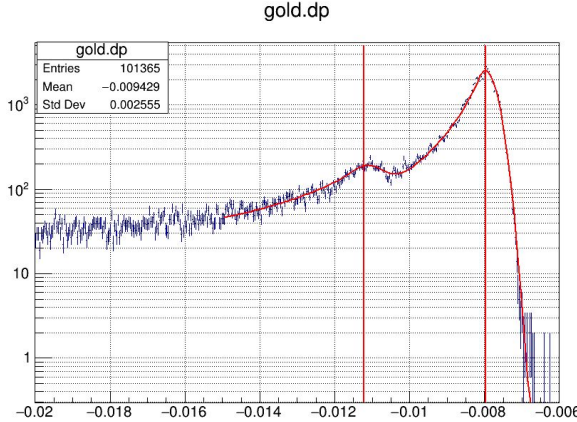


Figure 5.1: Momentum distribution of an optics run with the watercell target. The X-axis is the relative energy difference: $dp = \frac{p-p_0}{p_0}$. The two peaks result from ^1H (left) and ^{16}O (right), respectively. Plot from Siyu.

Eq. 1.98, the energy difference between the two elastic peaks of ^1H and ^{16}O is:

$$\Delta E' = E'_O - E'_H = E \left(\frac{1}{1 + \frac{E(1-\cos\theta)}{M_O}} - \frac{1}{1 + \frac{E(1-\cos\theta)}{M_H}} \right) \quad (5.5)$$

By reconstructing the momentum distribution from the watercell target, as shown in Fig. 5.1, the peak energy difference and therefore the scattering angle can be extracted. The advantage of the watercell target, compared with the production target, is that the energy difference between the two elastic peaks cancels many uncertainties due to the electron detection and trajectory reconstruction, therefore being more precise.

5.2 Carbon Contamination in PREX-II

As discussed in Chapter 2, the low thermal conductivity of the ^{208}Pb foil limits the highest beam current we can apply. With the pure ^{208}Pb foil, it will melt at $\sim 10 \mu\text{A}$. With the help of the surrounding diamond foils, the ^{208}Pb target could tolerate up to $\gtrsim 100 \mu\text{A}$. Besides, ^{12}C is an isoscalar, and spin-0 nucleus, whose PV asymmetry is well-measured, so the background is well understood.

In terms of the ^{48}Ca target in CREX, without the need of the auxiliary materials, the contamination mainly come from ^{40}Ca , which is also an isoscalar and spin-0 nucleus, so the background is benign.

Target Thickness

The ^{208}Pb foil is 0.5 mm thick, the upstream and downstream diamond foils have thicknesses of half the ^{208}Pb foil, as shown in Table 5.1.

The thickness of the target foils are measured in different ways. The diamond foil is measured directly using calipers with an accuracy of 0.0005 in (0.0127 mm). Given the thickness of diamond foils being 1 in (0.255 mm), an estimate of 5% relative error is reasonable. Foil to foil variations are smaller than 5% (the largest variation is 3.6%), as shown in Table 5.1.

As for the ^{208}Pb foil, its thickness (area density) is inferred from its mass (m) and area (A):

$$\rho t = \frac{m}{A} \quad (5.6)$$

where ρ and t being the density and thickness, respectively. The area is calculated from the measurement of the four corners of the ^{208}Pb foil, which means the resulted thickness is an average over the whole foil. While the raster area doesn't occupy the whole foil, this is a source of the uncertainty. The small irregularity in the edge (corner) is another error source. With these considerations and taking into account the thickness variations from foil to foil (the largest variation being 3.8%), a conservative estimate of 5% is used as the relative uncertainty of the thickness of the ^{208}Pb foil.

Simulation

In the simulation, the ^{208}Pb foil thickness is set to 0.552 mm (628.176 mg/cm²), the upstream diamond foil 0.2554 mm (89.9008 mg/cm²) and the downstream diamond foil 0.2556 mm (89.9712 mg/cm²). The central point angle being 4.74°, and the raster size is 6 mm × 4 mm. Only simple cuts are applied to the simulation, as shown in the following code snippet.

```
xcol != -333 && xvdc != -333 // collimator and vdc see the track
&& CollimatorL(xcol, ycol) // Q1 collimator geometry cut
&& (nuclA == 12 || nuclA == 208) // select only C or Pb208
&& Pz_peak- Pz < pcut // radiative tail cut; cut only on lower side
```

where P_z is the post target electron momentum and $P_z\text{_peak}$ (948.97 MeV) is the momentum peak without the momentum cut; other cuts are explained in the code block.

position	target	Upstream (mg/cm ²)	Center (mg/cm ²)	Downstream (mg/cm ²)	runs
1	C-Pb-C	88	556	88	
2	D#I-Pb-D#J	90	557	90	
3	C-208Pb#1-C	88	620	88	
4	Carbon 1%		445		
5	D#A-208Pb#2-D#B	89.0	632	88.6	3134-3636
6	D#C-208Pb#3-D#D	88.2	626	90.7	
7	D#E-208Pb#4-D#F	89.6	628	91.9	
8	D#G-208Pb#5-D#20	86.8	632	90	4372-4607
9	D#1-208Pb#6-D#2	90	618	90	4865-4980
10	D#3-208Pb#7-D#4	90	639	90	4608-4864
11	D#5-208Pb#8-D#6	90	620	90	4147-4370
12	D#7-208Pb#9-D#8	90	615	90	3822-4146
13	D#9-208Pb#10-D#10	90	623	90	3644-3821
14	C-Hole		N/A		
15	⁴⁸ Ca		1016		
16	⁴⁰ Ca		1004		

Table 5.1: Mass thickness of each target in the production ladder. Name convention: upstream material#label - central material#label - downstream material#label. Pb208 foils count from 1 to 10, diamond foils count 1-10, A-G, I, J, 20. The first two Pb targets are natural Pb foils, not the pure ^{208}Pb isotope foil. The third Pb target is sandwiched by graphite, not diamond. Red color marks out the targets used in PREX-II and CREX. To convert the mass thickness into the real thickness, use the density of $\rho_D = 3.52 \text{ g/cm}^3$ and $\rho_{\text{Pb}208} = 11.38 \text{ g/cm}^3$.

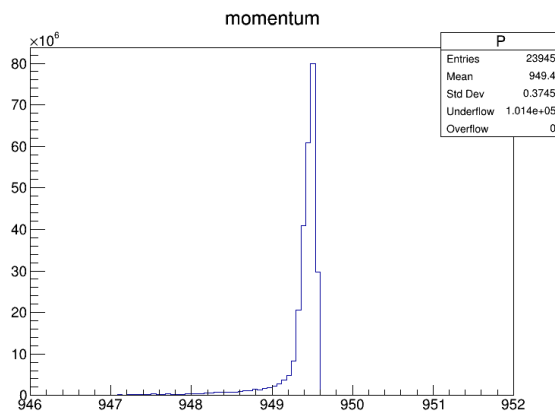


Figure 5.2: Post target electron momentum distribution. The lower end tail comes from multi-scattering and radiation.

With these cuts, we can count the scattering rate from ^{12}C and ^{208}Pb directly and

calculate the ratio between them, which is:

$$\frac{R_C}{R_{Pb}} = 6.71\% \quad f_C = \frac{R_C}{R_C + R_{Pb}} = 6.29\% \quad (5.7)$$

To study the systematic uncertainty, we varied the thickness of the ^{208}Pb and diamond foils (total thickness) by 5% from the nominal value, and applied different momentum cuts (varied from 1.8 to 2.6 MeV), the result is shown in Table 5.2 and 5.3.

^{208}Pb thickness variation	C thickness variation	p cut (MeV)	C rate (MHz)	^{208}Pb rate (MHz)	$\frac{R_C}{R_{Pb}}\text{ (%)}$	$f_c = \frac{R_C}{R_C + R_{Pb}}\text{ (%)}$
-5%	-5%	2.2	1.26E+2	1.88E+3	6.72	6.30
-5%	0%		1.34E+2	1.90E+3	7.05	6.59
-5%	5%		1.38E+2	1.90E+3	7.23	6.75
0%	-5%		1.22E+2	1.90E+3	6.43	6.04
0%	0%		1.29E+2	1.93E+3	6.71	6.29
0%	5%		1.35E+2	1.89E+3	7.11	6.64
5%	-5%		1.16E+2	1.95E+3	5.94	5.61
5%	0%		1.22E+2	1.94E+3	6.31	5.93
5%	5%		1.28E+2	1.91E+3	6.72	6.30

Table 5.2: Scattering rate from ^{208}Pb and diamond foils with different foil thicknesses.

^{208}Pb thickness variation	C thickness variation	p cut (MeV)	C rate (MHz)	^{208}Pb rate (MHz)	$\frac{R_C}{R_{Pb}}\text{ (%)}$	$f_c\text{ (%)}$
0%	0%	1.80	1.24E+2	1.86E+3	6.68	6.26
		1.90	1.25E+2	1.87E+3	6.69	6.27
		2.00	1.27E+2	1.89E+3	6.70	6.28
		2.05	1.27E+2	1.90E+3	6.70	6.28
		2.10	1.28E+2	1.91E+3	6.71	6.28
		2.15	1.29E+2	1.92E+3	6.71	6.29
		2.20	1.29E+2	1.93E+3	6.71	6.29
		2.25	1.30E+2	1.94E+3	6.72	6.30
		2.30	1.31E+2	1.95E+3	6.73	6.30
		2.35	1.31E+2	1.95E+3	6.73	6.31
		2.40	1.32E+2	1.96E+3	6.74	6.32
		2.60	1.34E+2	1.99E+3	6.74	6.32

Table 5.3: Scattering rate from ^{208}Pb and diamond foils with different momentum cuts.

The uncertainty for each variation is taken to be the absolute difference from the nominal value, as shown below:

Based on Table 5.4, a conservative error value (the larger one) is used , which gives out the final value of f_C

$$f_C = 0.0629 \pm 0.005 \quad (5.8)$$

variation	maximum	diff in f_C	minimum	diff in f_C
Pb	(-5, 0) - (0, 0)	2.98E-3	(+5, 0) - (0, 0)	-3.55E-3
C	(0, +5) - (0, 0)	3.53E-3	(0, -5) - (0, 0)	-2.49E-3
pcut	(2.6) - (2.2)	2.93E-4	(1.8) - (2.2)	-2.88E-4
total		4.63E-3		4.35E-3

Table 5.4: The maximum and minimum difference for each variation. (n1, n2) represents the configuration of the target foils thicknesses. n1 for the Pb foil and n2 for the C foil.

The goodness of the simulation can be checked by comparison with the optics data.

target thickness	p cut	(MeV)	post target Q^2 (GeV 2)				Asym (ppm)	
			Pb	C	C (US)	C (DS)	Pb	C
-5%	-5%	2.2	0.00625	0.00658	0.00658	0.00658	0.55774	0.53861
-5%	0%	2.2	0.00626	0.00656	0.00658	0.00654	0.55809	0.53776
-5%	5%	2.2	0.00627	0.00658	0.00658	0.00657	0.55883	0.53932
0%	-5%	2.2	0.00627	0.00657	0.00657	0.00657	0.55942	0.53917
0%	0%	2.2	0.00626	0.00658	0.00657	0.00660	0.55824	0.53936
0%	5%	2.2	0.00627	0.00658	0.00658	0.00658	0.55847	0.53847
5%	-5%	2.2	0.00625	0.00657	0.00655	0.00658	0.55674	0.53696
5%	0%	2.2	0.00627	0.00658	0.00659	0.00657	0.55782	0.53808
5%	5%	2.2	0.00629	0.00659	0.00659	0.00659	0.55847	0.53962
average			0.00626	0.00658	0.00658	0.00658	0.55820	0.53859

Table 5.5: Average post target Q^2 (left arm) for various thickness configurations. As expected, the Q^2 doesn't change with varied foil thicknesses. There is some fluctuations in the asymmetry.

Table 5.5 lists the Q^2 and asymmetry from the simulations, from which the combined Q^2 is calculated:

$$Q^2 = \frac{R_C Q_C^2 + R_{Pb} Q_{Pb}^2}{R_C + R_{Pb}} = \frac{6.71\% \times 0.00658 + 0.00629}{6.71\% + 1} = 0.00629 \text{ GeV}^2 \quad (5.9)$$

Comparing the simulation Q^2 to that of the optics data in Table 5.6. We see a quite good agreement between the simulation and the data (left arm), indicating the reliability of the simulation.

arm	θ	Q^2 (GeV 2)
Left	4.748 ± 0.006	0.00627 ± 0.00002
Right	4.813 ± 0.004	0.00642 ± 0.00001

Table 5.6: Average θ and Q^2 from the optics data.

Cross Check of the Simulation

Another cross check is done by comparing the simulation result with the theoretical prediction. Theoretically, the scattering rate is proportional to the cross section and the number of atoms in an unit area.

$$R \propto \sigma \times N = \sigma \times \frac{t}{m} \quad (5.10)$$

here, t and m are, respectively, the area density (mass thickness) and atomic mass. Therefore:

$$\frac{R_C}{R_{Pb}} = \frac{\sigma_C}{\sigma_{Pb}} \times \frac{t_c}{t_{Pb}} \times \frac{m_{Pb}}{m_C} \quad (5.11)$$

Take $E = 0.95$ GeV and $\theta = 4.8^\circ$ (based on Table 5.6), the cross section for $e^{-12}C$ and $e^{-208}Pb$ scatterings is numerically solved to be:

$$\sigma_C = 48.001 \text{ mbarn} \quad \sigma_{Pb} = 3386.100 \text{ mbarn} \quad (5.12)$$

The ratio of t_C/t_{Pb} is calculated as:

target	t_C (US + DS) (mg/cm ²)	t_{Pb} (mg/cm ²)	t_C/t_{Pb}	main detector error n	weight $1/\sqrt{n}$	weighted t_C/t_{Pb}
Pb208#2	177.6	632	0.281	42.743	0.1530	0.037
Pb208#10	180	623	0.289	33.3465	0.1732	0.043
Pb208#9	180	615	0.293	28.9264	0.1859	0.047
Pb208#8	180	620	0.290	33.5835	0.1726	0.043
Pb208#5	176.8	632	0.280	36.3435	0.1659	0.040
Pb208#7	180	639	0.282	32.7936	0.1746	0.042
Pb208#6	180	618	0.291	47.6238	0.1449	0.036
	179.2	625.6	0.286		1.1700	0.287

Table 5.7: Calculation of the weighted t_C/t_{Pb} , the main detector error is the uncertainty of the main detector mean value (reg_asym_us_avg); the weighted ratio is calculated as $\frac{w_j}{\sum_i w_i} \times (t_C/t_{Pb})_j$.

E (GeV)	θ	Target	σ (mbarn)	m	$\frac{R_C}{R_{Pb}}$ (%)	f_C (%)
0.95	4.8°	^{12}C	48.001	12.011	7.04	6.57
		^{208}Pb	3386.100	207.977		

Table 5.8: Theoretical calculation of f_C .

As shown in Table 5.8, the theoretical value is 4.6% higher than the simulation result.

Contribution to \mathcal{A}_{PV}

As said before, the asymmetry of the elastic electron-diamond scattering is well understood. The cross section and asymmetry of $e^{-12}C$ scattering at various energies and scattering angles are numerically solved from the Dirac equation by our theorist friends, and tabulated (Chuck's table). For ^{208}Pb , there is a similar table. The asymmetry of $e^{-12}C$ scattering is taken to be 539.36 ppb, as shown in Table 5.5 with the nominal ^{208}Pb and nominal diamond thicknesses. The relative uncertainty is taken to be a conservative estimate of 4%.

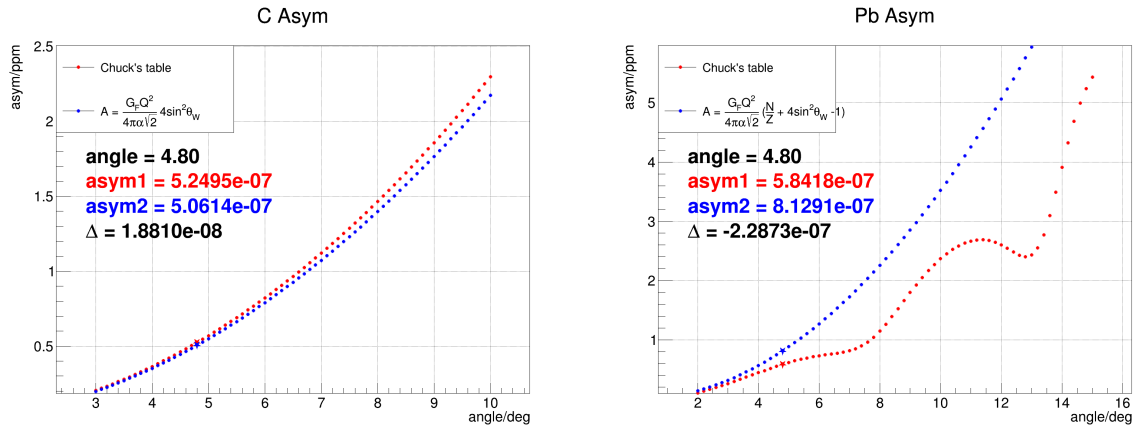


Figure 5.3: Theoretical asymmetries of the $e^{-12}C$ and $e^{-208}Pb$ scatterings in the experimental dynamics predicted by the Chuck's table, which includes the Coulomb correction. The Chuck's table is cross checked by the Standard Model Born approximation calculation. We see similar values between the two methods for both nuclei.

Using Eq. 5.4, the uncertainty contribution to \mathcal{A}_{PV} is calculated and summarized in Table 5.9.

$$\begin{aligned}\frac{\partial \mathcal{A}_{PV}}{\partial \mathcal{A}_C} \delta \mathcal{A}_C &= -\frac{0.0629}{1 - 0.0629} \times 4\% \times 539.36 = -1.4481 \text{ ppb} \\ \frac{\partial \mathcal{A}_{PV}}{\partial f_C} \delta f_C &= \frac{550 - 539.46}{1 - 0.0629} \times 0.00463 = 0.0521 \text{ ppb}\end{aligned}\quad (5.13)$$

$\mathcal{A}_{cor}/\mathcal{P}$ (ppb)	\mathcal{A}_C (ppb)	$\frac{\delta \mathcal{A}_C}{\mathcal{A}_C}$	f_C	δf_C	rel. error due to \mathcal{A}_C	rel. error due to f_C
549.34	539.36	4%	6.29%	0.463%	0.26%	0.01%

Table 5.9: Relative uncertainty due to \mathcal{A}_C and f_C .

The uncertainty caused by the error in f_C is negligible, and the one from \mathcal{A}_C is also tiny, which in hindsight, justifies our adoption of the sandwich target.

5.3 The CREX Acceptance Function

As said before, the spectrometer acceptance is mainly defined by the Q1 collimator, while other components may have some affections on it. The acceptance is not tiny (0.00377 sr), points within the acceptance may have different detection efficiencies and different asymmetries. In other words, what we measure is actually the average asymmetry over the acceptance:

$$\mathcal{A}_{\text{mea}} = \frac{\int d\theta \sin \theta \mathcal{A}(\theta) \frac{d\sigma}{d\Omega} \epsilon(\theta)}{\int d\theta \sin \theta \frac{d\sigma}{d\Omega} \epsilon(\theta)} \quad (5.14)$$

here $\epsilon(\theta)$ is the acceptance function, which is defined as the ratio of electrons that reach the main detector over all scattered electrons. This quantity depends on the scattering angle θ :

$$\epsilon(\theta) = \frac{N_{\text{det}}(\theta)}{N_{\text{sca}}} \quad (5.15)$$

From Eq. 5.14, we see the importance of the acceptance function. Firstly, it will contribute to the systematic uncertainty of \mathcal{A}_{PV} ; secondly, only with the acceptance function, can we compare the experimental measurement to theoretical predictions, to interpret our results.

To extract the acceptance function, again, we have to turn to simulations. To ensure the reliability of the simulation result, precise matches of various kinematic variables between the simulation and the optics data are required.

When we take the optics data, we can put in the sieve slit collimators. By reconstructing electron trajectories with the track info from the VDCs and the hole positions in the sieve plane, the scattering angle and beam energy can be inferred.

In terms of the simulation, we tuned some parameters to find out the best match with data – the best model, which was then used to calculate the acceptance function. The three parameters we explored are:

- Septum current
- Q1 collimator shift
- Pinch point shift

5.3.1 Transportation Matrix

Due to the existence of various magnetic fields (septum, HRS) between the target and the detector, there is no way to know the analytical expression of the transportation between them, though we can approximate and measure it.

An electron trajectory can be parameterized as:

$$\mathbf{X} = (x, \theta, y, \phi, \delta)^T \quad (5.16)$$

w.r.t. to a reference trajectory (usually the central ray). In the transport coordinate, \hat{z} is the moving direction of the reference trajectory; x is the displacement in the dispersive plane relative to the reference trajectory, and θ is the ‘velocity’ in the dispersive plane:

$$\theta = \frac{\partial x}{\partial z} \quad (5.17)$$

Similarly, y and ϕ are displacement and ‘velocity’ in the y-z plane.

$$\phi = \frac{\partial y}{\partial z} \quad (5.18)$$

\hat{y} is oriented such that \hat{x} , \hat{y} , \hat{z} are orthogonal to each other and they form a right-handed (RH) coordinate $\hat{z} = \hat{x} \times \hat{y}$.

$$\delta = \frac{\Delta p}{p} \quad (5.19)$$

represents the fractional deviation of momentum from that of the reference trajectory. With these definitions, the electron trajectory can be expressed as the Fourier expansion of the initial state of \mathbf{X}_0 :

$$x_i = \sum_j T_{ij} x_{j,0} + \sum_j \sum_k S_{ijk} x_{j,0} x_{k,0} + \dots \quad (5.20)$$

where T_{ij} is what we call the transportation matrix, whose elements indicate the reliance of the beam parameters on each other:

$$T_{ij} = \frac{\partial x_i}{\partial x_j} \quad (5.21)$$

Considering the fact that electron trajectories will be very close to the reference trajectory, the first order expansion is good enough to approximate Eq. 5.20. So we write:

$$\begin{pmatrix} x \\ y \\ \theta \\ \phi \\ \delta \end{pmatrix} = T \begin{pmatrix} x_{tg} \\ y_{tg} \\ \theta_{tg} \\ \phi_{tg} \\ \delta_{tg} \end{pmatrix} = \begin{pmatrix} x|x_{tg} & x|y_{tg} & x|\theta_{tg} & x|\phi_{tg} & x|\delta_{tg} \\ y|x_{tg} & y|y_{tg} & y|\theta_{tg} & y|\phi_{tg} & y|\delta_{tg} \\ \theta|x_{tg} & \theta|y_{tg} & \theta|\theta_{tg} & \theta|\phi_{tg} & \theta|\delta_{tg} \\ \phi|x_{tg} & \phi|y_{tg} & \phi|\theta_{tg} & \phi|\phi_{tg} & \phi|\delta_{tg} \\ \delta|x_{tg} & \delta|y_{tg} & \delta|\theta_{tg} & \delta|\phi_{tg} & \delta|\delta_{tg} \end{pmatrix} \begin{pmatrix} x_{tg} \\ y_{tg} \\ \theta_{tg} \\ \phi_{tg} \\ \delta_{tg} \end{pmatrix} \quad (5.22)$$

The ‘tg’ subscript refers to corresponding values on the target plane. With the transportation matrix, one can inverse it to propagate backward to calculate the electron state on the target plane, from what we detect with VDCs. Usually, we start from the focal plane \mathbf{X}_{fp} , then the electron state on the target plane will be:

$$\mathbf{X}_{tg} = T^{-1} \mathbf{X}_{fp} \quad (5.23)$$

The reason that we don’t use BPMs to ‘measure’ the electron position/angle at the target is that multi-scattering/radiation inside the target foil will distort the electron trajectory.

The typical HRS transportation plots are shown in Fig. 5.4:

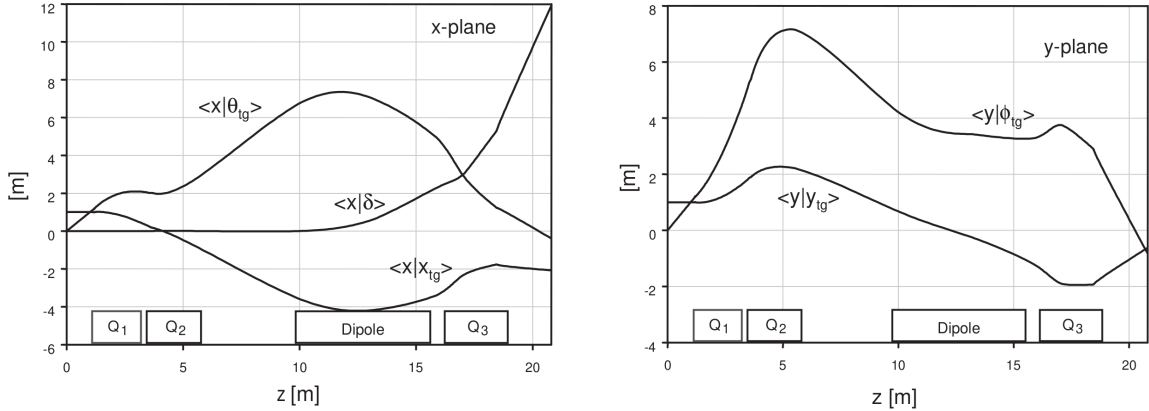


Figure 5.4: HRS transportation plot.

Actually, not every element of T needs to be measured, some elements are obviously 0. E.g. δ should not be changed by any magnetic field, so

$$T_{5i,i \neq 5} = 0 \quad (5.24)$$

The design of the HRS tells us that the dispersion depends only on δ , but not on θ or ϕ , therefore

$$x|\theta = 0 \quad (5.25)$$

Different planes should not interfere with each other, which means

$$x|y = x|\phi = \theta|y = \theta|\phi = y|x = y|\theta = \phi|x = \phi|\theta = 0 \quad (5.26)$$

That is to say T is a sparse matrix.

The transportation matrix is measured with the sieve data. When the sieve slit collimator is put in, the electron trajectories from different holes are naturally separated on the focal plane, which allows us to match them to the sieve holes one by one. With a reasonable initial value of the matrix (from previous experiments), we could reconstruct the electron state on the sieve plane using Eq. 5.23. By tuning the matrix elements, the one that minimizes the distance of the electron trajectory on the sieve plane from the closest hole center is identified as the transportation matrix. The selection of the septum and HRS current is based on the sieve pattern derived from the transportation matrix.

5.3.2 Scattering Angle $θ_{lab}$

The parameter that directly reflects the quality of the simulation is the scattering angle. It is more convenient to use the target coordinate system (TCS) than the hall coordinate system (HCS) in simulation, though the comparison to the data uses values in

the lab frame (HCS). The two coordinate systems and the transportation between them are defined below.

- Hall coordinate system: originated at the center of the hall and cross the beam line. \hat{Z} is along the beam line, pointing downstream; \hat{Y} points up and \hat{X} points left to form a RH coordinate system.
- Target coordinate system: which is the transport coordinate system at the target. \hat{Z} is along the beam trajectory, pointing away the target, \hat{X} is on the dispersive plane and points down, \hat{Y} is perpendicular to the dispersive plane and points away (toward) the beamline for LHRs (RHRs).

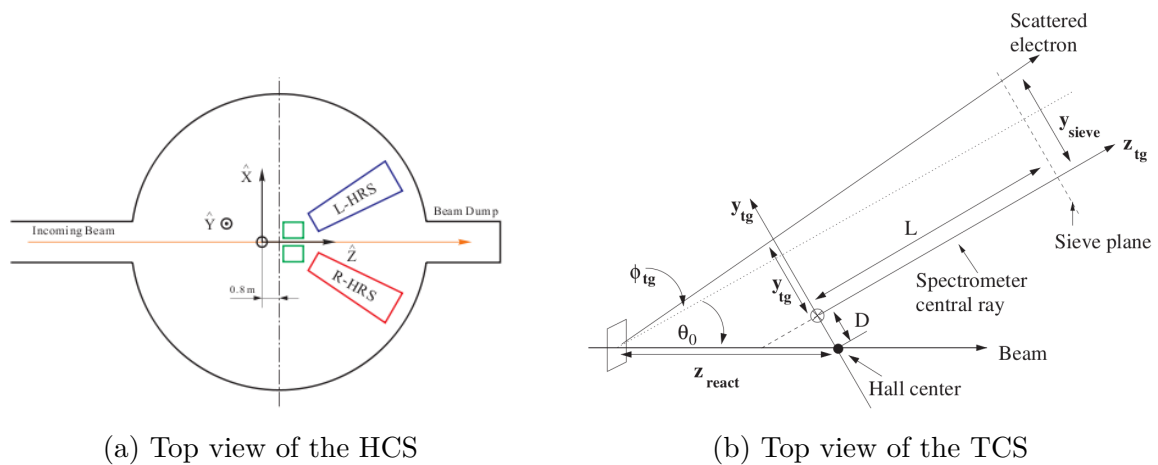


Figure 5.5: Schematic plot of the HCS and TCS. The hall center is the origin of the HCS, but the target doesn't necessary lie in the hall center. The distance from the hall center to the sieve plane (L) is a constant, which is used to identify the origin of the TCS. In the ideal case, the origins of both coordinate systems will overlap.

The relationship between the HCS and TCS is:

$$\begin{pmatrix} x_{tg} \\ y_{tg} \\ z_{tg} \end{pmatrix} = \begin{pmatrix} \cos(90^\circ) & -\sin(90^\circ) & 0 \\ \sin(90^\circ) & \cos(90^\circ) & 0 \\ 0 & 0 & 1 \end{pmatrix} \begin{pmatrix} \cos(-\theta_0) & 0 & -\sin(-\theta_0) \\ 0 & 1 & 0 \\ \sin(-\theta_0) & 0 & \cos(-\theta_0) \end{pmatrix} \begin{pmatrix} x \\ y \\ z \end{pmatrix} \quad (5.27)$$

which leads to:

$$\left. \begin{array}{l} x_{tg} = -y \\ y_{tg} = x \cos \theta_0 + z \sin \theta_0 \\ z_{tg} = -x \sin \theta_0 + z \cos \theta_0 \end{array} \right\} \iff \left. \begin{array}{l} x = y_{tg} \cos \theta_0 + z_{tg} \sin \theta_0 \\ y = -x_{tg} \\ z = -y_{tg} \sin \theta_0 + z_{tg} \cos \theta_0 \end{array} \right\} \quad (5.28)$$

where θ_0 is the scattering angle of the central ray in the lab frame.

The distance of an electron from the origin in both coordinate systems is:

$$R = (x^2 + y^2 + z^2)^{1/2} = z_{tg} (\phi_{tg}^2 + \theta_{tg}^2 + 1)^{1/2} \quad (5.29)$$

So the scattering angle in the lab frame will be:

$$\cos \theta = \frac{z}{R} = \frac{-\phi_{tg} \sin \theta_0 + \cos \theta_0}{(\phi_{tg}^2 + \theta_{tg}^2 + 1)^{1/2}} \quad (5.30)$$

For the data, θ_0 is identified to be 4.789° (4.771°) for the LHR (RHR). In the simulation, both arms use 4.74° . Note that θ_{lab} is a post-target (apparent) quantity, which includes effects from the post-vertex radiation and multi-scattering. It is not the ‘real’ scattering angle (vertex quantity) at the vertex where the interesting PV elastic scattering happens. The correction from the apparent distribution to the vertex distribution is about 1.5%.

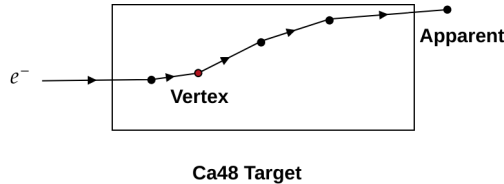


Figure 5.6: Schematic plot of the vertex and apparent quantities.

5.3.3 Data

Exp	Arm	Dipole p0 (GeV)	Septum (A)	Q1 (A)	A2 (A)	Q3 (A)
PREX-II	Left	0.95285	333	118.50	407.70	450.76
	Right	0.95284	333	118.55	404.07	446.90
CREX	Left	2.183522	801	225.387	934.273	981.301
	Right	2.183499	801	230.916	925.955	981.301

Table 5.10: PREX-II and CREX tunes of the septum and HRS.

To determine the new tune of the septum and HRS for CREX, we started with the PREX-II tune by scaling it to the CREX momentum. To know the appropriate septum current that will bridge the central ray into the HRS axis, we tuned the septum and Q1 current in two steps: the coarse and fine tunes. The septum or Q1 current was changed by a large step of 10% (the central ray search) in the coarse tune; and then fine tuned in a smaller step of 2.5% to find out the largest acceptance (the inner edge search).

In the central ray search, if the septum current is inappropriate, the central hole in the reconstructed sieve pattern plot would shift when we change the Q1 current, as shown in Fig. 5.7.

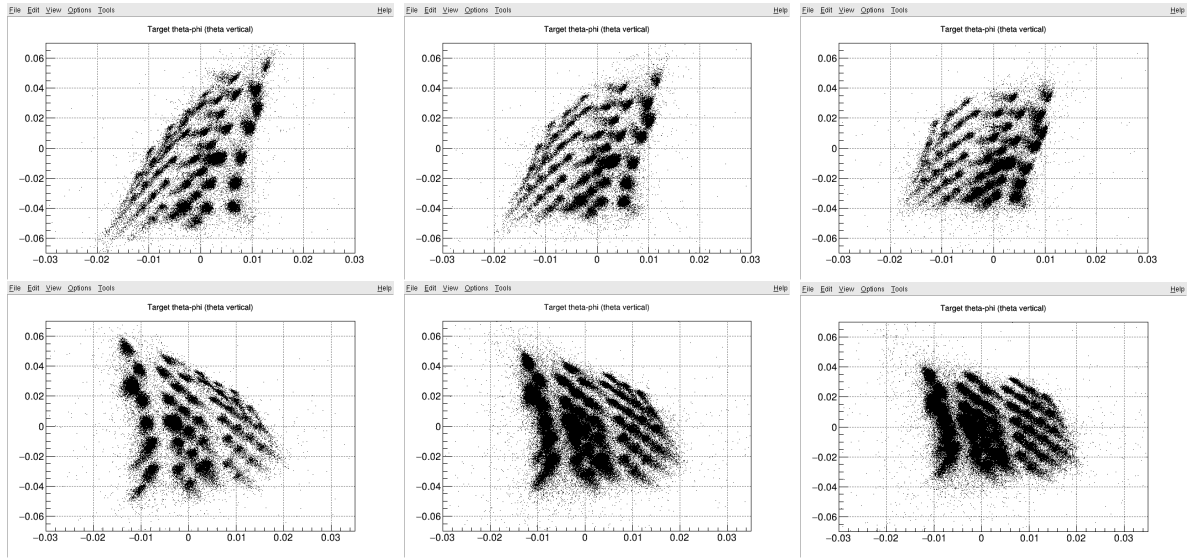


Figure 5.7: Sieve pattern plots for the -10% septum current and varied Q1 currents, from left to right: -10%, nominal and +10% Q1 current. The top (bottom) row shows the right (left) arm plot. With different Q1 currents, the sieve pattern twists, and the central hole shifts in θ (vertical axis), so the septum current is not a good value.

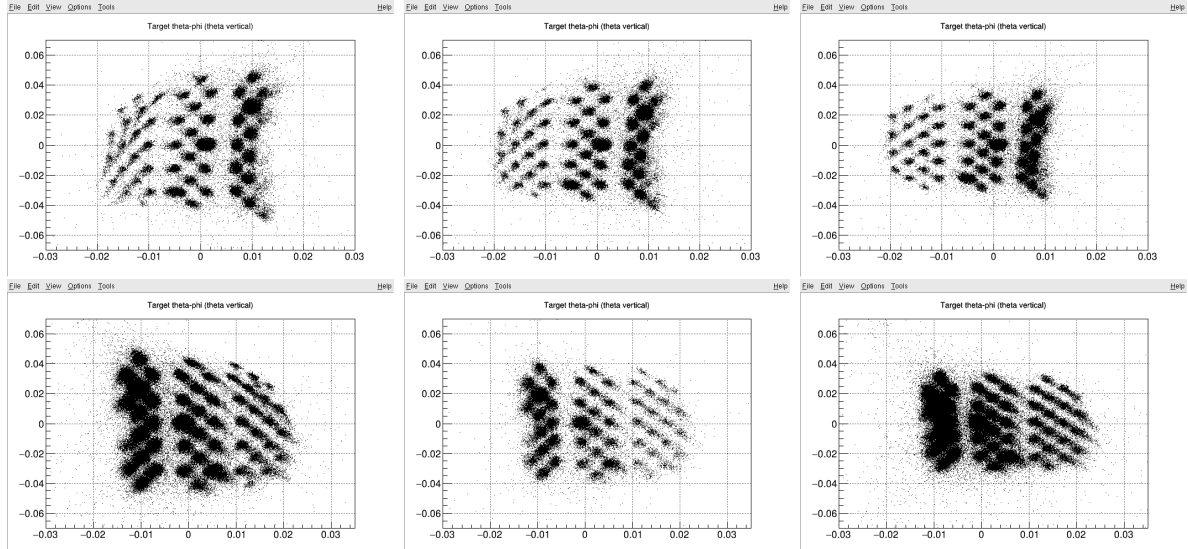


Figure 5.8: Sieve pattern plots for the nominal (scaled from PREX-II) septum current and varied Q1 currents, from left to right: -10%, nominal and +10% Q1 current. The top (bottom) row shows the right (left) arm plot. With different Q1 currents, the sieve pattern twists, but the central hole keeps at the same position, which means the central ray goes through the axis of the HRS.

Fig. 5.8 indicates that the nominal septum current and the nominal HRS setting is not a bad choice. Then we moved on to the inner edge search to see more inner holes – holes with the largest (smallest) ϕ in the left (right) arm. It turns out a 5% increment

from the nominal value allows the largest acceptance, which corresponds to a septum current of: $1.05 \times (333 * 2.183522 / 0.95285) = 801.25$ A.

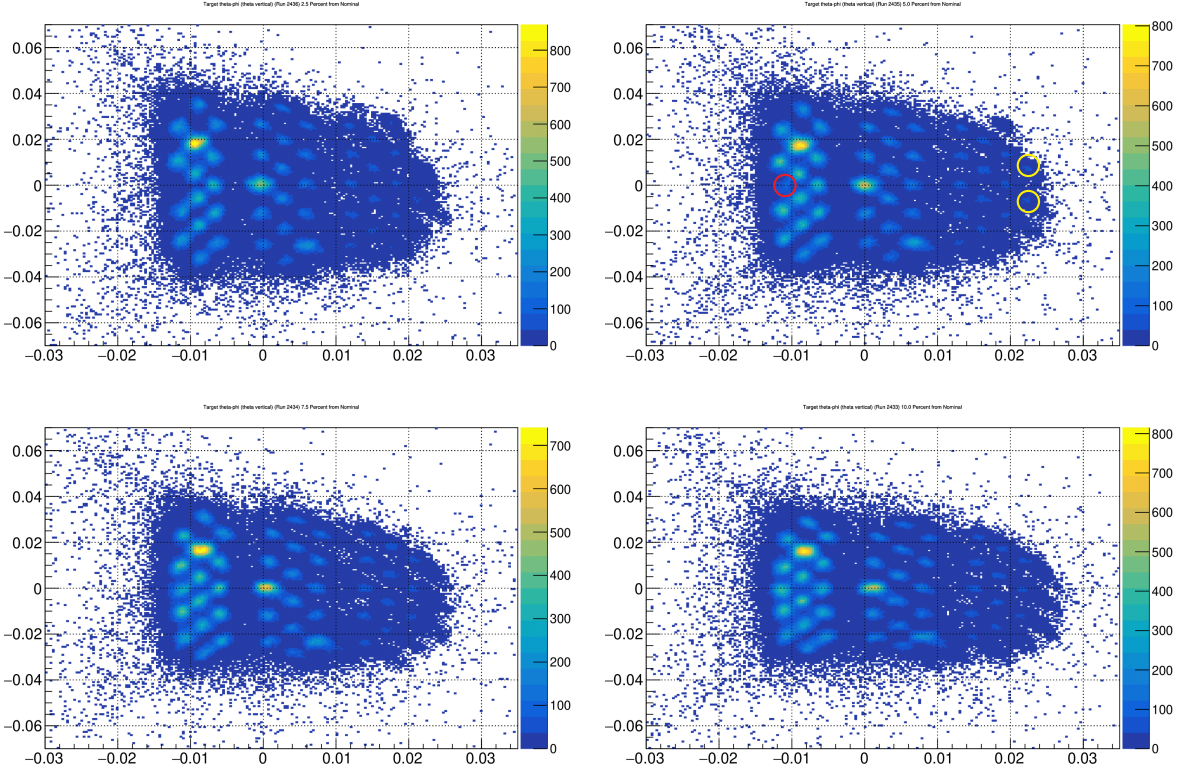


Figure 5.9: Inner edge search in the left arm. Septum currents from top left to bottom right are: +2.5%, +5%, +7.5%, +10%. The inner middle hole starts to appear since +5%, and outer holes disappear since 7.5%, so the best septum current was chosen to be +5%

With the selected septum current, we continued to minimize the beam spot size on the detector plane, which was achieved with the Q1 current being -17% (-15%) from the nominal value in the left (right) arm, and the Q3 current being -5% from the nominal value in both arms. The current values of the CREX tune is shown in Table 5.10.

5.3.4 Simulation

The simulation is not an exact reproduction of the reality. We used GEANT4 to simulate the geometry of each component based on the design values. The septum magnetic field was scaled from a field map file sampled from the septum with a current density of $j_0 = -1320$ A/cm²:

$$B'_{x,y,z} = \frac{j}{j_0} \times \frac{P}{P_0} \times B_{x,y,z} \quad (5.31)$$

where j is the current density and P being the electron momentum.

Q1(%)	Q3 (%)	Left			Right		
		run	σ_y (cm)	σ_x (cm)	run	σ_y (cm)	σ_x (cm)
0	0	2524	0.9604	1.634	21604	0.009564	0.01503
-5	0	2525	0.955	1.188		Left arm only	
-10	0	2526	1.005	0.9063		Left arm only	
-15	0	2527	0.1078	0.7314		Left arm only	
-20	0	2528	1.182	0.6801		Left arm only	
-11	0	2529	1.012	0.8767	21609	0.009315	0.007337
-12	0	2530	1.012	0.8349	21610	0.009429	0.006957
-13	0	2531	1.033	0.7835	21611	0.009526	0.006682
-14	0	2532	1.057	0.7515	21612	0.009623	0.06367
-13	+10	2533	1.754	1.929	21613	0.0162	0.0215
-13	+5	2534	1.374	0.7282	21614	0.01276	0.01174
-13	-5	2535	0.8357	0.9751	21615	0.008422	0.008514
-13	-10	2536	0.8855	1.482	21616	0.008891	0.01387
-13	-2	2538	0.9415	0.8761	21618	0.9117	0.7078
-13	-4	2539	0.8602	0.9181	21619	0.8493	0.7912
-13	-7	2540	0.8182	1.154	21620	0.8304	1.027
-13	-9	2541	0.8445	1.389	21621	0.8545	1.268
-15	-5	2542	0.8354	0.8869	21622	0.827	0.7563
-15 (R);-17 (L)	-5	2543	0.8409	0.8315	21623	0.8382	0.7615

Table 5.11: Beam spot size with different HRS settings. The septum current being the nominal value.

The same operation for the HRS field:

$$B'_{i=Q1,Q2,D,Q3} = \frac{P}{P_0} \times B_i \quad (5.32)$$

With Eq. 5.31, we could vary the septum current to find a value at which the sieve pattern plot from simulation agrees with that from data, then scanned through the collimator shift and the pinch point shift to select the best match between simulation and data, for various kinematic variables.

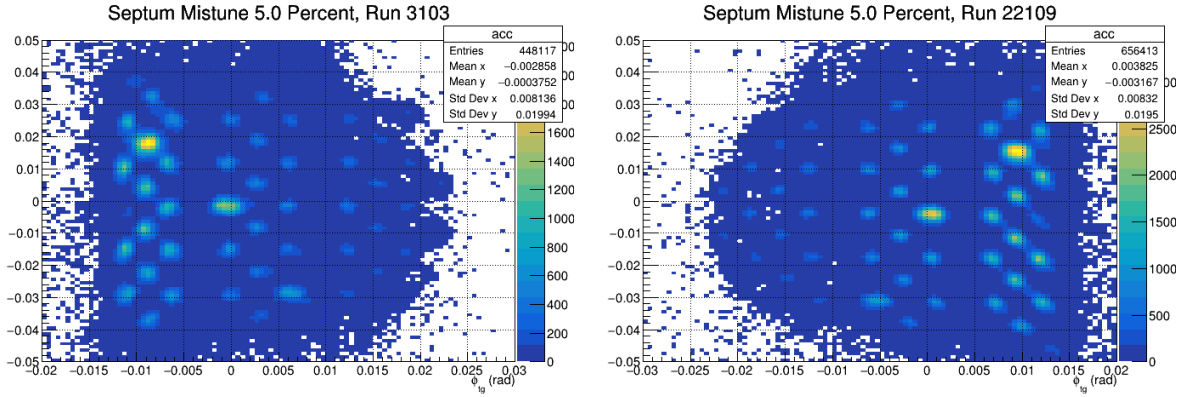


Figure 5.10: Sieve plot of the CREX tune. Centered at $(-0.3, -1.5)$, the new beam position for the new target.

Somewhat expected, a coarse scan through the septum current showed that the proper range for best match with data was about 0-5% above the nominal value, as shown in Fig. 5.11.

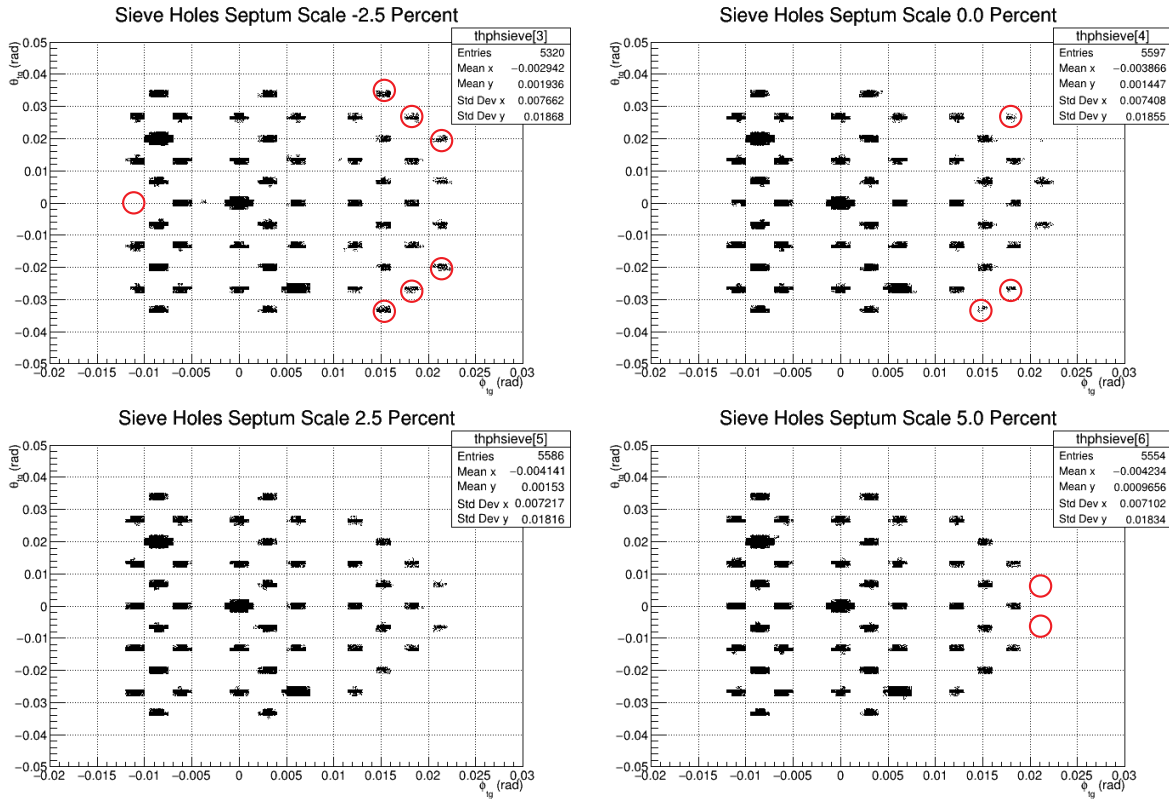


Figure 5.11: Sieve pattern plots from simulation with different septum currents. The red circles label extra or missing holes.

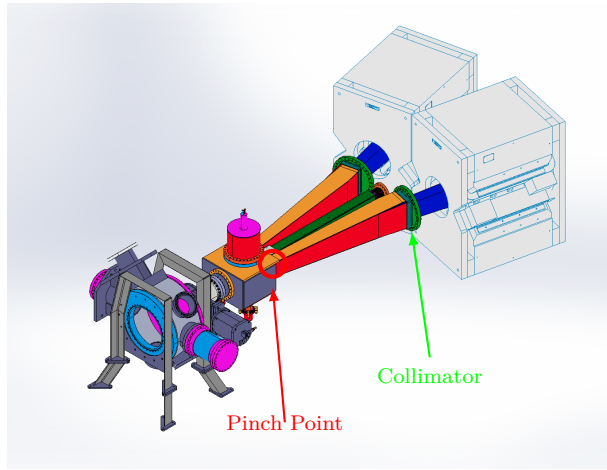


Figure 5.12: Position of the pinch point and the Q1 collimator.

With this narrow range, scan through the pinch point and collimator shift with a fine tune of the septum current (from -1% to +5%). The pinch point is the connection point between the septum beampipe and the upstream collimator box, whose misalignment will affect the acceptance; the other parameter we can adjust is the collimator y position (in the transport coordinate system), which has a large impact on the acceptance. For each simulation, we compared the average value of the scattering angle θ_{lab} , Q^2 and asymmetry to corresponding values from optics runs.

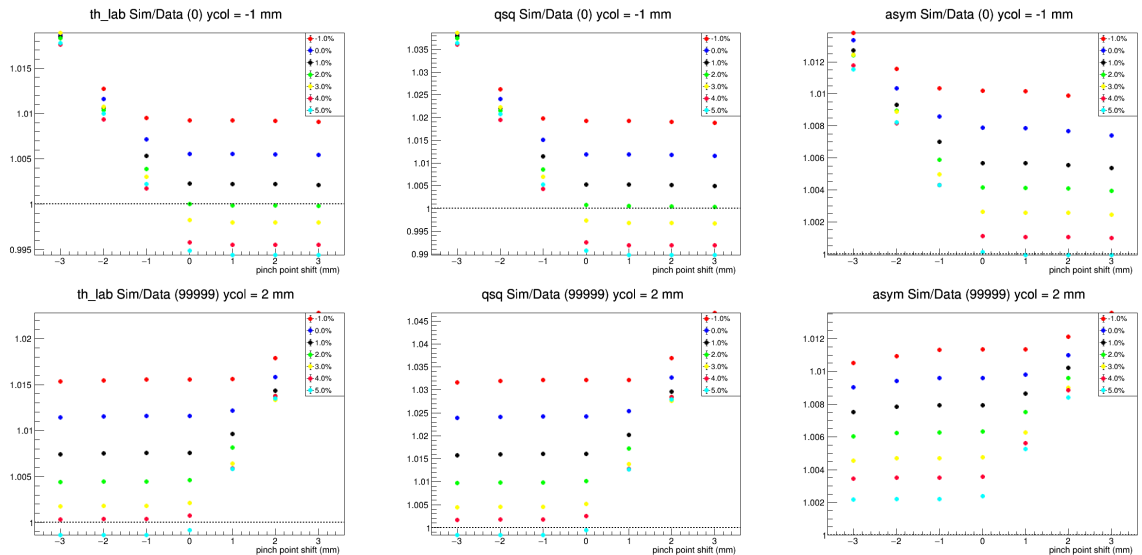


Figure 5.13: Ratio of simulation to data for average value of θ_{lab} , Q^2 and \mathcal{A} . Top (bottom) row corresponds to the left (right) arm. Data points whose y value is close 1 are good models.

As shown in Fig. 5.13, when we shift the pinch point toward the beam pipe (from negative values to positive values for the left arm, opposite for the right arm), the accep-

tance increases until the nominal value is reached, and then saturates. Similar trend is seen for shift in the Q1 collimator.

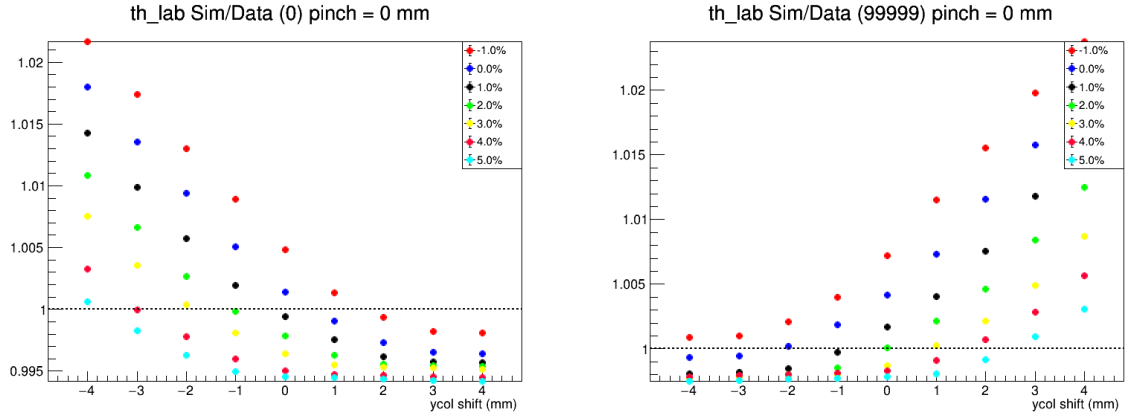


Figure 5.14: The θ_{lab} ratio plot for different models with pinch point shift = 0 mm. The left (right) arm plot is shown in the left (right). The best models are selected from these two plots.

Various corrections are applied to the simulation values, including the position difference between the production target and the calibration target, which is 20 mm; and the correction caused by the transportation matrix, whose optimization depends on the beam position.

$$\phi_a = \phi_r + 0.5 \text{ mrad/mm} \times (x - x_0) + 0.5 \text{ mrad/mm} \times (y - y_0) \quad (5.33)$$

where (x, y) is the actual beam position and (x_0, y_0) being the beam position with which the transportation matrix is optimized. ϕ_a and ϕ_r refer to the actual and reconstructed ϕ_{tg} . An extra acceptance is added to the right arm to get a better match.

From Fig. 5.14, we selected the best model which has the smallest difference between simulation and data in θ_{lab} and Q^2 :

	septum	col shift (mm)	pinch point shift (mm)
LHRS	+2%	-1	0
RHRS	+5%	2	0

Table 5.12: The best models we selected for LHRS and RHRS.

Check the best models against optics runs it terms of the distributions of θ_{lab} and Q^2 , as shown in Fig. 5.15. Quite good agreements are achieved for both arms.

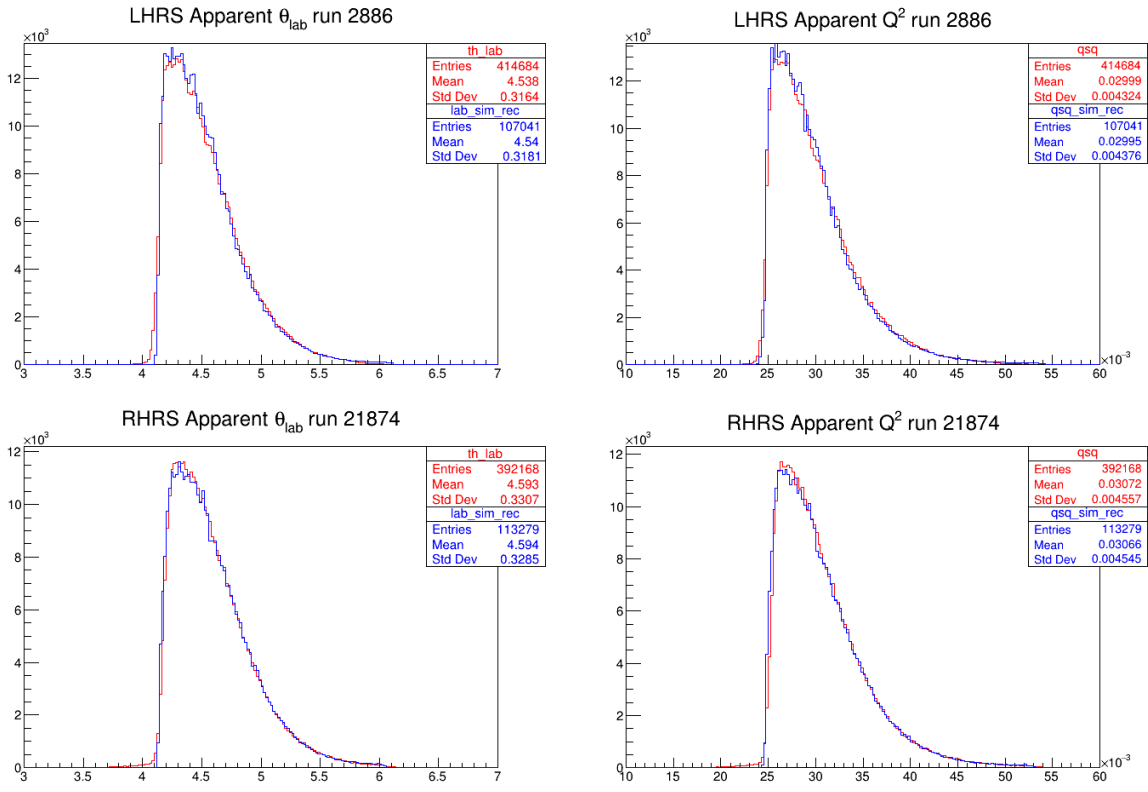


Figure 5.15: θ_{lab} and Q^2 comparison between the best models and data (apparent values). The red line is the simulation result while the blue line comes from data.

Using the selected best models, the acceptance function is calculated with Eq. 5.15 and drew in Fig. 5.16.

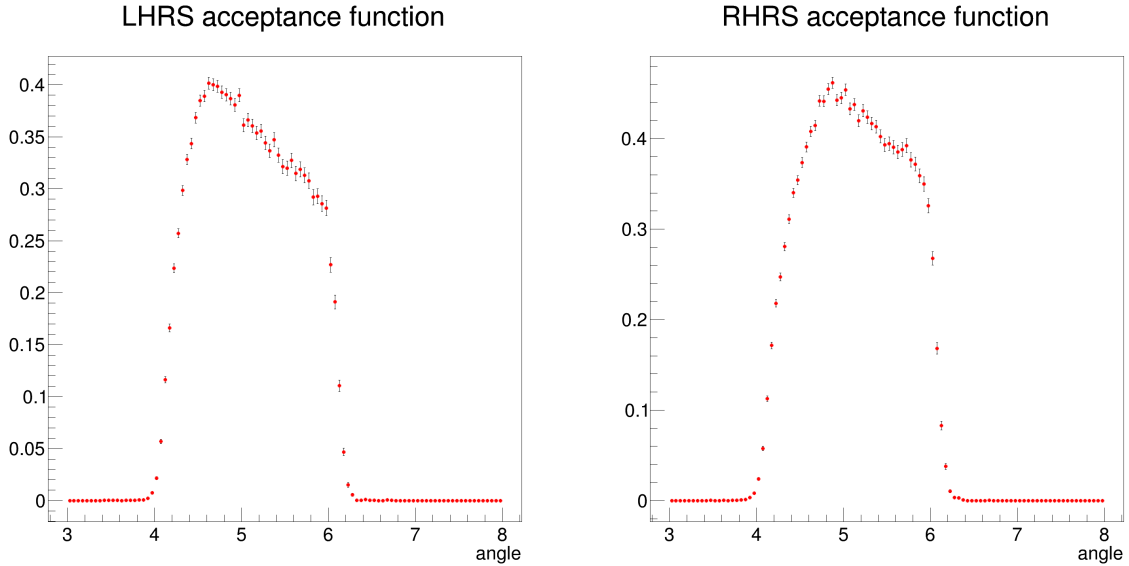


Figure 5.16: Acceptance function extracted with the best models.

5.4 Other Systematic Uncertainties

Other systematic uncertainties that are not talked about can be found in other PREX-II and CREX theses. The detector non-linearity is analyzed by Devi [61], and Ryan has a detailed discussion about the horizontal transverse asymmetry [70].

Chapter 6

Results and Discussion

6.1 Final Numbers

The overall beam polarization is the inverse-variance weighted average of the Compton and Moller measurements.

	PREX-II	CREX
Compton	$(89.68 \pm 0.15)\%$	$(87.115 \pm 0.453)\%$
Moller	$(89.67 \pm 0.80)\%$	$(87.06 \pm 0.74)\%$
Average	$(89.7 \pm 0.8)\%$	$(87.10 \pm 0.39)\%$

Table 6.1: Beam polarization measured by the Compton and Moller polarimeters.

After the beam false asymmetry correction in chapter 3 and identification of various background asymmetries in chapter 5, the PV asymmetry (blinded) will be extracted with Eq. 5.1, which we restate here:

$$\mathcal{A}_{\text{PV}} = \frac{\mathcal{A}_{\text{cor}}/\mathcal{P} - \sum_i \mathcal{A}_i f_i}{1 - \sum_i f_i}$$

The list of various corrections to the final result are shown in Table 6.2 and 6.3.

The last step is unblinding, in which we subtract $\mathcal{A}_{\text{blind}}$ from the blinded \mathcal{A}_{PV} . The blinding factor is a secret value that is randomly generated. It is added to every helicity quadruplet (octuplet) asymmetry by the JAPAN analyzer. Surprisingly, the PREX-II $\mathcal{A}_{\text{blind}}$ is very close to 0, making the unblinded \mathcal{A}_{PV} almost the same as the blinded value. The final asymmetry values are shown in Table 6.4.

6.1.1 Neutron Skin Thickness

With the physical PV asymmetry, the weak FF is calculated using Eq. 1.89.

$$F_W(^{208}\text{Pb}) = 0.368 \pm 0.013 \text{ (exp)} \pm 0.001 \text{ (theo)} \quad (6.1)$$

Correction	Absolute (ppb)	Relative (%)
Beam trajectory and energy	-60.4 ± 3.0	11.0 ± 0.5
Charge correction	20.7 ± 0.2	3.8 ± 0.0
Beam polarization	56.8 ± 5.2	10.3 ± 1.0
Target diamond foils	0.7 ± 1.4	0.1 ± 0.3
Spectrometer rescattering	0.0 ± 0.1	0.0 ± 0.0
Inelastic contributions	0.0 ± 0.1	0.0 ± 0.0
Transverse asymmetry	0.0 ± 0.3	0.0 ± 0.1
Detector nonlinearity	0.0 ± 2.7	0.0 ± 0.5
Angle determination	0.0 ± 3.5	0.0 ± 0.6
Acceptance function	0.0 ± 2.9	0.0 ± 0.5
Total correction	17.7 ± 8.2	3.2 ± 1.5
Statistical uncertainty	16	2.9

Table 6.2: Corrections and corresponding systematic uncertainties to \mathcal{A}_{PV} in PREX-II.

Correction	Absolute (ppb)	Relative (%)
Beam trajectory and energy	68 ± 7	2.5 ± 0.3
Beam charge asymmetry	112 ± 1	4.2 ± 0.0
Beam polarization	382 ± 13	14.3 ± 0.5
Isotopic purity	19 ± 3	0.7 ± 0.1
3.831 MeV (2^+) inelastic	-35 ± 19	-1.3 ± 0.7
4.507 MeV (3^-) inelastic	0 ± 10	0 ± 0.4
5.370 MeV (3^-) inelastic	-2 ± 4	-0.1 ± 0.1
Transverse asymmetry	0 ± 13	0 ± 0.5
Detector nonlinearity	0 ± 7	0 ± 0.3
Acceptance	0 ± 24	0 ± 0.9
Radiative corrections	0 ± 10	0 ± 0.4
Total systematic uncertainty	40	1.5
Statistical uncertainty	106	4.0

Table 6.3: Corrections and corresponding systematic uncertainties to \mathcal{A}_{PV} in CREX.

Asymmetry	PREX-II	CREX
\mathcal{A}_{raw}	431.64 ± 44.01	2106 ± 178.9
\mathcal{A}_{cor}	492.02 ± 13.52	2080.3 ± 83.8
Blinded \mathcal{A}_{PV}	$549.4 \pm 16.1 \pm 8.1$	$2412.3 \pm 106.1 \pm 38.7$
$\mathcal{A}_{\text{blind}}$	-0.5	-255.7
Unblinded \mathcal{A}_{PV}	$550 \pm 16 \pm 8$	$2668 \pm 106 \pm 40$

Table 6.4: The path to a physical PV asymmetry. All values are in units of ppb.

where the experimental uncertainty includes both statistical and systematic contributions. With the correlation between the weak radius and PV asymmetry, the weak radius

corresponding to the measured PV asymmetry in the correlation plot will be the experimental value. The neutron skin thickness is derived in the same way.

The correlation plot is produced in the following way: by fitting the weak charge densities predicted by a large variety of DFT models to a two-parameter Fermi function, the density and therefore the PV asymmetry and weak radius will be identified for each model, as shown in Fig. 6.1. The two-parameter Fermi function has been discussed in Sec. 1.1.1.

$$\rho_W(r) = \rho_W^0 \frac{\sinh(c/a)}{\cosh(r/a) + \cosh(c/a)}$$

here c denotes the nuclear size and a describes the surface thickness.

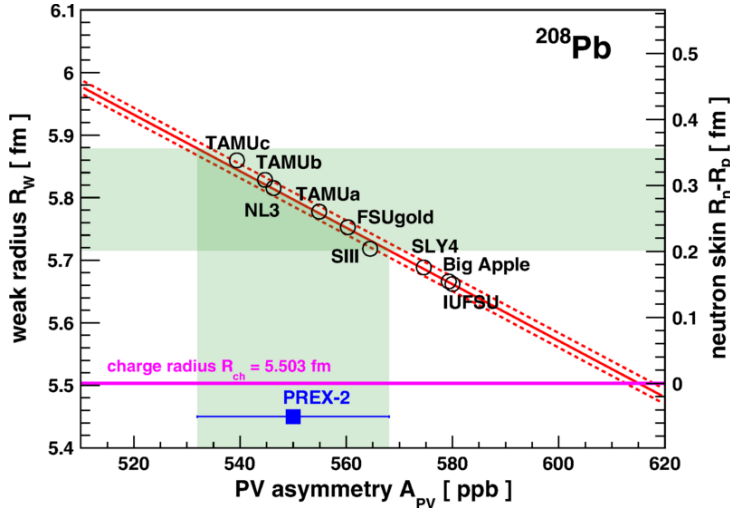


Figure 6.1: Correlation between the weak radius (left vertical axis)/neutron skin thickness (right vertical axis) and \mathcal{A}_{PV} for ^{208}Pb , predicted by a series of DFT models [71]. The red solid line describes the correlation fitted from the predictions of DFT models, the red dashed line and the green band indicate the $1-\sigma$ uncertainty for the correlation and measured values, respectively.

The weak charge radius of ^{208}Pb is extracted to be:

$$R_W(^{208}\text{Pb}) = 5.795 \pm 0.082 \text{ (exp)} \pm 0.013 \text{ (theo)} \text{ fm} \quad (6.2)$$

and the neutron skin thickness of ^{208}Pb :

$$R_{\text{skin}}(^{208}\text{Pb}) = R_n - R_p = 0.278 \pm 0.078 \text{ (exp)} \pm 0.012 \text{ (theo)} \text{ fm} \quad (6.3)$$

Similarly, the weak radius and neutron skin thickness of ^{48}Ca can be extracted, as summarized in Table 6.5.

Combining PREX-I and PREX-II results, the weak radius and the neutron skin are:

$$\begin{aligned} R_W(^{208}\text{Pb}) &= 5.800 \pm 0.075 \text{ fm} \\ R_{\text{skin}}(^{208}\text{Pb}) &= 0.283 \pm 0.71 \text{ fm} \end{aligned} \quad (6.4)$$

Exp	PREX-II	CREX
Target	^{208}Pb	^{48}Ca
$\langle Q^2 \rangle$ (GeV 2)	0.00616 ± 0.00005	0.0297 ± 0.0002
$\langle \mathcal{A}_{\text{PV}} \rangle$ (ppb)	$550 \pm 16 \text{ (stat)} \pm 8 \text{ (syst)}$	$2668 \pm 106 \text{ (stat)} \pm 40 \text{ (syst)}$
F_W	$0.368 \pm 0.013 \text{ (exp)} \pm 0.001 \text{ (theo)}$	$0.1304 \pm 0.0052 \text{ (stat)} \pm 0.0020 \text{ (syst)}$
$F_{ch} - F_W$	$0.041 \pm 0.013 \text{ (exp)} \pm 0.001 \text{ (theo)}$	$0.0277 \pm 0.0052 \text{ (stat)} \pm 0.0020 \text{ (syst)}$
R_W (fm)	$5.795 \pm 0.082 \text{ (exp)} \pm 0.013 \text{ (theo)}$	$3.640 \pm 0.026 \text{ (exp)} \pm 0.023 \text{ (theo)}$
$R_n - R_p$ (fm)	$0.278 \pm 0.078 \text{ (exp)} \pm 0.012 \text{ (theo)}$	$0.121 \pm 0.026 \text{ (exp)} \pm 0.024 \text{ (theo)}$

Table 6.5: Physical results extracted from PREX-II and CREX.

6.1.2 Density Dependence of the Symmetry Energy

In nuclear density functional theory, the neutron skin thickness of ^{208}Pb is correlated with the density dependence of the symmetry energy L . By drawing the predictions from DFT calculations with a set of energy density functionals, we can derive the linear correlation between L and R_{skin} , as shown in Fig. 6.2. With this correlation function, the symmetry energy slope L corresponding to our measurement of R_{skin} in ^{208}Pb , the L values at the nuclear saturation density $\rho_0 \sim 0.15\text{fm}^{-3}$ and the nuclear density $\rho_1 \sim 0.15\text{fm}^{-3}$ are determined to be:

$$L(\rho_0) = 106 \pm 37 \text{ MeV} \quad L(\rho_1) = 71.5 \pm 22.6 \text{ MeV} \quad (6.5)$$

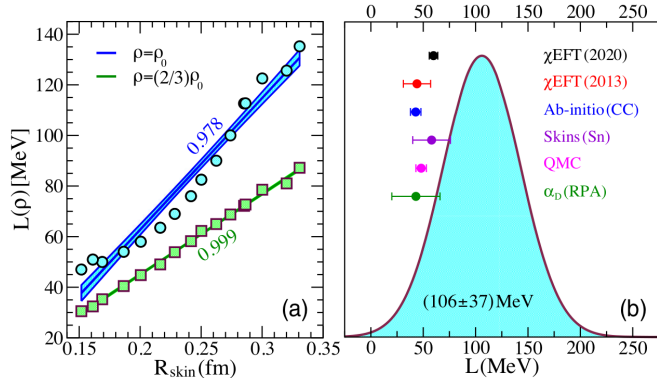


Figure 6.2: Left: correlation between the symmetry energy slope and the neutron skin thickness of ^{208}Pb at the nuclear saturation density (blue line) and the nuclear density (green line), numbers along the line are values for the correlation coefficients. Right: Gaussian probability distribution for $L(\rho_0)$ inferred from the left plot. The six data points are theoretical predictions of $L(\rho_0)$ from different approaches [72].

6.2 Physical Implication

6.2.1 Nuclear Structure

By comparing the experimental results with theoretical predictions of the neutron skin thickness of ^{208}Pb and ^{48}Ca , as shown in Fig. 6.3, we see a mild deviation between the experimental and theoretical values. Among all the models, only a few of them can successively predict the neutron skin thicknesses (weak FFs) of ^{208}Pb and ^{48}Ca simultaneously. To a extend, our measurements will guide the development of DFT and ab-initio calculations. In the future, more works, from both experimental and theoretical sides, are needed to accommodate the difference between them.

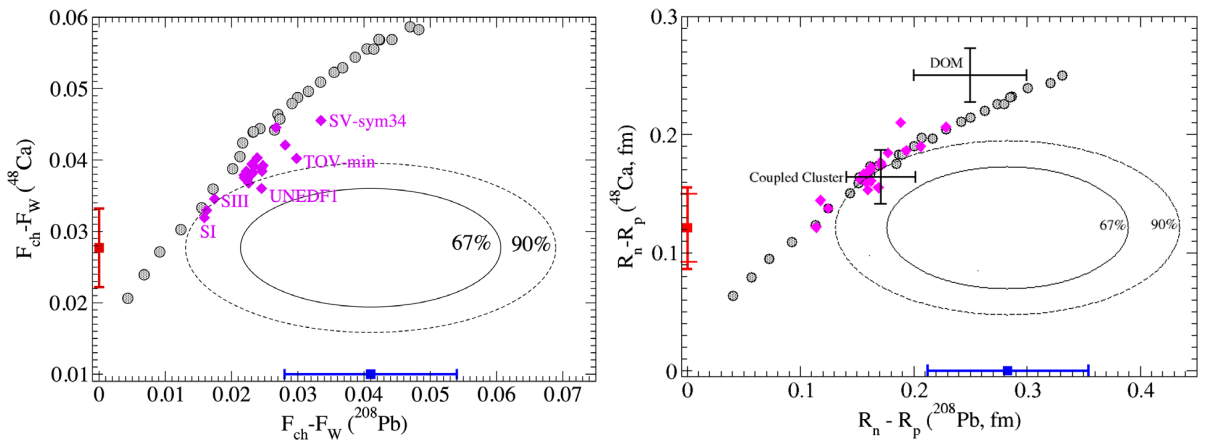


Figure 6.3: Experimental values and theoretical calculations of the FF difference (left) and the neutron skin thickness (right) of ^{208}Pb and ^{48}Ca . The two ellipses indicate the 67% and 90% probability intervals. The gray circles (magenta diamonds) come from the DFT calculation with a range of relativistic (nonrelativistic) density functionals. For clarity, only some of the functionals are labeled. Two ab-initio results: coupled cluster and dispersive optical model (DOM) are also shown in the neutron skin thickness plot [73].

Limit of the Nuclear Landscape

One straightforward application of nuclear DFT is to identify limits of the nuclear landscape. Every year, as many as dozens or as few as several new nuclides are discovered [74]. A clear guidance from the theory side about the possible existence of the neutron-rich nuclei will guide where to look for new rare isotopes, given the fact that the production rate of such neutron-rich nuclei is very low.

The possible atomic nuclei in the nuclear chart are bounded by the ‘drip line’, which determines the maximum number of protons (neutrons) for a given number of neutrons (protons). More specifically, across the drip line, the separation energy of one proton (S_{1p}) or neutron (S_{1n}) or two protons (S_{2p}) or neutrons (S_{2n}) changes sign (from positive

to negative). Surprisingly, the neutron drip line is known only up to neon ($Z = 10$), with the maximum number of neutron as $N = 24$ [75].

The neutron separation energy is defined as:

$$\begin{aligned} S_{1n}(Z, N) &= E(Z, N - 1) - E(Z, N) \\ S_{2n}(Z, N) &= E(Z, N - 2) - E(Z, N) \end{aligned} \quad (6.6)$$

where E is the binding energy. The same definition applies to proton. When the separation energy is positive, the nucleus is a bound state, otherwise unstable. We are interested in both S_{1n} and S_{2n} , rather than S_{1n} only, because nuclei with even-numbers of nucleons are more stable than their neighbors of odd-numbers of nucleons, due to the nucleonic superfluidity. Currently, the estimate of the neutron drip line depends on the choice of theoretical models and corresponding parameterizations, as shown in Fig. 6.4. By constraining DFT models with PREX-II and CREX results, we can improve the robustness of the theoretical prediction of the neutron drip line.

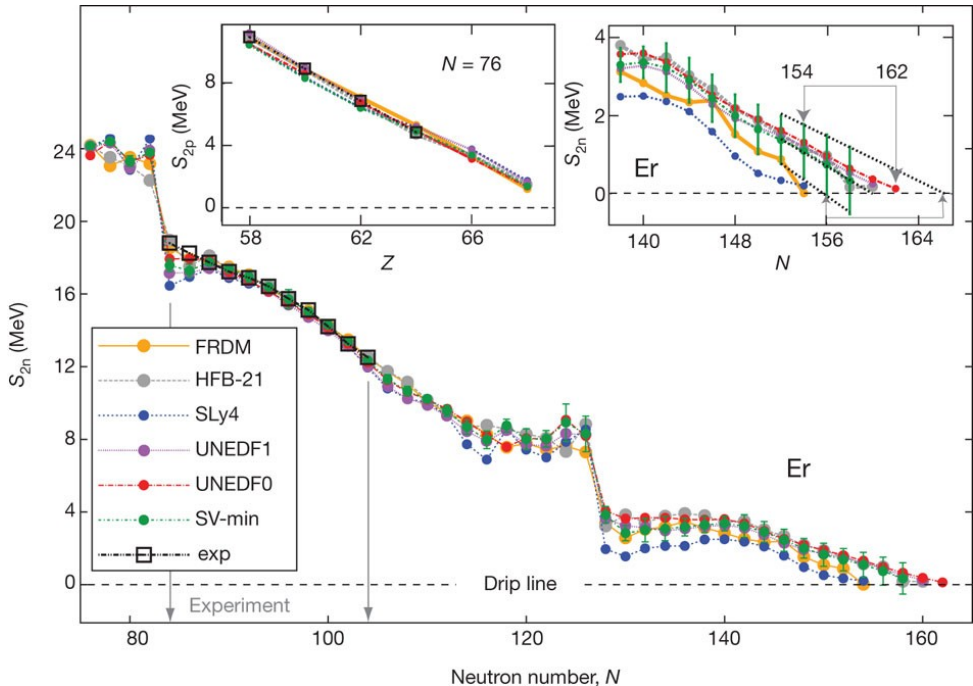


Figure 6.4: Theoretical and experimental two-nucleon separation energies of even-even erbium isotopes [76]. Dots represent DFT calculations and black squares correspond to experimental measurements.

Nuclear Saturation Density

The invariance of the binding energy per nucleon (E_b/A) w.r.t. A means that the interaction between nucleons is proportional to A , instead of $A(A - 1)$. That means nucleons saturate in space and hence the interior baryon density is approximately constant.

A stricter definition of the saturation density is the nucleon density at which the binding energy per nucleon is minimized.

Though the knowledge of nuclear saturation, it is never directly observed. ^{40}Ca is the largest stable symmetric nucleus, but still too small to have a nearly constant interior baryon density. For heavy nuclei, their charge densities have been precisely measured, but no direct observation of any interior neutron density. PREX-II is the first experiment to provide a value of the average interior baryon density of a heavy nucleus with only a little model dependence.

With the two-parameter Fermi function, the interior weak density is extracted from PREX-II data to be:

$$\rho_W^0(^{208}\text{Pb}) = \frac{3Q_W}{4\pi c(c^2 + \pi^2 a^2)} - 0.0798 \pm 0.0038 \text{ (exp)} \pm 0.0013 \text{ (theo)} \text{ fm}^{-3} \quad (6.7)$$

where Q_W is total weak charge of ^{208}Pb nucleus.

$$Q_W = -117.9 \pm 0.3 \quad (6.8)$$

Combining PREX-I and PREX-II results, ρ_W^0 is modified to be:

$$\rho_W^0(^{208}\text{Pb}) = -0.0796 \pm 0.0038 \text{ fm}^{-3} \quad (6.9)$$

The uncertainty includes contributions from both experiment and theory.

With the well-measured interior charge density, the interior baryon density in ^{208}Pb is measured to be:

$$\rho_b^0(^{208}\text{Pb}) = 0.1482 \pm 0.0040 \text{ fm}^{-3} \quad (6.10)$$

The extracted density plot is shown in Fig. 6.5.

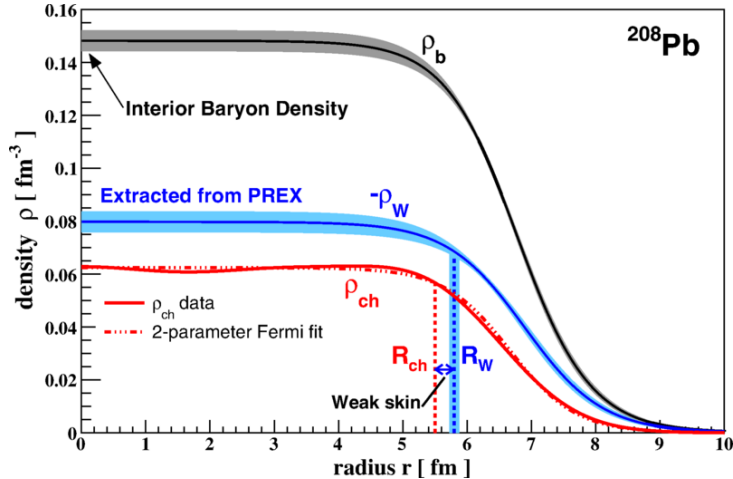


Figure 6.5: Density distributions for the EM charge (red), weak charge (blue) and baryon (black) in the ^{208}Pb nucleus [71].

With the scale factor between the nuclear saturation density (ρ_0) and the interior

baryon density in ^{208}Pb (ρ_b^0) [77]:

$$f = \frac{\rho_0}{\rho_b^0} \approx 1.02 \pm 0.03 \quad (6.11)$$

The nuclear saturation density will be:

$$\rho_0 = f \times \rho_b^0 = 0.1510 \pm 0.0059 \text{ fm}^{-3} \quad (6.12)$$

This value is fully consistent with $\rho_0 = 0.151 \pm 0.001 \text{ fm}^{-3}$ predicted by a relativistic EDF calibrated using exclusively physical observables [78], and lower than the phenomenological estimate of $\rho_0 = 0.164 \pm 0.007 \text{ fm}^{-3}$ [79] based on some selected density functionals.

6.2.2 Neutron Stars

As discussed in the introduction section, by measuring the neutron skin thickness of ^{208}Pb and ^{48}Ca , we can extract the density dependence of the symmetry energy, which will be used to constraint the size of a neutron star.

Multi-Messenger Measurements of the Neutron Star Ridius

NICER (Neutron star Interior Composition ExploreR) [80] is a X-ray telescope that can measure lightcurves of neutron stars (pulsars). A pulsar has a hot-spot, which is the magnetic pole of the neutron star. The observed light flux fluctuates with the orientation of the hot-spot. When it faces the earth, we will observe the maximum flux; when it points away, we will observe the minimum flux, due to curvature of the space caused by the neutron star. So by observing the depth of the modulation of the light flux, one can infer the curvature of the space near the neutron star, which depends on the radius of the neutron star. This is how NICER measures the radius of a neutron star.

One can also measure the size of a neutron star through the gravitational waves. The famous LIGO-Virgo event, GW170817 [81], observed the gravitational wave emission from a binary neutron star merger. In a binary system, neutron star deforms due to the tidal force from the other body, this property is described by the tidal deformability (quadrupole polarizability):

$$\Lambda = \sum_f \frac{|\langle f | r^2 Y_{20} | i \rangle|^2}{E_f - E_i} \propto R^5 \quad (6.13)$$

Tidal deformability can be probed by detection of the gravitational waves produced by the binary system. LIGO observation of GW170817 sets an upper limit on Λ of a typical $1.4 M_\odot$ neutron star[82].

$$\Lambda_{1.4} = 190^{+390}_{-120} \quad (6.14)$$

It favors a smaller deformability (< 580) and therefore a smaller neutron radius ($< 13 \text{ km}$)

Observables of a $1.4 M_\odot$ neutron star extracted from various experiments are shown

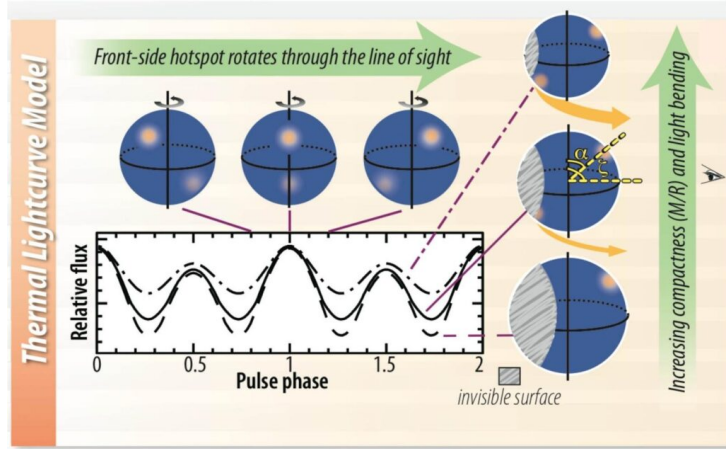
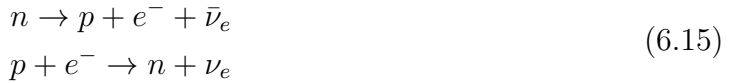


Figure 6.6: Modeling of the light flux from a neutron star. The three curves in the flux panel corresponding to the three neutron stars to the right with different compactness (mass/radius).

in Fig. 6.7. We see that the combined PREX measurement is consistent with the NICER result, while in mild tension with the LIGO observation.

Direct Urca Process

The direct Urca processes are neutrino emission processes:



which may explain the rapid cooling of some neutron stars [83].

The rate of the direct Urca process depends on the proton fraction in the stellar core. The proton fraction, in turn, is controlled by the density dependence of the symmetry energy [84]. Therefore, we can learn about the direct Urca threshold density from the measurement of $R_{\text{skin}}(^{208}\text{Pb})$, as shown in Fig. 6.8. The larger the neutron skin thickness in ^{208}Pb , the lower the threshold mass (density) for the direct Urca process. Our measurement of $R_{\text{skin}}(^{208}\text{Pb}) = 0.283$ fm suggests a threshold mass of $M_\star \approx 0.85M_\odot$ and corresponding threshold density of $\rho_\star \approx 0.24 \text{ fm}^{-3}$.

6.3 Future Outlook

Parity-violating electron scattering experiments are still developing and flourishing. Several PVES experiments have been proposed to explore different aspects of EW interactions, including MOLLER [85] and SoLID [45] at JLab, as well as P2 and MREX at Mainz [86].

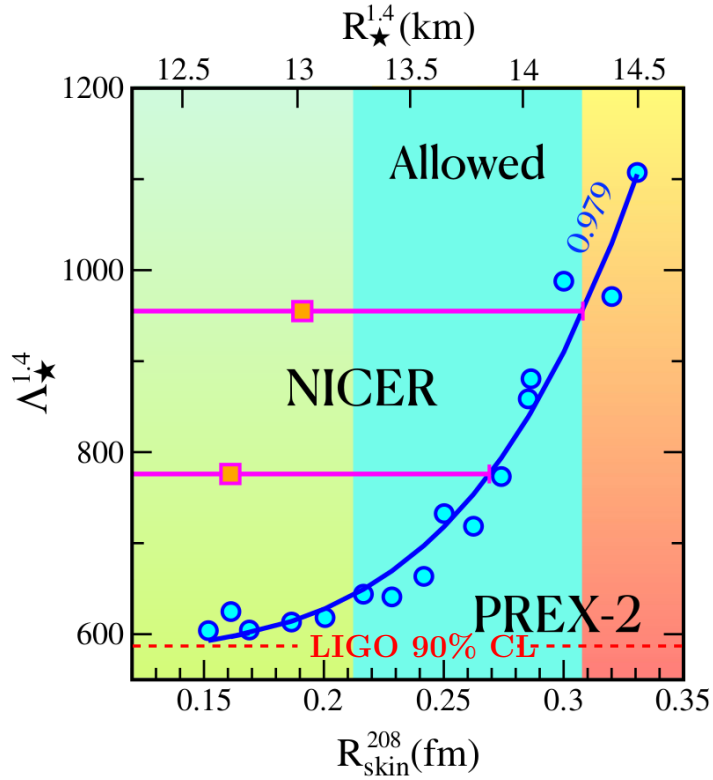


Figure 6.7: Tidal deformability of a $1.4 M_\odot$ neutron star versus its radius (upper X-axis) and the neutron skin thickness of ^{208}Pb (lower X-axis). Blue dots show theoretical predictions from a set of EDFs, the blue line is a fit to these dots. PREX-2 in the plot refers to the combined result of PREX-I and II. The light blue region corresponds to the radius range allowed by both NICER and PREX-2 [72]

Measurement Of a Lepton Lepton Electroweak Reaction (MOLLER)

As a test of the SM, the weak mixing angle ($\sin^2 \theta_W$) is of great importance and have been measured by different experiments, as shown in Fig. 6.9.

The proposed MOLLER experiment at JLab, as the successor to the SLAC E158 experiment [42], intends to improve the E158 result by a factor of five, which will be a 2.4% relative uncertainty in Q_W^e , corresponding to a 2.1% relative uncertainty in the measurement of \mathcal{A}_{PV} (33 ± 0.7 ppb). This low energy precision frontier experiment will produce the most precise measurement of $\sin^2 \theta_W$ over the next decade. With such high precision, the result will be sensitive to interference of the known EM amplitude and any possible new neutral currents, probing new particles beyond the Higgs mass up to a scale of ~ 27 TeV.

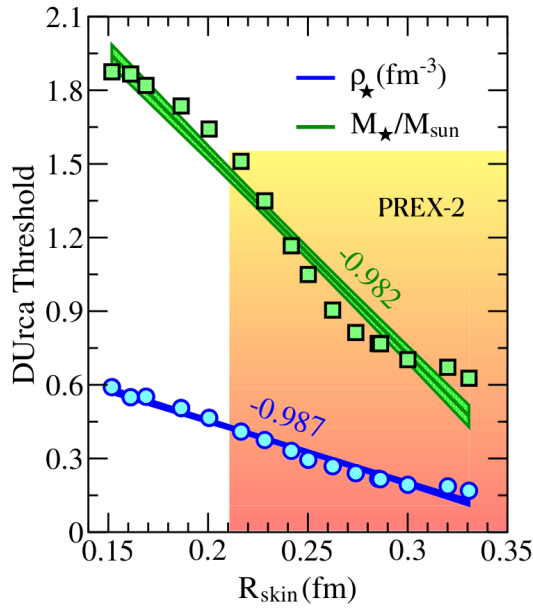


Figure 6.8: The direct Urca threshold densities (blue dots) and corresponding stellar mass (green dots) versus the neutron skin thickness of ^{208}Pb . PREX-2 in the plot refers to the combined result of PREX-I and II. The shaded area represents the combined PREX 1- σ confidence region [72].

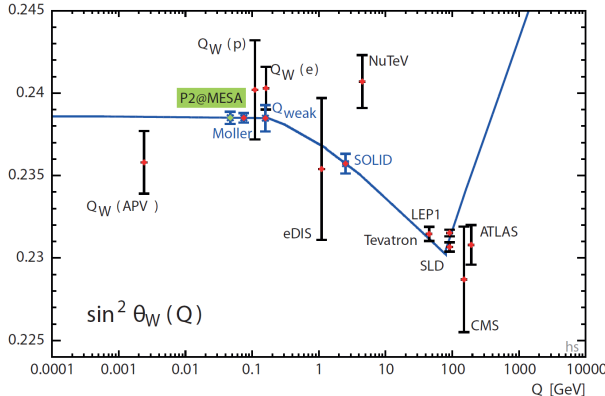


Figure 6.9: Various (proposed) measurements of the running weak mixing angle along the energy scale.

Solenoidal Large Intensity Device (SoLID)

SoLID is another JLab proposal to probe the parity-violating effect in deep inelastic scattering (PVDIS). SoLID refers to a new spectrometer of large angular and momentum acceptance, meanwhile, it can handle high luminosity. This new apparatus will measure \mathcal{A}_{PV} to a very high precision of about 0.5% over a wide range of the Bjorken x and Q^2 . The SoLID PVDIS project will use several different targets. Deuterium will provide a new measurement of the weak mixing angle in the medium energy region, which is shown

in Fig. 6.9; with a hydrogen target, the proton d/u ratio can be measured and a heavy nucleus like ^{208}Pb allows to study the flavor dependence of the EMC effect [87].

P2 and MREX

While MOLLER will be the most precise weak mixing angle measurement, the most precise weak charge measurement will be the P2 experiment at Mainz. P2 will measure the weak charge of the proton that has been measured by the Qweak experiment at JLab [43]. Compared to Qweak, P2 will improve the measurement precision by a factor of three, aiming for a 0.15% precision in the determination of the weak mixing angle. Similar to MOLLER, with this very high precision, P2 enables an indirect search for new physics up to a mass scale of 50 TeV.

Finally, the Mainz radius experiemnt (MREX) will measure the neutron skin thickness of ^{208}Pb again, at a lower q value and will improve the PREX result to a higher precision of 1.4% [86].

Overall, developments of the experimental technique encourage the next generation PVES experiments to pursue higher precision in the measurements of the parity-violating asymmetry, making them good candidates for searches of new physics beyond the standard model. In terms of nuclear physics, this trend will lead to better understanding of the nuclear structure, maybe a surprise in the future.

Bibliography

- [1] G. Royer. On the coefficients of the liquid drop model mass formulae and nuclear radii. *Nuclear Physics A*, 807(3):105–118, 2008. ISSN 0375-9474. doi: <https://doi.org/10.1016/j.nuclphysa.2008.04.002>. URL <https://www.sciencedirect.com/science/article/pii/S0375947408004739>.
- [2] H. De Vries, C.W. De Jager, and C. De Vries. Nuclear charge-density-distribution parameters from elastic electron scattering. *Atomic Data and Nuclear Data Tables*, 36(3):495–536, 1987. ISSN 0092-640X. doi: [https://doi.org/10.1016/0092-640X\(87\)90013-1](https://doi.org/10.1016/0092-640X(87)90013-1). URL <https://www.sciencedirect.com/science/article/pii/0092640X87900131>.
- [3] I. Angeli and K.P. Marinova. Table of experimental nuclear ground state charge radii: An update. *Atomic Data and Nuclear Data Tables*, 99(1):69–95, 2013. ISSN 0092-640X. doi: <https://doi.org/10.1016/j.adt.2011.12.006>. URL <https://www.sciencedirect.com/science/article/pii/S0092640X12000265>.
- [4] B.W. Allardyce, C.J. Batty, D.J. Baugh, E. Friedman, G. Heymann, M.E. Cage, G.J. Pyle, G.T.A. Squier, A.S. Clough, D.F. Jackson, S. Murugesu, and V. Rajaratnam. Pion reaction cross sections and nuclear sizes. *Nuclear Physics A*, 209(1):1–51, 1973. ISSN 0375-9474. doi: [https://doi.org/10.1016/0375-9474\(73\)90049-3](https://doi.org/10.1016/0375-9474(73)90049-3). URL <https://www.sciencedirect.com/science/article/pii/0375947473900493>.
- [5] J.C. Lombardi, R.N. Boyd, R. Arking, and A.B. Robbins. Nuclear sizes in 40, 44, 48ca. *Nuclear Physics A*, 188(1):103–114, 1972. ISSN 0375-9474. doi: [https://doi.org/10.1016/0375-9474\(72\)90186-8](https://doi.org/10.1016/0375-9474(72)90186-8). URL <https://www.sciencedirect.com/science/article/pii/0375947472901868>.
- [6] J. Zenihiro, H. Sakaguchi, T. Murakami, M. Yosoi, Y. Yasuda, S. Terashima, Y. Iwao, H. Takeda, M. Itoh, H. P. Yoshida, and M. Uchida. Neutron density distributions of $^{204,206,208}\text{Pb}$ deduced via proton elastic scattering at $E_p = 295$ mev. *Phys. Rev. C*, 82:044611, Oct 2010. doi: [10.1103/PhysRevC.82.044611](https://doi.org/10.1103/PhysRevC.82.044611). URL <https://link.aps.org/doi/10.1103/PhysRevC.82.044611>.
- [7] B. Kłos, A. Trzcińska, J. Jastrzebski, T. Czosnyka, M. Kisielński, P. Lubiński, P. Napiorkowski, L. Pieńkowski, F. J. Hartmann, B. Ketzer, P. Ring, R. Schmidt, T. von Egidy, R. Smolańczuk, S. Wycech, K. Gulda, W. Kurcewicz, E. Widmann, and B. A. Brown. Neutron density distributions from antiprotonic ^{208}Pb and ^{209}Bi

- atoms. *Phys. Rev. C*, 76:014311, Jul 2007. doi: 10.1103/PhysRevC.76.014311. URL <https://link.aps.org/doi/10.1103/PhysRevC.76.014311>.
- [8] A. Krasznahorkay, H. Akimune, A.M. van den Berg, N. Blasi, S. Brandenburg, M. Csatlots, M. Fujiwara, J. Gulyats, M.N. Harakeh, M. Hunyadi, M. de Huu, Z. Matte, D. Sohler, S.Y. van der Werf, H.J. Wołrtche, and L. Zolnai. Neutron-skin thickness in neutron-rich isotopes. *Nuclear Physics A*, 731:224–234, 2004. ISSN 0375-9474. doi: <https://doi.org/10.1016/j.nuclphysa.2003.11.034>. URL <https://www.sciencedirect.com/science/article/pii/S0375947403018712>.
- [9] X. Roca-Maza, B. K. Agrawal, G. Colò, W. Nazarewicz, N. Paar, J. Piekarewicz, P.-G. Reinhard, and D. Vretenar. Sensitivity of the electric dipole polarizability to the neutron skin thickness in $[sup 208]pb$. In *AIP Conference Proceedings*. AIP, 2012. doi: 10.1063/1.4764239. URL <https://doi.org/10.1063%2F1.4764239>.
- [10] V. Baran, M. Colonna, M. Di Toro, A. Croitoru, and D. Dumitru. Connecting the pygmy dipole resonance to the neutron skin. *Phys. Rev. C*, 88:044610, Oct 2013. doi: 10.1103/PhysRevC.88.044610. URL <https://link.aps.org/doi/10.1103/PhysRevC.88.044610>.
- [11] M. H. Johnson and E. Teller. Proton distribution in heavy nuclei. *Phys. Rev.*, 93: 357–358, Jan 1954. doi: 10.1103/PhysRev.93.357. URL <https://link.aps.org/doi/10.1103/PhysRev.93.357>.
- [12] E.H.S. Burhop, D.H. Davis, J. Sacton, and G. Schorochoff. k^- meson capture by nuclei and the existence of a neutron halo in heavy nuclei. *Nuclear Physics A*, 132(3):625–628, 1969. ISSN 0375-9474. doi: [https://doi.org/10.1016/0375-9474\(69\)90723-4](https://doi.org/10.1016/0375-9474(69)90723-4). URL <https://www.sciencedirect.com/science/article/pii/0375947469907234>.
- [13] Francesca Sammarruca and Randy Millerson. Nuclear forces in the medium: Insight from the equation of state. *Frontiers in Physics*, 7, 2019. ISSN 2296-424X. doi: 10.3389/fphy.2019.00213. URL <https://www.frontiersin.org/articles/10.3389/fphy.2019.00213>.
- [14] J. B. Bellicard, P. Bounin, R. F. Frosch, R. Hofstadter, J. S. McCarthy, F. J. Uhrhane, M. R. Yearian, B. C. Clark, R. Herman, and D. G. Ravenhall. Scattering of 750-mev electrons by calcium isotopes. *Phys. Rev. Lett.*, 19:527–529, Aug 1967. doi: 10.1103/PhysRevLett.19.527. URL <https://link.aps.org/doi/10.1103/PhysRevLett.19.527>.
- [15] B. Frois, J. B. Bellicard, J. M. Cavedon, M. Huet, P. Leconte, P. Ludeau, A. Nakada, Phan Zuan Hô, and I. Sick. High-momentum-transfer electron scattering from ^{208}Pb . *Phys. Rev. Lett.*, 38:152–155, Jan 1977. doi: 10.1103/PhysRevLett.38.152. URL <https://link.aps.org/doi/10.1103/PhysRevLett.38.152>.
- [16] L. C. Maximon and R. A. Schrack. The form factor of the Fermi model spatial distribution. *J. Res. Natl. Bur. Stand. B*, 70(1), 1966. doi: 10.6028/jres.070b.007.

- [17] B. G. Todd-Rutel and J. Piekarewicz. Neutron-rich nuclei and neutron stars: A new accurately calibrated interaction for the study of neutron-rich matter. *Phys. Rev. Lett.*, 95:122501, Sep 2005. doi: 10.1103/PhysRevLett.95.122501. URL <https://link.aps.org/doi/10.1103/PhysRevLett.95.122501>.
- [18] C. J. Horowitz. Parity violating elastic electron scattering and coulomb distortions. *Phys. Rev. C*, 57:3430–3436, Jun 1998. doi: 10.1103/PhysRevC.57.3430. URL <https://link.aps.org/doi/10.1103/PhysRevC.57.3430>.
- [19] X. Roca-Maza, M. Centelles, X. Viñas, and M. Warda. Neutron skin of ^{208}Pb , nuclear symmetry energy, and the parity radius experiment. *Phys. Rev. Lett.*, 106:252501, Jun 2011. doi: 10.1103/PhysRevLett.106.252501. URL <https://link.aps.org/doi/10.1103/PhysRevLett.106.252501>.
- [20] J. Schechter and H. Weigel. The skyrme model for baryons, 1999. URL <https://arxiv.org/abs/hep-ph/9907554>.
- [21] B. Alex Brown. New skyrme interaction for normal and exotic nuclei. *Phys. Rev. C*, 58:220–231, Jul 1998. doi: 10.1103/PhysRevC.58.220. URL <https://link.aps.org/doi/10.1103/PhysRevC.58.220>.
- [22] B. Alex Brown. Neutron radii in nuclei and the neutron equation of state. *Phys. Rev. Lett.*, 85(0):5296–5299, Dec 2000. doi: 10.1103/PhysRevLett.85.5296. URL <https://link.aps.org/doi/10.1103/PhysRevLett.85.5296>.
- [23] Hideki Yukawa. On the Interaction of Elementary Particles. I. *Progress of Theoretical Physics Supplement*, 1:1–10, 01 1955. ISSN 0375-9687. doi: 10.1143/PTPS.1.1. URL <https://doi.org/10.1143/PTPS.1.1>.
- [24] Steven Weinberg. Phenomenological lagrangians. *Physica A: Statistical Mechanics and its Applications*, 96(1):327–340, 1979. ISSN 0378-4371. doi: [https://doi.org/10.1016/0378-4371\(79\)90223-1](https://doi.org/10.1016/0378-4371(79)90223-1). URL <https://www.sciencedirect.com/science/article/pii/0378437179902231>.
- [25] G. Hagen, A. Ekström, C. Forssén, G. R. Jansen, W. Nazarewicz, T. Papenbrock, K. A. Wendt, S. Bacca, N. Barnea, B. Carlsson, C. Drischler, K. Hebeler, M. Hjorth-Jensen, M. Miorelli, G. Orlandini, A. Schwenk, and J. Simonis. Neutron and weak-charge distributions of the ^{48}Ca nucleus. *Nature Physics*, 12(2):186–190, Feb 2016. ISSN 1745-2481. doi: 10.1038/nphys3529. URL <https://doi.org/10.1038/nphys3529>.
- [26] J. M. Lattimer and M. Prakash. Neutron star structure and the equation of state. *The Astrophysical Journal*, 550(1):426–442, mar 2001. doi: 10.1086/319702. URL <https://doi.org/10.1086/319702>.
- [27] Enrico Fermi. Tentativo di una teoria dei raggi β . *Il Nuovo Cimento (1924-1942)*, 11(1):1–19, Jan 1934. ISSN 1827-6121. doi: 10.1007/BF02959820. URL <https://doi.org/10.1007/BF02959820>.

- [28] T. D. Lee and C. N. Yang. Parity nonconservation and a two-component theory of the neutrino. *Phys. Rev.*, 105:1671–1675, Mar 1957. doi: 10.1103/PhysRev.105.1671. URL <https://link.aps.org/doi/10.1103/PhysRev.105.1671>.
- [29] C. S. Wu, E. Ambler, R. W. Hayward, D. D. Hoppes, and R. P. Hudson. Experimental test of parity conservation in beta decay. *Phys. Rev.*, 105:1413–1415, Feb 1957. doi: 10.1103/PhysRev.105.1413. URL <https://link.aps.org/doi/10.1103/PhysRev.105.1413>.
- [30] M. Goldhaber, L. Grodzins, and A. W. Sunyar. Helicity of neutrinos. *Phys. Rev.*, 109:1015–1017, Feb 1958. doi: 10.1103/PhysRev.109.1015. URL <https://link.aps.org/doi/10.1103/PhysRev.109.1015>.
- [31] E. C. G. Sudarshan and R. E. Marshak. Chirality invariance and the universal fermi interaction. *Phys. Rev.*, 109:1860–1862, Mar 1958. doi: 10.1103/PhysRev.109.1860.2. URL <https://link.aps.org/doi/10.1103/PhysRev.109.1860.2>.
- [32] R. P. Feynman and M. Gell-Mann. Theory of the fermi interaction. *Phys. Rev.*, 109: 193–198, Jan 1958. doi: 10.1103/PhysRev.109.193. URL <https://link.aps.org/doi/10.1103/PhysRev.109.193>.
- [33] F.J. Hasert, S. Kabe, W. Krenz, J. Von Krogh, D. Lanske, J. Morfin, K. Schultze, H. Weerts, G. Bertrand-Coremans, J. Sacton, W. Van Doninck, P. Vilain, R. Baldi, U. Camerini, D.C. Cundy, I. Danilchenko, W.F. Fry, D. Haidt, S. Natali, P. Musset, B. Osculati, R. Palmer, J.B.M. Pattison, D.H. Perkins, A. Pullia, A. Rousset, W. Venus, H. Wachsmuth, V. Brisson, B. Degrange, M. Haguenuauer, L. Kluberg, U. Nguyen-Khac, P. Petiau, E. Bellotti, S. Bonetti, D. Cavalli, C. Conta, E. Fiorini, M. Rollier, B. Aubert, D. Blum, L.M. Chouinet, P. Heusse, A. Lagarrigue, A.M. Lutz, A. Orkin-Lecourtois, J.P. Vialle, F.W. Bullock, M.J. Esten, T.W. Jones, J. McKenzie, A.G. Michette, G. Myatt, and W.G. Scott. Observation of neutrino-like interactions without muon or electron in the gargamelle neutrino experiment. *Nuclear Physics B*, 73(1):1–22, 1974. ISSN 0550-3213. doi: [https://doi.org/10.1016/0550-3213\(74\)90038-8](https://doi.org/10.1016/0550-3213(74)90038-8). URL <https://www.sciencedirect.com/science/article/pii/0550321374900388>.
- [34] Ya. B. Zel'dovich. Parity nonconservation in the first order in the weak-interaction constant in electron scattering and other effects. *Journal of Experimental and Theoretical Physics*, 9(3):682, 1959. URL http://www.jetp.ras.ru/cgi-bin/dn/e_009_03_0682.pdf.
- [35] C.Y. Prescott, W.B. Atwood, R.L.A. Cottrell, H. DeStaebler, Edward L. Garwin, A. Gonidec, R.H. Miller, L.S. Rochester, T. Sato, D.J. Sherden, C.K. Sinclair, S. Stein, R.E. Taylor, J.E. Clendenin, V.W. Hughes, N. Sasao, K.P. Schüler, M.G. Borghini, K. Lübelsmeyer, and W. Jentschke. Parity non-conservation in inelastic electron scattering. *Physics Letters B*, 77(3):347–352, 1978. ISSN 0370-2693. doi: [https://doi.org/10.1016/0370-2693\(78\)90722-0](https://doi.org/10.1016/0370-2693(78)90722-0). URL <https://www.sciencedirect.com/science/article/pii/0370269378907220>.

- [36] P. A. Souder, R. Holmes, D.-H. Kim, K. S. Kumar, M. E. Schulze, K. Isakovich, G. W. Dodson, K. W. Dow, M. Farkhondeh, S. Kowalski, M. S. Lubell, J. Bellanca, M. Goodman, S. Patch, Richard Wilson, G. D. Cates, S. Dhawan, T. J. Gay, V. W. Hughes, A. Magnon, R. Michaels, and H. R. Schaefer. Measurement of parity violation in the elastic scattering of polarized electrons from ^{12}C . *Phys. Rev. Lett.*, 65:694–697, Aug 1990. doi: 10.1103/PhysRevLett.65.694. URL <https://link.aps.org/doi/10.1103/PhysRevLett.65.694>.
- [37] W. Heil, J. Ahrens, H.G. Andresen, A. Bornheimer, D. Conrath, K.-J. Dietz, W. Gasteyer, H.-J. Gessinger, W. Hartmann, J. Jethwa, H.-J. Kluge, H. Kessler, T. Kettner, L. Koch, F. Neugebauer, R. Neuhausen, E.W. Otten, E. Reichert, F.P. Schäfer, and B. Wagner. Improved limits on the weak, neutral, hadronic axial vector coupling constants from quasielastic scattering of polarized electrons. *Nuclear Physics B*, 327(1):1–31, 1989. ISSN 0550-3213. doi: [https://doi.org/10.1016/0550-3213\(89\)90284-8](https://doi.org/10.1016/0550-3213(89)90284-8). URL <https://www.sciencedirect.com/science/article/pii/0550321389902848>.
- [38] Sample at mit-bates. URL <https://bateslab.mit.edu/projects/sample>.
- [39] The g0 experiment. URL <http://research.npl.illinois.edu/exp/G0/publicWeb/>.
- [40] Happex collaboration. URL <https://hallaweb.jlab.org/experiment/HAPPEX/>.
- [41] A4 collaboration at mami. URL <https://www.blogs.uni-mainz.de/fb08-ag-maas/a4-collaboration-at-mami/>.
- [42] P. L. et al. Anthony. Precision measurement of the weak mixing angle in møller scattering. *Phys. Rev. Lett.*, 95:081601, Aug 2005. doi: 10.1103/PhysRevLett.95.081601. URL <https://link.aps.org/doi/10.1103/PhysRevLett.95.081601>.
- [43] D. et al. Androic. First determination of the weak charge of the proton. *Phys. Rev. Lett.*, 111:141803, Oct 2013. doi: 10.1103/PhysRevLett.111.141803. URL <https://link.aps.org/doi/10.1103/PhysRevLett.111.141803>.
- [44] D. et al. Wang. Measurements of parity-violating asymmetries in electron-deuteron scattering in the nucleon resonance region. *Phys. Rev. Lett.*, 111:082501, Aug 2013. doi: 10.1103/PhysRevLett.111.082501. URL <https://link.aps.org/doi/10.1103/PhysRevLett.111.082501>.
- [45] SoLID Collaboration. Precision measurement of parity-violation in deep inelastic scattering over a broad kinematic range. 2008. URL <https://hallaweb.jlab.org/collab/PAC/PAC34/PR-09-012-pvdis.pdf>.
- [46] Moller. URL https://moller.jlab.org/moller_root/.
- [47] Mesa-p2. URL <https://www.blogs.uni-mainz.de/fb08p2/>.

- [48] S. et al. Abrahamyan. Measurement of the neutron radius of ^{208}Pb through parity violation in electron scattering. *Phys. Rev. Lett.*, 108:112502, Mar 2012. doi: 10.1103/PhysRevLett.108.112502. URL <https://link.aps.org/doi/10.1103/PhysRevLett.108.112502>.
- [49] Juliette Mammei et al. Proposal to jefferson lab pac 40 crex: Parity-violating measurement of the weak charge distribution of 48 ca to 0.02 fm accuracy. 2013. URL https://hallaweb.jlab.org/parity/prex/c-rex2013_v7.pdf.
- [50] Kent D. Paschke et al. Proposal to jefferson lab pac 38 prex-ii: Precision parity-violating measurement of the neutron skin of lead. 2011. URL <https://hallaweb.jlab.org/parity/prex/prexII.pdf>.
- [51] The Hall A Collaboration. Jefferson lab hall a standard equipment manual. Jun 2019. URL <https://hallaweb.jlab.org/github/halla-osp/version/Standard-Equipment-Manual.pdf>.
- [52] E. L. Garwin D. T. Pierce and H. C. Siegmann. *Helv. Phys. Acta*, 47:393, 1974.
- [53] G. Lampel and C. Weisbuch. Proposal for an efficient source of polarized photo-electrons from semiconductors. *Solid State Communications*, 16(7):877–880, 1975. ISSN 0038-1098. doi: [https://doi.org/10.1016/0038-1098\(75\)90884-4](https://doi.org/10.1016/0038-1098(75)90884-4). URL <https://www.sciencedirect.com/science/article/pii/0038109875908844>.
- [54] L.S. Cardman. Polarized electron sources for the 1990’s. *Nuclear Physics A*, 546(1):317–336, 1992. ISSN 0375-9474. doi: [https://doi.org/10.1016/0375-9474\(92\)90518-O](https://doi.org/10.1016/0375-9474(92)90518-O). URL <https://www.sciencedirect.com/science/article/pii/0375947492905180>.
- [55] Caryn A. Palatchi. *Thesis: Laser and Electron Beam Technology for Parity Violating Electron Scattering Measurements*. PhD thesis, 2019. URL https://misportal.jlab.org/ul/publications/search/advanced_search.cfm.
- [56] Philip A. Adderley, Steven Covert, Joseph Grames, John Hansknecht, Kenneth Surles-Law, Danny Machie, Bernard Poelker, Marcy L. Stutzman, Riad Suleiman, and James Clark. Photoinjector improvements at cebaf in support of parity violation experiments. *Nuovo Cimento C*, 35(4), 7 2012. ISSN 1826-9885. doi: 10.1393/ncc/i2012-11288-3. URL <https://www.osti.gov/biblio/1059486>.
- [57] J. M. Grames, C. K. Sinclair, M. Poelker, X. Roca-Maza, M. L. Stutzman, R. Suleiman, Md. A. Mamun, M. McHugh, D. Moser, J. Hansknecht, B. Moffit, and T. J. Gay. High precision 5 mev mott polarimeter. *Phys. Rev. C*, 102:015501, Jul 2020. doi: 10.1103/PhysRevC.102.015501. URL <https://link.aps.org/doi/10.1103/PhysRevC.102.015501>.
- [58] Noah Sherman. Coulomb scattering of relativistic electrons by point nuclei. *Phys. Rev.*, 103:1601–1607, Sep 1956. doi: 10.1103/PhysRev.103.1601. URL <https://link.aps.org/doi/10.1103/PhysRev.103.1601>.

- [59] J. M. Grames, C. K. Sinclair, J. Mitchell, E. Chudakov, H. Fenker, A. Freyberger, D. W. Higinbotham, M. Poelker, M. Steigerwald, M. Tiefenback, C. Cavaata, S. Escoffier, F. Marie, T. Pussieux, P. Vernin, S. Danagoulian, V. Dharmawardane, R. Fatemi, K. Joo, M. Zeier, V. Gorbenko, R. Nasseripour, B. Rau, R. Suleiman, and B. Zihlmann. Unique electron polarimeter analyzing power comparison and precision spin-based energy measurement. *Phys. Rev. ST Accel. Beams*, 7:042802, Apr 2004. doi: 10.1103/PhysRevSTAB.7.042802. URL <https://link.aps.org/doi/10.1103/PhysRevSTAB.7.042802>.
- [60] J.-C. Denard, A. Saha, and G. Laveissiere. High accuracy beam current monitor system for cebaf's experimental hall a. In *PACS2001. Proceedings of the 2001 Particle Accelerator Conference (Cat. No.01CH37268)*, volume 3, pages 2326–2328 vol.3, 2001. doi: 10.1109/PAC.2001.987367.
- [61] Devi Lal Adhikari. *Thesis: Neutron Skin Measurement of ^{208}Pb Using Parity-Violating Electron Scattering*. PhD thesis, 2021. URL https://misportal.jlab.org/ul/publications/search/advanced_search.cfm.
- [62] Hall a images. URL <https://www.jlab.org/help/Ghelp/halla3d.html>.
- [63] K.G Fissum, W Bertozzi, J.P Chen, D Dale, H.C Fenker, J Gao, A Gavalya, S Gilad, C.R Leathers, N Liyanage, R.O Michaels, E.A.J.M Offermann, J Segal, J.A Templon, R Wechsler, B Wojtsekowski, and J Zhao. Vertical drift chambers for the hall a high-resolution spectrometers at jefferson lab. *Nuclear Instruments and Methods in Physics Research Section A: Accelerators, Spectrometers, Detectors and Associated Equipment*, 474(2):108–131, 2001. ISSN 0168-9002. doi: [https://doi.org/10.1016/S0168-9002\(01\)00875-0](https://doi.org/10.1016/S0168-9002(01)00875-0). URL <https://www.sciencedirect.com/science/article/pii/S0168900201008750>.
- [64] Coda. URL <https://coda.jlab.org/drupal/>.
- [65] Roger Flood, Scott Higgins, , and Riad Suleiman. Helicity control board user's guide (draft 2). 2010.
- [66] Epics. URL <https://epics.anl.gov/>.
- [67] Cameron Clarke. *Thesis: Measurement of Parity Violating Asymmetry in Elastic Electron Scattering off ^{48}Ca* . PhD thesis, 2021. URL https://misportal.jlab.org/ul/publications/search/advanced_search.cfm.
- [68] S. et al. Abrahamyan. New measurements of the transverse beam asymmetry for elastic electron scattering from selected nuclei. *Phys. Rev. Lett.*, 109:192501, Nov 2012. doi: 10.1103/PhysRevLett.109.192501. URL <https://link.aps.org/doi/10.1103/PhysRevLett.109.192501>.
- [69] Oleksandr Koshchii, Mikhail Gorchtein, Xavier Roca-Maza, and Hubert Spiesberger. Beam-normal single-spin asymmetry in elastic scattering of electrons from a spin-0

- nucleus. *Phys. Rev. C*, 103:064316, Jun 2021. doi: 10.1103/PhysRevC.103.064316. URL <https://link.aps.org/doi/10.1103/PhysRevC.103.064316>.
- [70] Ryan Richards. *Measurements of the Beam Normal Asymmetry using Polarized Elastic Electron Scattering off Various Spin-0 Nuclei at 1 GeV*. PhD thesis, 2021. URL https://misportal.jlab.org/ul/publications/search/advanced_search.cfm.
- [71] D. et al. Adhikari. Accurate determination of the neutron skin thickness of ^{208}Pb through parity-violation in electron scattering. *Phys. Rev. Lett.*, 126:172502, Apr 2021. doi: 10.1103/PhysRevLett.126.172502. URL <https://link.aps.org/doi/10.1103/PhysRevLett.126.172502>.
- [72] Brendan T. Reed, F. J. Fattoyev, C. J. Horowitz, and J. Piekarewicz. Implications of prex-2 on the equation of state of neutron-rich matter. *Phys. Rev. Lett.*, 126:172503, Apr 2021. doi: 10.1103/PhysRevLett.126.172503. URL <https://link.aps.org/doi/10.1103/PhysRevLett.126.172503>.
- [73] D. et al. Adhikari. Precision determination of the neutral weak form factor of ^{48}Ca . *Phys. Rev. Lett.*, 129:042501, Jul 2022. doi: 10.1103/PhysRevLett.129.042501. URL <https://link.aps.org/doi/10.1103/PhysRevLett.129.042501>.
- [74] Discovery of nuclides project. URL <https://people.nscl.msu.edu/~thoennes/isotopes/>.
- [75] D. S. Ahn, N. Fukuda, H. Geissel, N. Inabe, N. Iwasa, T. Kubo, K. Kusaka, D. J. Morrissey, D. Murai, T. Nakamura, M. Ohtake, H. Otsu, H. Sato, B. M. Sherrill, Y. Shimizu, H. Suzuki, H. Takeda, O. B. Tarasov, H. Ueno, Y. Yanagisawa, and K. Yoshida. Location of the neutron dripline at fluorine and neon. *Phys. Rev. Lett.*, 123:212501, Nov 2019. doi: 10.1103/PhysRevLett.123.212501. URL <https://link.aps.org/doi/10.1103/PhysRevLett.123.212501>.
- [76] Erler, Jochen, Birge, Noah, Kortelainen, Markus, Nazarewicz, Witold, Olsen, Erik, Perhac, Alexander M., Stoitsov, and Mario. The limits of the nuclear landscape. *Nature*, 486(7404):509–512, Jun 2012. ISSN 1476-4687. doi: 10.1038/nature11188. URL <https://doi.org/10.1038/nature11188>.
- [77] C. J. Horowitz, J. Piekarewicz, and Brendan Reed. Insights into nuclear saturation density from parity-violating electron scattering. *Phys. Rev. C*, 102:044321, Oct 2020. doi: 10.1103/PhysRevC.102.044321. URL <https://link.aps.org/doi/10.1103/PhysRevC.102.044321>.
- [78] Wei-Chia Chen and J. Piekarewicz. Building relativistic mean field models for finite nuclei and neutron stars. *Phys. Rev. C*, 90:044305, Oct 2014. doi: 10.1103/PhysRevC.90.044305. URL <https://link.aps.org/doi/10.1103/PhysRevC.90.044305>.

- [79] C. Drischler, K. Hebeler, and A. Schwenk. Chiral interactions up to next-to-next-to-next-to-leading order and nuclear saturation. *Phys. Rev. Lett.*, 122:042501, Jan 2019. doi: 10.1103/PhysRevLett.122.042501. URL <https://link.aps.org/doi/10.1103/PhysRevLett.122.042501>.
- [80] The neutron star interior composition explorer mission. URL <https://heasarc.gsfc.nasa.gov/docs/nicer/>.
- [81] B. P. et al. Abbott. Gw170817: Observation of gravitational waves from a binary neutron star inspiral. *Phys. Rev. Lett.*, 119:161101, Oct 2017. doi: 10.1103/PhysRevLett.119.161101. URL <https://link.aps.org/doi/10.1103/PhysRevLett.119.161101>.
- [82] B. P. et al. Abbott. Gw170817: Measurements of neutron star radii and equation of state. *Phys. Rev. Lett.*, 121:161101, Oct 2018. doi: 10.1103/PhysRevLett.121.161101. URL <https://link.aps.org/doi/10.1103/PhysRevLett.121.161101>.
- [83] Paweł Haensel. Urca processes in dense matter and neutron star cooling. *Space Science Reviews*, 74(3):427–436, Nov 1995. ISSN 1572-9672. doi: 10.1007/BF00751429. URL <https://doi.org/10.1007/BF00751429>.
- [84] Edward F. Brown, Andrew Cumming, Farrukh J. Fattoyev, C. J. Horowitz, Dany Page, and Sanjay Reddy. Rapid neutrino cooling in the neutron star mxb 1659-29. *Phys. Rev. Lett.*, 120:182701, Apr 2018. doi: 10.1103/PhysRevLett.120.182701. URL <https://link.aps.org/doi/10.1103/PhysRevLett.120.182701>.
- [85] MOLLER Collaboration. The moller experiment: An ultra-precise measurement of the weak mixing angle using møller scattering. 2014. doi: 10.48550/ARXIV.1411.4088. URL <https://arxiv.org/abs/1411.4088>.
- [86] Dominik et al. Becker. The p2 experiment. *The European Physical Journal A*, 54(11):208, Nov 2018. ISSN 1434-601X. doi: 10.1140/epja/i2018-12611-6. URL <https://doi.org/10.1140/epja/i2018-12611-6>.
- [87] Jean-Jacques et al. Aubert. The ratio of the nucleon structure functions F_2^N for iron and deuterium. *Phys. Lett. B*, 123:275–278, 1983. doi: 10.1016/0370-2693(83)90437-9. URL <https://cds.cern.ch/record/142300>.

Appendix A

Symmetry Energy

$$E_k = C(N^{5/3} + Z^{5/3})$$

Let: $A = N + Z$ and $B = N - Z$, then we have $N + \frac{A+B}{2}$, $Z = \frac{A-B}{2}$ and $B \ll A$:

$$\begin{aligned} E_k &= C \left(\left(\frac{A+B}{2} \right)^{5/3} + \left(\frac{A-B}{2} \right)^{5/3} \right) \\ &= C \left(\frac{A}{2} \right)^{5/3} \left(\left(1 + \frac{B}{A} \right)^{5/3} + \left(1 - \frac{B}{A} \right)^{5/3} \right) \\ &= C \left(\frac{A}{2} \right)^{5/3} \left(\left(1 + \frac{5B}{3A} + \frac{1}{2!} \frac{5}{3} \frac{2}{3} \left(\frac{B}{A} \right)^2 + \dots \right) + \left(1 + \frac{5}{3} \left(-\frac{B}{A} \right) + \frac{1}{2!} \frac{5}{3} \frac{2}{3} \left(-\frac{B}{A} \right)^2 + \dots \right) \right) \\ &= 2^{-2/3} C \left(A^{5/3} + \frac{5}{9} \frac{B^2}{A^{1/3}} \right) + O\left(\frac{B^4}{A^{7/3}}\right) \\ &= 2^{-2/3} C \left(A^{5/3} + \frac{5}{9} \frac{(N-Z)^2}{A^{1/3}} \right) + O((N-Z)^4) \end{aligned}$$

A.1 ^{208}Pb Foils Measurement

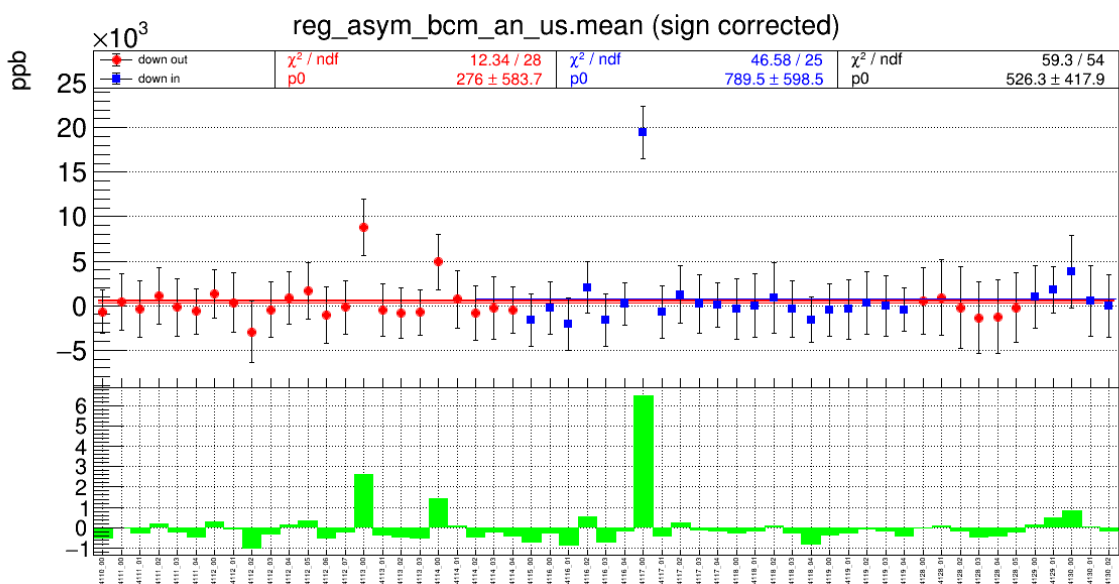


Figure A.1: charge asymmetry outlier in run 4117, minirun 0

Pb #	mass (g)	top left (mm)				top right (mm)				bottom right (mm)				bottom left (mm)				area (mm ²)	t (μ m)	area density (mg/cm ²)
		x1	y1	x2	y2	x3	y3	x4	y4	x4	y4	x3	y3	x2	y2	x1	y1			
1	3.6526	0.005	-0.015	24.221	0.532	24.956	-23.743	0.655	-24.249	588.3778	545.51	620.792								
2	3.6973	-0.005	-0.012	24.079	-0.2	23.897	-24.338	-0.327	-24.294	584.7683	555.60	632.267								
3	3.6325	-0.009	0.01	24.156	-0.039	24.08	-24.06	-0.194	-23.904	580.4809	549.89	625.774								
4	3.6722	-0.013	-0.003	24.1	-0.302	24.048	-24.386	-0.133	-24.363	584.8886	551.71	627.846								
5	3.6989	-0.002	-0.001	24.199	0.003	24.261	-24.136	0.083	-24.249	585.2287	555.40	632.044								
6	3.6162	-0.005	-0.001	24.328	-0.223	24.012	-24.386	0.026	-24.276	585.1189	543.08	618.028								
7	3.6966	0.001	0.003	24.208	0.007	24.155	-23.991	0.022	-23.869	578.5090	561.50	638.988								
8	3.6315	0.008	0.002	24.115	0.016	23.969	-24.312	-0.158	-24.204	585.2472	545.26	620.507								
9	3.6307	0.005	0.003	24.216	-0.268	23.992	-24.704	-0.149	-24.421	590.6197	540.18	614.727								
10	3.6283	-0.052	-0.029	23.973	-0.225	24.032	-24.234	-0.297	-24.213	582.5811	547.27	622.797								

Table A.1: area was calculated as $A = \frac{(x2-x1)+(x3-x4)}{2} \times \frac{(y1-y3)+(y2-y4)}{2}$. ^{208}Pb density is 11.38 g/cm^2 .

run	#entry	θ			Q^2		
		mean	RMS	mean error	mean	RMS	mean error
1853	248697	4.741	0.447	8.96E-4	0.006239	0.001204	2.41E-6
1983	746777	4.747	0.4536	5.25E-4	0.006264	0.001223	1.42E-6
1996	513128	4.740	0.4461	6.23E-4	0.006244	0.001203	1.68E-6
2052	573912	4.741	0.444	5.86E-4	0.006246	0.001198	1.58E-6
2199	387046	4.751	0.466	7.49E-4	0.006286	0.001259	2.02E-6
2291	250751	4.753	0.4633	9.25E-4	0.006282	0.001248	2.49E-6
2292	188412	4.753	0.4622	1.06E-3	0.006281	0.001244	2.87E-6
2293	248789	4.754	0.4637	9.30E-4	0.006284	0.001249	2.50E-6
2294	190029	4.752	0.462	1.06E-3	0.00628	0.001244	2.85E-6
2316	21379	4.752	0.464	3.17E-3	0.00628	0.001252	8.56E-6
2317	105672	4.746	0.4634	1.43E-3	0.006266	0.001251	3.85E-6
2319	15100	4.746	0.4621	3.76E-3	0.006266	0.001247	1.01E-5
2320	100386	4.742	0.4607	1.45E-3	0.006254	0.001243	3.92E-6
20981	245995	4.808	0.4409	8.89E-4	0.006401	0.001202	2.42E-6
21415	156514	4.814	0.4576	1.16E-3	0.006427	0.001245	3.15E-6
21435	19780	4.816	0.4597	3.27E-3	0.006434	0.001256	8.93E-6
21436	367261	4.812	0.4585	7.57E-4	0.006424	0.001252	2.07E-6
21438	59044	4.814	0.461	1.90E-3	0.006428	0.001259	5.18E-6

Table A.2: Optics data. The database used here was different from the final version. That's why the scattering angles were different from that in the published paper.